METHODOLOGY FOR PREDICTING AND/OR COMPENSATING THE BEHAVIOR OF OPTICAL FREQUENCY COMB

PhD. Thesis

By:

JAVIER FERNANDO BOTIA VALDERRAMA

UNIVERSIDAD DE ANTIOQUIA

FACULTY OF ENGINEERING

DEPARTMENT OF ELECTRONIC ENGINEERING

MEDELLÍN, COLOMBIA

2016

METHODOLOGY FOR PREDICTING AND/OR COMPENSATING THE BEHAVIOR OF OPTICAL FREQUENCY COMB

PhD. Thesis

By:

JAVIER FERNANDO BOTIA VALDERRAMA

Directed by:

PhD. ANA MARÍA CÁRDENAS SOTO

UNIVERSIDAD DE ANTIOQUIA

FACULTY OF ENGINEERING

DEPARTMENT OF ELECTRONIC ENGINEERING

MEDELLÍN, COLOMBIA

2016

Dedicatory

I would like to extend my sincere gratitude to my promoter PhD. Ana Maria Cárdenas Soto and my assessor PhD. Carlos Mario Sierra Duque, without whose academic support and orientation, this research would have been a great challenge for my professional life. I acknowledge their supports which were continuously extended very well beyond my research experience well–being with their continued ensuring my complete well–being throughout the course of this PhD research.

I am specially grateful to Faculty of Engineering, with its Professors from Graduate Program and with "Vicerrectoria de Investigaciones" at the "Universidad de Antioquia (UdeA)" who through "Fondo Beca Doctoral," collaborated to me with a scholarship for funding my doctorate studies.

I wish to express my thanks to COLCIENCIAS project called "Characterization of Ultra–short Pulses and Analysis of its Propagation in Standard Single Mode Fiber" for supporting my PhD career at the "Universidad de Antioquia". In addition, the PhD research leading to these main results has been supported by the CODI sustainability strategy 2014–2015 of the "Universidad de Antioquia".

I wish to express my sincere thanks to Prof. Andrew M. Weiner and Dr. Daniel E. Leaird for helping me and orienting me during my visiting scholar like researcher in Ultrafast Optics and Optical Fiber Communications Laboratory, Purdue University, West Lafayette, USA. In addition, I would like to thank to José Jaramillo, Amir, Poolad, Hyoung–Jun Kim, Xiaoxiao Xue, Dennis Lee, Yihan, Yang, AJ Metcalf, Pei–Hsun Wang, Joseph, Steven Chen, Ogaga, Oscar, and Abdullab for their companionship in my experience in the optical laboratory and other activities. In addition, I will always be pleased with CSAP (Colombian Students Association at Purdue) for the best moments in Lafayette and in the university.

I am specially grateful to all members of the Research Group on Telecommunications Applied (GITA) at Universidad de Antioquia (UdeA) who always were my others supports during my PhD experience, since Andrés Ocampo's jokes, Gabriel and Jesus' metal music charm, Wilmar's rock music charm, the "quartet" in speech recognition composed by Camilo "el mono", Elkyn "Kuy sabor", Tatiana (Colombian version of Emma Roberts), and "big boss" Rafael, the passion for football expressed by Jhon James (reincarnation of JR10), Ronal's madness, Jonny's seriousness, the future of single–mode fiber expressed by Andrés Betancourt (Beta[4]), the close friend in the sky and in a beautiful paradise, Edward Hernandez Arango, the expert in Capoeira, Andrés Gil, sweet and tender Stefany, Eduardo Avendaño's wisdom, Juan Diego's laughter, Roobert's responsibility, the samurai version represented by Nelson and Paola, and the undergraduates students belonging to GITA, were the source of happiness in my research experience. Moreover, I like to extend my gratitude to Prof. Alberto Florez, Prof. Natalia Gaviria, Prof. Juan Felipe Botero, and Prof. Gladys Quintero, as well as the reviewer committee integrated by Prof. José Roberto Amazonas de Almeida, Prof. Antonio Orantes, Prof. Miguel Ángel Mendoza, and Prof. Hector Hernández de León.

This PhD thesis also I want to dedicate to Botia's and Valderrama's families and to my eternal friends of my childhood, especially to José Luis Diaz Sánchez and Hernán Forero, and my friends from my formation like B.S. in Electronic Engineering, especially to Diana Riscanevo, Diego Chaparro, Julian Rodriguez, Francisco Bernal, Alex Ahumada, Giovanny Duarte, Liliana Becerra, and Miguel Andrés. In addition, I wish to say "thank you" to one of the best friend and wonderful woman for me, Jimena Rincón.

This PhD thesis also I want to dedicate to my undergraduate students of Discrete Mathematics 1 and Signal Processing Laboratory 1.

I am grateful for the rest of my life to my family for the wonderful warmth and beautiful gestures of familiar love of my dad, Prof. (r) José Salomón, my mom, Rosita, my brother, PhD. Diego José Luis, and my sister, Dra. Diana Natalia. Dad, this PhD thesis is reflected of a Salomón knew phrase that always tell me: "**Engineering as Science**". Thanks Dad by this wonderful life lesson as future scientific researcher since his teaching allows me to grow as a human being.

Finally, I extend my gratitude to Internazionale di Milano and Roman Reigns, my favorite football soccer game and my favorite wrestler man of WWE.

"During many years, science and engineering have been worked independently due to their differences and different point of view. However, in the century 21th, both are close between them and I propose a new direction in the scientific knowledge: Engineering as Science".

Prof. (r). José Salomón Botía Florez

"The word *ultrafast* is usually applied to the picosecond time scale and below. A picosecond has an extent of 0.3 mm, roughly the thickness of a business card. Given that typical garden–variety laser beams have beam diameters on the order of a few millimeters, we should perhaps envision pulses a picosecond and shorter not as pencils of light but as pancakes of light!"

Prof. Andrew M. Weiner
"Ultrafast Optics", 2009.

"Basically, *fuzzy logic* is a precise logic of imprecision and approximate reasoning. The real–world is pervaded with fuzziness. Fuzzy logic is needed to deal effectively with fuzzy reality."

Prof (r). Lotfi A. Zadeh
"*Is there a Need for Fuzzy Logic*?", 2008.

"The author is an optimist for the future of the IFSs (*Intuitionistic Fuzzy Sets*)".

Prof. Krassimir T. Atanassov
"My Personal View of Intuitionistic Fuzzy Sets Theory", 2008.

"*Cellular automata* are sufficiently simple to allow detailed mathematical analysis, yet sufficiently to exhibit a wide variety of complicated phenomena. Cellular automata are also of sufficient generality to provide simple models for a very wide variety of physical, chemical, biological, and other systems."

Stephen Wolfram
"Cellular Automata and Complexity", 1994.

ABSTRACT

Optical frequency comb spectrum can change its behavior due to temperature fluctuations, normal dispersion, and mechanical vibrations. Such limitations can affect the peak power and wavelength separation of comb lines. In the propagation through single−mode fiber, the linear and non−linear phenomena can modify spectral shape, phase shifts and flatness of spectrum. To find a strategy of compensation, the PhD thesis is focused on a prediction methodology based on fuzzy cellular automata, intuitionistic fuzzy sets and fuzzy entropy measures. The research work proposes a predictor called *intuitionistic fuzzy cellular automata based on mean vector* and a validation measure called *general intuitionistic fuzzy entropy based on adequacy and non−adequacy*. In the accomplished experiments, the method was used in three experiments: mode−locked lasers, cascaded intensity modulators−Mach Zehnder modulators, and microresonator ring. The obtained results showed that the power and phase distortions were reduced by using a pulse shaper, where the method was programmed. In addition, the stability and/or instability of spectrum were found for the microresonator ring.

Key words – Optical frequency comb; IFCA−MV; HIFEAN; mode−locked laser; IMs−MZM, optical microresonator; prediction; linear and non−linear phenomena.

TABLE OF CONTENT

Pag.

LIST OF FIGURES

Pag.

LIST OF TABLES

Pag.

LIST OF ABREVIATIONS – ELECTRICAL AND OPTICAL

AOM	Acoustic–optic modulator
APC	Adaptive fiber coupler
ASK	Amplitude–shift keying
BAPE	Brillouin–assisted power equalizer
BER	Bit error rate
CD	Chromatic dispersion
CPM	Cross–phase modulation
CPFSK	Continuous phase frequency shift keying
CMOS	Complementary metal–oxide semiconductor
CW	Continuous wave
DC	Direct current
DCF	Dispersion compensating fiber
DD–MZM	Dual drive Mach–Zehnder modulator
DGD	Differential group delay
DP–MZM	Dual parallel Mach–Zehnder modulator
DSP	Digital signal processor
DST	Direct space–to–time
EDFA	Erbium doped fiber amplifier
EPS	Electrical phase shifter
FLC	Feedback loop control
FCP	Fiber–compensating polarization
FPC	Fiber polarization controller
FPGA	Field–programmable gate array
FSR	Free spectral range
FT	Fourier transform
FWHD	Full–width at half–depth
FWHM	Full–width at half–maximum
FWM	Four wave mixing
GDD	Group–delay dispersion
GVD	Group–velocity dispersion
HVA	High voltage amplifier
HWHM	Half–width at half–maximum
IM	Intensity modulator
IR	Infrared
ISI	Inter–symbol interference
ITO	Indium tin oxide
KLM	Passively kerr–lens mode–locked vibronic–pulse lasers
LC	Liquid crystal
LCFG	Linearly chirped fiber Bragg grating
LCM	Liquid crystal modulator
MKFC	Microresonator Kerr frequency comb
MMF	Multimode fiber
MZM	Mach–Zehnder modulator
NLSE	Non–linear Schrödinger equation
O–AWG	Optical arbitrary waveform generation
OC	Optimal control

OFC	Optical frequency comb
OFCG	Optical frequency comb generation
OFCS	Optical frequency comb source
O–OFDM	Optical orthogonal frequency division multiplexing
OSA	Optical spectrum analyzer
OTNR	Optical tone–to–noise ratio
PM	Phase modulator
PMD	Polarization–mode dispersion
PMMA	Polymethyl methacrylate
PolM	Polarization modulation
PS	Pulse shaper
QAM	Quadrature amplitude modulation
QPSK	Quadrature phase–shift keying
RF	Radio frequency
SBS	Stimulated Brillouin scattering
SRS	Stimulated Raman scattering
SCSR	Side–comb suppression ratio
SESAM	Semiconductor saturable absorber mirrors
SLM	Spatial light modulator
SMF	Single–mode fiber
SPGD	Stochastic parallel gradient descent
SPM	Self–phase modulation
TCG	Tunable comb generator
TOD	Third–order dispersion
WDM	Wavelength division multiplexing
WGM	Whispering–gallery–mode

LIST OF ABREVIATIONS – FUZZY SETS THEORY AND PREDICTION METHODS

BCA	Binary cellular automata
CA	Cellular automata
CCA	Circular cellular automata
ECA	Elementary cellular automata
DNF	Disjunctive normal form
DUMPSP	Dynamic uncertain multi−project scheduling problem
FCA	Fuzzy cellular automata
FCM	Fuzzy C–means
FEAN	Fuzzy entropy by adequacy and non–adequacy
FE	Fuzzy entropy
FS	Fuzzy set
GA	Genetic algorithm
GAD	Global adequacy degree
GK	Gustafson and Kessel
GWCA	General weighted average rules
HIFEAN	General intuitionistic fuzzy entropy by adequacy and non–adequacy
HVS	Vlachos and Sergaidis's intuitionistic fuzzy entropy
IFCA–MV	Intuitionistic fuzzy cellular automata based on mean vector
IFE	Intuitionistic fuzzy entropy
IFEAN	Intuitionistic fuzzy entropy by adequacy and non–adequacy
IFS	Intuitionistic fuzzy set
IT2–FCM	Interval type–2 fuzzy cellular model
IT2–FL	Interval type–2 fuzzy logic
IV2FS	Interval−value type−2 fuzzy sets
LAMDA	Learning algorithm for multivariable data analysis
MAD	Marginal adequacy degree
NAR	Non–linear autoregressive neural network
NARX	Non–linear autoregressive neural network with external input
NIC	Non−informative class
OIUFCA	Outer−inner uncertainty fuzzy cellular automata algorithm
PDF	Probability density function
PID	Proportional−integral−derivative
PSO	Particle swarm optimization
ROC	Receiver operating characteristic
SVM	Support vector machine

CHAPTER 1: Introduction

1.1 Introductory Remarks and Motivation

From the development of optical communications, single–mode fiber (SMF) has allowed sending a large number of information channels at high transmission rate. The increase of data has generated high demand of bandwidth caused by users. The need for providing one solution has caused the search of novel techniques and methods for optical networks. One alternative is optical frequency comb (OFC) generation. For definition, an OFC is an optical spectrum with equispaced lines. The OFC generates a spectrum whose pulse train is a discrete set of frequency spaced by a constant repetition rate and their series of sharp spectral lines is well–known as *frequency combs* [SON12]. The OFC has been used for wavelength division multiplexing (WDM) and optical orthogonal frequency division multiplexing (O–OFDM) systems because can create multiple wavelengths through one laser source [SAK07a]. To obtain OFC spectrum, generation techniques such as mode–locked lasers, microresonator ring, use of non–linear phenomena, and electro–optic single–sideband modulator like Mach–Zehnder modulators (MZMs) have been developed. The OFC was applied in several scenarios such as: optical arbitrary waveform generation [JIA07], attosecond pulse generation [POP10], ultraviolet and infrared (IR) spectroscopy [GOH05], and optical communications [OHA06]. The importance of OFC has grown–up in the last years and its impact has been relevant, as shown in Fig. 1.1.

In the Annex A.10, a brief overview of the most recent advances in OFC generation is presented.

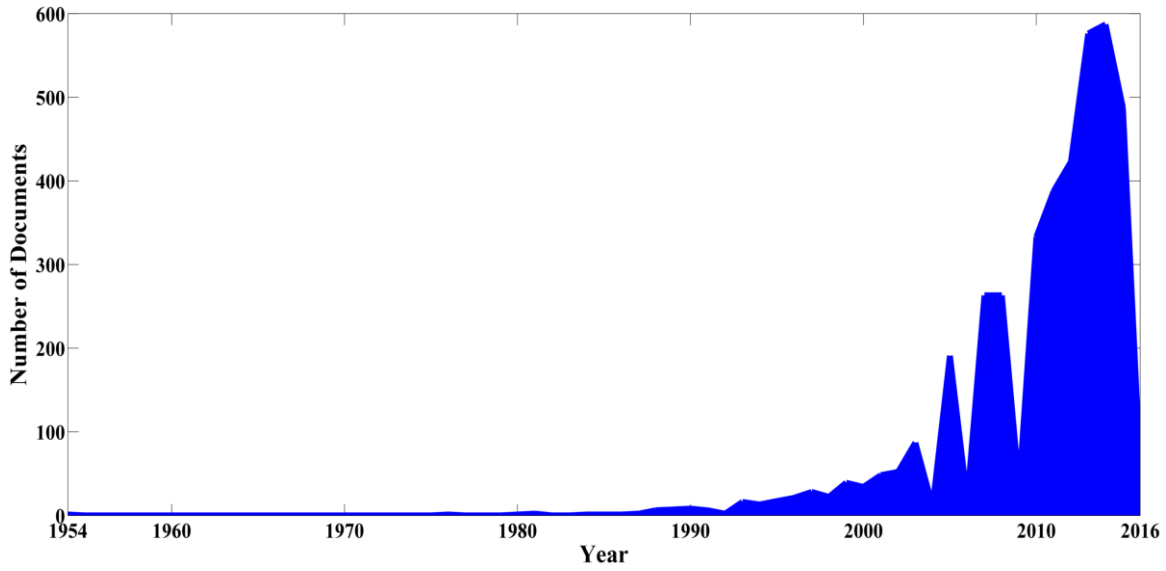

Fig. 1.1. Number of published papers per year about OFC, based on SCOPUS search. Courtesy of SCOPUS (consulted April 15, 2016).

In optics communications, mode–locked lasers, MZMs, and the Kerr microresonator ring have had greatest significance in C−band (1550 nm). Mode–locked laser is an optical signal with short duration of picoseconds, femtoseconds, and even attoseconds, although main feature is the large

spectral width [PEN11]. The OFC spectrum provides good stability but requires sophisticated control to maintain a stable operation [SHA14]. The tuning of center wavelength and frequency spacing of spectrum can become a difficult complex procedure [LEAI07]. Mode–locked lasers have been used as carriers to send data through SMF [OME02], coherent tomography, metrology, and chemical reactions measurements [SIL05].

A MZM is an optical modulator able to change the refractive index of a material (Lithium Niobate or $LiNbO_3$), generating a modulation in the beam of light [KARN96]. A beam splitter divides a continuous–wave (CW) pump laser light into two paths where the optical signal is modulated in phase according to the optical path length and the applied electric field. At the MZM output, the optical signal is phased 180° with respect to other optical signal, generating constructive or destructive interferences [YEP12]. The optical modulation is controlled by DCs and RFs source.

The microresonator ring (or microring resonator) has evolved the OFC generation at different fields due to the broad optical spectrum and good flatness. For definition, a microresonator is an ordinary waveguide that channels light in a closed loop [HEE08]. The loop has some shapes such as disk, racetrack, or ellipse but the ring shape supports transverse and longitudinal modes of beam of light. The main features of microresonator is the chip−scale integration, high repetition rates, broad spectral bandwidth, and high peak power of each comb line [HAY07]. In optical communications, the microresonator ring could create comb lines with high power (> 1 mW) and repetition rates for ranges from 25 – 100 GHz. Such advantages allow obtaining hundreds of optical channels from a single low–power off–chip source and to replace individual CW lasers.

The OFC generation is focused on how to obtain hundreds comb lines, flat spectrum, and broad spectral width. Considering the above, when one OFC spectrum is propagated through SMF, linear and non−linear phenomena affect the peak power of comb lines, generating phase shift and changing the spectral shape. Other consequence of these phenomena is the increase of BER (Bit Error Rate) and ISI (Inter−Symbol Interference), prejudicial for an optical communication system. The compensation systems have been a strategy to mitigate the impact of the linear and non−linear phenomena, improving the peak power and reducing phase shift.

Considering the impact of linear and non−linear phenomena, the main techniques for OFC generation, and the actual technology of OFC, the research is focused on the study of comb lines spectrum behavior through its propagation in SMF, the development of a novel compensation technique, and the likely limitations to recover the original spectral shape, phase, and peak power.

In the next section, the literature review and main limitation of each technique will be explained bellow.

1.2 Literature Review

In the following subsections, the most relevant compensation techniques in OFC are mentioned where the main limitation is explained in each case.

1.2.1 GVD and GDD Compensation with Prismatic Compressors and Chirp Mirrors

Description:

In optical communications, when OFC spectrum is propagated through SMF, the group–velocity dispersion (GVD) and group–delay dispersion (GDD) are generated. Since GVD and GDD are linear effects, an increase of pulse width and peak power attenuation are manifested. The linear effects generate inter–symbol interferences and a close eye diagram which the transmission rate is limited for long−haul transmission. Devices such as prismatic compressors and chirp mirrors can mitigate the chromatic dispersion. The former is a pair of prisms for developing a negative GVD or GDD [AKT06] [DUA09]. The latter is a set of reflective layers capable to provide a similar effect than prismatic compressors [NOH08].

Limitation:

The compensation techniques based on prismatic compressors and chirp mirrors are efficient in free space experiments but it is not useful in optical communications systems. The main reason is the complexity to manipulate the refractive angles and distance whether the number of prims or chirp mirrors is increased to compensate GVD and/or GDD. In addition, a collimator is required to collimate the light in free space to an optical fiber output.

1.2.2 GVD Compensation with Feedback Loop Control

Description:

The feedback loop control (FLC) was developed to reduce the chromatic dispersion in optical combs spectrum by using *control strategies and computational algorithms*. The technique uses an optimal control (OC), whose goal is the reduction of the electrical field variations produced by an OFC generator (in that case, mode–locked lasers) and to avoid the frequency combs shift [GOL08]. The OFC is expressed as an optimization model whose solution is obtained by genetic algorithms (GAs). The above is well–known as OC–GAs where the best model solution identifies the amount of phase and/or intensity correction to compensate the spectrum through a spatial light modulator (SLM)[1]. The feedback loop control has been applied in several fields as explained below. In [OME02], an experiment at 10 m SMF in feedback, using a picosecond pulsed laser and a pulse shaper (PS), achieved to mitigate GVD and residual dispersion. In [NUE09], the feedback control is used for the generation and characterization of polarization–shaped femtosecond laser pulses in the ultraviolet at 400 nm. In [SHE10], an adaptive algorithm in a closed loop was developed for compensating modal dispersion in multimode fiber (MMF) through SLM. The above is efficient to 10 Gb/s transmission through up to 2 km of 50– μm–core graded–index MMF. In [RÜT12], a time–frequency von Neumann representation of femtosecond laser pulses was proposed to obtain an intuitive picture for the time– and frequency–dependent polarization state and to carry out a

[1]For definition, a SLM is an optical programmable device controlled by voltage where its main feature is a thin layer of nematic liquid crystal placed between two glass substrates made by indium tin oxide [MON10].

quantum control. In [WEN14], an adaptive fiber coupler (APC) is used to mitigate angular jitters, improving the SMF coupling whose closed loop is established by a photodiode, a computer with a stochastic parallel gradient descent (SPGD) algorithm and a high voltage amplifier (HVA).

Limitation:

The feedback loop control has been useful in coherent laser control for quantum mechanical processes but in optical communications, it is limited due to that a large length of SMF in feedback is complex for the real optical network.

1.2.3 GVD Compensation with Open Loop Control

Description:

The open control loop considers the desired output waveform, reasonable knowledge of the input pulse and the desired transfer function (if it is known) for constructing one simple program the pulse shaping SLM [WEI11]. If an additional linear distortion occurs between the input and the output during the first iteration of control, the pulse shaping in SLM can be programmed to include a pre–compensation in the transfer function although *the high resolution and precise calibration of SLM is mandatory to obtain optimal results*. The open loop control was used to compensate GVD in a propagation of sub–500 fs pulses in 3 km SMF [CHA98] and 50 km SMF [JIA05], where a dispersion compensation fiber (DCF) is included to mitigate the lowest order dispersion. Others experiments made by [SAN03] use the pulse shaper (PS) to compensate residual dispersion after DCF in optical links at 10 Gb/s and it allows compensating dispersion in a CW laser modulated at 10 Gb/s at SMF of 240 km [LEE06]. Other relevant work presented by [YOU08], proposes an improvement of open loop control by using genetic algorithms (GAs) in order to mitigate GVD and self–phase modulation (SPM) effects. The used technique is called dispersion– and power–map co–optimization.

Limitations:

The open loop control is efficient to compensate residual dispersion after DCF but in real experiments, the GVD interacts with others non−linear phenomena. Therefore, the compensation will be restricted in the reduction of chromatic dispersion and the mathematical model of the algorithm control would be complex whether the interaction between linear and non−linear phenomena is considered. The above represents many physical variables and parameters in the optimization model, which generate an increase of computational time for tasks in real time.

1.2.4 Flatness Correction in OFC

Description:

One relevant aspect of study of OFC stabilization is the flatness correction to equalize comb carriers in a broad bandwidth. The flatness has been improved by different techniques such as spectral phase correction with a pulse shaper (PS) [FERD11], manual adjusting of DC Bias [SHA14], Stimulated Brillouin Scattering (SBS) fiber loop [DU13], nonlinear effect of intensity

modulator (IM) [DOU11], and cascaded four–wave mixing [SUP12]. Many works in flatness correction have been focused on OFC−MZM in the transmission stage. In [SAK07b], a conventional dual–drive MZM for optimizing large–amplitude sinusoidal signals at different values can generate OFC with good spectral flatness. In [DAI13], a flat spectral comb was generated by using a dual–drive MZM (DD–MZM) connected by a SMF, for inducing chromatic dispersion (CD) needed for the waveforms generation. The variables required to generate waveform are: the amplitudes of the modulating radio–frequency (RF) signals, the phase difference between the two RF signals, the difference of the two bias voltages of DD–MZM, and the CD of the SMF. In [CHEN14], a tunable comb generator (TCG) was developed by cascading a single–phase modulator (PM) with two identical intensity modulators (IMs). The TCG was proposed through the theoretical analysis of mathematical model for optical comb source generation to find out the modulation index and the normalized DC voltages. In [HRA14], the generation of an ultra–flat optical comb source (OFCS) was created by using an asymmetrically driven dual arm–MZM (DA–MZM). The above was carried out through a modified simulated annealing–based optimization method. In [HUA06], the stability of frequency was achieved with the monitoring mechanism for optical frequency fluctuations in MZM−OFC based on pulse shaper (PS) [HUA06].

Limitations:

The flatness and frequency stability methods are based on mathematical models which are validated by simulation or experimentation. However, none of those strategies include historical data to anticipate the OFC behavior. The above is required to obtain a flat and stable optical comb in the time [FERD11].

Based on the study of the main OFC generation techniques and the GVD and flatness compensation methods, the research problem is described in the next section.

1.3 Statement of Problem

Based on the explanations of compensation methods in OFC, several problems were identified, as shown below:

- The mentioned techniques and methods for anticipating the behavior of an OFC spectrum are based on mathematical models and numerical simulation. However, *the prediction with historical data* has not been considered in OFC. This alternative can improve the OFC behavior observations in a future time, without the use of numerical simulations or mathematical models. In addition, the prediction with data can be applied in real–time to analyze different behaviors of OFC spectrum and to carry out a correction process of power variation, phase, and spectral shape.

- If the optical system requires to *optimize several physical variables, e. g. optical shape, phase, polarization, average power, central wavelength variation, among others, the GAs must consider many variables which can increase the number of fitness objectives* (multi–objective optimization), *to readjust the constraints, and to modify their operators* (mutation, crossover, number of individuals, selection, etc). Therefore, the risk of a high computational cost for real–

time would be inefficient and the possibility of convergence in a global optimal may become critic. In addition, the GAs start from infactible solutions due to the used metaheuristics which it requires to known the number of generations (or iterations) to find the best solution.

- In literature, the open loop control have been applied to mitigate all kind of chromatic dispersion and in little opportunities with SPM, but in a real scenario, these phenomena are interacting with other non–linear effects such as Stimulated Brillouin Scattering (SBS), Stimulated Raman Scattering (SRS), four wave mixing (FWM), cross–phase modulation (CPM), and changes of polarization–states and propagation modes due to the transmission rate, the SMF geometry, and external variables variations like temperature or mechanical vibrations, associated with polarization–mode dispersion (PMD). Hence, if adaptive algorithm is used to mitigate them, *the optimization model will be complex and to fix a reasonable number of generations to find the solution could be difficult to obtain*. In addition, if the interaction of all phenomena will become critic, *a possible chaos condition can create abnormal behaviors and its mitigation could be difficult*.

By identifying the problems of open loop control and the limitations of prediction using mathematical models and numerical simulations, the next section will focus on the main topics to propose a novel methodology for predicting and/or compensating of abnormal behaviors of OFC spectrum after propagation in SMF.

1.4 Research Topics

Based on the limitations of open loop control and flatness correction in OFC, this section will explain new alternatives for proposing a novel approach for tasks of prediction and/or compensation of spectrum when the interaction of linear and non–linear phenomena are considerable in transmission. The PS is useful for monitoring the optical frequency fluctuations at the input comb was presented and experimentally validated by [HUA06]. The above was applied to the study of OFC behavior based on mathematical models and validated by simulation or experimentation. However, none of those strategies include historical data to analyze the OFC behavior with the purpose to design a compensation method. Due to this limitation, one alternative is the use of Fuzzy Sets (FSs) theory [ZAD65], which could anticipate the changes of peak powers and phase shifts for an OFC propagated through SMF.

Considering the scenario of research, three main topics are explained below:

1.4.1 On Prediction Method

Since the prediction method is relevant to achieve the compensation, the best prediction technique based on FSs must be identified. In literature, various prediction approaches have been developed in the last 50 years such as: Times Series Analysis, Extrapolation Method, Survival Analysis, Bayesian Classifiers, Cluster Analysis, Support Vector Machine (SVM), Monte Carlo Analysis, Lyapunov Exponent, Hurst Exponent, Non–linear Autoregressive Neural Network (NAR), and Non–linear Autoregressive Neural Network with External Input (NARX). Such methods have been useful in multiple applications such as: metrology, forecasting, dimensional reduction, decision making in business, among others. The main component of prediction methods is the temporal analysis of one or more variables of system. However, *the prediction methods do not*

*consider the **spatial analysis***. This additional component allows visualizing the evolution of variable through a spatial and geometrical representation before a global change in temporal domain. The spatial analysis is independent of time representation but the total evolution of variable can be observed in the temporal analysis.

Considering the need of temporal–spatial prediction, the *automata theory* has been a new key for developing novel robust systems from pattern recognition to tasks of prediction [MOD02]. Jhon von Neumann introduced the idea of cellular representation for dynamical systems with non–linear behaviors at end of 1940's. The above was known as *cellular automata* (CAs), where the dynamic is represented as a discrete system whose geometric structure is a *spatial representation*. CAs were developed as formal models of self–reproducing organisms in one– and two–dimensional infinite grids, although higher dimensions were used [SAR00]. Nevertheless, the *Game of Life* created by John Conway and written by Martin Gardner allowed increasing the popularity of CAs [GAR70]. Afterwards, Stephen Wolfram formalized the *elementary CA* where he showed that the universe is "intrinsically" discrete [WOL02]. Such works were applied to observe many types of behaviors and phenomena within a high non–linear system. Although the performance of CAs is useful to observe multiple behaviors, the discrete states representation on binary values is limited. The main reason is the little possibilities to find new behaviors of a non−linear system.

One alternative to observe more behaviors for a system is other cellular structure called *fuzzy cellular automata* (FCAs), developed by [CAT93] and [CAT97]. Unlike CAs, FCAs contain cells whose states are continuous between 0 and 1. The above is well–known as *continuous cellular automata* (CCAs). This type of FCA finds the *spatio–temporal prediction in chaotic system*. FCAs have evolved in the last 30 years and its importance can increase in the future, as shown in Fig. 1.2.

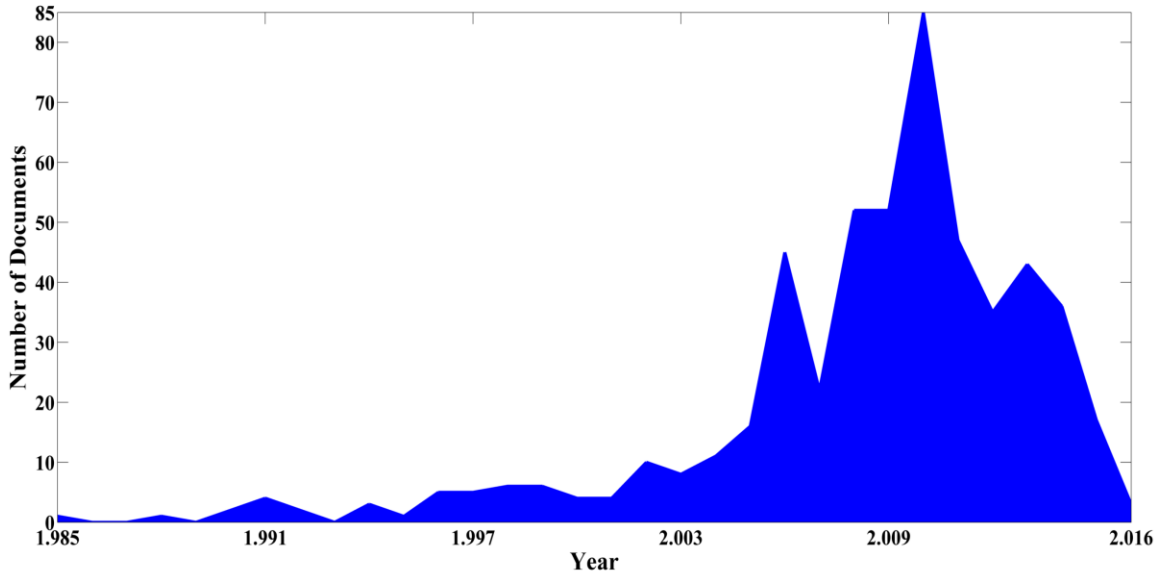

Fig. 1.2. Number of published papers per year about FCAs, based on SCOPUS search. Courtesy of SCOPUS (consulted April 15, 2016).

Taking into account the above, *the first topic of research will be focused on the proposal of a novel prediction approach based on FCAs* where the main development is the abnormal behaviors detection and prediction for OFCs spectra. Since the FCAs use type–1 fuzzy sets (FSs), *the*

evolution rules ignore the degree of indetermination or hesitancy degree of continuous states. This consideration can affect the identification of real chaotic behaviors when the prediction is generated in real−time. In addition, the influence of uncertainty in the prediction step can become critic. For instance, by observing the changes of flatness of OFCs spectrum in a future time while the optical spectrum is measured in real–time, the interaction between linear and non–linear phenomena can generate chaos during the propagation in SMF. This scenario can be critic when the average power increases and the transmission rate is over 40 Gb/s. Since polarization−mode dispersion (PMD) affects the interaction, the random variations of polarization states can limit the capacity of optical channel and the uncertainty of OFCs behavior can affect the prediction.

1.4.2 On Intuitionistic Fuzzy Sets

To improve the capacity of FCAs, other type of FSs must be selected. In literature, various proposals have been developed from 1970's where the most relevant are: interval–value fuzzy sets (IVFSs), ℓ–fuzzy, type–2 fuzzy sets, interval–value type–2 fuzzy sets (IV2FS), and rough–fuzzy sets. Although FSs have been expanded in several extensions, the indetermination among FSs is little explored in tasks of prediction. Seeking the different proposals, the *intuitionistic fuzzy sets* (IFSs) bring this requirement. IFSs were developed by Krassimir T. Atanassov [ATA86] [ATA12] where the degree of non–determinacy is defined through the membership and non–membership degrees for a FS. The concept of intuitionism was introduced by L. Brouwer [BRO75] to remove Aristoteles' law of excluded middle[2]. According to [SZM14b], IFSs analyze the imprecise information of any real world phenomenon when the system has various and inherent facets of imperfect information. In OFC scenario, IFSs could be useful to know the changes of phase and/or power in an OFC spectrum when the interaction between linear phenomena, non−linear phenomena, and PMD can generate random behaviors. Based on the above explanation, IFSs can contribute to improve the capacity of prediction for novel FCA applied to OFC spectra.

In Fig. 1.3, the exponential increase since 2002 until present day allows verifying the impact of IFSs in the development of FSs theory. Therefore, *the second topic of research is the FCAs proposal based on IFSs* with an additional component: low computational costs and optimal performance for tasks in real–time to compensate the flatness and phase shifts in OFCs spectrum.

1.4.3 On Fuzzy Entropy and Intuitionistic Fuzzy Entropy Measures

One relevant aspect of novel approach is the prediction validation. In [PALM08], various validation measures to analyze the performance of pattern recognition methods such as receiver operating characteristic (ROC) analysis, sensibility analysis, Rini's analysis, cross–validation, Bootstrap, among others, have been developed. Although these analysis techniques are used, the prediction of one variable is changing in a future time which the data can vary. In OFCs spectrum, if the linear and non–linear phenomena are interacting, the spectrum can carry toward the instability of power and phase. Due to this type of situation, the OFC spectrum can change in phase, power, and shape and therefore, the future variation of any physical variable could be biased.

[2]The idea of intuitionism is to simply the following case: "For an event *X*, we can state that either A is true, or A is false, or that we do not know whether A is true or false"

One alternative to validate any prediction from OFC spectrum is the *entropy theory*. For definition, the entropy measures the amount of information of an event. Extending the concept of entropy, the uncertainty for one FS can be measured through *fuzzy entropy* (FE) which it will be the point of start to create a novel entropy measure. In [LUC72], the axioms of FE were defined through Shannon's probability theory to measure the fuzziness for a

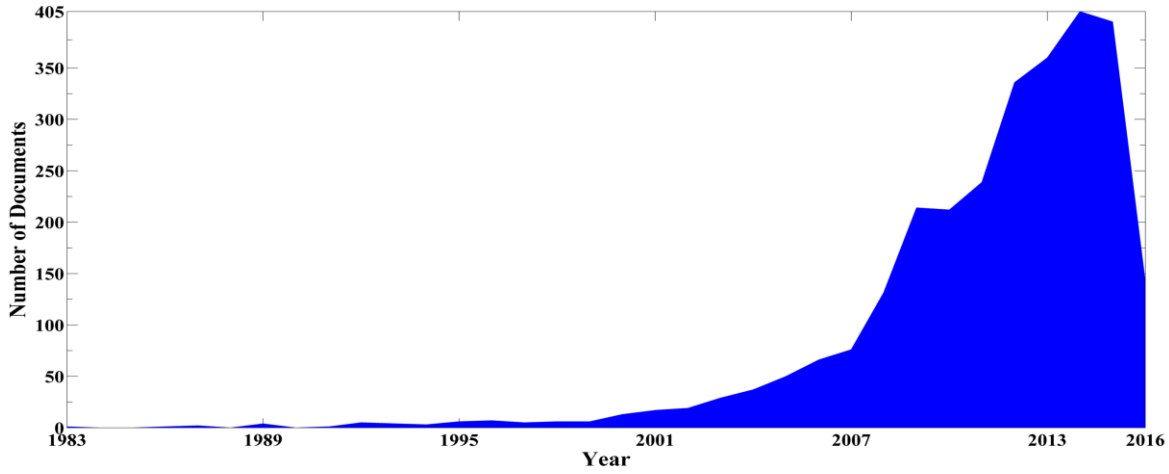

Fig. 1.3. Number of published papers per year about IFSs, based on SCOPUS search. *Courtesy of SCOPUS* (consulted April 15, 2016).

Based on this work, several proposals for measuring the uncertainly within a FS were developed in the last 43 years (in chapter 3, a full explanation of FE will be presented). Since 1992 until present day, the number of publications has been increased, as observed in Fig. 1.4. Since the importance of IFSs to create robust FCAs was mentioned before, the FE must consider the degree of indeterminacy, which the *intuitionistic fuzzy entropy* (IFE) (in chapter 3, a depth explanation of

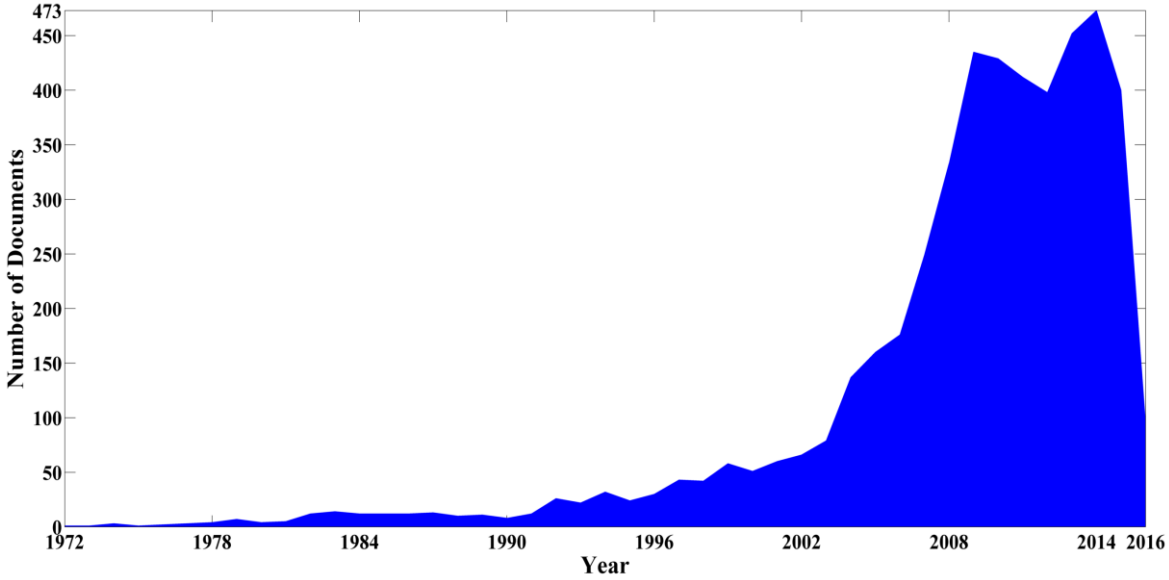

Fig. 1.4. Number of published papers per year about Fuzzy Entropy, based on SCOPUS search. *Courtesy of SCOPUS* (consulted April 15, 2016).

IFE will be shown) will be considered for proposing a validation measure for FCAs based on IFSs. Considering FE and IFE, *a generalized measure is the most relevant strategy to validate OFC spectra after the prediction. The above will be the third topic of research.*

By means of the three research topics, the main idea is the development of *a general methodology for tasks of prediction and/or compensation of OFCs spectrum* where the stability of each comb, the conservation of spectral shape after its propagation in SMF, or the identification of relevant and chaotic changes of spectrum will be the point of attention. In the research, three different OFC generators are considered: mode–locked lasers (picosecond and femtosecond pulses generators), cascaded MZMs, and microresonator ring. To make a full analysis of performance of proposed approach, the computational costs, analysis of correlation, and ANOVA (analysis of variance) will be shown in the document, as well as the throughput of prediction and/or compensation.

In the next section, the organization of document and the goals of research will mention below.

1.5 Thesis Outline and Goals

In PhD thesis, goals of research are shown below:

Main goal:

Propose a prediction approach of dynamic of optical frequency combs using fuzzy cellular automata, intuitionistic fuzzy sets, and fuzzy entropy measures to improve the open loop control for an optical communication system.

Secondary goals:

- Understand the linear and non–linear phenomena that affect the OFC propagation in a single–mode fiber.
- Select some temporal and/or spectral representation of OFC spectra that allow evaluating its dynamic during the propagation in single–mode fiber.
- Propose a prediction approach based on data spectral or temporal in order to identify and/or compensate the OFC spectrum due to the presence of linear and non–linear phenomena during the propagation in single–mode fiber, instabilities of its flatness in the transmission step, or possible external variation that affect its throughput.
- Evaluate the performance and robust of prediction approach using simulations of optical communications networks.
- Carry out several experimental set–up to analyze the results of prediction approach through the measurements of computational costs and statistical tools.

The present document is organizing as follows:

Chapter 2: Preliminaries

In this chapter, the concepts of OFC, the main OFCs generators, and the OFCs throughput during the propagation in SMF are described whose main point of interest is to mention the most relevant aspects, advantage, and disadvantage for optical communications. The second part of

chapter is focused on the fuzzy sets theory, intuitionistic fuzzy sets, and fuzzy clustering. These concepts will be used for the development of the following chapters.

A first exploration of the use of fuzzy clustering methods in OFC spectrum was published in IEEE−COLCOM 2012, although paper is called "*GVD and SPM Optimization in Optical Fiber Using a Hybrid Method*". Another exploration about the interaction PMD and SPM during the OFC propagation in SMF was published in COMTEL 2013, entitled "*Influence of the Interaction PMD and SPM in the Polarization Shift Keying (PolSK) Modulation Using Ultrashort Pulse as Carrier*".

Chapter 3: HIFEAN: General Intuitionistic Fuzzy Entropy by Adequacy and Non–Adequacy

A brief introduction of fuzzy entropy and its importance in the analysis of OFCs spectrum is mentioned. The explanation of a novel fuzzy entropy measure based on the adequacy and non–adequacy degrees for a FS is shown. The new measure is called fuzzy entropy by adequacy and non–adequacy (FEAN). Considering FEAN, the concept is extended for IFSs which allows developing a general measurement of entropy for FSs and IFSs. This novel approach is called general intuitionistic fuzzy entropy by adequacy and non–adequacy (HIFEAN). The novel entropy measure will be used in the experiments set–up like prediction validation of OFC spectrum. To evaluate the performance from simulation, three applications were selected: analysis of optical combs spectra using one MZM, optical combs spectra detection using cascaded MZMs, and second–order PMD detection in an ultra–short pulse spectrum.

The mathematical models and the main results of this chapter allowed writing one international conference paper (IEEE−CIVEMSA 2013), called "*Fuzzy Entropies by Adequacy and Non−Adequacy Applied to the Analysis of Combs Spectra Stability*", and one journal paper (in processing to be submitted to Information Science, ElSevier), called "*General Intuitionistic Fuzzy Entropy by Adequacy and Non–adequacy (HIFEAN): Applications for Analyzing the Comb Lines Behavior in Optical Spectra*".

Chapter 4: IFCA–MV: Intuitionistic Fuzzy Cellular Automaton based on Mean Vectors

This chapter explains the novel prediction approach. An introduction and the evolution of cellular automata are exposed where fuzzy cellular automata are detailed from point of view mathematic and illustrative. Considering the main basis of FCAs, the proposed approach called intuitionistic fuzzy cellular automaton based on mean vectors (IFCA–MV) is explained. To verify the performance of approach, a simulation of ultra–short pulses behavior represented by a spatial light modulator (SLM) is shown. The simulation considers a mask representation of liquid crystal of SLM (LC–SLM). The main idea of simulation is to observe the optical spectrum behavior by observing the influence of free space where the pulsed signal is propagated. Based on the obtained results and the mathematical model of prediction approach, the analysis and discussion of results are shown.

The mathematical model of IFCA−MV and its application in OFC allowed writing one journal paper (in processing to be submitted to Engineering Applications of Artificial Intelligence,

ElSevier), called "*Intuitionistic Fuzzy Cellular Automata Based on Mean Vector (IFCA−MV) and its Application in OFC generated by Mode−Locked Lasers*".

Chapter 5: Experimental set–up and Results

The chapter begins with a brief introduction of general methodology using IFCA–MV and HIFEAN and its application in a laboratory. Based on the description, three experiments were carried out during the internship in the *ultrafast optics and optical fiber communications laboratory in Purdue University, West Lafayette, USA*.

The first experiment is the correction of phase and/or peak power in OFC spectra generated by picosecond and femtosecond pulses lasers. The OFC spectrum is propagated through 25 km of SMF. At the SMF output, one pulse shaper (PS) is used to carry out the correction of spectrum through a laptop or computer where the proposed method is written in Matlab.

The second experiment is a correction of flatness in one OFC spectrum generated by cascaded MZMs (Intensity modulators) where the prediction allows verifying the stability of flatness before and after the correction carried out by one PS.

The third experiment is the analysis of stability of OFC spectra generated by several microresonator ring sizes. For the experiment, the influence of noise in OFC generation is considered. The prediction results are analyzed to identify the best and the worst stability of spectrum, considering the presence of external physical variables such as temperature and mechanical vibrations.

An analysis of proposed method is shown in the document. To do the method evaluation, the calculation of computational cost, analysis of correlation, ANOVA, phase shifts, changes of power of comb lines, and SCSR are described.

From the experiments results of this chapter, one journal paper was submitted to Engineering Applications of Artificial Intelligence− ElSevier, called "*Fuzzy Cellular Automata and Intuitionistic Fuzzy Sets Applied to Optical Frequency Comb Spectral Shape"*

The rest of document is organized as follows: conclusion of PhD thesis, references, VITA, and annexes.

CHAPTER 2: Distortions Compensation in OFC with Pulse Shaping and Study of Fuzzy Sets Theory

2.1 Introduction

The optical frequency comb (OFC) is an optical spectrum composed by equispaced lines. The OFC has been a large spotlight for community in optical communications and photonic due to great quantity of comb lines that allows generating multiple optical channels in a broad range of wavelength. This advantage has helped to reduce the number of Continuous Wave (CW) lasers and the complexity of multi−carrier communications systems like WDM (Wavelength Division Multiplexing) and O−OFDM (Optical−Orthogonal Frequency Division Multiplexing). In real experiments, OFC is not separated due to the changes between phase and group velocities. In addition, the power variations of OFC also affect the quality of optical comb spectrum which the flatness is not constant. Other important aspect is the capacity of OFC spectrum to support the linear and non–linear phenomena when it is propagated through Single–Mode Fiber (SMF). Since optical communications requires flat comb lines and a stable separation among them, the OFC characteristics must be considered as well as to find novel alternatives in OFC generation.

Inside of multiple alternatives to improve OFC spectrum, the open loop control can reduce the influence of chromatic and residual dispersion as well as to control the changes of phase and peak power. Inside open loop control, the pulse shaper is a device useful for manipulating spectral components in intensity, phase and/or polarization states of an optical wave. To carry out the control of pulse shaper (PS), an efficient computational algorithm is required to achieve the best correction OFC spectrum as possible. Given the advantages of fuzzy clustering to classify historical data and with the possibility to carry out adjustable compensations in the optical system, in this chapter, the basic concepts of fuzzy sets (FSs) theory are explained. In that case, the FSs theory is the best point of start for creating a novel method to recover the original OFC spectrum after its propagation in SMF.

The chapter is organized as follows: 2.2) Optical Frequency Comb; 2.3) Pulse Shaping; 2.4) Fuzzy Sets Theory; 2.5) Fuzzy Clustering Methods and 2.6) Summary.

2.2 Optical Frequency Comb

An optical frequency comb (OFC) consists of an optical spectrum of equispaced lines; its spectrum is a pulse train represented by a discrete set of frequencies spaced with a constant repetition rate [SON12]. The applications using comb lines have been used in research areas, including attosecond pulse generation [KIP11], ultraviolet and infrared spectroscopy [YOS11], astronomical spectrograph calibration [MUR12], and telecommunications [PFE14].

In a general expression, an OFC is defined as complex electrical field lines, given by:

$$E(f)=\sum_{m=0}^{\infty}A_m\delta\left(mf_{rep}\right)exp\left(j\phi_m\right) \tag{2.1}$$

where f_{rep} refers to the repetition frequency, A_m is the amplitude of the m–comb line, ϕ_m is the phase of the m–comb line, and $\delta(mf_{rep})$ is the Kronecker delta function of the m–comb line

associated with the repetition frequency. Usually, Eq. (2.1) is derived from mode–locked lasers (in the subsection 2.2.1, a full explanation about these lasers will be shown), where it generates a Gaussian envelope. Considering a real experimentation to obtain OFC spectra, each OFC has a difference in–phase, amplitude, and group velocity with respect to other OFC which a frequency offset is presented. In Eq. (2.2), a realistic OFC expression is defined as [UDE02]:

$$f_m = mf_{rep} + \varepsilon \tag{2.2}$$

where mf_{rep} represents the multiples of the laser repetition rate and ε is the carrier envelope offset frequency which is time–varying and can undergo large fluctuations without stabilization mechanisms. In Fig. 2.1a and Fig. 2.1b, the ideal and real representations of an OFC spectrum are illustrated.

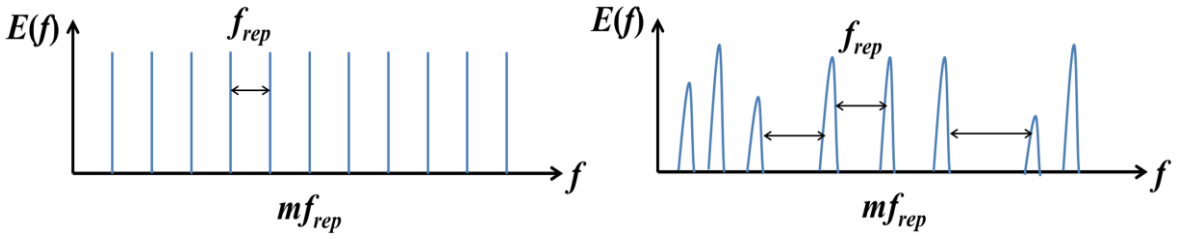

a) Ideal OFC spectrum b) Real OFC spectrum

Fig. 2.1 OFC spectrum for: a) ideal OFCs and b) real OFCs.

Other OFC representation is obtained by phase–modulating a continuous–wave (PMCW) in the time–domain although output time–domain field is defined by Bessel's series, as shown below [HUA08]:

$$\begin{aligned} \boldsymbol{E(t) = E_0 exp\left\{ j\left(\omega_0 t - \beta cos\left(\omega_{rep} t\right)\right)\right\}} \\ = E_0 \sum_{m=-\infty}^{\infty} J_m(\beta) exp\left\{ j\left(\omega_0 - m\omega_{rep}\right)t\right\} \end{aligned} \tag{2.3}$$

where ω_0 is the carrier frequency (in radians), E_0 is the magnitude of electrical field, ω_{rep} is the frequency repetition (in radians), J_m is the Bessel function of m–comb line, and $\beta = \pi V_p / V_\pi$ (modulation index), being V_p the applied peak signal voltage and V_π the voltage required to create a π phase shift by the modulator. Considering the frequency–domain, OFC amplitudes are expressed in terms of $J_m(\beta)$ and f_{rep}. The Eq. (2.3) is a typical expression to understand the OFC generation using Mach–Zehnder Modulator (MZM), which is explained in subsection 2.2.2.

In the following subsection, an extend explanation of mode–locked lasers is described below.

2.2.1 Mode Locked Lasers

- *Evolution of Mode Locked Lasers:*

A laser is said "mode–locked" when the oscillating modes are forced to maintain equal frequency spacing at a fixed phase relationship to each other, which its output will vary as a function of time in a well–defined manner [SMI70]. According to the generated phase and modes, the form of output can be different (e.g. cosh, Gaussian, among others).

Theodore Maiman proposed in 1960 the first working laser by using Q–switching in a laser cavity. This technique allows generating pulses that are much shorter than the round–trip time in the cavity and it is based on the generation of many longitudinal modes with defined phase relations [WEI95]. The modes can be obtained by applying a light modulator into a laser cavity. In literature, two kind of mode−locked have been proposed. *Active mode−locking* generates a periodic modulation through a resonator losses or modulating the round–trip phase variation with an acoustic−optic or electro−optic modulator or a semiconductor electro−absorption modulator. By considering this idea, the first work ultrashort pulse (picosecond) is developed by using a cavity of a ruby or Nd as a saturable media [MAR66]. On the other hand, *passive mode−locking* [MAR69] allows generating pulses at ultra−short duration (femtosecond) due to a saturable absorber able to modulate the resonator losses much faster than an electronic modulator. The above creates an ultrafast pulse that involves a sufficiently short recovery time faster than active mode−locking.

A theoretical model explains the ultra–short pulse formation in passive mode–locked was proposed as a fluctuation model. This fluctuation is explained through the need of removing from the cavity all the elements capable of selecting longitudinal modes [KRY72]. The result of this model is a *saturable absorber* as an element to reach a short relaxation time of pulse. In this short time is explained by two thresholds. In the first threshold, a free–running multimode lasing is generated and, therefore, a certain excess over the amplification allows observing a train of ultra–short pulse. The second threshold occurs if absorption of the saturable absorber is presented and the amplification decreases. Another important characteristic is the different change of pulse shape defined by [LIND72].

During the evolution of ultra–short pulse (picosecond duration) and ultra–rapid pulse (femtosecond duration), several generation techniques were developed such as: organic dye laser [IPP75], additive pulse mode–locking [BLO88], passive saturable absorber [PAY89], Semiconductor Saturable Absorber Mirrors (SESAM) [KEL94], passively Kerr–lens mode–locked vibronic–pulse lasers (KLM) [ELL01], Diode–pumped femtosecond fiber lasers [NEL97], and mode–locked fiber lasers [CHO08]. The actual tendency is the attosecond pulses [CORK07] generated by over–dense plasmas to develop constructive interferences of many harmonics of the pump laser locked in–phase [LAV11]. Other tendency is the revolution of femtosecond OFC in optical synthesis and metrology [UDE02], and molecular spectroscopy and optical clocks to optical and radio–frequency arbitrary waveform generation [NEW11].

- *Ultra–short Pulses:*

Ultra–short pulses are electromagnetic energy impulses of short duration, typically of order of picosecond, femtosecond, and even attosecond, although power peak can reach the order of MW [MON10]. Mathematically, an ultra–short pulse is represented by the electrical field in time–and frequency–domains, given by:

$$E(t)=\frac{1}{2\pi}\int_{-\infty}^{\infty}E(\omega)exp\left(-j\omega_0 t\right)d\omega \tag{2.4}$$

$$E(\omega)=\int_{-\infty}^{\infty}E(t)exp\left(j\omega_0 t\right)dt \tag{2.5}$$

From Eq. (2.4), $E(t)$ can be defined as the product between the temporal amplitude, $A(t)$, and the temporal phase, $\phi(t)$. Also, from Eq. (2.5), $E(\omega)$ can be expressed as the product between the spectral amplitude, $A(\omega)$, and the spectral phase, $\phi(\omega)$. Both definitions are shown below:

$$E(t) = A(t)exp(j\phi(t)) \tag{2.6}$$

$$E(\omega) = A(\omega)exp(j\phi(\omega)) \tag{2.7}$$

A relevant aspect of ultra–short pulses is the pulse intensity per area unit, $I(t)$, dependent of refraction index of material, η, and E(t), expressed by [GOL08]:

$$I(t) = \frac{1}{2}\varepsilon_0 c\eta |E_o|^2(t) \tag{2.8}$$

where ε_0 refers to the dielectric constant in vacuum, c is the light velocity ($3x10^8$ m/s), and $|E_o|^2(t)$ is the pulse intensity in Watts unit. In frequency–domain, the average of spectral intensity of a pulse, $I(\omega)$, is expressed as:

$$I(\omega) = \frac{1}{4\pi}\varepsilon_0 cn |E_o|^2(\omega) \tag{2.9}$$

being $|E_o|^2(\omega)$ the pulse intensity in frequency–domain. The useful of Eq. (2.8) and (2.9) carry towards the measurement of pulse duration in terms of time, Δt, or in terms of frequency, $\Delta\omega$, which two kind of measurements are widely used: *half–width at half–maximum* (HWHM) and *full–width at half–maximum* (FWHM) [WEI09]. The term Δt can be calculated by a statistical model through an average of pulse duration, $<\Delta t>$ [ANT06], as shown below:

$$\langle \Delta t \rangle = \frac{\int_{-\infty}^{\infty} t|E(t)|^2 dt}{\int_{-\infty}^{\infty} |E(t)|^2 dt} \tag{2.10}$$

Being $|E(t)|^2$ the intensity of electrical field. The spectral width, $<\Delta\omega^2>$, is defined as the standard deviation of $\Delta\omega$, given by:

$$\langle \Delta\omega^2 \rangle = \frac{\int_{-\infty}^{\infty} \omega^2|E(\omega)|^2 d\omega}{\int_{-\infty}^{\infty} |E(\omega)|^2 d\omega} \tag{2.11}$$

Based on Eq. (2.10) and (2.11), the relationship between $\Delta\omega$ and Δt is expressed by Heisenberg's uncertainly principle, defined as:

$$\Delta\omega \cdot \Delta t \geq K \tag{2.12}$$

where K is a constant parameter dependent of pulse shape. Taking into account the criterion FWHM, several pulse shapes can be generated but the most popular are: Gaussian (K = 0.441), Secant Hyperbolic (K = 0.315), and Lorentzian (K = 0.142). Eq. (2.12) is important to find out the complexity measure of a specific pulse shape and this condition allows establishing that any shape cannot overcome the K value. The above is important to indicate that the pulse shape is maintained

only if it is limited by Fourier's transform [WEI09]. Considering the typical pulse shapes, Eq. (2.13), (2.14), and (2.15) show the electrical fields for Gaussian, secant hyperbolic and Lorentzian envelopes, respectively.

$$E(t) = exp\left(-\frac{\left(\frac{t}{t_0}\right)^2}{2} \right) \tag{2.13}$$

$$E(t) = \frac{1}{cosh\left(\frac{t}{t_0}\right)} \tag{2.14}$$

$$E(t) = \frac{1}{\left(1+\left(\frac{t}{t_0}\right)\right)^2} \tag{2.15}$$

where t_0 is the instant of time where the peak power of pulse is maximum. Eq. (2.12) can be redefined as the minimal pulse duration in terms of wavelength width, $\Delta\lambda$ (μm or nm), considering FWHM, as shown below:

$$\Delta t \cdot \Delta\lambda \geq K \frac{\lambda_0^2}{c} \tag{2.16}$$

where λ_0 is the central wavelength.

Since in Eq. (2.2) is mentioned that the OFCs are derived from ultra–short pulses, the parameter ε is associated with the time–varying without stabilization mechanisms for mode–locked lasers. Due to the phase variations in each comb, the stabilization of frequency offset position is relevant to guarantee an optimal performance [JON00]. An example of problem of frequency offset is illustrated in Fig. 2.2. To get stables ultra–short pulses, it is necessary to consider four aspects: number of *comb lines*, *bandwidth*, *spectral flatness*, and *optical tone–to–noise ratio* (OTNR) [ZOU13]. Evaluating these aspects, the mode–locked lasers can create OFCs with large bandwidth and high stability but they need sophisticated control to obtain stable operation (low frequency offset) [SHA14]. Therefore, to guarantee the best spectrum of ultra–short pulses, the center wavelength and frequency spacing must be tuned constantly in a wide range [LEAI07]. In recent years, an Origami–10 mode–locked femtosecond laser from Onefive for generating a 100 MHz pulse train at 1047 nm of central wavelength guarantees a noise reduction at 10^{-22}, which could be an innovator mode–locked laser for improving the tuning process [KUN14].

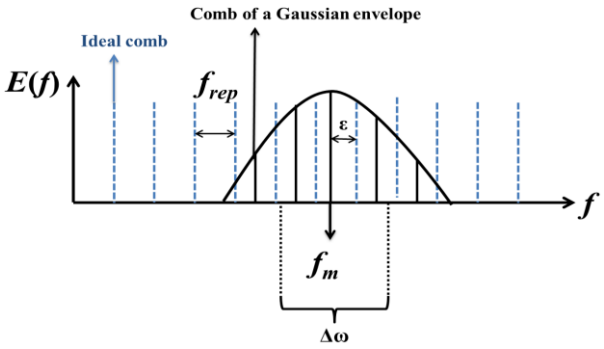

Fig. 2.2. OFCs generated by a Gaussian shape in comparison with OFCs ideal in order to observe the impact of frequency offset.

In section 5.3, a real application to get a OFCs spectrum with a picosecond pulses source and a femtosecond pulses sources will be shown.

2.2.2 Mach–Zehnder Modulator

A Mach–Zehnder modulator (MZM) is an external modulator made of Lithium Niobate ($LiNbO_3$). There are two types of MZMs: intensity modulator (IM) and phase modulator (PM), which are used to create OFCs spectra at high transmission rates.

As shown in Fig. 2.3, MZM consists of an input Y–junction (splitter), two phase modulated arms ($LiNbO_3$ waveguides) with independent drive electrodes, and an output Y–junction (combiner). MZM operation is based on the electro–optical effect which the refractive index of the material (Lithium Niobate) can be changed by a DC voltage. The changes of the refractive index modify the phase of an optical field propagating inside the material. The variation of phase is converted into amplitude modulation by using two $LiNb0_3$ waveguides [AGR05].

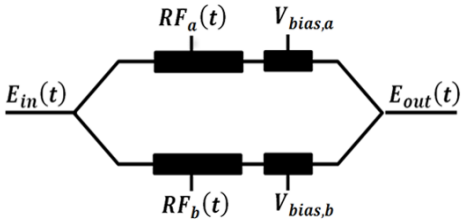

Fig. 2.3. MZM scheme.

The principle of OFC based on MZM uses a CW laser for modulating high amplitude radio frequency (RF) signals and to generate high–order sidebands components. These components are observed as comb lines due to constant frequency spacing. The intensity of each comb depends on the harmonic order and, therefore, it is possible to obtain a flat spectrum whether appropriated parameters are set to MZM control, such as the phase, the bias voltage, RF amplitude, and frequency from an electrical signal generator [SAK07b]. The principle for generating a OFCs spectrum based on MZM is illustrated in Fig. 2.4.

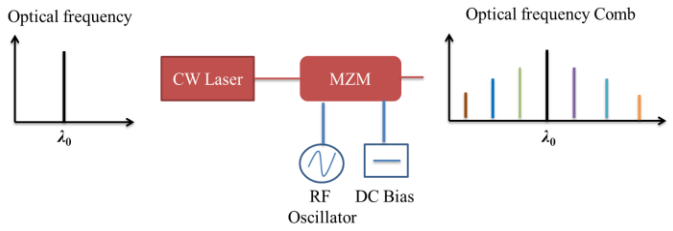

Fig. 2.4. General scheme of OFC generation using MZM.

Based on Fig 2.4, a general description is mentioned below: the optical phase imparted onto the CW laser is $(\pi V / V_\pi)\cdot\cos(2\pi f)$, where V is the voltage amplitude from RF oscillator and V_π is the half–wave voltage amplitude. The latter represents the amount of RF amplitude needed to obtain a π–phase change and it is dependent on the electro–optic coefficient of the material (in that case, $LiNb0_3$) and the waveguide configuration. In the lithium niobate, the typical parameters are 2V to 11V (V_π) and more at 10 GHz (operation frequency of MZM) [TOR14]. To get a OFC spectrum with broad bandwidth, the modulation index, $\beta_{MZM} = \pi V / V_\pi$, must be the largest magnitude. In real MZM, the V_π value must be high to achieve the best OFC spectrum, but it is required to maintain below the maximum power that MZM can support. If a most amount of comb lines and larger bandwidths are needed, it can be achieved with several PMs and/or Ims where the effective modulation index will be increased by a factor of N–number of modulators [TOR14]. However, the increase of OFCs is limited by the modulator's bandwidth, considering the generated frequency spacing. MZMs can provide until a bandwidth at 40 GHz but other kind of material called polymer structures could be a relevant option to achieve bandwidths until 100 GHz [MAC12].

Mathematically, the OFCs generation with MZM can be explained by two cascaded IM– MZMs, as illustrated in Fig. 2.5.

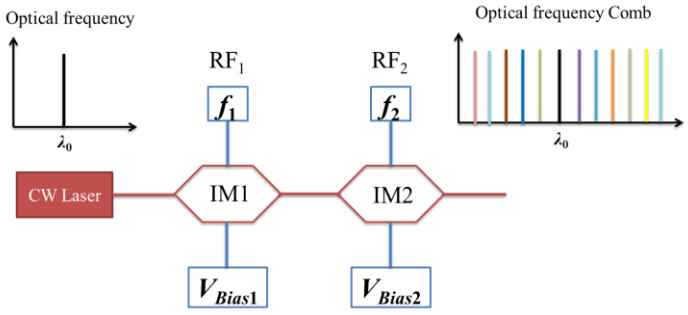

Fig. 2.5. General scheme of two cascaded IM–MZMs.

Assuming that the field of CW laser is $E_{in}(t) = E_0\, cos(\omega_0 t)$, where E_0 refers to the amplitude of the optical field and ω_0 the central frequency (in radians), and $V_1(t) = V_1\, sin(\omega_1 t)$ and $V_2(t) = V_2\, sin(\omega_2 t)$ are the electrical RFs for IM1 and IM2, being V_1 and V_2 the corresponding amplitudes and ω_1 and ω_2 the corresponding frequencies of microwave signals, the optical fields at the output of the IM1 and IM2 are expressed as [SHA14]:

$$E_{out1}(t) = jE_{in}(t)\sum_{n=-\infty}^{\infty} J_{2n-1}(\beta_1)\ exp\left(j(2n-1)\omega_1 t\right) \tag{2.17}$$

$$E_{out2}(t) = \frac{E_{out1}(t)}{2}\sum_{n=-\infty}^{\infty}\left[J_n(\beta_2)\ exp\left(jn\omega_2 t + j\phi\right) + J_n(-\beta_2)\ exp\left(jn\omega_2 t - j\phi\right)\right] \tag{2.18}$$

where $J_n(\cdot)$ denotes the n–order Bessel function, $\beta_1 = \pi V_1 / V_\pi$, $\beta_2 = \pi V_2 / V_\pi$, and $\phi = \pi V_{\text{Bias2}} / V_\pi$. The last one denotes the phase shift due to the DC source of IM2. Eq. (2.17) and (2.18) are mathematical representation by two cascaded IM–MZMs, based on the general expression indicated in Eq. (2.3).

Eq. (2.17) analyzes whether IM1 is biased at its minimum transmission and all even harmonic sidebands are suppressed. If the magnitude of any n−harmonic is equal to the magnitude of $–n$ harmonic, then $|J_n(\beta_1)| = |J_{-n}(\beta_1)|$. When $|J_3(\beta_1)| = |J_1(\beta_1)|$, the magnitudes of ±3th and ±1th harmonics are equal ($\beta_1 = 3.05$) and the IM1 can generate 4 comb lines in a specific bandwidth. In that case, the bandwidth can be *6 times* f_1 and the frequency spacing is *twice* f_1.

When Eq. (2.17) is analyzed when IM1 is biased at its maximum transmission and optical carrier and all odd harmonic sidebands are suppressed, $|J_0(\beta_1)| = |J_2(\beta_1)| = |J_{-2}(\beta_1)|$ if the magnitudes of ±0, +2th, and –2th harmonics are equal ($\beta_1 = 1.84$).Therefore, the optical fields $|E_{0,-2}| = |E_{0,2}| = |E_{0,0}|$ and 3 comb lines can be generated. Since this condition reduces one comb line with respect to the last case (IM1 is biased at its minimum transmission and optical carrier and all even harmonic sidebands are suppressed), the bandwidth is reduced at *4 times* f_1 but the frequency spacing is hold.

In Eq. (2.18), several optical carriers can be obtained, as defined below:

$$E_{0,0} = \frac{E_{out1}}{2} J_0(\beta_2)\ \left[exp(j\phi) + exp(-j\phi)\right]cos(\omega t) \tag{2.19}$$

$$E_{0,1} = \frac{E_{out1}}{2} J_1(\beta_2)\ \left[exp(j\phi) - exp(-j\phi)\right]cos\left((\omega+\omega_2)t\right) \tag{2.20}$$

$$E_{0,-1} = \frac{E_{out1}}{2} J_{-1}(\beta_2)\ \left[exp(j\phi) - exp(-j\phi)\right]cos\left((\omega-\omega_2)t\right) \tag{2.21}$$

$$E_{0,2} = \frac{E_{out1}}{2} J_2(\beta_2)\ \left[exp(j\phi) + exp(-j\phi)\right]cos\left((\omega+2\omega_2)t\right) \tag{2.22}$$

$$E_{0,-2} = \frac{E_{out1}}{2} J_{-2}(\beta_2)\ \left[exp(j\phi) + exp(-j\phi)\right]cos\left((\omega-2\omega_2)t\right) \tag{2.23}$$

From Eq. (2.19) to (2.23), five comb lines can be obtained only in IM2 if $\beta_2 = 1.84$ and ϕ is less or equal to 0.5. These parameter conditions allows establishing that the magnitudes, $|E_{0,-2}| = |E_{0,2}| = |E_{0,0}| = |E_{0,-1}| = |E_{0,1}|$ only if $J_0(\beta_2) = J_2(\beta_2)$ and $J_0(\beta_2)\cdot[exp(j\phi) + exp(–j\phi)] = J_1(\beta_2)\cdot[exp(j\phi) – exp(–j\phi)]$. Since IM2 is linked to IM1 (cascade), f_1 and f_2 satisfy that $5f_2 = f_1$ and therefore, each

comb line in IM1 will split to be 5 comb lines by IM2. The above condition can be reached when DC bias voltages are maintained stable and f_1 and f_2 are synchronized. Based on this model, the output of two IM–MZMs can achieve until 20 comb lines, according to the frequency spacing and the frequency offset (see Eq. (2.2)) generated. In section 5.4, a real application to obtain an OFC spectrum with two IM–MZMs will be explained and shown.

In literature, there are others MZM configurations to create comb lines using cascaded IM–MZM and PM–MZM, Dual–Drive MZM (DD–MZM), two cascaded MZM–PMs using a linearly chirped fiber Bragg grating (LCFG), and two cascaded IM–MZMs and connected with a PM–MZM with electrical phase shifter (PS), RF amplifier, and electrical attenuator. For more information, see [TOR14] and [SHA14].

2.2.3 Microresonator Ring

A microresonator ring is an ordinary waveguide that channels light in a closed loop [HEE08]. The loop is made at different shapes like disk, racetrack, or ellipse, although the ring shape is the most used. The ring shape is a curved waveguide closed onto it−self forming a resonant cavity that is able to maintain transverse and longitudinal modes. The supporting of these modes is presented by the presence of optical *whispering–gallery–modes* (WGMs) in a microdisk resonator, microspheres, microtoroids, or microrings [KIP11], which concentrate light by total internal reflection around the perimeter of an air–dielectric interface. The whispering–gallery effect was discovery by Lord Rayleigh where he analyzed the channeling of acoustic waves by the dome of St. Paul's cathedral in London as a precursor to similar techniques applied to electromagnetic waves. Based on this principle, the first integrated ring resonator in the optical domain was carried out by [MARC69]. Other relevant advance in optical ring resonator was Weber and Ulrich's device [ULR72], which is a 5 mm–diameter–glass rod coated with Rhodamine–6G–doped polyurethane, creating a resonator circumference of 31.4 mm. This advance allowed developing an integrated bus waveguides with doped polymethyl methacrylate (PMMA) film on quartz substrate [HAA80]. Afterwards, the first optical glass fiber ring resonator was made by [STO82], but the resonator circumference was 3 m. By means of this change of resonators, several researches were focused on integrated ring resonators based on glass [WAL83] [MAH86]. Nevertheless, the great advance of microresonator with GaInAsP–InP and Nitrates using the whispering–gallery reduced the resonator circumference until 15 μm [REX00]. In spite of this advantage, the limitation of GaInAsP–InP is the high device losses and the processing difficulties since it is a passive microring. In recent years, the direction of microresonator has been with integrated silicon nitride (Si_3N_4), whose fabricating is made through approaches compatible with widespread complementary metal–oxide semiconductor (CMOS) [LEV10]. In addition, the presence of octave spanning comb spectra (relevant to get repetition rate stable by self–referencing technique), has been found with silica microtoroids [HAY11]. In the section 5.5, the experiments made with microresonators ring are fabricated with Si_3N_4 integrated with CMOS.

In Fig. 2.6a, the representation of a ring microresonator, type Add–Drop, is illustrated. The configuration has two waveguides where the resonant modes are accessed through evanescent coupling (physical phenomenon analogous to tunneling in solid–state physics). The presence of a second waveguide in the ring enables extraction of the resonant which it is circulating the optical signal. The above allows an increased circulation of intensity in the resonator and facilities the

resonant–state between the central wavelength component from a CW laser source and the optical cavity. This effect is important to generate an integer number of wavelength components and so, the microresonator acts as a temporary compressor of energy density or as a special spectral filter [HEE08]. In Fig. 2.6b, the ring microresonator type All–Pass is shown.

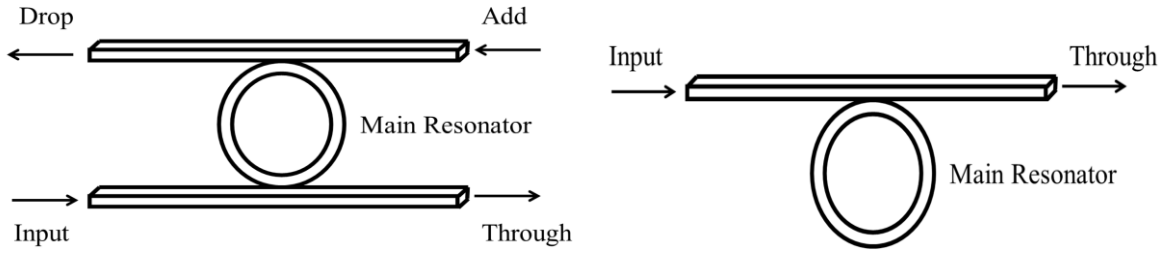

Fig. 2.6. Representation of a microresonator ring, a) Add–Drop ring resonator, and b) All–Pass ring resonator.

In the evolution of optical microresonator, different resonators were proposed where the most popular are Fabry–Perot resonators, Gires–Tournois resonators, and ring resonators. In this research work, the explanation will be oriented to ring resonators with an all–pass ring resonator configuration.

The ring resonators were developed to be adapted with planar wave−guiding geometry, useful for one or two ordinary waveguides. This configuration allows reducing the resonator size and to increase the comb line power. Considering Fig 2.6b, an all–pass ring resonator exhibits a periodic cavity resonance whether light traversing the ring generates a phase shift of 2π or nth–2π. This condition is relevant to formulate the resonator behavior in a component that refers to a coupling strength and other component that defines a feedback path. The above represents the optical fields, considering the field–matching method to find a mathematical expression. In Fig. 2.7, a representative scheme for an all–pass ring resonator is illustrated.

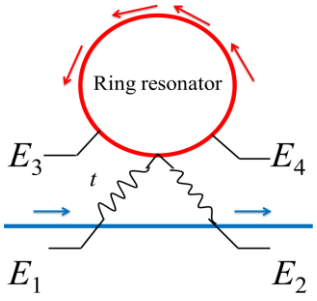

Fig. 2.7. Optical fields representation for an all–pass ring resonator configuration. The schematic is a modified version from [HEE08].

The optical fields E_1 and E_2 are incident field and transmitted field which they are traveled toward the ring resonator. In the ring, the optical fields E_3 and E_4 are generated by the combination between the optical field on the coupler and the optical field on the feedback path. The coupling region of these fields is related, as shown in Eq. (2.24):

$$\begin{pmatrix} E_4(\omega) \\ E_2(\omega) \end{pmatrix} = \begin{pmatrix} r & it \\ it & r \end{pmatrix} \begin{pmatrix} E_3(\omega) \\ E_1(\omega) \end{pmatrix} \tag{2.24}$$

being $E_1(\omega)$, $E_2(\omega)$, $E_3(\omega)$, and $E_4(\omega)$, the optical fields in the spectral domain, r and t are the lumped self– and cross–coupling coefficients that satisfies the relation of a circumference, $r^2 + t_c^2 = 1$, where t_c is the time delay of circulating optical intensity within resonator. Based on Eq. (2.24), the output optical field from $E_4(\omega)$ back into $E_3(\omega)$ can be expressed as a feedback path at $2\pi R$, being R the circumference radius:

$$E_3(\omega) = a \cdot \exp\left(i\phi_{phase\ shift}\right) \cdot E_4(\omega) \tag{2.25}$$

where a is the single–pass amplitude transmission and $\phi_{phase\ shift}$ is the single–pass phase shift. The variable $\phi_{phase\ shift}$ is defined in terms of the radian frequency, $\phi_{radian\ freq} = \omega \cdot T_R$, being T_R the transit time of the ring resonator. In the microresonator case, $\phi_{radian\ freq}$ represents the normalized frequency detuning. The above is a relevant condition to explain why the best resonance–state of resonant can be reached at a specific central wavelength of a CW laser.

A relevant factor of all–pass ring resonator is the amount of optical energy storage due to the time delay generated by the feedback path. To build–up the constructive interference at the coupler, the circulating optical intensity must generate a magnitude greater than the average peak power from the injected laser or CW laser. It is essential to guarantee an optimal equalization of carriers. In order to establish the capacity of a resonator to store the most quantity of optical energy, a factor B or *buildup factor* is defined (it is responsible of enhanced non–linear response of ring), as shown in Eq. (2.26) [HEE08]:

$$B = \frac{\left(1 - r^2\right)a^2}{1 - 2 \cdot ra \cdot \cos\left(\phi_{radian\ freq}\right) + r^2 a^2} \tag{2.26}$$

In Eq. (2.26), a particular situation can present if the incident light of ring resonator, $\phi_{radian\ freq} = m2\pi$, where m is a resonator mode, and $a = 1$, the maximum B factor of a resonator is $B = (1 + r) / (1 - r) \approx 4 / t_c^2$. This condition can be achieved when the resonator attenuation is negligible. Other characteristic of ring resonator is the relation of spectral shape and the B factor, which is defined through a *finesse parameter*. The finesse is a relation between resonances peaks divided by the *full–width at half–depth* (FWHD) (an explanation of FWHD is shown in [PER11]). The above gives rise of *free spectral range* (FSR), which if the FSR is high, the ring is preferable; otherwise, if the FSR is low, the ring geometry is better and the extra loss must be considered [HAG97]. The finesse function is expressed by Eq. (2.27):

$$F = \frac{2\pi}{2 \cdot \arccos\left(\dfrac{2r}{1 + r^2}\right)} \tag{2.27}$$

In Eq. (2.27), if $r \approx 1$, $F = \pi / (1 - r) \approx 2\pi / t^2$, which indicates the maximum finesse value with absence of internal losses of ring resonator.

In several research reports [KIP11] [CHEM10] [HER14], indicate the high influence of the *quality factor Q* in the OFC generation with any microresonator. The factor *Q* is measured by the sharpness of the resonance relative and its central frequency, which allows establishing the ratio of the stored energy circulating within the resonator [HEE08]. This factor also considers the energy lost per optical cycle during the resonant–state, generating the following mathematical expression:

$$Q = \omega_0 \frac{Stored\ energy}{Power\ Loss} \tag{2.28}$$

The *Q* and *F* factors are related due to that light interacts with the coupling interface for a finesse number of times while interacting with the cavity of the microresonator, i.e. a *Q* number of cycles[3].

Based on the above explanation, the relation of *Q* and *F* factors is given by:

$$Q = mF \tag{2.29}$$

The Eq. (2.24)–(2.29) are shown in the document since they are essential definitions to understand the OFC generation in microresonator ring. In Fig. 2.8, the OFC spectrum of a microresonator ring is illustrated. In the resonator, parametric oscillations are created within of resonator, responsible of multiple sidebands and increase of spectral width. This bandwidth can be rise by stimulating four wave mixing (FWM) through two steps: degenerate FWM (converts two photons of the same frequency inside a frequency up–shifted and down–shifted pair of photons) and non–degenerate FWM (four photons have different frequencies). The former occurs when the CW laser can convert pump photons to secondary sidebands, spaced according to FSRs. This process is able of leading pairwise equidistant sidebands although the frequency offset can alter that. On the other hand, the latter is presented when the generated signal and idler sidebands serve as "seeds" for creating parametric frequency conversion, taking into account the two pump photons have different frequencies [KIP11]. The non–degenerate FWM can behave as cascaded FWM, explained by [SUP12]. The cascaded FWM has a relevant importance whether the signal and idler sidebands contain comparable carrier powers with the CW laser power. The comparison allows generating carriers at the same separation (but the frequency offset can modify such separation) and to increase the bandwidth of OFC.

[3]For example, to obtain an enhanced microresonator operating as sensor, the variation of a uniform optical property like the refractive index is required to develop a large cavity. The above increases high *F*−factor.

On the other hand, if this microresonator is used as sensor, the variation of a localized optical property is maintained. Otherwise, if a displacement of one coupler is generated, the variation is increased. *Therefore, a large cavity will not be benefit*. This kind of application can increase the sensibility with respect to the thermal and vibrational noise.

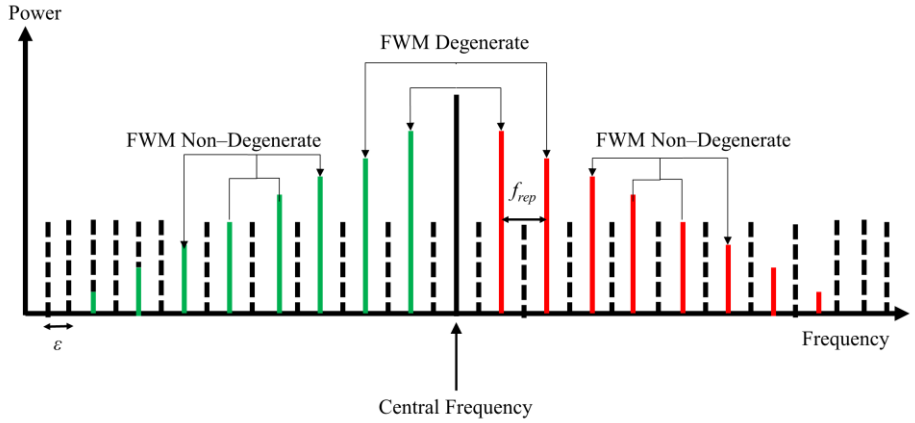

Fig. 2.8. OFC generation in a microresonator ring, where the green and red lines are microresonator modes, and the dotted line is equidistant comb mode.

To guarantee an OFC spectrum with a large bandwidth, the microresonator must have a high Q factor (> 100 million [KIP04]) with small mode volume that is made of a material with a thrid–order nonlinearly and low dispersion [KIP11]. The dispersion is a relevant aspect due to that a typical microresonator can generate normal dispersion, generating that some high optical frequencies are propagated slower than low frequencies. This situation can vary FSR and to limit a finite bandwidth because of the cascaded FWM is weak and loss several comb modes. Other limitation of bandwidth of microresonator is the repetition rate variation when the device is dependent of the intensity round–trip time of the ring cavity. The thermal noise and Kerr nonlinearity are responsible of power variation in the CW laser, where these variations can change the mode spacing of the frequency comb and reducing the effective path length of resonator [HAY08]. In contrast, the thermal effects can create a refractive index fluctuation, converting the optical energy in heat energy. One strategy to observe the impact of thermal noise and vibrational noise is a frequency noise measurement in the comb modes since in small volume, the thermo–refractive and thermo–elastic noise are enhanced [HAY09]. However, for a huge volume, such conditions do not allow enhancing the comb modes generation. In that case, one alternative is a phase control to mitigate the frequency offset. In the section 5.5, the noise measurements in the microresonator rings are shown.

On the other hand, to get the best OFC spectrum in a microresonator ring, the average power and central frequency of a tunable diode laser are tuned until to find the best flat spectrum. Sometimes, the carrying of central frequency is realized each 0.2 nm in order to achieve the resonant state of microresonator. The main results of this procedure will be shown in section 5.5.

2.2.4 Linear and Non–Linear Phenomena in Optical Frequency Comb

In optical communication, the performance of OFC spectrum during its propagation in SMF is a relevant aspect for considering its useful in real applications. Due to the presence of linear and non–linear phenomena in the propagation, the mathematical model is required to know the OFC behavior and the consequences of these effects in the time–and–frequency domain. To define a general expression of the OFC propagation, the pulse–and–spectral shapes will be considered as a Gaussian function, assuming a spectrum generated by a mode–locked laser. By using the non–linear

Schrödinger equation (NLSE) in *z*–direction (propagation direction in a SMF), the OFC propagation is given by Eq. (2.30):

$$\frac{\partial A}{\partial z}+\beta_1\frac{\partial A}{\partial t}+i\frac{\beta_2}{2}\frac{\partial^2 A}{\partial t^2}+\frac{\alpha}{2}A=i\gamma|A|^2A \tag{2.30}$$

Being A the envelope amplitude of Gaussian pulse, β_1 and β_2 are linear dispersion parameters, α is the SMF losses (typical value, 0.2 dB), and γ refers to the non–linear parameter (typical value, 1.37 W^{-1}/m). In [YOU09], a reduction of Eq. (2.30) can be applied if $T = t - z/v_g = t - \beta_1 z$, where v_g is the group velocity. In Eq. (2.31), the reduction is indicated.

$$i\frac{\partial A}{\partial z}+i\frac{\alpha}{2}A-\frac{\beta_2}{2}\frac{\partial^2 A}{\partial T^2}+\gamma|A|^2A=0 \tag{2.31}$$

The Eq. (2.31) allows finding the general expressions of dispersion and the most relevant non–linear phenomenon for an OFC. Assuming that $\gamma = 0$, the chromatic dispersion is the relevant phenomenon. The dispersion can alter the temporal shape of a pulse, triggering inter–symbol interference (ISI) and an increase of BER in the reception step of spectrum [RAM10]. These limitations are prejudicial for a real application in optics communications. The chromatic dispersion is considered as linear phenomenon refraction–index–dependent at a specific wavelength, as shown in Eq. (2.32):

$$\beta(\omega)=\beta_0+\beta_1(\omega-\omega_0)+\frac{1}{2}\beta_2(\omega-\omega_0)^2+\frac{1}{6}\beta_3(\omega-\omega_0)^3+\cdots \tag{2.32}$$

where β_1, β_2, β_3 …, β_n are dispersion parameters and ω_0 is the central frequency (in radians). In OFC propagation, β_2 is the relevant parameter and responsible of group–velocity dispersion (GVD), which it can generate an increase of pulse width in temporal domain at different group velocities [AGR05]. Based on the above explanation, Eq. (2.31) is reduced to the following expression:

$$i\frac{\partial A}{\partial z}+i\frac{\alpha}{2}A-\frac{\beta_2}{2}\frac{\partial^2 A}{\partial T^2}=0 \tag{2.33}$$

By means of Eq. (2.33), the Gaussian envelope with GVD, the magnitude of Gaussian envelope with GVD and the linear phase shift are given by:

$$U(z,T)=\left|U(z,T)\right|\exp\left[i\phi(z,T)\right] \tag{2.34}$$

$$\left|U(z,T)\right|=\left(1-i\frac{z}{L_D}\right)^{-1/2}\exp\left[-\frac{T^2}{2T_0^2}\left(1-i\frac{z}{L_D}\right)\right] \tag{2.35}$$

$$\phi(z,T)=-\left\{\frac{\operatorname{sgn}(\beta_2)\cdot\left(z/L_D\right)}{\left[1+\left(z/L_D\right)^2\right]}\right\}\left(\frac{T}{T_0}\right)^2+\frac{1}{2}\tan^{-1}\left(\frac{z}{L_D}\right) \tag{2.36}$$

being $U(z,t)$ the Gaussian envelope function, $|U(z,t)|$ is the normalized magnitude of Gaussian pulse, $\phi(z,T)$ is the linear phase shift, T_0 is the pulse width measured in the power peak and a smooth decay of 1/exp(1), and L_D is the dispersion length of SMF, $L_D = T_o^2 / |\beta_2|$. Analyzing Eq. (2.36), small variations of T with respect to T_0 can present linear phase shift and an increase of pulse width, which ISI and BER can raise during the OFC propagation in SMF. In addition, if $\beta_2 > 0$, the normal dispersion is predominant and the high frequencies will be propagated faster than the low frequencies. In contrast, if $\beta_2 < 0$, the abnormal dispersion is relevant and the high frequencies will be propagated slower than the low frequencies.

Changing roles in the explanation, if $\beta_2 = 0$ in Eq. (2.31), the non–linear effects are predominant in the OFC propagation in SMF, which the reduction of NLSE expression is shown in Eq. (2.37):

$$i\frac{\partial A}{\partial z} + i\frac{\alpha}{2}A + \gamma|A|^2 A = 0 \tag{2.37}$$

The Eq. (2.37) represents the general expression of NLSE of self–phase modulation (SPM), considers as the most relevant non–linear phenomenon in the OFC propagation in SMF [YOU09]. The SPM occurs when an increase of pulse width is dependent of the change of refraction index in SMF. It can induce spectral phase fluctuations which a positive non–linear chirp and an increase of spectral width can present. In Eq. (2.38), the Gaussian envelope with SPM, the magnitude of Gaussian envelope with SPM, and the non–linear phase shift are given by:

$$U(L,T) = |U(0,T)| \exp\left[i\phi_{NL}(L,T) \right] \tag{2.38}$$

$$U(0,T) = \exp\left(-\frac{T^2}{T_0^2} \right) \tag{2.39}$$

$$\phi_{NL}(L,T) = |U(0,T)| \left(\frac{L_{ef}}{L_{NL}} \right) \tag{2.40}$$

where $U(L,T)$ is the Gaussian envelope dependent of length of SMF, $U(0,T)$ is the Gaussian magnitude with $L = 0$ km, $\phi_{NL}(z,T)$ is the non–linear phase shift, L_{ef} is the effective length of SMF, $L_{ef} = (1 - \exp(-\alpha/L))/\alpha$, and L_{NL} is the non–linear length of SMF, being $L_{NL} = 1 / \gamma \cdot P_0$ and P_0 is the power peak of Gaussian pulse. Due to the characteristic non–linear of phase shift in SPM, the frequency variations have a non–linear behavior, inducing a chirp positive given by:

$$\Delta\omega = 2\left(\frac{L_{ef}}{L_{NL}} \cdot \frac{T}{T_0^2} \right) \exp\left(-\frac{T^2}{2T_0^2} \right) \tag{2.41}$$

In Eq. (2.41), the increase of length of SMF during the propagation can generate a frequency component shit and the worst situation can present when $L_{NL} >> L_{ef}$. When $L_{NL} = L_{ef}$, the maximum phase shift can occur, where $\phi_{NL}(L,T) = \phi_{máx} = |U(0,T)|^2$. If $L_{NL} << L_{ef}$, the SPM effect has little influence in the propagation.

At this point, GVD and SPM were explained but in real applications, they are presented at the same instant of time. The above shows the needs for knowing the interaction between them. In Eq. (2.42), the general expression of GVD and SPM interaction is defined.

$$\sigma_p^2(L) = \sigma_L^2(L) + \frac{1}{2}\gamma P_0 f_s \beta_2 L^2 \tag{2.42a}$$

$$\frac{\sigma_L^2}{\sigma_0^2} = \left(1 + \frac{C\beta_2 L}{2\sigma_0^2}\right)^2 + \left(1 + V_\omega^2\right)\left(\frac{\beta_2 L}{2\sigma_0^2}\right)^2 \tag{2.42b}$$

$$\frac{\sigma_L^2}{\sigma_0^2} = \left(1 + \frac{C\beta_2 L}{2\sigma_0^2}\right)^2 + \left(\frac{\beta_2 L}{2\sigma_0^2}\right)^2 \tag{2.42c}$$

Being P_0 the peak power of pulse, f_s is an adimensional value (≈ 0.7) if the spectrum has a Gaussian shape, σ_p is the total pulse width, σ_L is the pulse width when $\gamma = 0$, σ_0 is the initial pulse width, C is the positive chirp parameter generated by SPM, and V_ω is an adimensional parameter associated with the Gaussian shape generated by the pulsed source. Eq. (2.42a) defines the combined effect of GVD, SPM, and induced chirp. Based on the last equation, Eq. (2.42b) indicates the influence of spectral width of Gaussian pulsed laser with respect to the combined effect. Finally, Eq. (2.42c) is a reduced expression from Eq. (2.42b), where the effects of spectral width are depreciable.

Taking into account Eq. (2.42a) and (2.42b), the relation between L_D and L_{NL} is listed in the Table 2.1.

Table 2.1. Relation between L_D and L_{NL} in the GVD and SPM interaction.

Relation L_D and L_{NL}	**Description**
$L << L_{NL}$; $L << L_D$	GVD and SPM do not generate any significant change in the temporal–and–spectral domain of OFC. Only the SMF loss has a significant change in penalty of power in OFC.
$L << L_{NL}$; $L \sim L_D$	Pulse propagation is dependent of GVD and the SPM effect is negligible.
$L << L_D$; $L \sim L_{NL}$	Pulse propagation is dependent of SPM and the GVD effect is negligible.
$L >> L_{NL}$; $L >> L_D$ o $L \sim L_{NL}$; $L << L_D$	GVD and SPM can create phase shift, increase of pulse width, and changes of spectral shape, where GVD can have a normal dispersion and GVD can have a significative impact when the power peak is high.

The Eq. (2.41b) and (2.41c) can be expressed in terms on spectral width, V_ω, whether the laser generates a Gaussian shape and it is defined as second–order chromatic dispersion and SPM. However, the high–orders dispersion has relevance in its interaction with SPM. In that case, the third–order dispersion (TOD) can affect the interaction. Therefore, Eq. (2.43) shows an expansion of interaction of TOD and SPM is given by:

$$\frac{\sigma_L^2}{\sigma_0^2}=\left(1+\frac{C\beta_2 L}{2\sigma_0^2}\right)^2+\left(1+V_\omega^2\right)\left(\frac{\beta_2 L}{2\sigma_0^2}\right)^2+\frac{1}{2}\left(1+C^2+V_\omega^2\right)^2\left(\frac{\beta_3 L}{4\sigma_0^3}\right)^2 \quad (2.43)$$

where β_3 is the dispersion value of TOD.

In the propagation of any OFC spectrum, the interaction of chromatic dispersion and SPM is attached of other relevant phenomenon: polarization–mode dispersion (PMD). Considering the propagation of an optical signal (for example, a Gaussian pulse) through a SMF, the imperfections of this media generates two orthogonal polarization–modes at different group velocities [MAL11]. This behavior is explained by two main causes: intrinsic and extrinsic perturbations [WAF09]. The former is presented in manufacturing process that cause random imperfections in the construction of SMF, mechanical stress, and even changes of temperature. The latter is generated by the random circular symmetry and changes of environmental. These imperfections are common in SMF with low birefringence from the fabricant (usually, SMF is designed to guarantee low PMD but the handling in the optical communication networks can rise its negative impact). Therefore, if the propagation distance increases, the birefringence will be high, creating an increase of the pulse width, shape pulse distortion, and attenuation (if chromatic dispersion is considered). In the fiber output, one mode is more retard than other which presents differential group delay (DGD) that measures the amount of PMD of an optical signal [RAJ11]. Owing to that the DGD effect can present several levels of pulse broadening, it is likely a high ISI and an increase of BER. DGD is associated with first–order PMD. Other important consideration is the dependence of frequency of DGD and its variations of bandwidth of the pulses. This case is well–known as second–order PMD, although behavior is similar to chromatic dispersion due to it is dependent of spectra width of the pulse [RAM10].

In several explanation of PMD behavior use the scalar component of NLSE, but one polarization–state is considered. For large length of SMF, Schrödinger's vector equation is required to observe the PMD coupler with the Kerr nonlinearity effect. Therefore, a full physical model of PMD for a Gaussian shape generated by a mode–locked laser must contain the interaction chromatic dispersion and SPM. By using the polarization rotation in the Poincaré Sphere [BET05], the interaction PMD–SPM–GVD [MEN06] is defined as follows:

$$j\frac{\partial U(z,t)}{\partial z}+j\Delta\beta^{(1)}(z)\bar{\sigma}_3(z)\frac{\partial U(z,t)}{\partial z}-\frac{1}{2}\beta^{(2)}(z)\frac{\partial^2 U(z,t)}{\partial t^2}+\frac{8}{9}\gamma\left|U(z,t)\right|^2 U(z,t)=0 \quad (2.44)$$

where $\beta^{(1)}$ and $\beta^{(2)}$ are first–and–second order dispersion in *z*–direction, and $\bar{\sigma}_3$ is Pauli matrix. The present model allows defining the penalty of closed eye in an eye diagram after the propagation in SMF, as well as the limitation for developing robust techniques to reduce PMD of high order interacting with GVD and SPM.

2.3 Pulse Shaping

2.3.1 Brief Description of Pulse Shaping

Pulse shaping is a technique in which intensity and phase of frequency comb lines are controlled in the spectral–domain through a liquid crystal modulator (LCM) [HUA08] [WEI00]. An advantage of pulse shaping is its capacity of generating user–defined time–domain waveforms such as optical arbitrary waveform generation (O–AWG). In OFC, the pulse shaping can address the intensities and phases of the comb carriers, but the current pulse shapers are able to mitigate dispersion normal and to add delays for correcting phase shift. During the evolution of pulse shaping, two techniques have been developed, direct space–to–time (DST) pulse shaping and Fourier transform (FT) pulse shaping [HUA08]. Focusing on a basic FT pulse shaping (also known as *4f–line* configuration) consists of diffraction gratings, positive lenses, a mask, and a modulator array (usually 1D or 2D), where the individual frequency components are organized angularly through the first diffraction grating [WEI11]. After the diffraction grating, they are focused at the back focal plane of the first positive lens in order to separate them spatially in 1D [SON12]. This separation allows manipulating the intensity and phase of the spatially dispersed frequency components, through the one–dimensional modulator array. By recombining all optical frequencies through the second lens and diffraction grating, the shaped spectral is generated at output pulse shaper. The Fourier transform of the complex pattern transferred by the masks onto the OFC spectrum result in programmable user–defined waveforms [SON12].

In Fig. 2.9, a FT pulse shaping representation is illustrated.

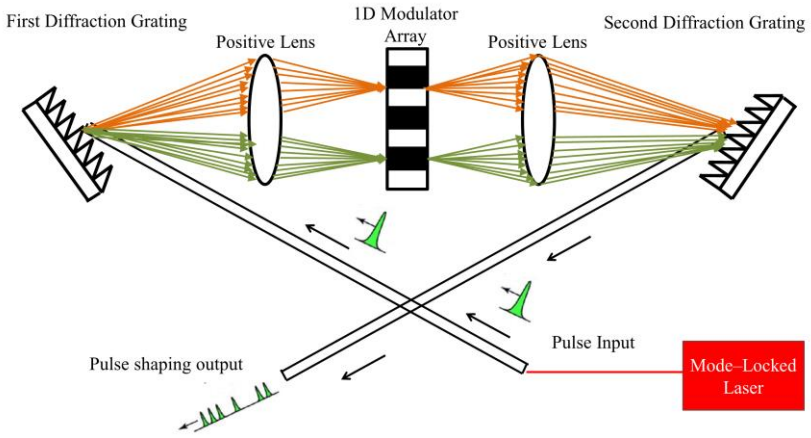

Fig. 2.9. Basic FT pulse shaping. Adapted from [WEI11].

Considering the shown schematic of Fig. 2.9, a FT pulse shaping is defined as the relation between the input optical field at a specific frequency (in radians), $E_{in}(\omega)$, and the output optical field, $E_{out}(\omega)$, given by [MON10]:

$$E_{out}(\omega) = H(\zeta\omega)E_{in}(\omega) \tag{2.45}$$

where ζ is a dispersion component of the transfer function of mask (in the free space and its unit is adimensional), $H(\zeta\,\omega)$, expressed in terms of a Gaussian filter function with amplitude, $A_{mask}(\omega)$, and the phase filter, $\phi_{mask}(\omega)$:

$$H(\zeta\,\omega) = A_{mask}(\omega)\exp\left[i\phi_{mask}(\omega)\right] \tag{2.46}$$

Converting Eq. (2.45) in the time domain through Fourier's transform inverse, it is obtained:

$$E_{out}(t) = E_{in}(t)\left[\frac{1}{2\pi}F^{-1}\left\{H(\zeta\,\omega)\right\}\right] \tag{2.47}$$

To consider the spatial distribution of light in the FT pulse shaping, three variables are defined if the Gaussian input pulse is felt the first half of configuration and the kind of measurement is FWHM: $\Delta\omega_L$ or spectral separation between modes [nm or μm], Δt or pulse width [s], and Δx_{in} or spatial separation [m], $\Delta x_{in} = \omega_{in}\cdot[2\cdot\ln(2)]^{-1/2}$ (ω_{in} is the frequency at the waist of the beam at the input of FT pulse shaping) [MON10]. In Fig. 2.10, the light propagation in the half of FT pulse shaping is shown, where:

- f is the focal length [m].
- $X_{spatial}$ is the spatial coordinate in the plane [adimensional].
- g($X_{spatial}$) is the spatial extension of a frequency component [in radians].
- θ_i is the incident angle on the diffraction grating [rad].
- d is the grating period [s].
- θ_d is the diffraction angle [rad].

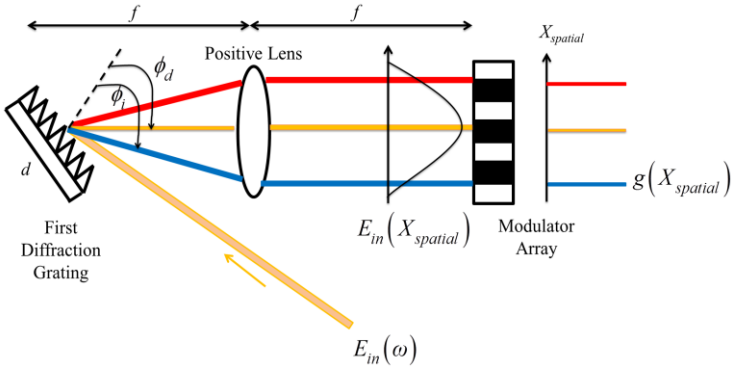

Fig. 2.10. Half FT pulse shaping. Adapted from [MON10].

Since the Gaussian input pulse can diffract through the first diffraction grating with an angle θ_d at a central wavelength, λ_0, the Fourier plane for each spectral component has always a finite size, Δx_0 [m], due to the influence of diffraction [DAN89], as shown in Eq. (2.48):

$$\Delta x_0 = 2\cdot\ln(2)\cdot\left[\frac{\cos(\theta_i)}{\cos(\theta_d)}\cdot\frac{f\lambda_0}{\pi\,\Delta x_{in}}\right] \tag{2.48}$$

Assuming that the dispersion is linear when the light beam is represented in the Fourier plane, each element in the modulator array, *pos*, at a frequency ω_{pos}, is located in a spatial position, X_{pos}, given by:

$$X_{pos} = \zeta \, \omega_{pos} \tag{2.49}$$

and the dispersion component (adimensional) is expressed as:

$$\zeta = \frac{\lambda_0^2 \, f}{2\pi \cdot c \cdot d \cdot \cos\left(\theta_d\right)} \tag{2.50}$$

Considering the Eq. (2.48) and Eq. (2.50), the frequency resolution of pulse shaping is defined as:

$$\Delta\omega_L = \frac{\Delta x_0}{\zeta} \tag{2.51}$$

The Eq. (2.51) is important to obtain the best throughput of FT pulse shaping due to more frequency resolution is used; more frequency components can be manipulated in intensity and/or phase. Other relevant is the time window for each Δx_{in}. It defines a temporal upper bound for shaping achievable with such a FT pulse shaping: the duration or the time delay of the shaped pulse should stay below T_{win}; otherwise, high distortions will be presented [MON10]. T_{win} is expressed by Eq. (2.52):

$$T_{win} = \frac{\Delta x_{in}}{|v_e|} \tag{2.52}$$

where $|v_e|$ is the spatio–temporal coupling velocity of light beam in the FT pulse shaping, $|v_e| = c \cdot d \cdot \cos(\theta_i) / \lambda_0$ (more information of $|v_e|$ in [FRE09]).

Since the FT pulse shaping uses a LCM–SLM, a brief description of the device is explained below.

2.3.2 Spatial Light Modulator

A spatial light modulator (SLM) is a programmable wave–plate controlled by voltage, which is made of a thin layer of nematic liquid crystal placed between glass substrate electrodes (usually, indium tin oxide or ITO). By applying a voltage an each pixel, the longitudinal waves are oriented in direction along of electrical field. When no voltage is applied, the nematic liquid crystals (LCs) orient all longitudinal waves in parallel to the substrate. This behavior occurs for the changes of the birefringence in the medium, which leads a modification of the optical path for light polarized along the anchorage direction [MON10].

Inside SLM, the molecules of liquid crystal cells are aligned in the *y*–direction, as shown in Fig. 2.11. In this state, the light polarized along *y*–direction sees a larger refractive index than generates light polarized along *x*–direction [WEI11]. Nevertheless, if any voltage is applied in the liquid

crystal (see Fig. 2.12), the longitudinal waves in *z*–direction are aligned with the direction of molecules. The above produces a change of phase of *y*–polarized light transmitted through the cell. The quantity of phase shift can be controlled through a voltage control that generally is carried out via computer, digital signal processor (DSP), or field–programmable gate array (FPGA). The maximum phase shift (at least 2π) of any SLM depends on minimum birefringence generated by the applied maximum voltage. To guarantee the maximum phase shift, the light is polarized at 45° in *x*– and–*y* axes for maintaining a linear polarization and the polarization at the output is transformed with respect to the voltage–dependent birefringence [WEI09]. Assuming a linear polarization, the relation between transmitted power, P_{out}, and initial power, P_{in}, through a crossed–polarized is expressed by Eq. (2.53).

$$\frac{P_{out}}{P_{in}} = \sin^2\left(\frac{\Delta\phi(V)}{2}\right) \tag{2.53}$$

where $\Delta\phi(V)$ is the change of the voltage–dependent birefringence.

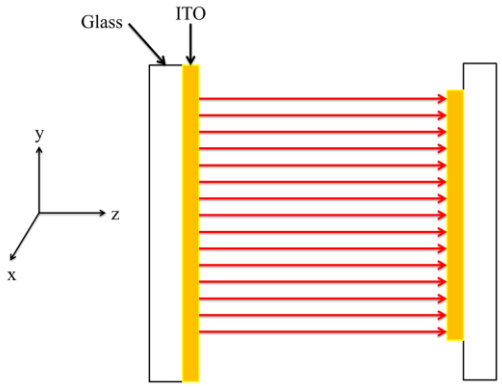

Fig. 2.11. SLM without presence of electrical field. Adapted from [WEI11].

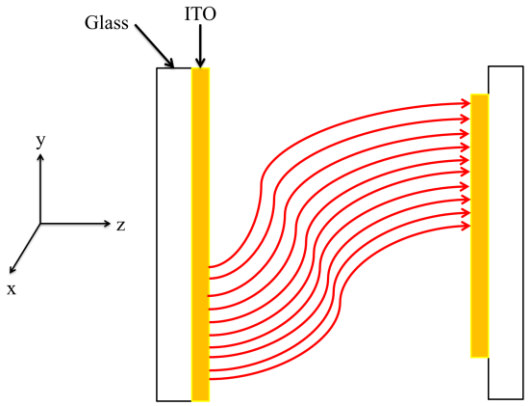

Fig. 2.12. SLM with electrical field. Adapted from [WEI11].

By applying a required voltage in SLM, the inside surface of each piece of glass is coated with an ITO, as shown in Fig. 2.12. This piece must be patterned according to the quantity of electrodes separated between them and the used electrical links to fabricate the liquid crystal. Assuming that

the electrodes are separated equitably and the molecules of ITO at input and output are aligned at 45° and –45° (linear polarization), the output field in any pixel is given by Eq. (2.54a) [WEI09] [WE11]:

$$E_{SLMout} = E_{SLMin}\exp\left[\frac{\Delta\phi_1(V_1)+\Delta\phi_2(V_2)}{2}\right]\cos\left[\frac{\Delta\phi_1(V_1)-\Delta\phi_2(V_2)}{2}\right] \tag{2.54a}$$

where $\Delta\phi_1(V_1)$ and $\Delta\phi_2(V_2)$ are the voltage dependent birefringence of the first and second layer of ITO, and E_{SLMin} and E_{SLMout} are the input–and–output electrical field. In the practical, $\Delta\phi_1(V_1)$ is selected to control amplitude while $\Delta\phi_2(V_2)$ is chosen to control phase [WEI11]. The above is defined due to that the transmitted power depends on the difference in the birefringence between both ITO layers and the phase shift depends on the average of birefringence [WEI09].

Other characteristic of SLM is the matrix representation of mask in terms of amplitude and phase functions, considering the pixels position in the modulator, as shown in Eq. (2.54b) and (2.54c):

$$M(x) = \sum_{n=-\frac{N}{2}}^{\frac{N}{2}-1} \text{square}\left(\frac{x-x_n}{\Delta x}\right) A_n \exp(i\phi_n) \tag{2.54b}$$

$$\phi(\omega) = A(\omega-\omega_0) + B(\omega-\omega_0)^2 + C(\omega-\omega_0)^3 \tag{2.54c}$$

where the *square* function is defined as *square*(x) = 1 if $|x| \leq ½$ and *square*(x) = 0 if $|x| > ½$; $M(x)$ is the sum of modulation functions per pixel with respect to the uniform amplitude modulation, A_n, and phase modulation, ϕ_n, according to the distance, Δx, and focused on the position, x_n, being N the vector size; $\phi(\omega)$ is the spectral phase function of SLM, where $A(\omega - \omega_0)$ is a pulse variation in the frequency domain when the pulse is phased with respect to original phase, ω_0; the parameter $B(\omega - \omega_0)^2$ is a quadratic pulse variation which allows compressing or broadening the pulse; the parameter $C(\omega - \omega_0)^3$ is a third−order pulse variation useful to mitigate residual dispersion of pulse.

The limitation of a SLM is focused on the speed with which the pulse shaper may be reprogrammed with respect to the response time of the device. If a comb spectrum with a repetition frequency is higher than frequency resolution of pulse shaper, the SLM will be limited by the dynamic of the liquid crystal itself (response time of miliseconds). Therefore, the amplitude and phase control could be used with little frequency components of comb spectrum. Due to this limitation, it is recommendable to choose the best pulse shaper with a large operation spectral width and high frequency resolution. However, other kinds of mask have been proposed to improve some characteristics of LC–SLM, as summed–up in Table 2.2. According to this information, acoustic–optic modulator (AOM) [DUG97], are other alternative to control phase and amplitude and some characteristics are similar to LC–SLM, except the response time and discretization levels. The time response is relevant to improve the spectral shape in wide spectral width of a comb spectrum, but *its efficient is less than LC–SLM*. Nevertheless, the discretization levels of AOM are larger than LC–SLM, which the frequency resolution is high.

In the experiment set−up (chapter V), the PS with LC−SLM has a one−dimensional array of independent LC pixels which were controlled by an accurate voltage, through an adjustable attenuation and phase shift in the incident light. The applied voltage in each pixel was adjusted by

the information supplied through the attenuation and phase vectors generated by the proposed methodology (it will be explained in chapter III and IV). In this particular case, the PS contains one 1D LC−SLM with a size 1 x *N*, being *N* = 5025 (number of pixels). To build the attenuation and phase vectors, the Eq. (2.54) is considered. In chapter V, the explanation about the PS configuration will be mentioned.

Table 2.2. Characteristics of SLM mask compared with other kind of masks. Adapted from [ZEE00].

Characteristic	Fixed mask	Acoustic–Optic Modulator (AOM)	Deformable mirrors	LC–SLM
Phase modulation	YES	YES	YES	YES
Amplitude modulation	YES	YES	NO	YES
Discretization levels	–	~2000	~39	~640
Stability	NO	YES	YES	YES
Response time	–	Ms	~1 ms	~35 – 200 ms
Efficiency	High	~40%	High	High

Until here, the concepts were oriented towards OFC generation, OFC propagation in SMF, and pulse shaping. In the next sections, the concepts will be focused towards *fuzzy sets theory*.

2.4 Fuzzy Sets Theory

When we have inexact data and vague information about a system, the most intuitive strategy is to denote the knowledge closer to human–like thinking and to carry out decision–making with presence of uncertainly. This knowledge can be obtained by fuzzy representation where the use of fuzzy rules allows obtaining a fuzzy system. For definition, a fuzzy system is a rule–based expert system whose fuzzy rules and fuzzy inference machine are capable of finding the best representation of system knowledge. The fuzzy rules show in a straightforward way "common sense" knowledge and skills, or knowledge that is subjective, ambiguous, vague, or contradictory [KAS98]. The term "common sense" may be associated a minimum experience of a group of people, high experience of one human expert or more people, or mathematical knowledge of dynamic of system. Nevertheless, when the exact fuzzy rules are unknown, the fuzzy clustering method is an interesting alternative to build a fuzzy representation of inexact data of system. This representation is useful to observe the behavior of a set of physical variables through fuzzy sets (FSs) or classes [BOT13]. Hence, each class can be related with a particular behavior of system and to be labeled as a normal state, critical state, or other state, identified by the human expert. In certain cases, the number of classes is difficult to find out when no human expert is presented. Therefore, the application of validation index of fuzzy classification can estimate an approximate number of classes and by means of the result, to interpret the physical significant of each one [ISA07].

The above description shows the great potential of FSs theory in many fields and systems. Through of the above introduction, the main aspects of FSs will be explained below.

2.4.1 Basic concepts

The main concept of fuzzy set (FS) was developed by Lotfi Zadeh [ZAD65], where many methods of fuzzy logic were defined by many scientists on simple notions. For definition, let a crisp

set X (or universe of discourse) be fixed and let $A \subset X$ be a fixed set, a FS(A) in X is an object of the following form:

$$A = \left\{ \left\langle x, \mu_A(x) \right\rangle \middle| x \in X \right\} \tag{2.55}$$

being $\mu_A(x)$ the membership degree of the element $x \in X$ to the set A, where μ_A: $X \rightarrow [0,1]$, and $<x, \mu_A(x)>$ means *order pairs*. When $\mu_A(x_i) = 1$, being x_i a specific element of X, $x_i \in X$, it represents the maximum membership degree; otherwise, if $\mu_A(x_i) = 0$, it refers to the minimum membership degree. FS(A) fulfills a set of axioms, defined in Table 2.3:

Table 2.3. Axioms of fuzzy sets, for all $x \in X$.

Axiom	**Mathematical Expression**
Double Negation	$\mu_{\bar{A}}(x) = \mu_A(x)$
Idempotence	$\mu_A(x) \vee \mu_A(x) = \mu_A(x)$ $\mu_A(x) \wedge \mu_A(x) = \mu_A(x)$
Commutative	$\mu_A(x) \vee \mu_B(x) = \mu_B(x) \vee \mu_A(x)$
Associative	$\left[\mu_A(x) \wedge \mu_B(x)\right] \wedge \mu_C(x) = \mu_A(x) \wedge \left[\mu_B(x) \wedge \mu_C(x)\right]$
Absorption	$\mu_A(x) \wedge \left[\mu_A(x) \vee \mu_B(x)\right] = \mu_A(x)$
Morgan's laws	$\overline{\left(\mu_A(x) \vee \mu_B(x)\right)} = \left(\mu_A(x) \wedge \mu_B(x)\right)$ $\overline{\left(\mu_A(x) \wedge \mu_B(x)\right)} = \left(\mu_A(x) \vee \mu_B(x)\right)$

In FSs theory, there are two representation widely used to define a *membership function*: Discrete and Continuous [KAS98], given by:

$$A = \left\{ \sum_{i=1}^{N} \frac{\mu_A(x_i)}{x_i} \right\} \tag{2.56}$$

$$A = \left\{ \int_{x \in X}^{N} \frac{\mu_A(x)}{x} \right\} \tag{2.57}$$

where N is the number of samples of X. It is important to denote that the signs $\sum$ and $\int$ do not mean sum or integration operators but the union of pairs $<x, \mu_A(x)>$. In both equations, the horizontal line does not mean division. It is only a bounding bar. The main characteristic of a membership function is defined by the α–cut [ZIM01]. For definition, the α–cut is a sharp or fuzzy set that contain the elements of A with a membership degree value greater than or equal at scalar value of α–constant, being $\alpha \rightarrow [0,1]$. Sometimes, the use of inverse α–cut is applied for membership degree values minor less than or equal to α–constant. The α–cut is defined by Eq. (2.58):

$$A = \left\{ \left\langle x, \mu_A(x) \geq \alpha \right\rangle \middle| x \in X \right\} \tag{2.58}$$

Through Eq. (2.58), the kernel α–cut is expressed as, $A = \{<x, \mu_A(x) = 1> | \, x \in X\}$, the cross or junction α–cut is expressed as, $A = \{<x, \mu_A(x) = 0.5> | \, x \in X\}$, and the support α–cut is, $A = \{<x,$

$\mu_A(x) > 0 >| x \in X\}$. Other known α–cut is the *center*, where average of elements is $\mu_A(x) = 1$, fuzzy Singleton, whose support is a point x_i in X has $\mu_A(x_i) = 1$, and height, where the $\max\{\mu_A(x_1),\ldots, \mu_A(x_N)\} = 1$ (It is known as normal FS). Other important characteristic of a membership function is its cardinality, Card(A). In a crisp set, the cardinality is the number of elements of a set. In FSs, the cardinality of FS(A) is the sum of all membership degrees of all elements of $x \in X$. In Eq. (2.59) and Eq. (2.60), the cardinality of a discrete FS(A) and a continuous FS(A), are expressed, respectively:

$$Card(A) = \sum_{i=1}^{N} \mu_A(x_i) \tag{2.59}$$

$$Card(A) = \int_{x \in X} \mu_A(x) dx \tag{2.60}$$

In membership functions, several geometrical representations can be built, where each one has specific characteristics, as summed–up in Table 2.4:

Table 2.4. Some kinds of membership function. Adapted from [ZIM01] and [DRI96].

Membership Function	**Equation**
Triangular	$f(x) = \begin{cases} a \le x \le b \rightarrow \frac{x-a}{b-a} \\ b \le x \le c \rightarrow \frac{c-x}{b-c} \\ 0, \textit{otherwise} \end{cases}$
Trapezoid	$f(x) = \begin{cases} x \le a \rightarrow 0 \\ a \le x \le b \rightarrow \frac{x-a}{b-a} \\ b \le x \le c \rightarrow 1 \\ c \le x \le d \rightarrow \frac{c-x}{d-c} \\ 0, \textit{otherwise} \end{cases}$
Cauchy Bell or Generalized Bell	$f(x) = \frac{1}{1 + \left[\frac{x-c}{a}\right]^{2b}}$
Gamma	$f(x) = \begin{cases} x \le a \rightarrow 0 \\ a \le x \le b \rightarrow \frac{x-a}{b-a} \\ x \ge b \rightarrow 1 \end{cases}$

L–function	$f(x)=\begin{cases} x \le a \rightarrow 0 \\ a \le x \le b \rightarrow \dfrac{b-x}{b-a} \\ x \ge b \rightarrow 1 \end{cases}$
S–function or Zadeh function	$f(x)=\dfrac{1}{1+\exp\left(-a\left(x-b\right)\right)}$

The different kinds of membership functions shown in Table 2.4, allows creating several operations among FSs. When any FSs operator is used, the membership degrees that conform a FS can change since some require one or more FSs and others only one FS. Regardless the kind of FS operator, each one carries out a mapped between crisp values (from universe of discourse) and FSs, obtaining a new membership function. A mathematical basis of FS operators is *T–norm* or triangular norm, and *S–norm* or Co–norm. The T–norm is based on abelian monoid[4] partially ordered in a unitary interval [0,1]. It is defined as the mapped T :[0,1] x [0,1] → [0,1], where fulfills the following axioms:

- Commutative: Let *A* and *B* as two FSs, T(*A*,*B*) = T(*B*,*A*).
- Monotonicity: Let *A*, *B*, *C*, and *D* as four FSs, T(*A*,*B*) ≤ T(*C*,*D*) iff *A* ≤ *C* and *B* ≤ *D*.
- Associative: Let *A*, *B*, and *C* as three FSs, T[*A*, T(*B*,*C*)] = T[T(*A*,*B*),*C*].
- Identity: Let *A* as one FS, T(*A*,1) = *A*.

In FS, The T–norm is used to represent intersection between FSs. On the other hand, S–norm are dual of T–norm, mapped S :[0,1] x [0,1] → [0,1], under the operation of order revision, i.e. ⊥(*A*,*B*) = 1 – T(1–*A*,1–*B*). The above is defined as a generalization of Morgan's laws. Independently of T–norm, the S–norm fulfills the following axioms:

- Commutative: Let *A* and *B* as two FSs, S(*A*,*B*) = S(*B*,*A*).
- Monotonicity: Let *A*, *B*, *C*, and *D* as four FSs, S(*A*,*B*) ≤ S(*C*,*D*) iff *A* ≤ *C* and *B* ≤ *D*.
- Associative: Let *A*, *B*, and *C* as three FSs, S[*A*, S(*B*,*C*)] = S[S(*A*,*B*),*C*].
- Identity: Let *A* as one FS, S(*A*,0) = *A*.

In FS, The S–norm represents union between FSs. In Table 2.5, the most representative T–norm and S–norm are summed–up.

[4]A *monoid* is an algebraic structure that associates binary operation and an identity element; *abelian group* is the result of using a group operation of two group elements independent of order and fulfills the axiom of commutability.

Table 2.5. Some T–norm and S–norm function for FSs.

Function	T–norm	S–nom
Min and Max	$\mu_{A\cap B}(x)=\mu_A(x)\wedge\mu_B(x), for\ \forall x\in X$	$\mu_{A\cup B}(x)=\mu_A(x)\vee\mu_B(x), for\ \forall x\in X$
Algebraic	$\mu_{A\cdot B}(x)=\mu_A(x)\mu_B(x), for\ \forall x\in X$	$\mu_{A+B}(x)=\mu_A(x)+\mu_B(x)-\mu_A(x)\mu_B(x),$ $for\ \forall x\in X$
Yager	$\mu_{T(A,B)}(x)=1-\min\left[1,\left(\left(1-\mu_A(x)\right)^w+\left(1-\mu_B(x)\right)^w\right)^{\frac{1}{w}}\right]$, $for\ \forall x\in X$ and $w\in(0,\infty)$	$\mu_{S(A,B)}(x)=\min\left[1,\left(\mu_A^w(x)+\mu_B^w(x)\right)^{\frac{1}{w}}\right]$, $for\ \forall x\in X$ and $w\in(0,\infty)$
Dubois–Prade	$\mu_{T(A,B)}(x)=\frac{\mu_A(x)\mu_B(x)}{\max\left(\mu_A(x),\mu_B(x),\alpha\right)}$, $for\ \forall x\in X$ and $\alpha\in(0,\infty)$	$\mu_{S(A,B)}(x)=\frac{\mu_A(x)+\mu_B(x)-\mu_A(x)\mu_B(x)-\min\left(\mu_A(x),\mu_B(x),1-\alpha\right)}{\max\left(1-\mu_A(x),1-\mu_B(x),\alpha\right)}$, $for\ \forall x\in X$ and $\alpha\in(0,\infty)$
Einstein Product	$\mu_{T(A,B)}(x)=\frac{\mu_A(x)\mu_B(x)}{2-\left[\mu_A(x)+\mu_B(x)-\mu_A(x)\mu_B(x)\right]}$, $for\ \forall x\in X$	$\mu_{S(A,B)}(x)=\frac{\mu_A(x)+\mu_B(x)}{1+\mu_A(x)\mu_B(x)}$, $for\ \forall x\in X$
Dombi	$\mu_{T(A,B)}(x)=\frac{1}{1+\left[\left(\frac{1}{\mu_A(x)}-1\right)^{\xi}+\left(\frac{1}{\mu_B(x)}-1\right)^{\xi}\right]^{\frac{1}{\xi}}}$, $for\ \forall x\in X$ and $\xi\in(0,\infty)$	$\mu_{S(A,B)}(x)=\frac{1}{1+\left[\left(\frac{1}{\mu_A(x)}-1\right)^{-\xi}+\left(\frac{1}{\mu_B(x)}-1\right)^{-\xi}\right]^{-\frac{1}{\xi}}}$, $for\ \forall x\in X$ and $\xi\in(0,\infty)$
Hamacher	$\mu_{T(A,B)}(x)=\frac{\mu_A(x)\mu_B(x)}{\mu_A(x)+\mu_B(x)-\mu_A(x)\mu_B(x)}$ $for\ \forall x\in X$	$\mu_{S(A,B)}(x)=\frac{\mu_A(x)+\mu_B(x)-2\mu_A(x)\mu_B(x)}{1-\mu_A(x)\mu_B(x)}$ $for\ \forall x\in X$
Drastic sum	$\mu_{T(A,B)}(x)=\begin{cases}\mu_A(x)\ \text{iff}\ \mu_B(x)=1\\ \mu_B(x)\ \text{iff}\ \mu_A(x)=1,\ \text{for}\ \forall x\in X\\ 0,\ \text{otherwise}\end{cases}$	$\mu_{S(A,B)}(x)=\begin{cases}\mu_A(x)\ \text{iff}\ \mu_B(x)=0\\ \mu_B(x)\ \text{iff}\ \mu_A(x)=0,\ \text{for}\ \forall x\in X\\ 1,\ \text{otherwise}\end{cases}$

Defining the main operations with membership functions, the relation among FSs can be expressed in terms of an implication function. In FSs, it is based on the relation between crisp set and FS, in which can have as basis the Cartesian product or collection of elements of a set and its relation with the elements of other set (this concept is supported by the extension principle. For more information, see [KAS98] [ZIM01]).

For definition, a *fuzzy relation*, R(*A*,*B*), is any FS expressed on the cross–product universe X x Y = $\{(x,y)|\ x \in X, y \in Y\}$, given by [KAS98]:

$$\mu_{R(A,B)} : X \text{ x } Y \rightarrow [0,1] \tag{2.61}$$

Eq. (2.61) fulfills the following propositions:

- Reflexiveness: $\mu_R(x,x) = 1$.
- Irreflexiveness: $\mu_R(x,x) = 0$.
- Symmetry: $\mu_R(x,y) = \mu_R(y,x)$.
- Transitivity: $\vee_y\{\mu_R(x,y) \wedge \mu_R(y,x)\} \leq \mu_R(x,z)$, for $\forall x \in X$, $\forall y \in Y$, and $\forall z \in Z$.

During the evolution of fuzzy implication, several functions have been proposed where the most popular is the Mamdami implication. In the Table 2.6, the most relevant fuzzy implications are shown.

Table 2.6. Fuzzy implications. Adapted from [ZIM01] [BUC02] [GON12].

Implication	**Mathematical Expression**
Mandami	$\mu_M(x,y) = \max\left[\min\left\{\mu_{R_1}(x), \mu_{R_2}(y)\right\}\right]$
Zadeh	$\mu_Z(x,y) = \max\left[\min\left\{\mu_{R_1}(x), \mu_{R_2}(y)\right\}, 1-\mu_{R_1}(x)\right]$
Gödel	$\mu_G(x,y) = \begin{cases} 1 \text{ iff } \mu_{R_1}(x) \leq \mu_{R_2}(y) \\ \mu_{R_2}(y), \text{otherwise} \end{cases}$
Lukasiewicz	$\mu_L(x,y) = \min\left\{1,\ 1-\mu_{R_1}(x)+\mu_{R_2}(y)\right\}$
Dienes–Rescher	$\mu_{DR}(x,y) = \max\left\{1-\mu_{R_1}(x), \mu_{R_2}(y)\right\}$

Through the implication functions, the fuzzy system can be built. For definition, a fuzzy system consists of four main steps:

- Fuzzy input and output variables and their respective fuzzy values.
- A set of fuzzy rules.
- Fuzzy inference method.
- Fuzzification and desfuzzification.

In the fuzzy rules, two methods have been popular in several applications: Zadeh–Mandani's fuzzy rules, Eq. (2.62), and Takagi–Sugeno's fuzzy rule, Eq. (2.63) and Eq. (2.64), where the last equation is defined as a lineal function. Both fuzzy rules are expressed as [PALM08]:

$$Rule\ r:\ IF\ x_1\ is\ A_1, AND\ x_2\ is\ A_2, ..., AND\ x_n\ is\ A_n, n, THEN\ y\ is\ B_n \tag{2.62}$$

$$Rule\ r:\ IF\ x\ is\ A_n\ AND\ y\ is\ B_n,\ THEN\ z\ is\ f_n(x,y) \tag{2.63}$$

$$Rule\ r:\ IF\ x_1\ is\ A_1\ AND\ ,...,\ AND\ x_n\ is\ A_n,\ THEN\ z = C_{0,n} + C_{1,n}x_1 + ... + C_{m,n}x_n \tag{2.64}$$

where r is the number of fuzzy rule, n is the n–th FS, m is the m–th constant value C, $f_n(x,y)$ is any function, and $z = C_{0,n} + C_{1,n}\cdot x_1 + \cdots + C_{m,n}\cdot x_n$. A fuzzy rule is divided in an antecedent, starting with the connotation IF, and a consequent, starting with the connotation THEN. It is important to mention that the operator AND is equivalent to "max", and it can be replaced by others operators, OR, equivalent to "min", and NOT, equivalent to Zadeh's negation implication, $1-\mu_A(x)$. In addition, A_n and B_n are identified in the fuzzy rules as fuzzy labels based on human expert's knowledge, e,g, "normal", "critical", "very critical", etc. The above facilities the fuzzy rules application.

On the other, the fuzzy inference is an inference method (it refers to a process of matching current facts from the domain space to the existing knowledge and inferring new facts [KAS98]) that uses any fuzzy implication relation and fuzzy operators connected with the fuzzy rules. This process allows inferring new facts based on the fuzzy rules and fuzzy inputs. In Eq. (2.65), the fuzzy inference is defined.

$$B^* = A^* \circ (A \rightarrow B) = A^* \circ M \tag{2.65}$$

being A^* and B^* (it means as new facts of inference method) are two FSs with two fuzzy labels inferred through A and B, and M is a fuzzy relational matrix that represents the implication relation between A and B. The symbol "$\circ$" is a compositional operator (more information [SHAP93]). The fuzzy inference can mix the results B^* with the output fuzzy variable, y, inferred by the interaction of all fuzzy rules according to the set of fuzzy inputs. The above is called *else–link* between fuzzy rules, where the most used are OR–link and AND–link (For more information others else–link, see [KAS98]).

To the fuzzy inference output, a *fuzzification* process is used to find the membership degrees of $\mu_{A1}(x),\ldots,\mu_{An}(x)$ to which input data x belong to FSs in the antecedent of a fuzzy rule. This process is usually applied with a Singleton function (a point x_i in X has $\mu_A(x_i) = 1$) [GON12]. After fuzzification, the *desfuzzification* process is used to transform fuzzy values in concrete values defined in the output variable, $y \in Y$ (In [ZIM01], several desfuzzification function are explained).

In Fig. 2.13, a representation of a fuzzy system is illustrated.

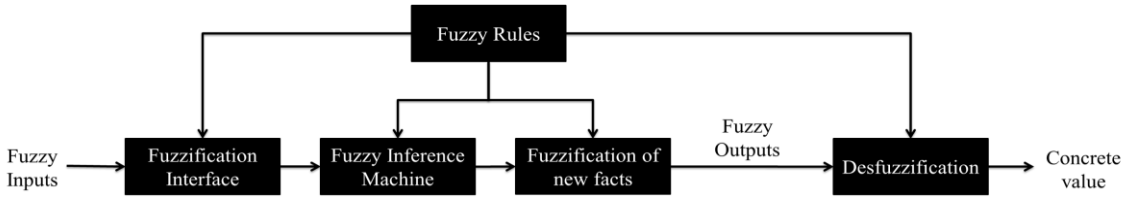

Fig. 2.13. Fuzzy system.

2.4.2 Intuitionistic Fuzzy Sets

In the last subsection, the FS considers the membership degree of a fuzzy set with respect to an element x, in the universe of discourse X. By calculating the non−membership degree of this fuzzy set, for the FS theory, Zadeh complement is applied, $\mu_A{}^c(x) = 1 - \mu_A(x)$, for all $x \in X$. Summing both degrees, $\mu_A(x) + \mu_A{}^c(x) = 1$. For the human being, by expressing the membership degree of an element in a FS, very often he does not define, when asks, the non−membership degree as the complementation to 1 [SZM14b]. This assumption can change due to that in real systems, the imprecise information is implicitly present. Therefore, the sum of membership and non−membership degree is lesser than 1. The above shows the human being can express this kind of situations under a lack of knowledge and hesitancy or imprecision with respect to a real system, real phenomenon, or other case. To represent the hesitancy of the imprecision data or information, [ATA86] proposed the concept of *intuitionistic fuzzy set* (IFS) (In section 1.3, the brief concept of intuitionism was mentioned). The main concepts of IFS are explained below:

Let a data set, $X = \{x_1, \ldots, x_i, \ldots, x_N\}$, where N is the number of samples, a fuzzy set (FS) is defined as, $A = \langle (x, \mu_A(x)) | \, x \in X \rangle$. $\mu_A(x)$ represents the *membership degree* of $x \in X$ in A, where μ_A: $X \rightarrow [0,1]$. Let $\upsilon_A(x)$ as a *non–membership degree* of $x \in X$ in A, where υ_A: $X \rightarrow [0,1]$, an *intuitionistic fuzzy set* (IFS) is expressed as: $A = \langle (x, \mu_A(x), \upsilon_A(x)) | \, x \in X \rangle$.

$$A = \left\{ \left\langle \left(x, \mu_A(x), \upsilon_A(x) \right) \middle| x \in X \right\rangle \right\} \tag{2.66}$$

where for each $x \in X$, it must be fulfilled:

$$0 \leq \mu_A(x) + \upsilon_A(x) \leq 1, \text{ for all } x \in X \tag{2.67}$$

According to Eq. (2.67), a *hesitancy degree*, $\pi_A(x)$, is defined as the intuitionistic index of x in A, as shown in Eq. (2.68):

$$\pi_A(x) = 1 - \mu_A(x) - \upsilon_A(x), \text{ for all } x \in X \tag{2.68}$$

where $0 \leq \pi_A(x) \leq 1$, for $x \in X$. Eq. (2.68) expresses the uncertainty degree or lack of knowledge of whether x belongs to A or not. Considering Zadeh's complement, $\upsilon_A(x) = 1 - \mu_A(x)$, and replacing in Eq. (2.68), it is obtained:

$$\pi_A(x) = 1 - \mu_A(x) - \left[1 - \mu_A(x) \right] = 0 \tag{2.69}$$

In Eq. (2.69), $\pi_A(x) = 0$ which Zadeh's complement turns an IFS to FS, such that $A = \{\langle (x, \mu_A(x), 1 - \mu_A(x)) | \, x \in X \rangle\}$. If $\mu_A(x) = 1$ and $\upsilon_A(x) = 0$, then $\pi_A(x) = 0$; if $\mu_A(x) = 0$ and $\upsilon_A(x) = 1$, then $\pi_A(x) = 0$. In that case, the crisp set does not consider the hesitancy degree. Other functions as the *Sugeno–Hamacher complement* [SUG97] and the *Yager complement* [YAG80] are also used to find the hesitancy degree, as shown below in Eq. (2.70) and Eq. (2.71):

$$\upsilon_A(x) = \frac{1 - \mu_A(x)}{1 - \Omega \mu_A(x)}, \text{ for all } x \in X \tag{2.70}$$

$$\upsilon_A(x)=\left[1-\left(\mu_A(x)\right)^{\alpha}\right]^{\frac{1}{\alpha}},\ \text{for all } x \in X \tag{2.71}$$

where $-1 < \Omega \leq \infty$ and $\alpha \geq 1$. One of the complement function used in the PhD research is the Dombi complement [DOM99] (In chapter 3 and 4, this complement is considered to propose the prediction approach), as shown in Eq. (2.72):

$$\upsilon_A(x)=\frac{\gamma^2\left(1-\mu_A(x)\right)}{\gamma^2\left(1-\mu_A(x)\right)+\left(1-\gamma\right)^2\mu_A(x)},\ \text{for all } x \in X \tag{2.72}$$

where $\gamma \geq 0$. If $\gamma = ½$, Eq. (2.72) is converted in the Zadeh complement. Otherwise, if $\gamma = 1$, Eq. (2.72) is converted in the Sugeno–Hamacher complement, when $\Omega = 1$. Both cases show that then Dombi complement is a particular representation of Eq. (2.70) and Eq. (2.71).

Another important aspect in IFS is when two IFSs are considered, $A, B \in$ IFSs, defining the following relations and operations (in that case, the symbol "$\preccurlyeq$" means "less fuzzy than" and "$\succcurlyeq$" means "greater fuzzy than") [ATA12]:

$$A \preceq B \text{ iff } \mu_A(x) \leq \mu_B(x) \text{ and } \upsilon_A(x) \geq \upsilon_B(x) \text{ or } \mu_A(x) \geq \mu_B(x) \text{ and } \upsilon_A(x) \leq \upsilon_B(x), \text{ for } \forall x \in X \tag{2.73}$$

$$A \succeq B \text{ iff } B \preceq A \tag{2.74}$$

$$A=B \text{ iff } \mu_A(x)=\mu_B(x) \text{ and } \upsilon_A(x)=\upsilon_B(x), \text{ for } \forall x \in X \tag{2.75}$$

$$A \cap B=\left\{\left\langle x,\min\left(\mu_A(x),\mu_B(x)\right),\max\left(\upsilon_A(x),\upsilon_B(x)\right)\right\rangle \middle| \text{ for } \forall x \in X\right\} \tag{2.76}$$

$$A \cup B=\left\{\left\langle x,\max\left(\mu_A(x),\mu_B(x)\right),\min\left(\upsilon_A(x),\upsilon_B(x)\right)\right\rangle \middle| \text{ for } \forall x \in X\right\} \tag{2.77}$$

$$A+B=\left\{\left\langle x,\mu_A(x)+\mu_B(x)-\mu_A(x)\mu_B(x),\upsilon_A(x)\upsilon_B(x)\right\rangle \middle| \text{ for } \forall x \in X\right\} \tag{2.78}$$

$$A \cdot B=\left\{\left\langle x,\mu_A(x)\mu_B(x),\upsilon_A(x)+\upsilon_B(x)-\upsilon_A(x)\upsilon_B(x)\right\rangle \middle| \text{ for } \forall x \in X\right\} \tag{2.79}$$

$$\bar{A}=\left\{\left\langle\left(x,\upsilon_A(x),\mu_A(x)\right)\middle| x \in X\right\rangle\right\} \tag{2.80}$$

$$A@B=\left\{\left\langle x,\frac{\mu_A(x)+\mu_B(x)}{2},\frac{\upsilon_A(x)+\upsilon_B(x)}{2}\right\rangle \middle| \text{ for } \forall x \in X\right\} \tag{2.81}$$

In the chapter 4, Eq. (2.78) and Eq. (2.79) are used to define the evolution rules of prediction approach. In IFSs, a relevant aspect is the geometrical interpretation to observe the relation of $\mu_A(x)$ and $\upsilon_A(x)$ in the universe of discourse X. [ATA12] shown three type of geometrical interpretation, but the Euclidean plane inspired in a Cartesian coordinate system or also well–known as IFS–intepretational triangle, is the most recommended. The above is illustrated in Fig. 2.14.

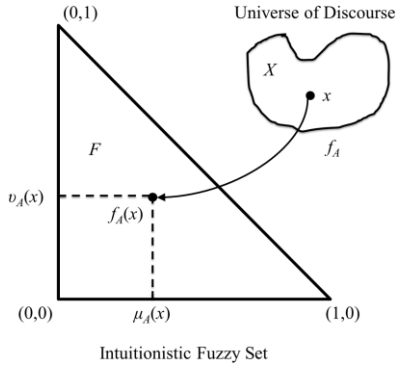

Fig. 2.14. IFS–interpretational triangle. Adapted from [ATA12].

From Fig. 2.14, let $A \subseteq X$ be a fixed set, a function mapped f_A: $X \rightarrow F$, can be located in a point p, whose coordinates are ($\mu_A(x)$, $\upsilon_A(x)$). This point p is equivalent a point of $f_A(x)$, which is established that:

$$p = f_A(x) \in F \tag{2.82}$$

The condition given by Eq. (2.82), is fulfilled for all $x \in X$. Considering the two important IFSs relations to propose the prediction approach (they will be used in the chapter 4), Eq. (2.78) and Eq. (2.79), the geometrical interpretations can be illustrated as in Fig. 2.15 and Fig. 2.16. Let two functions, f_{A+B}: $X \rightarrow F$ and $f_{A \cdot B}$: $X \rightarrow F$, for a point p, $f_{A+B}(x) \in F$ and $f_{A \cdot B}(x) \in F$, for all $x \in X$, two coordinates are assigned:

$$\langle \mu_A(x) + \mu_B(x) - \mu_A(x)\mu_B(x), \upsilon_A(x)\upsilon_B(x) \rangle \tag{2.83}$$

$$\langle \mu_A(x)\mu_B(x), \upsilon_A(x) + \upsilon_B(x) - \upsilon_A(x)\upsilon_B(x) \rangle \tag{2.84}$$

The coordinates of Eq. (2.83) and Eq. (2.84), fulfill for all $x \in X$.

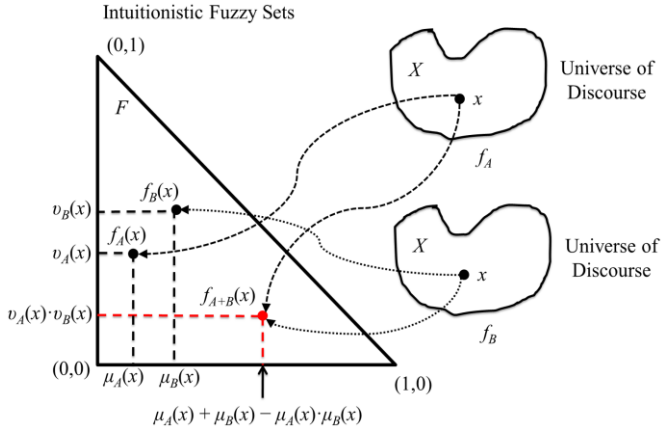

Fig. 2.15. IFS–interpretational triangle of Eq. (2.78) and Eq. (2.83). Adapted from [ATA12].

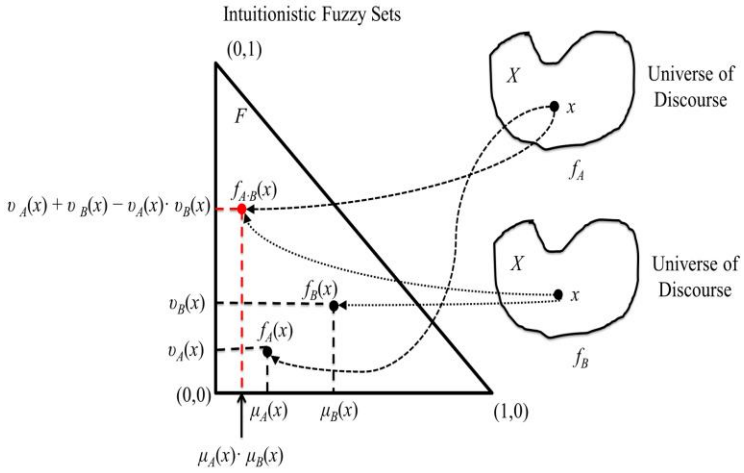

Fig. 2.16. IFS–interpretational triangle of Eq. (2.79) and Eq. (2.84). Adapted from [ATA12].

Since in FSs the cardinality is the sum of all of membership degrees of a set *A*, for IFSs the cardinality is a main concept but its interpretation is different. In [SZM01], the cardinality for an IFS is expressed in terms of *Count* [YAG93], as mentioned below:

- The least cardinality of an IFS(*A*) or sigma−count is represented as min∑*Count* or min−sigma−count, as shown below:

$$\min \sum Count(A) = \sum_{i=1}^{N} \mu_A(x_i) \tag{2.85}$$

- The biggest cardinality for an IFS(*A*) is defined in terms of max∑*Count* or max−sigma−count, as shown below:

$$\max \sum Count(A) = \sum_{i=1}^{N} \left[\mu_A(x_i) + \pi_A(x_i) \right] \tag{2.86}$$

If $A = A^c$ or *A* complement, then:

$$\max \sum Count(A) = \sum_{i=1}^{N} \left[\upsilon_A(x_i) + \pi_A(x_i) \right] \tag{2.87}$$

By means of Eq. (2.85) and Eq. (2.86), the cardinality for an IFS is expressed as an interval, given by:

$$Card\ IFS(A) = \left[\min \sum Count(A), \max \sum Count(A) \right] \tag{2.88}$$

2.5 Fuzzy Clustering Methods

In some applications, the exact of amount of fuzzy rules, the best membership function, the appropriated quantity of fuzzy inputs, the quantity of fuzzy labels, and other aspects of a fuzzy system, are difficult of finding out when the system has a complex behavior and the knowledge is limited. [GEN07] defines a complex system as a physical structure in an open environment where

uncertainly and dynamic of physical phenomena are difficult of understanding. Due to this limitation, the mathematical models that describe the dynamic of system are approached but not exact.

In OFC, the spectrum can be submitted to different linear and non−linear phenomena, changes of temperature, external vibrations, and changes of polarization when is generated or propagated through SMF. The interaction of all the mentioned events are problematic for real applications in optical communication and to determinate the exact mathematical model. In section 1.2.4, a recent advance in analysis of OFC behavior was mentioned, where the mathematical models were expressed in terms of nonlinear oscillations and bifurcations. The use of these techniques shows the need for using notions on nonlinear dynamic, in which the presence of complex behaviors can be presented in OFC spectrum. However, the increasing of the physical variables can become problematic in the global dynamic of OFC due to the complexity of mathematical models. Thus, the application of approximated models to reduce the mathematic complexity can limit some observations relevant of OFC behavior. In addition, a complex behavior of system is presented by imprecisions in the measurements, non−linear dynamic of physical variables, and unpredictable variations [GEN07] [ISA07].

Based on the above context, one alternative widely used for analyzing complex systems are the fuzzy clustering methods, mentioned in [KEM06] [ISA07] [AGU07a] [ISA08] [DIE08] [BOT13] [ISA14]. The main characteristics are explained below.

2.5.1 Concept of Clustering

The clustering is a technique that establishes the relation of a set of elements with respect to a group. The group is also called *class*. The clustering makes a correlation and classification of a set of data, $X \in R^D$, corresponding to *D−descriptors or physical variables* of an sample *I*, given by $x_i = \{x_{i,1},..., x_{i,d},\ldots,x_{i,D}\}$. In Fig. 2.17, a clustering representation is illustrated.

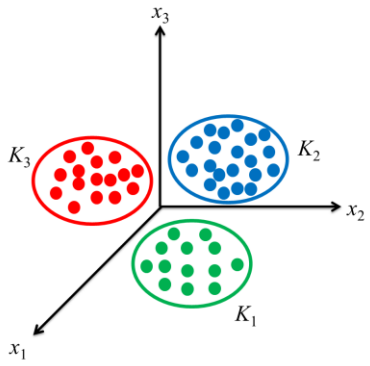

Fig. 2.17. Clustering representation where K_1, K_2, and K_3 are classes and x_1, x_2, and x_3 are three descriptors or physical variables. The scheme is shown for a classification of 3 Dimensions.

The clustering can be made through two alternatives [ISA07]:

- *Non−Supervised*: it means that the clustering is carried out through preprocessing data to find the appropriated classes without the use of information of an expected classification.

- *Supervised*: through expected classification, i.e. the number of classes was defined by the knowledge of system or human−expert's opinion, the clustering is used for tasks of pattern recognition.

For the case of clustering without any information of expected classification, the best option is the non−supervised learning. A main characteristic of this alternative consists on the association of data with the classes through a similarity measure. In several clustering algorithms, the distance measure between a data vector and classes' centroids is the most used [BOT13]. Usually, the centroids are randomly expressed and an optimization algorithm for distance minimization is applied for updating the data distribution in assigned classes. The optimization algorithm takes into account an *objective function* or minimization mean−square−error function, in order to find homogeneous classes and differentials between them.

The data partition in the data space can be generated in two ways: hard and fuzzy partition. The former is generated by techniques like K−Means. The latter is obtained by methods inspired by K−Means, called Fuzzy C−Means and GK−Means, or other option based on statistical functions as LAMDA. Each one is explained below:

2.5.2 K–Means

K−Means is one of the most famous clustering techniques. It uses the number of classes, K, input data, X, and initial centroids, c_j, as input parameters [PALM08]. The input data are defined as a matrix $X = \{x_1,\ldots, x_i,\ldots, x_N\}$, being x_i the data of associated to a sample i. One curiosity of K−means is to find out K, in which can be introduced by user's knowledge or human−expert's criterion. Defining this requisite, each sample of the descriptors or physical variable, $x_i = \{x_{i,1},\ldots, x_{i,d},\ldots, x_{i,D}\}$, is assigned at class with a distance closer at centroid, achieving a geometrical representation of classification. The above generates a hard data partition where each sample belongs or not to a class. Since K−means is iterative, once the classes with their elements are distributed, the centroids are recalculated to realize a new assignation until to get a concrete classification.

In order to find the best classification ever of data, the objective function J is used to update the centroids and the assignation of data to each class, expressed as:

$$J = \sum_{i=1}^{N}\sum_{j=1}^{K} d_{i,j}^2 \tag{2.89}$$

where $d_{i,j}$ is the distance of a sample I with respect to the centroid, c_j, of the j−th class,$\{1,\ldots, j,\ldots, K\}$, given by:

$$d_{i,j} = \left\| x_i - c_j \right\|_A = \left(x_i - c_j \right)^T A \left(x_i - c_j \right) \tag{2.90}$$

being A the distance metric in matrix−way. If $A = I$, the identity matrix is considered, which $\|\cdot\|_{A=I} = (\cdot)^{\mathrm{T}}(\cdot)$, defined as norm−2 distance or also well−known Euclidian distance [KEM04], given by:

$$d_{i,j}^2 = \left\| x_i - c_j \right\|_{A=I} = \left(x_i - c_j \right)^T \left(x_i - c_j \right) \tag{2.91}$$

Based on Eq, (2.89) and Eq. (2.91), the K−means algorithm operates as follows:

1) Input Parameters are assigned: $X = \{x_1,\ldots, x_i,\ldots, x_N\}$, number of classes, K, for all $K > 1$, and error e..

2) Select randomly an initial centroids matrix.

3) Select one sample of matrix X and approximates at the closest centroid, associated with a class j.

4) Recalculate the centroid, c_j, and associates it to each sample $x_i \in X$.

5) Iterate η−iterations in the steps 3 and 4 until to get a centroids stable matrix and the function J value does not change.

2.5.3 Fuzzy C–Means (FCM)

Fuzzy C−Means (FCM) [BEZ81] is a clustering algorithm inspired on fuzzy sets theory and K−Means. The method seeks to minimize the Euclidian distance (see Eq. (2.91)) between the sample x_i and the centroid, c_j, and each sample, according to its closeness at centroid, a membership degree is assigned, $\mu_j(x_i) \rightarrow [0,1]$. The membership degree associates a sample x_i to the class j. The objective function of FCM adds the term $\mu_j(x_i)$, as shown in Eq. (2.92):

$$J = \sum_{i=1}^{N}\sum_{j=1}^{K}\mu_j^m(x_i)d_{i,j}^2 \tag{2.92}$$

where m is fuzzification constant, $m \in (1,\infty)$. Usually, $m = 2$. By comparing Eq. (2.89) and Eq. (2.92), both allow minimizing the data distance of one class to each centroid. The difference between them establishes that the function J of FCM associates the membership degree of each sample to one class, and the function J of K−Means does not consider this kind of membership. Therefore, FCM can obtain partitions in the data space more smooth than K−Means. Based on this condition, FCM generates a geometric representation of classes in Hiper−spheres of D−dimensions.

In FCM, the initial parameters are the same for K−means. Hence, knowledge of number of classes is required. Like K−Means, the algorithm starts with random centroids and they recalculated in η−iterations. For each iteration, a *membership degree matrix*, U, is updated, of dimensions N x K. The matrix U (Eq. 2.93) considers $\mu_j(x_i)$ of a sample x_i to the class j. One importance of matrix U is all data are represented by a fuzzy partition different than hard partition of K−means.

$$U = \begin{bmatrix} \mu_1(x_1) & \cdots & \mu_j(x_1) & \cdots & \mu_K(x_1) \\ \vdots & \ddots & \vdots & \cdots & \vdots \\ \mu_1(x_i) & \cdots & \mu_j(x_i) & \cdots & \mu_K(x_i) \\ \vdots & \cdots & \vdots & \ddots & \vdots \\ \mu_1(x_N) & \cdots & \mu_j(x_N) & \cdots & \mu_K(x_N) \end{bmatrix} \tag{2.93}$$

In the Eq. (2.94) and Eq. (2.95), the updating functions for the centroids and membership degrees for η−iteration are expressed.

$$c_j(\eta) = \frac{\sum_{i=1}^{N} \left[\mu_j(x_i)(\eta-1)\right]^m \cdot x_i}{\sum_{i=1}^{N} \left[\mu_j(x_i)(\eta-1)\right]^m}, \text{ for all } j \in K \tag{2.94}$$

$$\mu_j(x_i)(\eta) = \frac{1}{\sum_{j=1}^{K} \left[\frac{d_{i,j}^2(\eta)}{d_{i,j}^2(\eta-1)}\right]}, \text{for all } x_i \in X \tag{2.95}$$

Based on Eq, (2.92)−Eq. (2.95) and the structure of the K−means algorithm, the FCM algorithm works the following procedure:

1) Input Parameters are assigned: $X = \{x_1, \ldots, x_i, \ldots, x_N\}$, number of classes, K, for all $K > 1$, a fuzzification parameter $m > 1$ and error e.

2) Select randomly an initial centroids matrix.

3) Calculate the Euclidian distance.

4) Calculate the matrix U, using for each iteration, Eq. (2.94) and Eq. (2.95).

5) Repeat steps 3 and 4 until to obtain a convergence of matrix U, i.e. $|U(\eta+1) - U(\eta)| < e$ when the function J does not change.

It is important to clarify if $\mu_j(x_i)(\eta) = 1$, the distance is 0, which a hard partition can obtain as in K−means algorithm.

2.5.4 Gustafson and Kessel Means (GK−Means)

The GK−means method [GUS79] is similar to the FCM method but its main difference is the distance measure, called Mahalanobis distance [GUS92]. Considering Eq. (2.90), the matrix A is replaced by the following expression:

$$A = \left[\partial_j \cdot \det\left|F_j\right|\right]^{\frac{1}{\eta}} \left[F_j\right]^{-1} \tag{2.96}$$

where ∂_j is the volumetric index of classes (usually, $\partial_j = 1$), and det $|F_j|$ is the determinant of fuzzy covariance matrix, expressed for each class j as:

$$F_j = \frac{\sum_{i=1}^{N} \mu_j^m(x_i) \cdot (x_i - c_j)^T (x_i - c_j)}{\sum_{i=1}^{N} \mu_j^m(x_i)} \tag{2.97}$$

By using Mahalanobis distance, the data partition in the data space is represented by Hiper−ellipsoids, which allows defining the membership degree of a sample x_i to the class j much more efficient than FCM.

The GK−means algorithm is similar to FCM algorithm but the Eq. (2.96) and Eq. (2.97) must be included, as well as the additional parameter, $\hat{\partial}_j$, for each class *j*.

2.5.5 LAMDA

The FCM and GK−means methods have a good performance for tasks of data classification through the information of matrix *U*. However, they depend on number of classes and can become sensible with respect to the initial fuzzy partition or random selection of initial centroids. In consequence, the number of samples among classes can change once of algorithm is started again. Due to this limitation, other method has been a great performance for tasks of classification and pattern recognition: learning algorithm for multivariable data analysis (LAMDA).

LAMDA [AGU82] [PIE89] [KEM04] is a clustering method based on fuzzy sets theory that works with quantitative and qualitative data. Unlike FCM and GK−Means, the LAMDA method *can generate classes*, i.e. it does not require knowing the number of classes. To carry out this generation, LAMDA estimates the *adequacy degree* of each sample x_i with respect to the descriptors or physical variables, *d*, to each class *j*. According to [ISA07] [BOT13], the adequacy degree is an adaptation in the "posibilistic sense".

Before to apply LAMDA, it is important to normalize data, $\hat{x}_{i,d}$, given by:

$$\hat{x}_{i,d} = \frac{x_{i,d} - xmin_d}{xmax_d - xmin_d} \tag{2.98}$$

where $x_{i,d}$ is the data of a sample *I* associated with a descriptor *d*, $xmax_d$ is the maximum value of descriptor *d*, and $xmin_d$ is the minimum value of descriptor *d*. The data normalization has a range, $\hat{x}_{i,d} \rightarrow [0,1]$. The LAMDA method calculates the adequacy degree through statistical functions where Binomial and Gaussian functions are the most used. [AGU82] defined the *marginal adequacy degree* (MAD) of each data associated to one descriptor, $\hat{x}_{i,d}$, to each class *j*. For each class, the MAD is attributed as a vector, expressed as $\{MAD_1(\hat{x}_{1,1}, K_j), \ldots, MAD_d(\hat{x}_{i,d}, K_j), \ldots, MAD_D(\hat{x}_{N,D}, K_j)\}$. The main MAD functions are explained below:

- *Fuzzy Binomial Function*: This function is an extension of binomial function based on FSs [HERN06]. It is defined as a monotonous function that satisfices boundary conditions and can be considered as fuzzy function according to adequacy and non−adequacy possibilities, $p_{i,j}$ and $1-p_{i,j}$, respectively. Mathematically, this MAD function is expressed as:

$$MAD\left(\hat{x}_{i,d} \middle| K_j\right) = p_{i,j}^{\hat{x}_{i,d}} \left(1 - p_{i,j}\right)^{1-\hat{x}_{i,d}} \tag{2.99}$$

  The minimum and maximum values of MAD are 0 and 1, respectively, if $p_{i,j} \neq 0.5$. Otherwise, if $p_{i,j} = 0.5$, it is not possible that data is adjusted to the class *j*, and therefore, the element is classified as *non−informative class* (NIC). By default, $\rho_{i,j}$ (NIC)= 0.5. NIC represents the minimum decision threshold to classify one element to a specific class.

The Eq. (2.99) has been extended through a *H*−function, defined in Eq. (2.100):

$$MAD\left(\hat{x}_{i,d}\middle|K_j\right)=H\cdot p_{i,j}^{\hat{x}_{i,d}}\left(1-p_{i,j}\right)^{1-\hat{x}_{i,d}} \tag{2.100}$$

where *H* is given by:

$$H=\frac{\log\left(\dfrac{p_{i,j}}{1-p_{i,j}}\right)}{2p_{i,j}-1} \tag{2.101}$$

- *Centered Binomial Function*: It is a binomial function that considers a partition around of classes' centroids [WAI98] [KEM04]. The MAD function is calculated by the Euclidian distance of normalized data, $\hat{x}_{i,d}$, and the descriptor centroid, c_d, $dis_{i,d} = \| \hat{x}_{i,d} - c_d \|$. The MAD is defined as:

$$MAD\left(\hat{x}_{i,d}\middle|K_j\right)=p_{i,j}^{1-dis_{i,d}}\left(1-p_{i,j}\right)^{dis_{i,d}} \tag{2.102}$$

There is a modification of Eq. (2.102), considering *I*−function, as shown below:

$$MAD\left(\hat{x}_{i,d}\middle|K_j\right)=I\cdot p_{i,j}^{1-dis_{i,d}}\left(1-p_{i,j}\right)^{dis_{i,d}} \tag{2.103}$$

Being *I*−function:

$$I=\frac{\log\left(\dfrac{p_{i,j}}{1-p_{i,j}}\right)}{2p_{i,j}-p_{i,j}^{c_d}\left(1-p_{i,j}\right)^{1-c_d}-p_{i,j}^{1-c_d}\left(1-p_{i,j}\right)^{c_d}} \tag{2.104}$$

- *Gaussian Function*: It establishes a distribution normalized function of descriptors, calculating the mean, $m_{i,j}$, and standard deviation, $\sigma_{i,j}$, of each sample x_i to the class *j* [SAM08]. In Eq. (2.105), the MAD Gaussian function is defined (the NIC value has a typical value of 0.6165).

$$MAD\left(\hat{x}_{i,d}\middle|K_j\right)=\exp\left[-\frac{\left(\hat{x}_{i,d}-m_{i,j}\right)^2}{2\sigma_{i,j}}\right] \tag{2.105}$$

By means of MAD functions, a global adequacy can be considered to include all adequacy degrees of a class *j*. The above is called *global adequacy global* (GAD) of a sample $\hat{x}_i$ to the class *j*, given by [KEM04]:

$$GAD\left(\hat{x}_i\middle|K_j\right)=\psi\cdot\left[MAD\left(\hat{x}_{1,1}\middle|K_j\right),\ldots,MAD\left(\hat{x}_{i,d}\middle|K_j\right),\ldots,MAD\left(\hat{x}_{i,D}\middle|K_j\right)\right] \tag{2.106}$$

Being $\psi[\cdot]$ an aggregation function. To link MADs to GAD, the S−norm and T−norm function shown in Table 2.5, are considered. Specifically, LAMDA applies Min−Max and Algebraic functions. By using an disaggregation function, $\Theta = 1 - \psi$, the connectivity's Min−Max and Probabilistic are given by:

$$\psi(A,B) = A \cup B$$
$$\psi(A,B) = A + B - AB \tag{2.107}$$

$$\Theta(A,B) = A \cap B$$
$$\Theta(A,B) = AB \tag{2.108}$$

Considering Eq. (2.106) – Eq.(2.108), GAD can be defined as a linear interpolation function between S−norm and T−norm [PIE91], as shown in Eq. (2.109):

$$\begin{aligned} GAD(\hat{x}_i|K_j) = \varepsilon \cdot \psi\left[MAD(\hat{x}_{1,1}|K_j),...,MAD(\hat{x}_{i,d}|K_j),...,MAD(\hat{x}_{i,D}|K_j)\right] + \\ (1-\varepsilon)\cdot\Theta\left[MAD(\hat{x}_{1,1}|K_j),...,MAD(\hat{x}_{i,d}|K_j),...,MAD(\hat{x}_{i,D}|K_j)\right] \end{aligned} \tag{2.109}$$

Being ε an exigency parameter, $\varepsilon \rightarrow [0,1]$. If $\varepsilon = 1$, GAD will restrict the samples classification according to the used S−norm and the T−norm will be little significant. Otherwise, if $\varepsilon = 0$, GAD will take into account the classification with respect to the T−norm function and the S−norm will be little significant.

MAD and GAD functions consider the NIC that allows establishing automatically a minimum threshold, where:

- If GAD value of a sample $\hat{x}_i$ is lesser than GAD(NIC), it means no adequacy is generated to nothing of current classes. In that case, the current class is conserved.
- If GAD value of a sample $\hat{x}_i$ is bigger than GAD(NIC), it allows generating a new class with the NIC information and the sample $\hat{x}_i$.

LAMDA can carry out three kinds of learning, as mentioned below [KEM04] [ISA07]:

- *Passive Recognition*: it is used whether the data have incorporated known classes, which LAMDA generates an off−line classification and through new measured data of system, the method recognizes the belonging of a new sample to one of the known classes (this task is realized in online). If the new data is not recognized to one of the classes, LAMDA classifies it to NIC.
- *Self−Learning*: it allows creating or updating the number of classes of each sample when no classification is known and the user needs to find it. By analyzing the first sample, it is classified in the NIC, and immediately it generates a class with the mean of NIC and the sample value. The second sample is analyzed whether it belongs to the created class or NIC. If the sample belongs to the NIC, a new class is created. Otherwise, if the sample belongs to the created class, the parameters are updated (in that case, the moving mean and/or the moving standard deviation) to the class with the maximum membership degree. The procedure is repeated until all samples are analyzed. Therefore, this learning does not require knowing a priori the number of classes and iterations.

- *Supervised Learning*: it is used when the data have incorporated the classes, allowing a learning of data through an initial set of classes, but they can be modified by analyzing new samples. The above generates new classes or an updating of applied parameters.

The general scheme of LAMDA is illustrated in Fig. 2.18. The scheme shows MADs of each one of the descriptors or physical variables, {1,…, *d*,…, *D*}of the sample $\hat{x}_i$ to the class *j*, being {1,…, *j*,…, *K*}. The MADs of descriptors for a sample $\hat{x}_i$ of each class *j*, allows calculating GAD of sample $\hat{x}_i$ to each class *j*, through fuzzy T−norm and S−norm. The maximum GAD is the maximum membership degree of sample $\hat{x}_i$ to one class *j*. For the classes' adequacy, NIC is used to establish automatically a minimum threshold to be overcome, in order to find the belonging of one data to one class. In case that it does not overcome the membership degree of NIC, means no adequacy is associated to current classes and therefore, a new class is created with NIC information and the actual data.

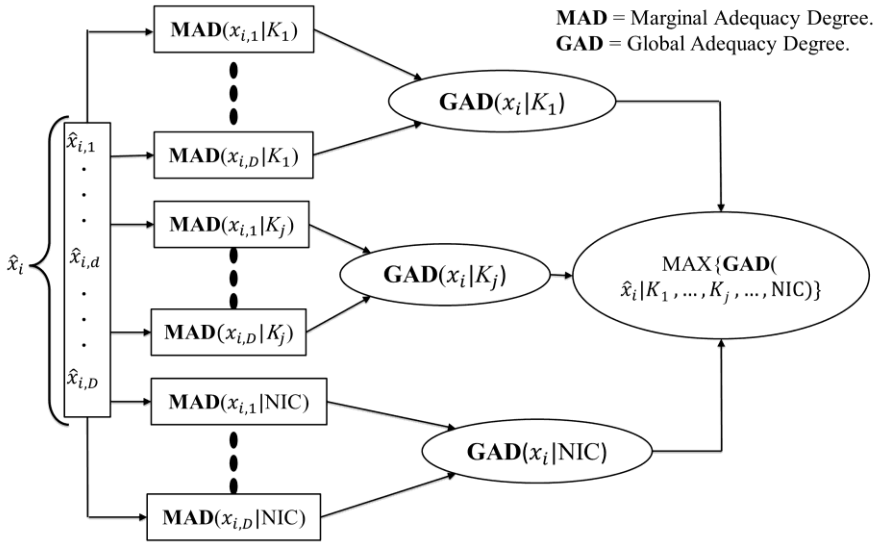

Fig. 2.18. General scheme of LAMDA method. Adapted from [BOT13].

2.6 Summary

This chapter explained the main concepts of OFC generation, its behavior during its propagation in SMF, the correction method of spectral shape through pulse shaping, as well as the fuzzy sets theory. During the exploration of OFC generation proposed from 1960's, the microresonator ring exhibits a relevant throughput to create hundreds of optical carriers in a wide spectral width through one frequency comb. Nevertheless, the microresonator is sensible front to changes of temperature, vibrational variations, and minimal polarization fluctuations, which the mode−locked lasers and MZMs can offer better stability in power variation. However, both generation techniques cannot maximize the spectral wide than microresonator.

On the other hand, the GVD and SPM phenomena are relevant in OFC propagation through SMF, analyzed by means of Gaussian function behavior generated by mode−locked laser. If the

transmission rate is increased in an optical link, the PMD interacts with GVD and SPM and the harmful effects in the temporal and spectra domain of OFC can become critics. In that case, the ISI and BER can increase until the optical link generates high losses in power and several changes of phase. Hence, the interaction PMD−GVD−SPM must be taken into account when the correction in intensity and phase are carried out by pulse shaping techniques. The pulse shaper offers an interesting alternative to compensate dispersion and possible non−linear effects in an OFC spectrum, but the dependence of number of pixels, spectral resolution, response time, and efficient, can be limited. Comparing AOM and LC−SLM, the former has the fastest response time but the latter offers the best efficient. Therefore, the advantages and disadvantages of both devices are "balanced" for tasks of correction of intensity and phase of OFC.

In optical communications systems, the fuzzy sets theory is an alternative to understand the OFC behavior propagated through SMF or to observe the stability of an OFC spectrum. In addition, it is likely to develop a fuzzy system to do a control action in a compensation system that mitigates the presence of any linear and non–linear phenomena. These application scenarios are some of other alternatives to be applied in optical systems. The IFSs is an interest fuzzy extension of FSs, which the uncertainly in such sets is considered. In OFC spectrum, IFSs will allow verifying when a critical change in phase and intensity may convert in critical spectral shape fluctuation or high positive phase shift in optical carriers. On the other hand, the fuzzy clustering methods can become useful for detecting presence of GVD, SPM and/or PMD in an OFC spectrum or spectral shape variations, through the assignation of labels classes found by FCM, GK−Means, and LAMDA. Since the knowledge of number of classes must be known for OFC applications, the LAMDA method can be the best choice due to the fact that can generate automatically the classes through MAD and GAD functions. This technique is key to get an initially membership degrees matrix for applying the prediction method, divided in two parts and explained in chapters 3 and 4.

CHAPTER 3: HIFEAN – General Intuitionistic Fuzzy Entropy by Adequacy and Non–Adequacy

3.1 Introduction

The chapter begins with the antecedents of fuzzy entropy (FE) and intuitionistic fuzzy entropy (IFE) (section 3.2). The FE is defined as a measure to find the amount of information or uncertainly of a fuzzy set (FS). This kind of uncertainly refers that much membership of a sample, *x*, belongs to a FS or class. For example, one class can be a specific power level of a spectrum and by using FE, the certainly that one power level belongs to this class can be found. In the present chapter, two entropy measures are proposed: fuzzy entropy by adequacy and non−adequacy (FEAN) and general intuitionistic fuzzy entropy by adequacy and non−adequacy (HIFEAN). The former, expressed as E_A, allows measuring the adequacy and non−adequacy degrees of a sample to one FS or class (section 3.3). The latter, expressed as H_{IFEAN}, is based on intuitionistic fuzzy sets (IFSs) and FEAN, where the degree of intuitionism, expressed as H_{HC}, and the degree of fuzziness, H_{AN}, are proposed (section 3.4). Both measures are compared in the analysis of optical frequency comb (OFC) behavior and second−order polarization−mode dispersion (PMD) detection in OFC propagated in single–mode fiber (SMF) (section 3.5, 3.6, and 3.7). To demonstrate these measures, four axioms defined in the literature, sharpness, maximization, resolution, and symmetry are used to verify its validity.

The chapter III is organized as follows: 3.2) Antecedents; 3.3) Proposal I: FEAN; 3.4) Proposal II: HIFEAN; 3.5) Application of FEAN: Analysis of Optical Combs Spectra: 3.6) Application of HIFEAN: Optical Combs Spectra Detection; 3.7) Application of HIFEAN: Second−Order PMD Detection and 3.8) Summary.

3.2 Antecedents

The concept of intuitionistic fuzzy sets (IFSs) was proposed by [ATA86], where the operators and the geometrical interpretation of IFSs were established. Based on the notion of IFS and fuzzy entropy (FE), [BUR96] developed the first measure of intuitionistic fuzzy entropy (IFE) based on the hesitancy degree of IFSs. Unlike FE, IFE is able to calculate the uncertainly and credibility of FSs [CHE10], which increases the capacity for measuring the fuzziness. On the other hand, the IFE was defined in terms of the geometrical interpretation of IFSs [SZM01], using Kosko's geometrical interpretation for FSs [KOS86].

Since 2003, several interpretations of IFE were developed until the present day. [COR03] explained the notion of a graded inclusion indicator through the FSs and IFSs oriented to the approximate reasoning and non–probabilistic entropy. [HUN03] uses the distance measures between the degree of membership and the degree of non–membership to define two IFEs. [LIU05] found the relationship between entropy and subsethood to introduce FEs for interval–valued intuitionistic fuzzy sets (IVIFSs). [HUN06] constructed up two families of IFEs through the degree of intuitionism and the geometrical representation established by Havrda and Charavát's entropy and Rényi's entropy. An important work defined by [VLA07], collected the IF cross–entropy and

established an intuitive and mathematical connection of FSs and IFSs through the degree of fuzziness and the degree of intuitionism. This contribution set up the connection between De Luca and Termini's entropy and Burillo and Bustince's entropy. Other interesting interpretation was shown by [YE10], where two IFEs based on a generalized version of weighted fuzzy entropy and a complementary was defined. Another work made by [FAT11] defined an intuitionistic fuzzy cross–entropy measure considering stochastic IFSs for a future alternative in image processing applications. Other important proposal developed by [LI12], found an axiom to show the existing relationship between the similarity measure and entropy for IFSs.

Since 2013 and present day, the contribution in IFE have been different directions. [VER13] found a generalized version of exponential IFE and its connection with exponential FE. [PAL13] justified the need for using two facets of uncertainly for IFSs, integrating the fuzziness and lack of knowledge or non–specificity to build–up a generating family of measures. Recently, [SZM14a] have proposed a measure to find out the amount of knowledge conveyed in IFSs and its relationship with the amount of information through positives and negatives information.

By means of the last mentioned contributions, the following section will explain initially a new Fuzzy Entropy.

3.3 Proposal I: FEAN

In this section, a new FE is proposed through two concepts in FSs: Diez–Lledo and Aguilar's FE and the adequacy degree. The former was defined by [DIE06], considering De Luca and Termini's axioms and Yager's entropy that measures the specificity for FSs. The latter is defined as a Singleton Function that relates and the maximum membership degree for a FS and the membership degree of a sample x_n. By using the above, Diez–Lledo and Aguilar's FE is expressed as:

$$H_D(A) = 1 - \frac{\sum_{n=1}^{N} \delta_A(x_n) \exp\left(\delta_A(x_n)\right)}{N \cdot \mu m_A \cdot \exp\left(\mu m_A\right)} = 1 - I_D(A) \tag{3.1}$$

where:

- $\mu m_A = \max\{\mu_A(x_1), \ldots, \mu_A(x_n), \ldots, \mu_A(x_N)\}$, represents the maximum membership degree for FS(A).
- $\delta_A(x_n) = \mu m_A - \mu_A(x_n)$, refers to the adequacy degree for a sample x_n.
- $I_D(A)$ is the amount of information for FS(A).

In Eq. (3.1), $H_D(A)$ is an approach that replaces the "sharpness" relation by $\mathrm{REL}(A) \leq \mathrm{REL}(A^*)$ and to use as reference the Singleton function instead of the corresponding crisp set [DIE08]. The REL relation or reliability of a FS is given by:

$$REL(A) = \mu m_A + \mathrm{card}\left[\delta_A(x)\right] = \mu m_A + \sum_{n=1}^{N} \delta_A(x_n) \tag{3.2}$$

By considering Eq. (3.1) and (3.2), $H_D(A)$ fulfills the following axioms:

(P.1) $H_D(A) = 0$ iff $\mu_A(x)$ is a Singleton function, for all $x \in X$.

(P.2) $H_D(A)$ is maximum iff $\mu_A(x) = 0.5$, for all $x \in X$.

(P.3) $H_D(A) \leq H_D(A^*)$ iff $H_D(A^*)$ is the entropy of A^* and a "REL" version of A.

As the adequacy degree is represented by the Singleton function, $\delta_A{}^c(x_n) = \mu m_A{}^c - \mu_A{}^c(x_n)$, is defined as the non–adequacy degree for a sample x_n, being $\mu m_A{}^c = \max\{\mu_A{}^c(x_1),\ldots, \mu_A{}^c(x_n),\ldots, \mu_A{}^c(x_N)\}$ as the maximum non–membership degree for FS(A) and $\mu_A{}^c(x_n) = 1 - \mu_A(x_n)$ as the Zadeh complement. The above allows establishing two FSs, $A = \langle (x, \delta_A(x))| \forall x \in X\rangle$ and $A^c = \langle (x, \delta_A{}^c(x))| \forall x \in X\rangle$, and taking into account Eq. (3.1), the fuzzy entropy by adequacy and non–adequacy (FEAN) is expressed as:

$$E_A^{(1)} = 1 - \frac{1}{N}\left| \frac{\sum_{n=1}^{N} \delta_A(x_n)\exp\left(\delta_A(x_n)\right)}{\mu m_A \exp\left(\mu m_A\right)} - \frac{\sum_{n=1}^{N} \delta_A^c(x_n)\exp\left(\delta_A^c(x_n)\right)}{\mu m_A^c \exp\left(\mu m_A^c\right)} \right| \tag{3.3}$$

Comparing Eq. (3.1) and Eq. (3.3), the latter allows calculating the fuzziness for FS(A) with the adequacy degree, the non–adequacy degree and the Zadeh complement. This consideration allows calculating more accuracy in the uncertainly measure for FS(A). On the other hand, Eq. (3.3) is linked–up to Eq. (3.2), but there exists a REL(A^c) relation for FS(A^c), given by:

$$\mathrm{REL}\left(A^c\right) = \mu m_A{}^c + \mathrm{card}\left\{\delta_A{}^c(x)\right\} = \mu m_A{}^c + \sum_{n=1}^{N} \delta_A{}^c(x_n) \tag{3.4}$$

Such as Eq. (3.1), Eq. (3.3) must fulfill with the following axioms:

(P.1) $E_A = 0$, if $\mu_A(x)$ and $\mu_A{}^c(x)$ are Singleton sets, for all $x \in X$.

(P.2) E_A is maximum (i.e. $E_A = 1$) if $\mu_A(x) = \mu m_A$ and $\mu_A{}^c(x) = \mu m_A{}^c$, for all $x \in X$.

(P.3) $E_A \geq E_{A^*}$, if E_{A^*} is the entropy of A^* and a REL version of A.

(P.4) $E_A = E_A{}^c$ if $E_A{}^c$ is the entropy of the complement set of A^c.

Proof:

(P.1) If there exists one sample x_i in the universe of discourse where $\mu_A(x_i) = \mu m_A$ and $\mu_A{}^c(x_n) = \mu m_A{}^c$, then the rest of samples of FS(A) have membership degree equal to 0 and FS(A^c) equal to 1. Therefore, $E_A{}^{(1)} = 0$ if the above consideration is presented in FS(A) and FS(A^c).

(P.2) If $\mu_A(x) = \mu m_A$ and $\mu_A{}^c(x) = \mu m_A{}^c$, for all $x \in X$, $E_A{}^{(1)}$ will be maximum.

(P.3) Considering a FS(A^*):

$$E_{A^*}^{(1)}=1-\frac{1}{N}\left|\frac{\sum_{n=1}^{N}\delta_{A^*}(x_n)\exp\left(\delta_{A^*}(x_n)\right)}{\mu m_{A^*}\exp\left(\mu m_{A^*}\right)}-\frac{\sum_{n=1}^{N}\delta_{A^*}^{c}(x_n)\exp\left(\delta_{A^*}^{c}(x_n)\right)}{\mu m_{A^*}^{c}\exp\left(\mu m_{A^*}^{c}\right)}\right|$$

Then:

$$E_{A}^{(1)}-E_{A^*}^{(1)}=-\frac{1}{N}\left|\frac{\sum_{n=1}^{N}\delta_{A}(x_n)\exp\left(\delta_{A}(x_n)\right)}{\mu m_{A}\exp\left(\mu m_{A}\right)}-\frac{\sum_{n=1}^{N}\delta_{A}^{c}(x_n)\exp\left(\delta_{A}^{c}(x_n)\right)}{\mu m_{A}^{c}\exp\left(\mu m_{A}^{c}\right)}\right|$$
$$+\frac{1}{N}\left|\frac{\sum_{n=1}^{N}\delta_{A^*}(x_n)\exp\left(\delta_{A^*}(x_n)\right)}{\mu m_{A^*}\exp\left(\mu m_{A^*}\right)}-\frac{\sum_{n=1}^{N}\delta_{A^*}^{c}(x_n)\exp\left(\delta_{A^*}^{c}(x_n)\right)}{\mu m_{A^*}^{c}\exp\left(\mu m_{A^*}^{c}\right)}\right|$$

In FS(A) and FS(A^c), there exists one sample x_n such that $\mu_A(x_i) = \mu m_A$ and $\mu_A{}^c(x_n) = \mu m_A{}^c$, which $\delta_A(x_i) = \delta_A{}^c(x_n) = 0$.Therefore:

$$E_{A}^{(1)}-E_{A^*}^{(1)}=-\frac{1}{N}\left|\frac{\sum_{n=1}^{N-1}\delta_{A}(x_n)\exp\left(\delta_{A}(x_n)\right)}{\mu m_{A}\exp\left(\mu m_{A}\right)}-\frac{\sum_{n=1}^{N-1}\delta_{A}^{c}(x_n)\exp\left(\delta_{A}^{c}(x_n)\right)}{\mu m_{A}^{c}\exp\left(\mu m_{A}^{c}\right)}\right|$$
$$+\frac{1}{N}\left|\frac{\sum_{n=1}^{N-1}\delta_{A^*}(x_n)\exp\left(\delta_{A^*}(x_n)\right)}{\mu m_{A^*}\exp\left(\mu m_{A^*}\right)}-\frac{\sum_{n=1}^{N-1}\delta_{A^*}^{c}(x_n)\exp\left(\delta_{A^*}^{c}(x_n)\right)}{\mu m_{A^*}^{c}\exp\left(\mu m_{A^*}^{c}\right)}\right|$$

$$E_{A}^{(1)}-E_{A^*}^{(1)}=\frac{1}{N}\left(\frac{\sum_{n=1}^{N-1}\delta_{A^*}(x_n)\exp\left(\delta_{A^*}(x_n)\right)}{\mu m_{A^*}\exp\left(\mu m_{A^*}\right)}-\frac{\sum_{i=1}^{N-1}\delta_{A}(x_n)\exp\left(\delta_{A}(x_n)\right)}{\mu m_{A}\exp\left(\mu m_{A}\right)}\right)$$
$$+\frac{1}{N}\left(\frac{\sum_{n=1}^{N-1}\delta_{A}^{c}(x_n)\exp\left(\delta_{A}^{c}(x_n)\right)}{\mu m_{A}^{c}\exp\left(\mu m_{A}^{c}\right)}-\frac{\sum_{n=1}^{N-1}\delta_{A^*}^{c}(x_n)\exp\left(\delta_{A^*}^{c}(x_n)\right)}{\mu m_{A^*}^{c}\exp\left(\mu m_{A^*}^{c}\right)}\right)$$

If $\delta_A{}^c(x) > \delta_A(x)$ and $\delta_{A^*}{}^c(x) > \delta_A{}^*(x)$, then $\delta_A{}^c(x) > \delta_A(x) > \delta_{A^*}{}^c(x) > \delta_A{}^*(x)$, for all $x \in X$, then:

$$E_A^{(1)} - E_{A^*}^{(1)} = \frac{1}{N}\frac{\sum_{n=1}^{N-1}\delta_A^c(x_n)\exp\left(\delta_A^c(x_n)\right)}{\mu m_A^c \exp\left(\mu m_A^c\right)} \geq \frac{1}{N}\frac{\sum_{n=1}^{N-1}\delta_A(x_n)\exp\left(\delta_A(x_n)\right)}{\mu m_A \exp\left(\mu m_A\right)}$$
$$\geq \frac{1}{N}\frac{\sum_{n=1}^{N-1}\delta_{A^*}^c(x_n)\exp\left(\delta_{A^*}^c(x_n)\right)}{\mu m_{A^*}^c \exp\left(\mu m_{A^*}^c\right)} \geq \frac{1}{N}\frac{\sum_{n=1}^{N-1}\delta_{A^*}(x_n)\exp\left(\delta_{A^*}(x_n)\right)}{\mu m_{A^*} \exp\left(\mu m_{A^*}\right)}$$

Therefore, $E_A^{(1)} \geq E_A^{*(1)}$.

(P.4) This axioms is fulfilled when $E_A^{(1)}(\delta_A(x), \delta_A^c(x)) = E_A^{c(1)}(\delta_A^c(x), \delta_A(x))$.□

From Eq. (3.3) and using Kosko's geometrical interpretation [KOS86] to show other FE measure, others FEANs are proposed below:

$$E_A^{(2)} = \frac{RET\left(A \cap A^c\right)}{RET\left(A \cup A^c\right)} \tag{3.5}$$

$$E_A^{(3)} = \frac{\sum_{n=1}^{N} Q_A(x_n)\exp\left(Q_A(x_n)\right)}{\sum_{n=1}^{N} L_A(x_n)\exp\left(L_A(x_n)\right)} \tag{3.6}$$

where $Q_A(x_n) = 1–\delta_A(x_n) \wedge 1–\delta_A^c(x_n)$ and $L_A(x_n) = 1–\delta_A(x_n) \vee 1–\delta_A^c(x_n)$, and:

$$RET\left(A \cap A^c\right) = \sum_{n=1}^{N}\left[\delta_A(x_n) \wedge \delta_A^c(x_n)\right];\ RET\left(A \cup A^c\right) = \sum_{n=1}^{N}\left[\delta_A(x_n) \vee \delta_A^c(x_n)\right] \tag{3.7}$$

In A.1 and A.2, the demonstrations of Eq. (3.5) and Eq. (3.6) are shown. In the section 3.5, Eq. (3.3), Eq. (3.5), and Eq. (3.6) will be applied in the optical combs spectra in order to analyze its behavior according to three parameters (DC–BIAS, RF Amplitude, and RF Frequency) take into account in MZM.

3.4 Proposal II: HIFEAN

Considering Eq. (3.3) and Eq. (3.4), the FE measure is extended to IFSs. The adequacy degree was defined as $\delta_A(x_n) = \mu m_A – \mu_A(x_n)$, for a sample x_n. Based on above, the non–adequacy degree can be expressed as $\xi_A(x_n) = \mu m_A – \upsilon_A(x_n)$, for a sample x_n, where $\upsilon_A(x_n)$ refers to the non–membership degree of x_n. By considering $\delta_A(x)$ and $\xi_A(x)$, for all $x \in X$, a new kind of IFS is found, that for this these, is called intuitionistic fuzzy sets by adequacy and non–adequacy (IFSAN). Mathematically, the set is expressed as IFSAN(A) = $<(x, \delta_A(x), \xi_A(x)), x \in X>$. One important aspect of IFSAN is to show the geometrical interpretation of cardinality explained by [SZM01]. Let two cardinalities as a REL relation (based on Eq. (3.4)), it is shown that:

$$min\sum Count(A)=\mu m_A+\sum_{n=1}^{N}\mu_A(x_n) \tag{3.8}$$

$$max\sum Count(A)=\mu m_A+\sum_{n=1}^{N}\left[\mu_A(x_n)+\pi_A(x_n)\right]=\mu m_A+\sum_{n=1}^{N}\left[\mu m_A\ -\ \upsilon_A(x_n)\right] \tag{3.9}$$

where $\pi_A(x)$, for all $x \in X$, represents the hesitancy degree of IFS(A). Eq. (3.8) is the min–sigma count version for IFSAN and Eq. (3.9) is the max–sigma count version or the biggest cardinality of IFSAN. It is important to consider that $\delta_A(x)$ and $\xi_A(x)$ will be handled as normal fuzzy sets, i.e. $\mu m_A = 1$ which $\delta_A(x) = 1 - \mu_A(x)$ and $\xi_A(x) = 1 - \upsilon_A(x)$, for all $x \in X$.

By using $\pi_A(x)$ and Dombi's complement [DOM99], the complement for the hesitancy degree, $\pi_A{}^c(x)$, can be expressed below:

$$\pi_A^c(x)=\frac{\gamma^2\left(1-\mu_A(x)-\upsilon_A(x)\right)}{\gamma^2\left(1-\mu_A(x)-\upsilon_A(x)\right)+\left(1-\gamma\right)^2\left(\mu_A(x)+\upsilon_A(x)\right)}, \text{ for all } x\in X \tag{3.10}$$

where $\pi_A{}^c(x)+ \mu_A(x) + \upsilon_A(x) = 1$ and γ is a parameter of Dombi's complement, such that $\gamma \rightarrow [0,1]$. If $\gamma = ½$, the same $\pi_A(x)$ is found and by using $\upsilon_A(x) = 1 - \mu_A(x)$, Zadeh's complement condition is fulfilled. Dombi's complement is selected because the obtained results (section 5.3, 5.4, and 5.5) shown a better sensitivity and more information about the prediction than other complements like Zadeh's Complement and Sugeno−Hamasher's Complement.

To relate $\pi_A(x)$ and $\pi_A{}^c(x)$, a distance measure can be found in terms of Hamming distance:

$$d\left(\pi_A(x),\pi_A^c(x)\right)=\left|\pi_A(x)-\pi_A^c(x)\right|, \text{ for all } x\in X \tag{3.11}$$

Eq. (3.11) has a direct relation with the similarity measure but this case is view as the equality, far away or close of $\pi_A(x)$ and $\pi_A{}^c(x)$. The above interpretation is explained in Fig. 3.1. In Fig. 3.1a, the $d(\pi_A(x), \pi_A{}^c(x))$ is illustrated as the separation between them. In Fig. 3.1b, $\pi_A(x) = \pi_A{}^c(x)$ is shown if $d(\pi_A(x), \pi_A{}^c(x)) = 0$. In Fig. 3.1c, $\pi_A(x) \neq \pi_A{}^c(x)$ is observed when the distance is maximum, i.e. $d(\pi_A(x), \pi_A{}^c(x)) = 1$.

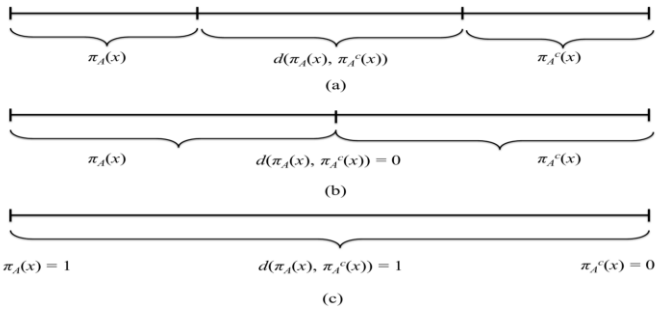

Fig. 3.1. Hamming distance between $\pi_A(x)$ and $\pi_A{}^c(x)$, for: a) separation $\pi_A(x)$ and $\pi_A{}^c(x)$, b) $\pi_A(x) = \pi_A{}^c(x)$, and c) $\pi_A(x) \neq \pi_A{}^c(x)$.

Knowing $\pi_A(x)$ and $\pi_A^c(x)$, two IFEs are proposed through the hesitancy degree interpretation, given by:

$$H_{R1}(A)=\frac{1}{N}\sum_{n=1}^{N}\left[1-\left|\mu_A(x_n)-\upsilon_A(x_n)\right|\right] \tag{3.12}$$

$$H_{R1}^{*}(A)=\frac{1}{N}\sum_{n=1}^{N}\left[\frac{\gamma^2\left(1-\left|\mu_A(x_n)-\upsilon_A(x_n)\right|\right)}{\gamma^2\left(1-\left|\mu_A(x_n)-\upsilon_A(x_n)\right|\right)+(1-\gamma)^2\left|\mu_A(x_n)-\upsilon_A(x_n)\right|}\right] \tag{3.13}$$

Eq. (3.12) and Eq. (3.13) must satisfy the following axioms:

(P.1) [Sharpness]. $H_{R1}(A) = H^{*}_{R1}(A) = 0$, if $\upsilon_A(x) = 0$ and $\mu_A(x) = 1$ or $\upsilon_A(x) = 1$ and $\mu_A(x) = 0$, for all $x \in X$.

(P.2) [Maximization]. $H_{R1}(A)$ and $H^{*}_{R1}(A)$ are maximum if $\upsilon_A(x) = \mu_A(x)$, for all $x \in X$.

(P.3) [Resolution]. Considering B as an IFS, $H_{R1}(A) < H_{R1}(B)$ and $H^{*}_{R1}(A) < H^{*}_{R1}(B)$, if A is less fuzzy than B.

(P.4) [Symmetry]. $H_{R1}(A) = H_{R1}(A^c)$ and $H^{*}_{R1}(A) = H^{*}_{R1}(A^c)$, if $A^c = \langle (x, \upsilon_A(x), \mu_A(x)) | \, x \in X \rangle$.

In Annex A.3, the proof of these axioms is explained.

By means of Eq. (3.12) and Eq. (3.13), the degree of intuitionism is proposed as the difference between the intuitionistic fuzzy entropy by hesitancy degree and its complement, as shown below:

$$\begin{aligned} H_{HC}(A)=\frac{1}{N}\sum_{n=1}^{N}\Bigg|&\left(1-\left|\mu_A(x_n)-\upsilon_A(x_n)\right|\right) \\ &-\left(\frac{\gamma^2\left(1-\left|\mu_A(x_n)-\upsilon_A(x_n)\right|\right)}{\gamma^2\left(1-\left|\mu_A(x_n)-\upsilon_A(x_n)\right|\right)+(1-\gamma)^2\left|\mu_A(x_n)-\upsilon_A(x_n)\right|}\right)\Bigg| \end{aligned} \tag{3.14}$$

In Eq. (3.14), it is required to known the following: if $\gamma = ½$, then $H_{HC}(A) = 0$, and if $\gamma = 0$, then $H_{HC}(A) = H_{R1}(A)$. When $\mu_A(x) = \upsilon_A(x)$, for all $x \in X$, $H_{HC}(A) = 0$; on the other hand, if $\mu_A(x) = 1$ and $\upsilon_A(x) = 0$, or $\mu_A(x) = 0$ and $\upsilon_A(x) = 1$, then $H_{HC}(A) = 0$. The maximum intuitionism degree is achieved in the particular case that $\gamma = 0$ and $\mu_A(x) = \upsilon_A(x)$, where $H_{HC}(A) = 1$.

On the other hand, the degree of fuzziness is another important factor to measure the uncertainly of IFSs. In that case, the measure will be called intuitionistic fuzzy entropy by adequacy and non–adequacy (IFEAN), where is a mix of Eq. (3.3) and Eq. (3.14), as shown below:

$$H_{AN}(A)=1-\left[\frac{Q+W}{N\cdot\exp(1)}\right] \tag{3.15}$$

where:

$$Q=\left|\sum_{n=1}^{N}\left(1-\mu_A(x_n)\right)\exp\left(1-\mu_A(x_n)\right)-\sum_{n=1}^{N}\left(1-\upsilon_A(x_n)\right)\exp\left(1-\upsilon_A(x_n)\right)\right| \tag{3.16}$$

$$\begin{aligned} W=&\left|\sum_{n=1}^{N}\left|\mu_A(x_n)-\upsilon_A(x_n)\right|\exp\left(\left|\mu_A(x_n)-\upsilon_A(x_n)\right|\right)-\right.\\ &\sum_{n=1}^{N}\left(1-\frac{\gamma^2\left(1-\left|\mu_A(x_n)-\upsilon_A(x_n)\right|\right)}{\gamma^2\left(1-\left|\mu_A(x_n)-\upsilon_A(x_n)\right|\right)+(1-\gamma)^2\left|\mu_A(x_n)-\upsilon_A(x_n)\right|}\right)\\ &\left.\exp\left(1-\frac{\gamma^2\left(1-\left|\mu_A(x_n)-\upsilon_A(x_n)\right|\right)}{\gamma^2\left(1-\left|\mu_A(x_n)-\upsilon_A(x_n)\right|\right)+(1-\gamma)^2\left|\mu_A(x_n)-\upsilon_A(x_n)\right|}\right)\right| \end{aligned} \tag{3.17}$$

In annex A.4, the proof is shown.

To join the Eq. (3.14) and Eq. (3.15), the idea of sum the degree of fuzziness and the degree of intuitionism recommended by [VLA07] is taken into account. In that case, it is proposed below:

$$H_{IFEAN}(A)=H_{AN}(A)+H_{HC}(A) \tag{3.18}$$

Eq. (3.18) is called as the generalized measure of IFEAN (HIFEAN) for IFSAN(A). This measure contains two types of measure. The first term defines the degree of fuzziness of an IFEAN. If $\mu_A(x) = \upsilon_A(x) = ½$, for all $x \in X$, IFEAN(A) can become a FS(A) representation. The second term is the degree of intuitionistic between the hesitancy degree and its complement. In section 3.6 and 3.7, Eq. (3.18) will be compared with the IFE measure proposed by [VLA07], in order to verify its performance in optical communications system.

3.5 Application of FEAN: Analysis of Optical Combs Spectra

In order to verify the performance of FEANs in optical communication systems, the optical combs spectrum generation is selected. The goal is to evaluate the stability of combs spectrum when MZM parameters are changing. Some of the combs behaviors are known through theoretical and experimental analysis, which the simulations are, appropriated to valid the results of FEANs.

In Fig. 3.2, the simulation of a combs spectrum generator based on MZM is shown. The used software in this application is VPI Transmission Marker V8.5. The CW laser is connected to the MZM input and it is launched into the OSA. The MZM control is adjusted by means of two DC source (connected towards the two arms of MZM) and one RF source connected with the first arm. The MZM parameters are configured according to the characteristics of LN58S Analog Intensity Modulator from Thorlabs Quantum Electronics (TQE). The half wave voltage (or V_π) is 5V and the insertion losses is 2.5 dB. On the other hand, the CW laser has the following parameters: power of 1 mW, linewidth of 100 MHz, and wavelength of 1550 nm. Through simulations, different output optical combs spectra are stored via OSA.

The MZM parameters are shown in Table 3.1. The case 1 refers to the changes of DC bias voltage in the second arm of MZM. The case 2 represents the changes of phase in the second arm. The case 3 and 4 are variations of DC bias, phase, and RF frequency for the first and second arm. The voltage bias is varied each 0.5 V and the phase is changed in values of 0°, 30°, 45°, 60°, 90°, 120°, 150°, and 180°. Meanwhile, RF signal frequency changes in 1 GHz, 5 GHz, 10 GHz, 12.5 GHz, and 20 GHz (cases 3 and 4). The cases 3 and 4 generated eight different variations to observe the changes in the separation among comb lines.

Table 3.1. MZM parameters.

CASE	V_1 [V]	V_2 [V]	θ_1 [°]	θ_2 [°]	f_1 [GHz]	f_2 [GHz]
1	6.5	3–6.5	0	180	10	10
2	6.5	6.5	0	0–180	10	10
3	3–6.5	6.5	0–180	0	1–20	10
4	6.5	3–6.5	0	0–180	10	1–20

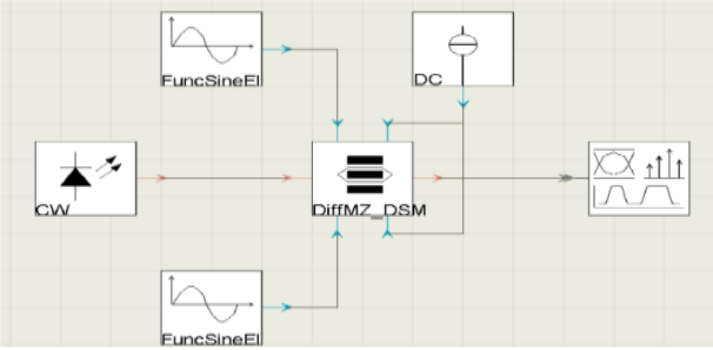

Fig. 3.2. Optical combs generation using MZM (VPI Transmission Marker V8.5).

Each case from Table 3.1 generates 8 comb lines spectra, where each contains 4096 samples (in wavelength, span of 20 nm). Considering all the varied parameters, 32 comb spectra are stored and they will represent as the historical data of optical system. In Fig. 3.3–3.6, the comb spectra of four mentioned cases are illustrated. To convert the data in membership degrees, the historical data must be normalized (ranging from 0 to 1). These degrees are obtained by using the LAMDA method as fuzzy classifier, where an algorithm developed by [URI10] is applied. Based on this algorithm, other MAD functions are added such as Binomial and Centered Binomial functions. Since the idea is to achieve the best classification, a validation index is applied [ISA07]. In Annex A.5, the calculated values of validation index are shown. To obtain the best classification, the highest value of validation index in all MADs is selected, where the connectivity and the found exigency value are suitable to store the membership degrees. This task is carried out in each case of Table 3.1. According to Annex A.5, the Gaussian MAD (Gauss) and the connective MIN–MAX are the best parameters to obtain the membership degree matrix, U (N–samples x K–classes). In Fig. 3.7, the four best U matrices are shown, where the x–axis is converted in wavelength.

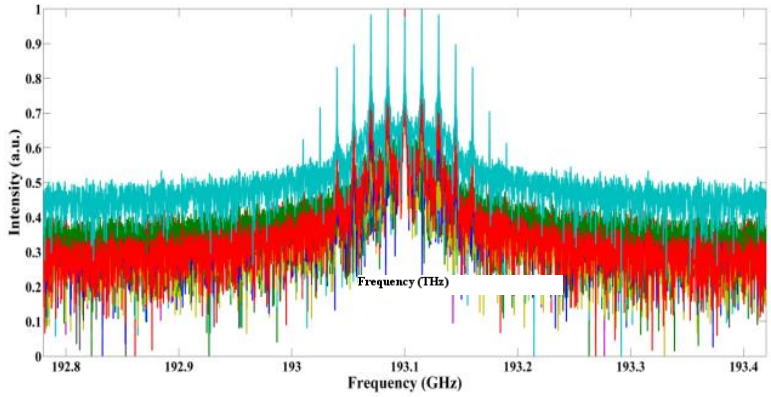

Fig. 3.3. Comb spectra for case 1: changes of DC bias voltage in the second arm of MZM.

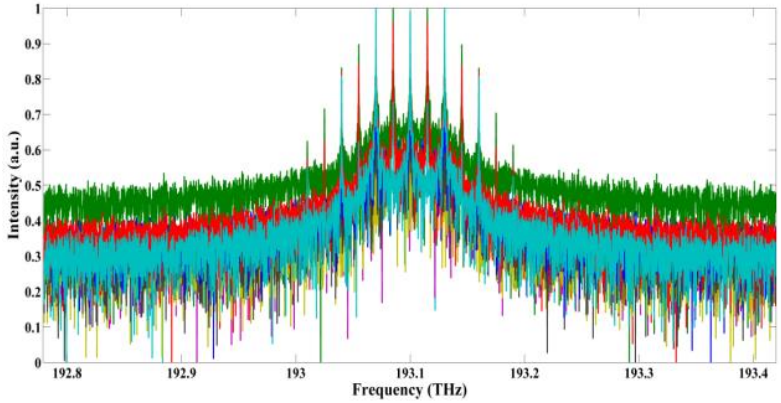

Fig. 3.4. Comb spectra for case 2: changes of phase in the second arm.

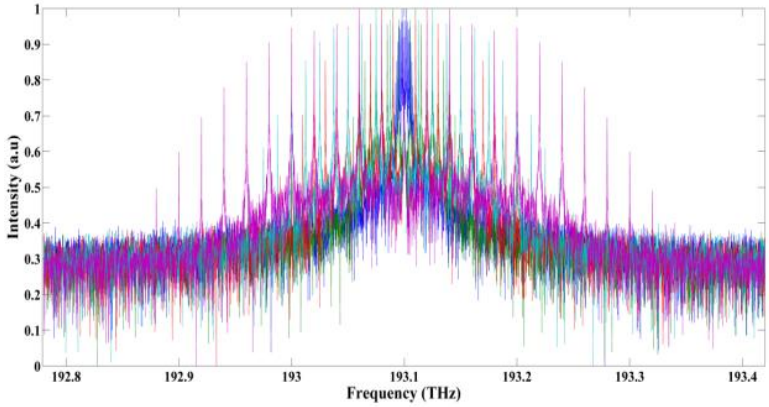

Fig. 3.5. Comb spectra for case 3: variations of DC bias, phase, and RF frequency for the first arm.

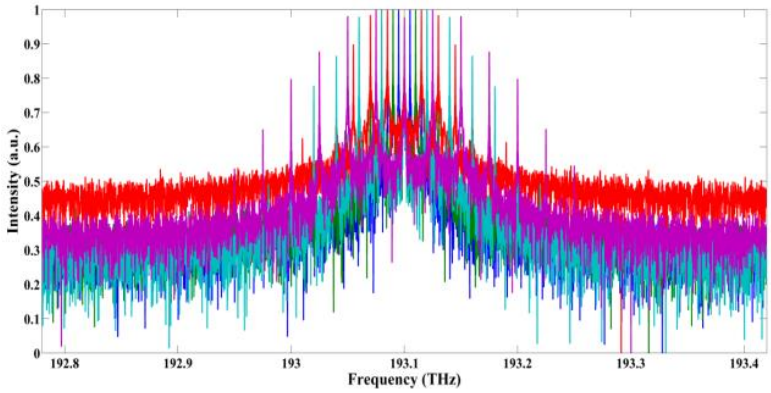

Fig. 3.6. Comb spectra for case 4: variations of DC bias, phase, and RF frequency for the second arm.

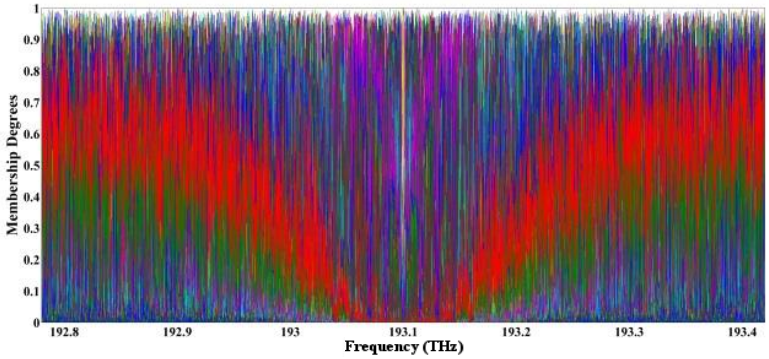

a)

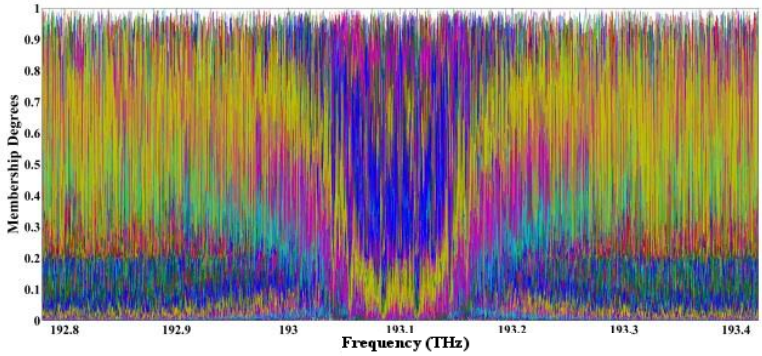

b)

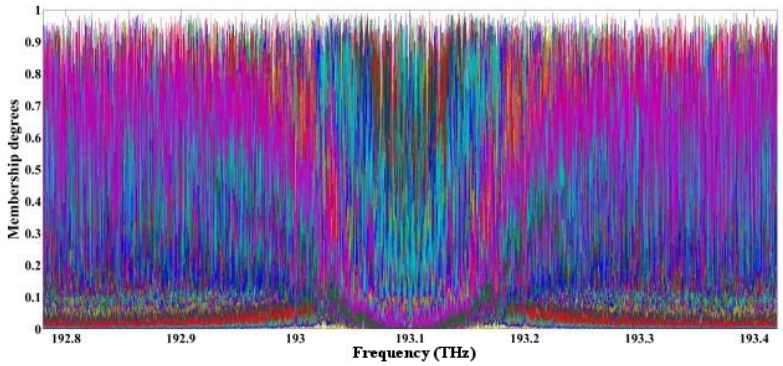

c)

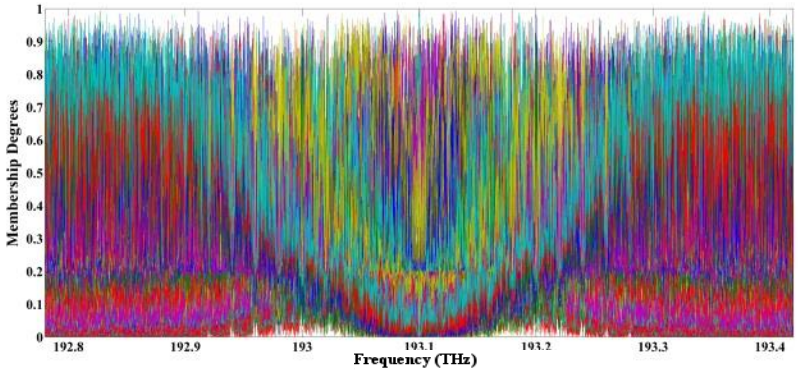

d)

Fig. 3.7. Membership degrees representation (the best) for: a) case 1, b) case 2, c) case 3, and d) case 4.

To reduce the number of classes (or FSs) of U matrices from Fig. 3.7 and to facilitate the analysis of comb spectra, a distance measure among classes is implemented [BOT13]. Four new membership degree matrices, U_{NEW} (N–samples x K–reduced classes), are generated with values of validation index of 0.098, 0.075, 0.087, and 0.090 (see Fig. 3.8). To obtain the K–reduced classes through U_{NEW}, the maximum membership degree is calculated in each sample x_n (where one sample is equivalent to one frequency value of the comb spectrum), $\mu max(x_n) = \max\{\mu_1(x_n),\ldots, \mu_{K\text{–reduced classes}}(x_n)\}$, for any $x_n \in X$. The K–reduced classes for four cases are illustrated in Fig. 3.9. By means of Fig. 3.8 and Fig. 3.9, the Eq. (3.1), (3.3), (3.5), and (3.6) are used to find out which are the most important K–reduced classes that contribute in the analysis of combs spectra behavior. In that case, a decision threshold of 0.25 is proposed where a value of FEAN below it is considered as "high information" and a value under it is defined as "low information". To facilitate the high and low information detection, the former is labeled as "1" and the latter as "0", as is shown in Fig. 3.10. The above task is applied with each FEAN to observe the most relevant changes of comb spectra behavior.

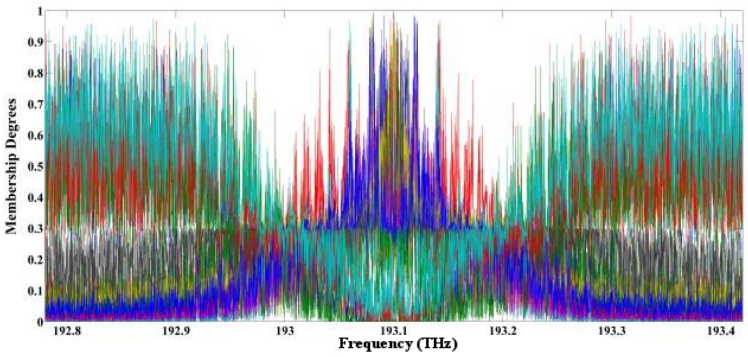
Membership Degrees
Frequency (THz)
192.8
192.9
193
193.1
193.2
193.3
193.4

a)

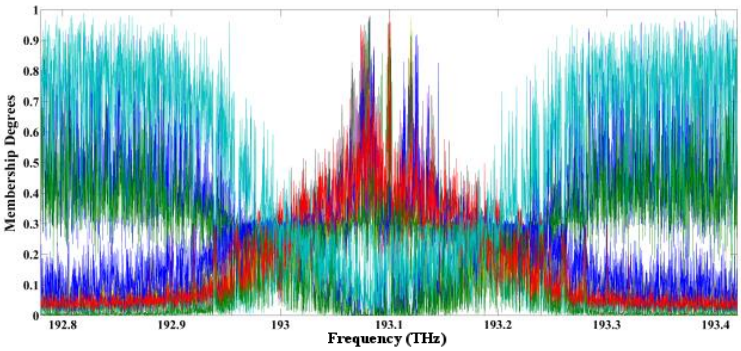
Membership Degrees
Frequency (THz)
192.8
192.9
193
193.1
193.2
193.3
193.4

b)

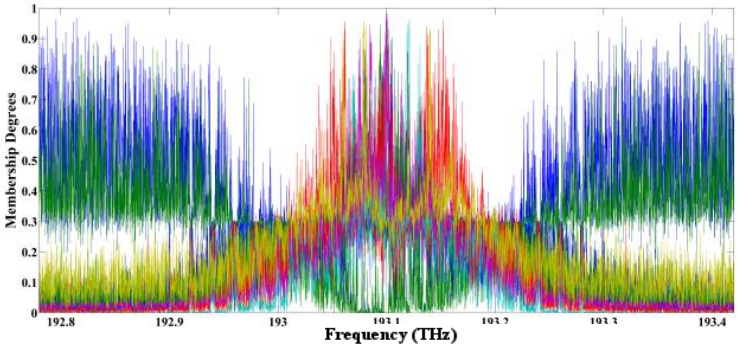
Membership Degrees
Frequency (THz)
192.8
192.9
193
193.4

c)

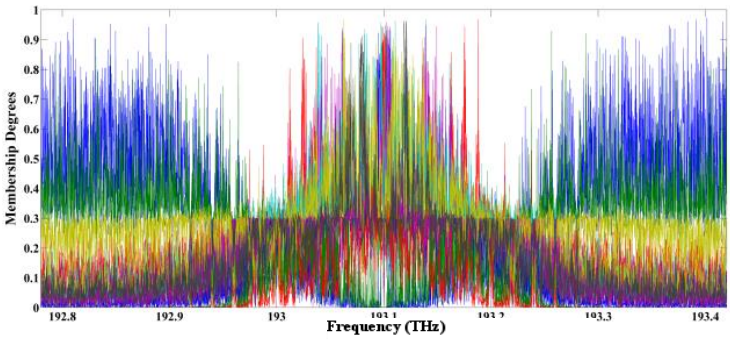

d)

Fig. 3.8. New membership degrees representation (using the distance measure proposed by [BOT13]) for: a) case 1, b) case 2, c) case 3, and d) case 4.

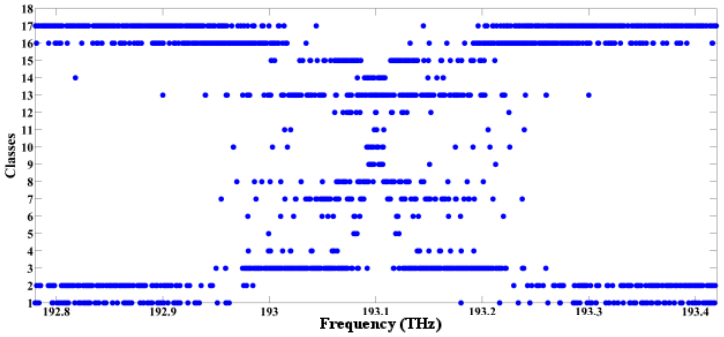

a)

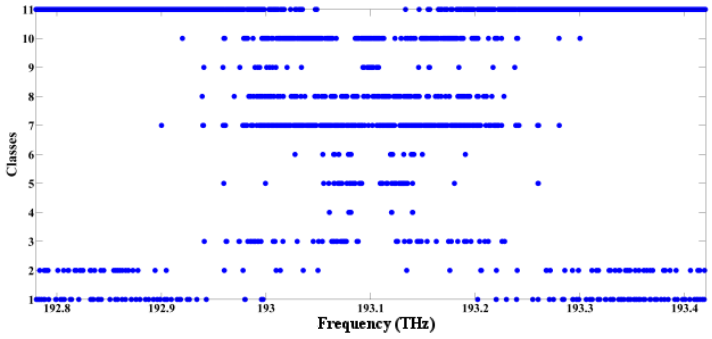

b)

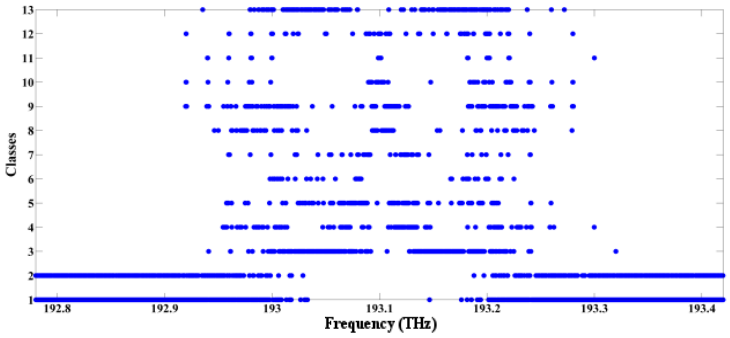

c)

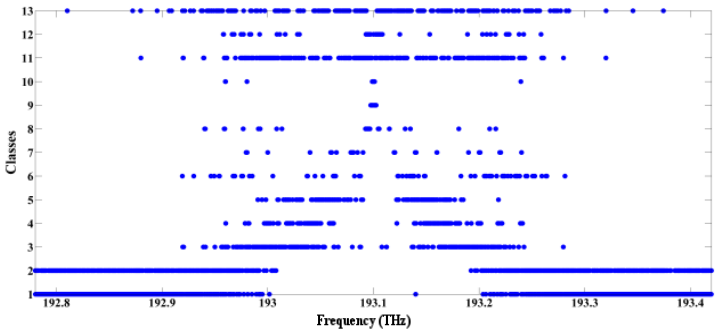

d)

Fig. 3.9. *K*–reduced classes for: a) case 1, b) case 2, c) case 3, and d) case 4.

By analyzing the Fig. 3.10a and Fig. 3.10b, show that FEANs detect little changes in power and spacing among comb lines, which the uncertainly is low. The above verifies that the changes of phase and voltage bias for the second arm of MZM do not affect the combs generation. On the other hand, Fig. 3.10c and Fig. 3.10d show variations of power and spacing of optical combs in both arms of MZM. This result indicates an increase of uncertainly; therefore, the changes of frequency are considerable for generating the comb lines spectrum. The above results indicate FEANs can provide quantitative information about stability of combs spectra. Moreover, FEANs detect variations in frequency and power which the critical changes of flatness of combs can be found.

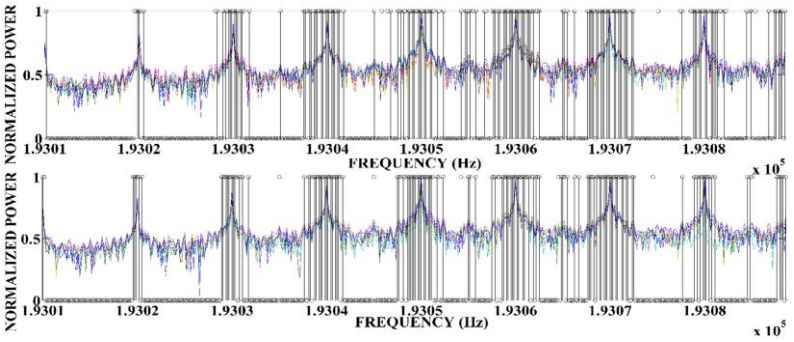

a)

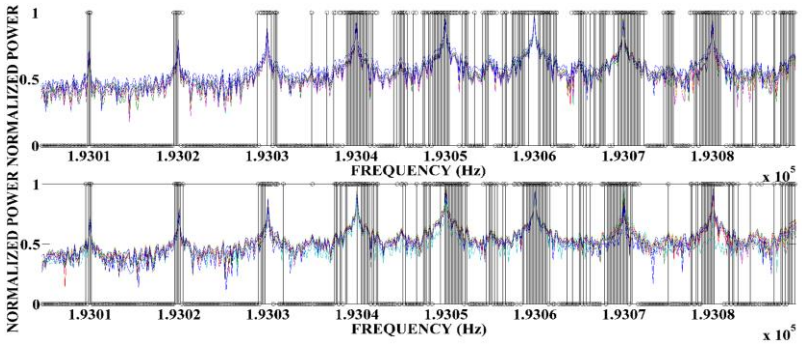

b)

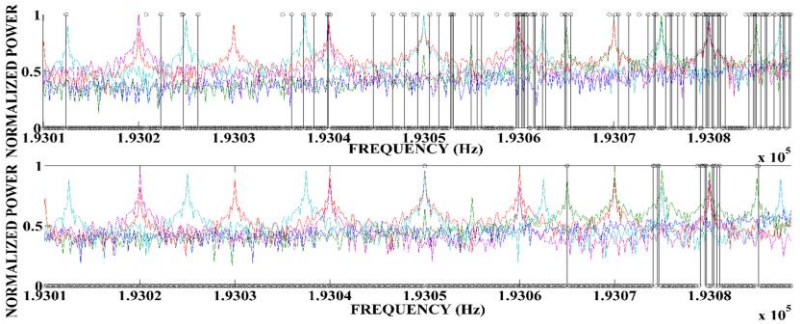

c)

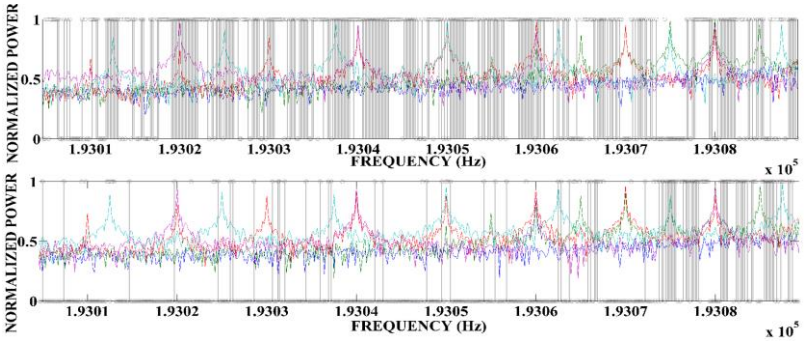

d)

Fig. 3.10. Application of FEANs, considering the label conversion for: a) case 1, b) case 2, c) case 3, and d) case 4.

There is inquisitiveness over the influence of changes of MZM parameters with calculations of FEANs and the classification of databases to find if the comb lines behavior is real or fake. In that case, a fuzzy entropy average value is suggested as an interesting alternative for validating the results with respect to the known behavior in laboratory. To observe the influence in each case (Table 3.1), if the changes of FEAN average generate little variations in the information, the parameter from MZM does not alter the phase and/or intensity of comb lines. Otherwise, if the variations are high, the parameter from MZM is important in the combs generation. Taking into account the above, Fig. 3.11a and Fig. 3.11b show the phase and DC voltage bias for the second

arm present little influence and the changes of information are weak. On the other hand, Fig. 3.11c and Fig. 3.11d indicate that the RF signal frequency parameter presents more influence in the combs behavior than the cases 2 and 3, either power as spacing. This observation is consistent with the real MZM behavior for generating optical combs spectra. According to this result, FEANs are closed with the known behavior detection of combs spectra when phase, voltage bias or RF signal frequency are changed.

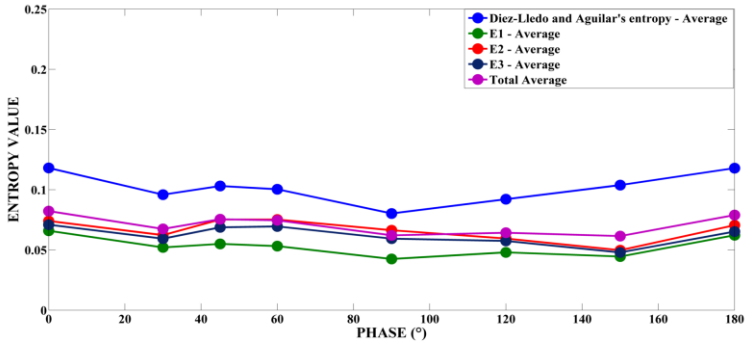

a)

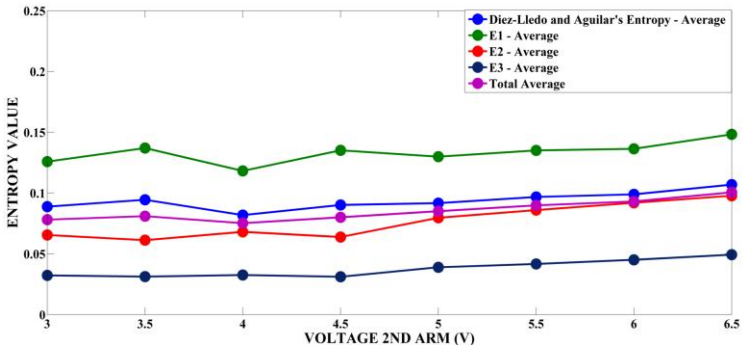

b)

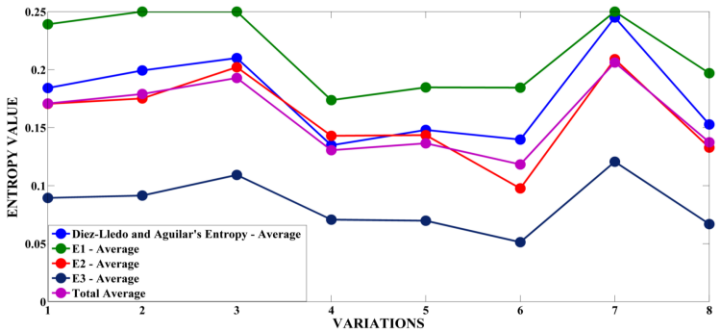

c)

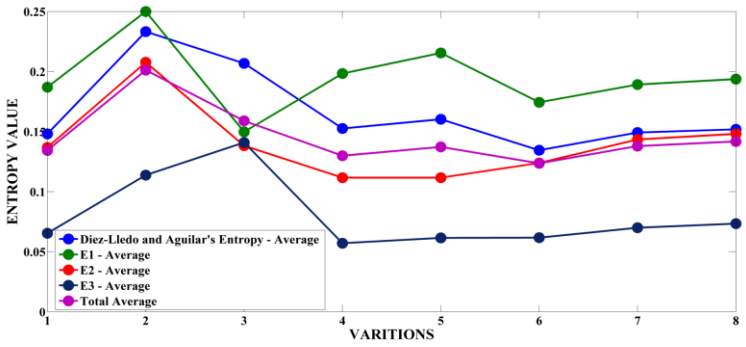

d)

Fig. 3.11. FEANs average, for: a) case 1, b) case 2, c) case 3, and d) case 4.

Based on the results presented in Fig. 3.11, an analysis of the performance of FEAN can be interpreted. By using Eq. (3.3), the most relevant changes of combs spectra can be identify and it is useful to observe critical variations in the combs frequency. Meanwhile, Eq. (3.6) is appropriated if the combs spectrum has or not little changes in its behavior. As the phase and DC–bias voltage do not affect the comb lines generation, the above equation allows a better estimation when the changes are little considerable. Nevertheless, if the RF frequency is increase, Eq. (3.3) is recommendable when the critical changes of combs are high. Considering Eq. (3.5), this measure has an interesting result due to its behavior is closed to the total average of all FEANs and Eq. (3.1). The above concludes that Eq. (3.5) allows calculating entropy value "middle" with respect to the others FEANs.

In the next section, HIFEAN application is shown in two scenarios: task of detection of comb lines and second–order PMD.

3.6 Application of HIFEAN: Optical Combs Spectra Detection

To validity the throughput of the HIFEAN measure, the combs lines generation based on MZMs is selected to observe the capacity of the comb lines detection. Since some optical combs spectrum behavior are known, the use of HIFEAN will be focused on the combs lines detection by considering chromatic dispersion during its propagation in single–mode fiber (SMF). Using VPI transmission market V 9.1, a general schematic is designed as shown in Fig. 3.12. In the scheme, a CW laser and a RF generator are connected towards a MZM although DC Bias input is felt as dual–drive. The MZM output is linked to SMF input where the linear polarization is maintained for default to facilitate the combs generation with chromatic dispersion. To observe the spectrum output, an optical signal analyzer (OSA) is connected. As several configurations to generate comb lines with MZM can be carried out due to the intensity and separation among them can change, DC Bias and RF amplitude and frequencies are modified to obtain different spectra. In Table 3.2, the parameters of simulation are shown. To compare the changes of shape and/or comb lines generation in the spectrum, three cases are proposed as described below:

Case 1: DC Bias (0 – 5 V) with steps of 0.5 V, maintaining RF amplitude at 3 V (11.76 dBm) and channel spacing at 15 GHz.

Case 2: RF amplitude (0 – 3V) with steps of 0.3 V, maintaining DC Bias at 4 V and RF at 15 GHz.

Case 3: RF (5 – 25 GHz) with steps of 5 GHz, conserving DC Bias at 3 V and RF amplitude at 4 V.

In each case, 4096 samples corresponding at range 192.780 THz – 193.419 THz are obtained (each sample is associated with a frequency value) where three databases are generated as described below:

- 4096 samples and 11 descriptors that represent the increases of DC bias between 0 and 5 V.
- 4096 samples and 11 descriptors that define the increases of RF amplitudes between 0 and 3 V.
- 4096 samples and 5 descriptors that indicate the changes of RF frequencies between 5 and 25 GHz.

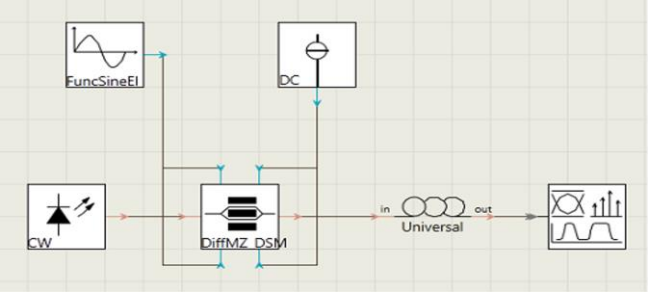

Fig. 3.12. Simulation set–up with a dual–drive Mach–Zehnder Modulator (MZM).

Table 3.2. Simulation parameters.

Device	Parameter	Magnitude
Laser (CW)	Power	1 mW
	Line width	10 MHz
	Wavelength	1550 nm
MZM	Insertion loss	6 dB
	Extinction ratio	30 dB
	RF Driving	6 Vpp
	DC Bias	± 15 V
SMF	Distance	50 km
	Dispersion	16.0 ps/nm.km
	Attenuation	0.2 dB/km

Based on three cases, the spectra must be normalized to carry out the classification step and to apply HIFEAN, as shown in Fig. 3.13. To find the best classification, the validation index applied in the case of study mentioned in section 3.5, is used and the results are summed–up in the annex A.6. According to the results, the Gaussian MAD (Gauss) and the connective MIN–MAX are the best parameters. To compare the performance of HIFEAN, Vlachos and Sergaidis's intuitionistic fuzzy entropy (HVS) is implemented by using Eq. (2.72) as implication operator. Considering changes of parameter γ each 0.1, different changes of entropy values are obtained. In Fig. 3.14, the HIFEAN and HVS results are illustrated. In Fig. 3.14a and Fig. 3.14b, the entropy values have

similar behaviors where the range of classes 80–140 presents the largest amount of information. In Fig. 3.14c and Fig. 3.14d, the range of classes 60–120 shows the most relevant information of the combs lines behavior. In Fig. 3.14e and Fig. 3.14f, the range of classes 100–180 is found the most important information although both entropies generate different changes of entropy behavior.

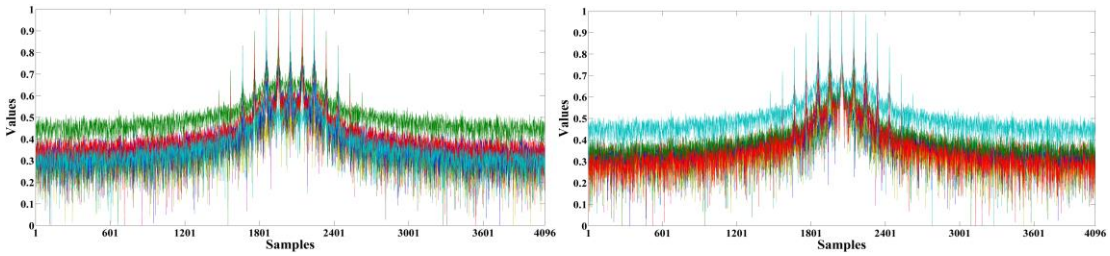

a) b)

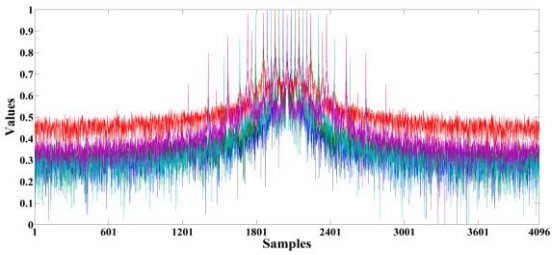

c)

Fig. 3.13. Comb lines spectra, for a) DC Bias, b) RF amplitude, and c) RF frequency.

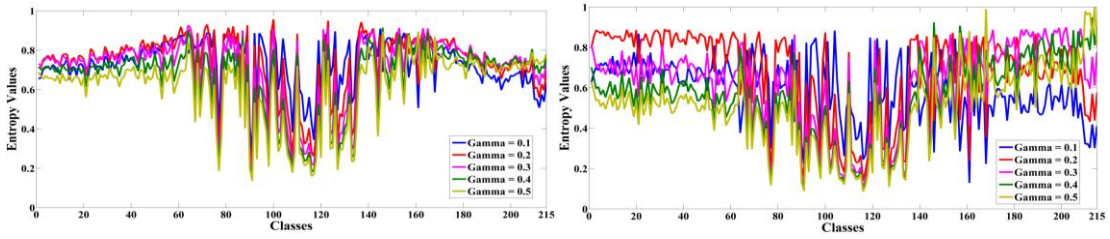

a) b)

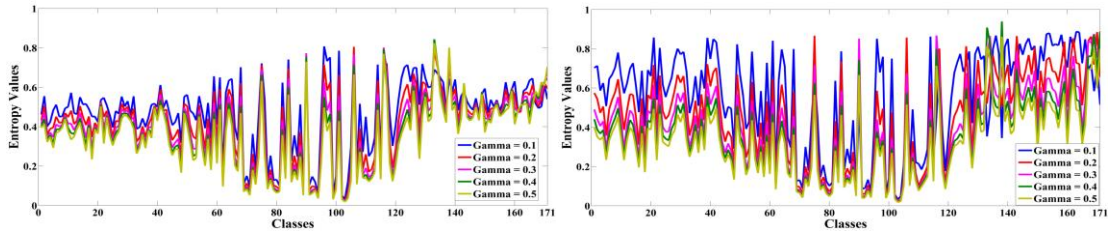

c) d)

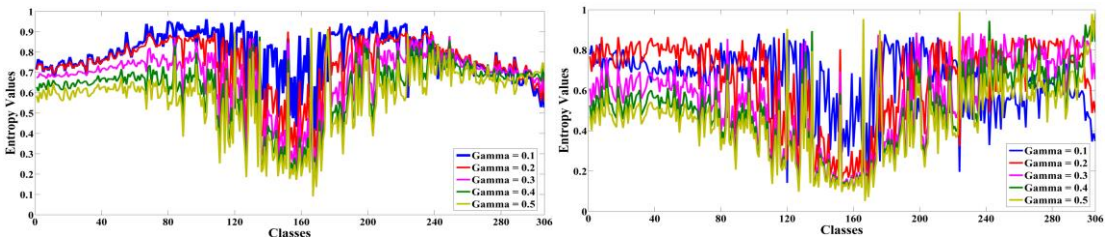

e) f)

Fig. 3.14. Entropy behavior for a) HVS–DC BIAS case, b) HIFEAN–DC BIAS case, c) HVS–RF amplitude case, d) HIFEAN–RF amplitude case, e) HVS– RF frequencies, and f) HIFEAN–RF frequencies.

Based on Fig. 3.14, a threshold of 0.25 is defined to find those classes with an entropy value below of it. The above threshold will allow establishing the most important classes that generate high information and to analyze the efficiently for both entropy measures. To represent the obtained classification with LAMDA, the maximum membership degree for each sample is calculated to find a vector of classes (1 x *N* samples). Based on the vector of classes, the class labels are modified to obtain the set of relevant classes. The above facilities the comb lines detection, as shown in Fig. 3.15. To understand the interpretation, the class labeled as "1" is a class without important information and the class with label different than 1 is relevant to analyze. According to Fig. 3.15a and Fig. 3.15b, HIFEAN finds a more quantity of combs lines than HVS which the capacity of detection is optimal in the former. The same observation is identified in Fig. 3.15e and Fig. 3.15f. In Fig. 3.15c and Fig. 3.15d, HVS identified 34 classes whilst HIFEAN established 45 classes but the proportion of samples with labels different than 1 is approached similar.

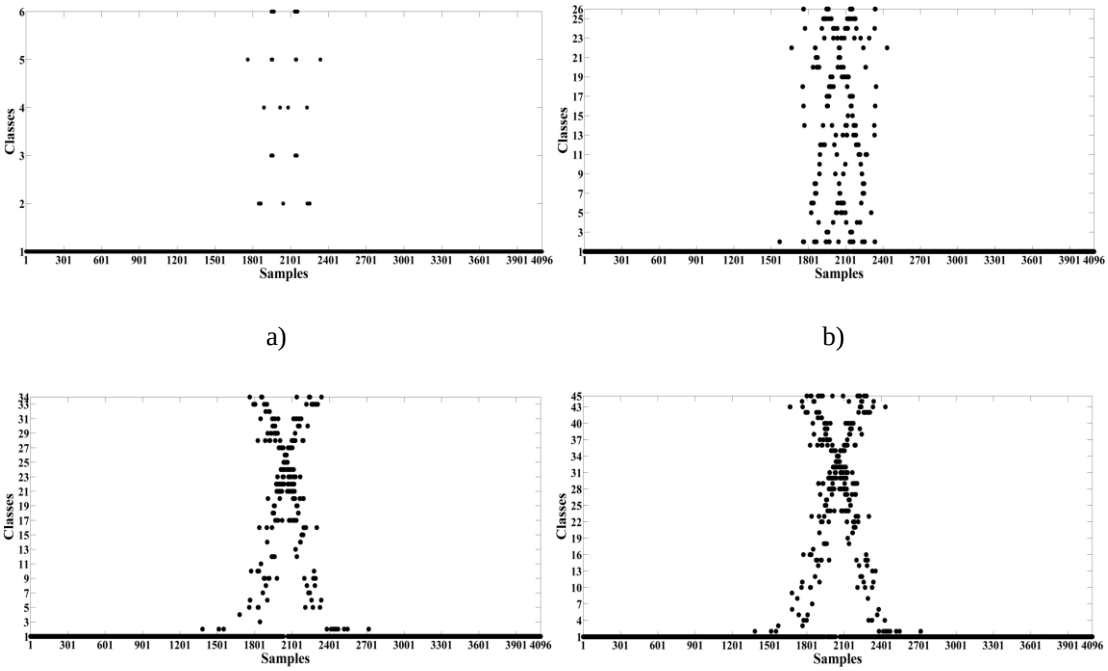

a) b)

c) d)

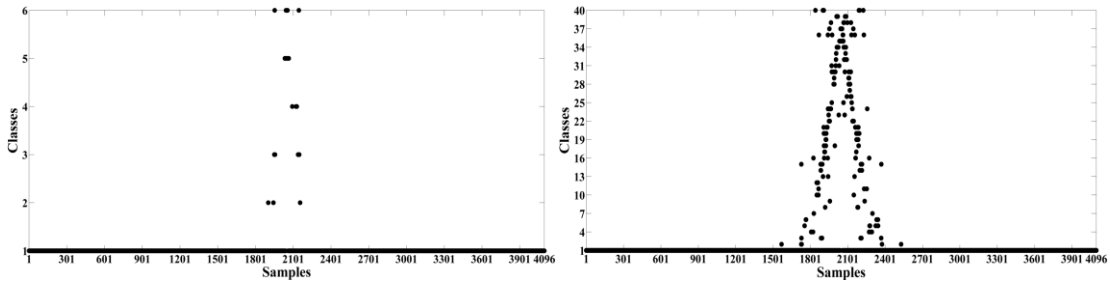

e) f)

Fig. 3.15. Classes representation with a threshold at 0.25 applied to HVS and HIFEAN, for: a) HVS–DC BIAS case, b) HIFEAN–DC BIAS case, c) HVS–RF amplitude case, d) HIFEAN–RF amplitude case, e) HVS–RF frequencies, and f) HIFEAN–RF frequencies.

To analyze the number of combs lines identified in both entropies, Fig. 3.13 and Fig. 3.15 are compared. In Table 3.3, the results of combs lines detection are shown where each sample is associated with a frequency value. In the case 1, HVS and HIFEAN find 4 and 7 comb lines; in addition, both entropies achieved to detect 3 close comb lines. From Fig. 3.13a, 13 combs lines are observed and HIFEAN is reached to identify more combs than HVS. Adding the detected combs and its closest combs, HVS determined 7 comb lines and HIFEAN around 10 comb lines. The above shows that HIFEAN allows finding combs lines with low power and presence of chromatic dispersion due to its propagation in SMF. Nevertheless, 3 comb lines were not detected by HIFEAN but HVS cannot identify 6 comb lines. A relevant result is reached when HIFEAN detected the main comb in the center frequency (sample 2049 or 193.1 THz) and HVS only identified frequencies near to 193.1 THz. In the case 2, HVS identify 3 comb lines and 5 closest comb lines, summing 8 comb lines; HIFEAN detected 7 main comb lines and 4 closest combs lines, summing 11 comb lines. Comparing the last result with Fig. 3.13b, HIFEAN would be detected almost 13 comb lines. In the case 3, the number of comb lines is larger than the case 2 which the complexity is increased and the exigency of both entropies must be high. Considering this scenario, HVS detected 2 comb lines and 2 close comb lines (total = 4 comb lines) whilst HIFEAN is able to identify 9 comb lines and 12 close comb lines (total = 21 comb lines). The above result shows the good throughput of HIFEAN for tasks of combs detection after its propagation in SMF.

Table 3.3. Comb lines detection after propagation in SMF.

MZM Parameter: DC BIAS			
HVS		**HIFEAN**	
Detected comb lines	Possible identified comb lines	Detected comb lines	Possible identified comb lines
1761 (193.055 THz) **1953 (193.085 THz)** **2145 (193.115 THz)** **2237 (193.145 THz)**	1848 (193.0685938 THz), 1850 (193.0689063 THz), 1864 (193.0710938 THz) → **1857 (193.070 THz)** 2042 (193.0989063 THz) → **2049 (193.1 THz)** 2231 (193.1285938 THz), 2234 (193.1289063 THz), 2250 (193.1314063 THz), and 2252 (193.1317188 THz) → **2241 (193.130 THz)**	**1665 (193.040 THz)** **1761 (193.055 THz)** **1953 (193.085 THz)** **2049 (193.1 THz)** **2145 (193.115 THz)** **2337 (193.145 THz)** **2433 (193.160 THz)**	1851 (193.0690625 THz), 1854–1856 (193.0695313 THz – 193.0698438 THz), and 1859–1864 (193.0703125 THz – 193.0710938 THz) → **1857 (193.070 THz)** 1946–1952 (193.0839063 THz – 193.0848438 THz) and 1954–1956 (193.0851563 THz – 193.0854688 THz) → **1957 (193.085625 THz)** 2238 (193.1295313 THz), 2239 (193.1296875 THz), 2242–2244 (193.1301563 THz – 193.1304688 THz)→ **2241 (193.130 THz)**
MZM Parameter: RF Amplitude			
HVS		**HIFEAN**	
Detected comb lines	Possible identified comb lines	Detected comb lines	Possible identified comb lines
1761 (193.055 THz) **2049 (193.1 THz)** **2337 (193.129375 THz)**	1854–1856 (193.0695313 THz – 193.0698438 THz), and 1858–1860 (193.0701563 THz – 193.0704688 THz) → **1857 (193.070 THz)** 1942–1949 (193.0832813 THz – 193.084375 THz) and 1955–1961 (193.0853125 THz – 193.08625 THz) → **1953 (193.085 THz)** 2143 (193.1146875 THz) and 2149–2153 (193.115625 THz – 193.11625 THz) → **2145 (193.115 THz)** 2238 (193.1279688 THz), 2239 (193.1296875 THz), and 2242–2244 (193.1301563 THz – 193.1304688 THz) → **2241 (193.130 THz)** 2437 (193.160625 THz) → **2433 (193.160 THz)**	**1761 (193.055 THz)** **1857 (193.070 THz)** **1953 (193.085 THz)** **2049 (193.1 THz)** **2145 (193.115 THz)** **2241 (193.130 THz)** **2337 (193.129375 THz)**	1570 (193.02515625 THz) → **1569 (193.0265625 THz)** 1664 (193.03984375 THz) and 1666 (193.04015625 THz) → **1665 (193.040 THz)** 2432 (193.15984375 THz) and 2437 (193.160625 THz) → **2433 (193.160 THz)** 2519 (193.1734375 THz) → **2520 (1931.7359375 THz)**
MZM Parameter: RF Frequency			
HVS		**HIFEAN**	
Detected comb lines	Possible identified comb lines	Detected comb lines	Possible identified comb lines
1953 (193.085 THz) **2049 (193.1 THz)**	1902 (193.0770313 THz) → **between 1889 (193.075 THz) and 1921 (193.080 THz)** 2129 (193.1125 THz) → **between 2113 (193.110 THz) and 2143 (193.1146875 THz)**	**1569 (193.0265625 THz)** **1729 (193.050 THz)** **1869 (193.071875 THz)** **1953 (193.085 THz)** **2049 (193.1 THz)** **2145 (193.115 THz)** **2209 (193.125 THz)** **2370 (193.15015625 THz)** **2529 (193.175 THz)**	1764 (193.05546875 THz) and 1766 (193.05578125 THz) → **1761 (193.055 THz)** 1807 (193.0621875 THz) → **1793 (193.060 THz)** 1851 (193.0690625 THz), 1852 (193.06921875 THz), 1861 (193.070625 THz), and 1865 (193,07125 THz)→ **1857 (193.070 THz)** 1916 (193.07921875 THz), 1917 (193.079375 THz), 1919 (193.0796875 THz), 1924 (193.08046875 THz), and 1925 (193.080625 THz) → **1921 (193.080 THz)**

Detected comb lines	Possible identified comb lines	Detected comb lines	Possible identified comb lines
			1987 (193.0903125 THz) and 1989 (193.090625 THz) → **1985 (193.090 THz)** 2013–2016 (193.094375 THz – 193.09484375 THz), and 2018–2020 (193.09515625 THz – 193.09546875 THz)→ **2017 (193.095 THz)** 2079 (193.1046875 THz), 2080 (193.10484375 THz), and 2082–2088 (193.10515625 THz – 193.10609375 THz) → **2081 (193.105 THz)** 2111 (193.1096875 THz), 2115 (193.1103125 THz), and 2117 (193.110625 THz) → **2113 (193.110 THz)** 2175 (193.1196875 THz) and 2179 (193.1203125 THz) → **2177 (193.120 THz)** 2236 (193.12765625 THz) → **2241 (193.130 THz)** 2299 (193.1390625 THz) → **2305 (193.140 THz)** 2332 (193.14421875 THz), 2335 (193.1446875 THz), and 2343 (193.1459375 THz) → **2337 (193.145 THz)**

3.7 Application of HIFEAN: Second–Order PMD Detection

In the second application of HIFEAN, the scenario of the ultra–short pulse propagation is selected by considering the impact of second–order PMD. The simulation is carried out in VPI Transmission Market V 9.5, with a SMF at 190 km, attenuation at 0.2 dB/km, and wavelength at 1550 nm (or 193.1 THz). In Fig. 3.16, the general scheme is shown. An ultra–short pulse source is created with an impulse function generator, a Gaussian low–pass filter at 10 GHz (to generate the Gaussian shape in the spectrum), and an optical pulse laser at 1 MHz of linewidth and power at 1 mW. The generator output (with 5 ps of pulse–width) is linked towards SMF input although PMD is configured with a coefficient of 0.5 ps/km$^{1/2}$ (considering 10 Gpbs). The SMF output is connected towards an OSA to see the optical spectrum. Due to the randomness of PMD, 52 birefringence matrices are elaborated with MATLAB, modifying the birefringence angles and the square core for each km of SMF. Joining all matrices, historical data are organized in 52 variables and 4096 samples (range 193.020 THz – 193.179 THz), where each one is an optical spectrum (see Fig. 3.17). The historical data are classified with the LAMDA method to acquire the membership degrees matrix and to use HVS and HIFEAN. To observe the impact of PMD in the spectrum, the chromatic dispersion and non–linear effects are not added in the simulation (however, in the experimental set–up of chapter 5, these phenomena are generated in real application and HIFEAN will be evaluated in this scenario), and the linear polarization is established. The above will allow detecting the influence of second–order PMD.

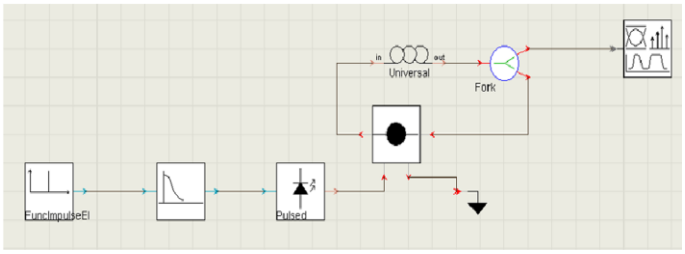

Fig. 3.16. General scheme of second–order PMD generator in the ultra–short pulse propagation in SMF.

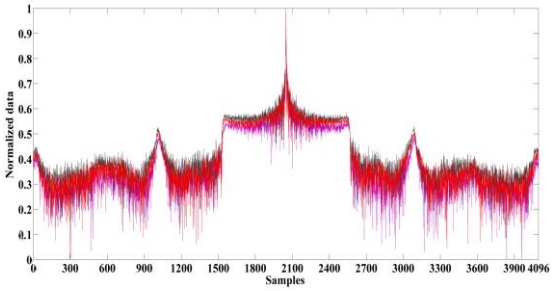

Fig. 3.17. Optical spectra of ultra–short pulse after its propagation in SMF, changing the angle of birefringence. All Data are normalized and the range 1–4096 is equivalent to 193.020 THz–193.179 THz.

The historical data are classified with the LAMDA method and the best classification is obtained with a partition quality index at 0.006328 with connective MIN–MAX, Gaussian function, an exigency value at 0.8 and 1 iteration (see Annex A.7). Using the found parameters, a membership degrees matrix with 175 classes or fuzzy sets and 4096 samples is generated to obtain the best classification. Calculating the maximum membership degrees for each sample, the classes' representation is created, as illustrated in Fig. 3.18. Due to the high quantity of found classes, HIFEAN and HVS are used to reduce the number of classes and so, to identify the presence of second–order PMD. In Fig. 3.19, the results of both entropies are shown, where the parameter γ is varied between 0.1 and 0.5. Analyzing the HIFEAN and HVS measures, both entropies have similar performance in classes 1–75 and 120–175 although the classes' 80–119 are presented the most important changes of spectra. In Fig. 3.19a and Fig. 3,19b, HIFEAN shows some variations with respect to HVS, however, Fig. 3.19c, Fig. 3.19d, and Fig. 3.19e indicate that spectra can become stable. The above is calculated when γ has a value close to 0.5.

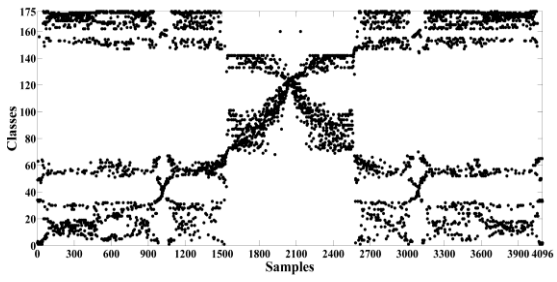

Fig. 3.18. Classes representation obtained by LAMDA and the validation index.

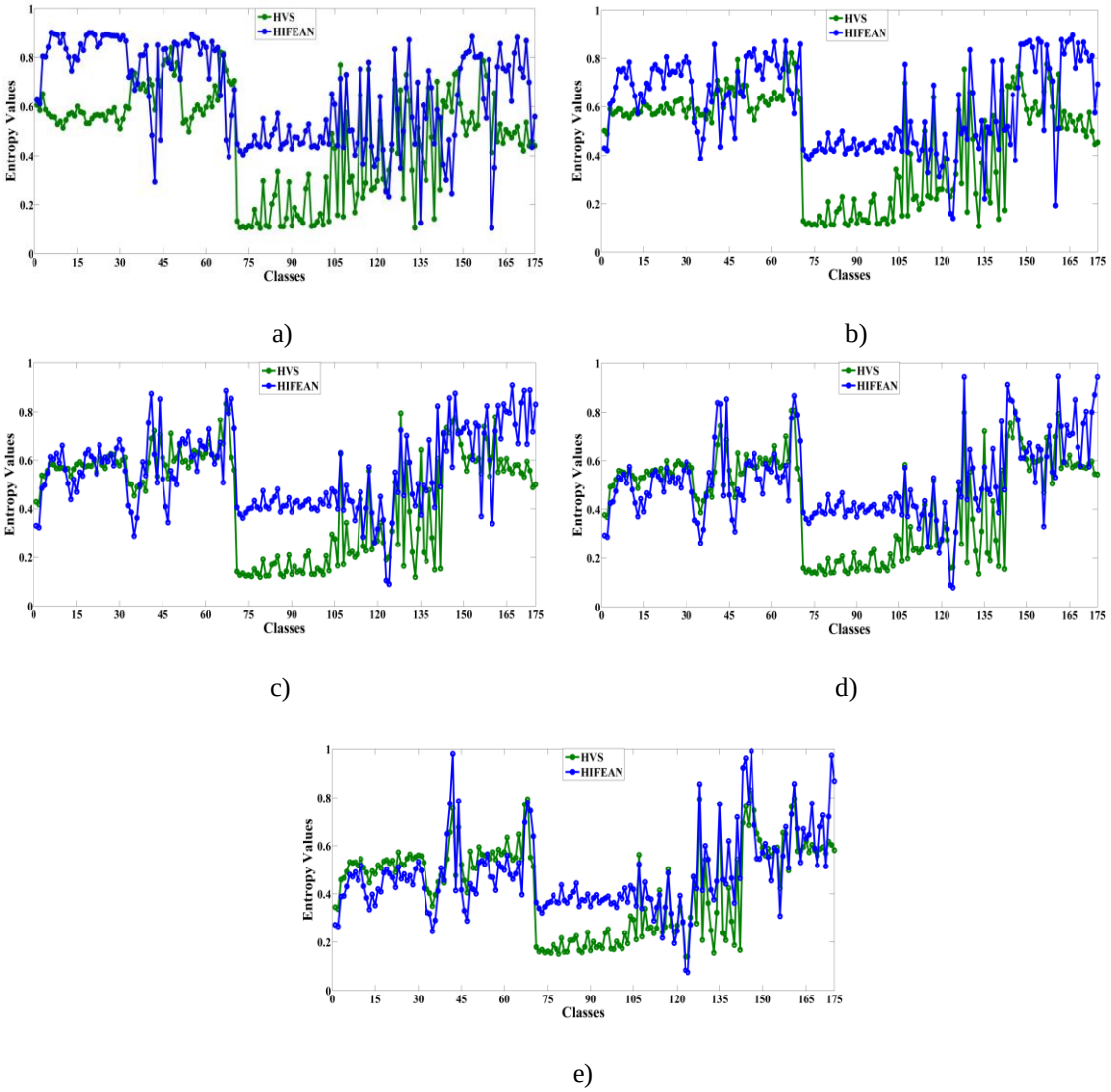

Fig. 3.19. HIFEAN and HVS results for a) γ = 0.1, b) γ = 0.2, c) γ = 0.3, d) γ = 0.4, and e) γ = 0.5.

In order to find out the range of classes where the second–order PMD detection, a threshold is defined in HIFEAN and HVS, as explained below:

- If entropy value > 0.4, then the amount of information is not relevant and the class is labeled as 1.
- If entropy value ≤ 0.4, then the amount of information is relevant and the class is labeled with a value different to 1.

Using the two mentioned conditions, a new vector of classes is get. In Fig. 3.20, the results of applied threshold are shown. Analyzing the results, Fig. 3.20a illustrates 64 classes with HVS and the highest amount of information is focused on the samples 1538 – 2561 (193.080 THz – 193.120 THz). In Fig. 3.20b, 29 classes are obtained with HIFEAN and 5 ranges of samples are observed, as mentioned as follows:

- The range 1–39 (193.020 THz–193.021 THz).
- The range 974–1069 (193.058 THz–193.061 THz).
- The range 1514–2592 (193.079 THz–193.121 THz).
- The range 3029–3131 (193.138 THz–193.142 THz).
- The range 4071–4096 (193.178 THz–193.179 THz).

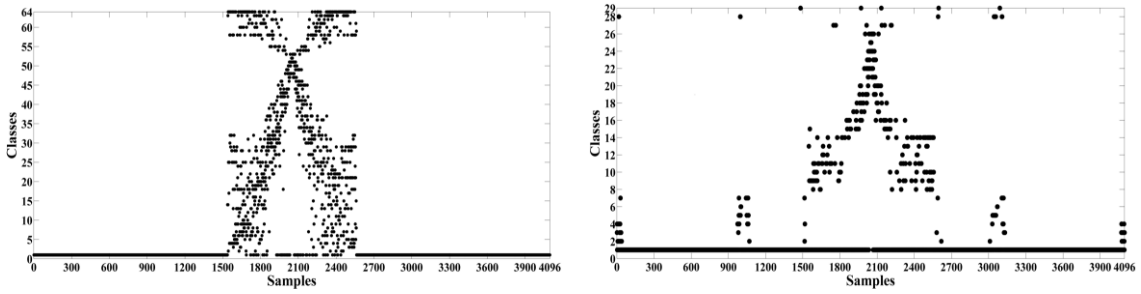

a) b)

Fig. 3.20. Comparison of the results through a threshold of 0.4, for: a) HVS and b) HIFEAN.

To compare both results, the HVS and HIFEAN averages are calculated in all classes, where the lowest entropy values are considered. The above is shown in Table 3.4. The threshold is modified now at 0.25 for both entropy measures to increase the exigency. In the HVS case, the range 1538 – 1935 (193.080 THz – 193.095 THz) and 2184 – 2556 (193.105 THz–193.119 THz) correspond to the most important amount of information where they define the initial and final ultra–short pulse spectra. Nevertheless, the range of interest corresponds to 1960 – 2143 (193.096 THz – 193.103 THz) although classes are 52, 53, and 54 have the highest entropy. The above shows the amount of information is little and therefore, these entropy values are larger than the entropy values of classes 2 – 10, 12 – 15, 17 – 19, 21 – 25, 28 – 32, 34, 37 – 38, 51, 55, 58, and 63 – 64. The found result evidences HVS ignored the main components of spectra and its useful in second–order PMD is reduced.

In the HIFEAN case, the results show a high throughput with respect to HVS. The classes 24 and 25 present the lowest entropy values, where the ranges of samples are:

- 2029 (193.09921 THz).
- 2039 (193.09961 THz).
- 2041 – 2056 (193.09968 THz – 193.1003 THz).
- 2059 (193.1004 THz).
- 2061 (193.10048 THz).
- 2064 – 2065 (193.10058 THz – 193.100625 THz).
- 2078 (193.101 THz).

The above ranges of samples are located within the range of interest. Furthermore, the optimal performance of HIFEAN by identifying the range of samples close to the main frequency components of ultra–short pulse. Others classes, 28 and 29, also were identified by HIFEAN as relevant, where their ranges correspond to 16 (193.02058 THz), 995 (193.05882 THz), 997

(193.05890 THz), 3090 (193.14066 THz), 3107 (193.14132 THz), and 3109 (193.14140 THz). These ranges are located in the harmonics where PMD is generated after the ultra–short pulse propagation, observed in Fig. 3.17. Comparing HVS and HIFEAN, the latter achieves to find the relevant harmonics from the spectra even in classes as 28 and 29 with entropy values of 0.33598 and 0.21262. The above indicates the high variations of optical spectra in these samples and the difficult to detect important harmonics with entropy values between 0.2 and 0.35. Nevertheless, HIFEAN is able of identify small changes of optical spectra considerable to analyze the impact of PMD.

Table 3.4. Entropy average values of HVS and HIFEAN.

HVS							
C1	**C2**	**C3**	**C4**	**C5**	**C6**	**C7**	**C8**
0.59174	**0.14861**	**0.13079**	**0.13693**	**0.12776**	**0.13199**	**0.12693**	**0.16711**
C9	**C10**	**C11**	**C12**	**C13**	**C14**	**C15**	**C16**
0.14053	**0.12339**	0.22193	**0,13059**	**0.12984**	**0,18659**	**0.19834**	0.23969
C17	**C18**	**C19**	**C20**	**C21**	**C22**	**C23**	**C24**
0.13465	**0.12787**	**0.15204**	0.23608	**0.13516**	**0.17802**	**0.15281**	**0.15399**
C25	**C26**	**C27**	**C28**	**C29**	**C30**	**C31**	**C32**
0.14179	0,22652	0.25426	**0.13693**	**0.13672**	**0.16043**	**0.15878**	**0,13717**
C33	**C34**	**C35**	**C36**	**C37**	**C38**	**C39**	**C40**
0.23832	**0,15411**	0.34505	0.31758	**0.17505**	**0.17911**	0.39830	0.24297
C41	**C42**	**C43**	**C44**	**C45**	**C46**	**C47**	**C48**
0.25396	0.20176	0.23035	0.23910	0.24979	0.24685	0.25832	0.27365
C49	**C50**	**C51**	**C52**	**C53**	**C54**	**C55**	**C56**
0.39174	0.27520	**0.19580**	0.21956	0.33287	0.29702	**0.18933**	0.37015
C57	**C58**	**C59**	**C60**	**C61**	**C62**	**C63**	**C64**
0.25592	**0.12463**	0.36663	0.26087	0.21739	0.32930	**0.15669**	**0.18217**
HIFEAN							
C1	**C2**	**C3**	**C4**	**C5**	**C6**	**C7**	**C8**
0.59658	0.39050	0.38173	0.34914	0.37047	0.32377	0.31406	0.36937
C9	**C10**	**C11**	**C12**	**C13**	**C14**	**C15**	**C16**
0.35279	0.36615	0.38220	0.38146	0.36904	0.36871	0.37061	0.37660
C17	**C18**	**C19**	**C20**	**C21**	**C22**	**C23**	**C24**
0.36892	0.33635	0.28816	0.35212	0.26877	0.31658	0.31985	**0.13814**
C25	**C26**	**C27**	**C28**	**C29**			
0.12365	0,32421	0.24076	0.33598	0.21262			

To sum–up, second–order PMD is measured within the central frequency and its harmonics, calculating difference between them. Considering the central frequency (193.1 THz) and its near frequencies, the largest frequency variation is 620 MHz, i.e. between 193.09968 THz and 193.1003 THz, due to the second–order PMD and the smallest change is 45 MHz, i.e. between 193.10058 THz and 193.100625 THz. In the harmonics case, the most important variation is calculated in 660 MHz, i.e. between 193.14066 THz and 193.14132 THz. These results show the excellent performance of HIFEAN to carry out tasks of PMD detection.

3.8 Summary

Several entropy measures are proposed for fuzzy sets and intuitionistic fuzzy sets for tasks of detection oriented to optics communications. FEAN is proposed to detect changes in the optical

combs lines spectra generated by MZM configuration. Due to the need for controlling phase, RF amplitude, RF frequency, and DC Bias in MZM, FEAN can be applied to identify the most relevant parameter to obtain the best flatness of spectrum. By considering the four cases described in the chapter, FEAN was able to identify more sensibility to the variations of RF signal frequency than the changes of phase and DC Bias. The results are consistent with the known observations of preliminary studies of optical combs lines with MZM. Comparing FEAN and Diez–Lledo and Aguilar's entropy, both have a better throughput for the analysis of combs lines behavior.

Based on FEAN, an extension called HIFEAN is proposed to optimize the task of detection in combs spectra and other applications. HIFEAN is defined through the degrees of fuzziness and intuitionistic which is different of FEAN. The proposed entropy was applied to two cases of optics communications to analyze its robust with respect to the intuitionistic fuzzy entropy proposed by Vlachos and Sergaidis (HVS). The obtained results show HIFEAN has a better performance than HVS in both applications. In the comb lines generation with MZM, HIFEAN presents an optimal detection of combs lines in the optical spectra when the parameters like DC BIAS, RF amplitude, and RF frequency are considered. In the second–order PMD detection, HIFEAN finds important range of frequencies (or range of samples) where the phenomenon is critical in the optical spectra. By contrast, HVS identified little presence of PMD in all spectra because the entropy values are high in the majority of measurements. Therefore, HIFEAN generated a better performance to measure the impact of second–order PMD in the ultra–short pulse propagation in SMF. All results show the optimal performance of HIFEAN for applications in optics communications.

CHAPTER 4: IFCA–MV: INTUITIONISTIC FUZZY CELLULAR AUTOMATON BASED ON MEAN VECTORS

4.1 Introduction

In the chapter 3, new fuzzy entropy and intuitionistic fuzzy entropy measures were defined for tasks of detection of the most relevant combs lines and second–order PMD in ultra–short pulses after propagation in SMF. The above was applied without the presence of an interaction between chromatic dispersion and non–linear effects. To improve the entropy measures when the interaction is considered, a method is proposed to optimize the analysis of spectrum stability. Since these interactions are difficult to identify in an optical spectrum, the tasks of prediction is the key to find the most relevant ranges of frequency or wavelength.

The chapter 4 shows a method based on fuzzy cellular automata (FCAs) due to the need for predicting the spatio−temporal behavior of comb lines spectrum. The spatial dimensional refers to the variability among the comb lines to observe the stability or not of flatness, as well as the likely changes of phase. Since these variations occur in the time, the temporal domain must be considered.

For the FCA proposal, antecedents about the evolution of FCA theory are mentioned in section 4.2. Afterwards, section 4.3 shows the main concepts of cellular automata (CAs) and FCAs. While that FCA is useful in the dynamical analysis of a system based on FS theory, the use of IFS in FCA has not been explored yet and neither its application in the OFC prediction. The mixing between FCA and IFS allows creating a new prediction method able to detect minimum variations of one or more physical variables of system. In section 4.4, the new method called intuitionistic fuzzy cellular automaton based on mean vectors (IFCA−MV) is presented. The flow diagram of IFCA−MV is shown. By means of diagram, several steps of method are explained as follows:

1) Conversion of the membership and non−membership degrees matrices, **U** and **V** (obtained by LAMDA and the use of Dombi's complement), to build the mean vectors or features vectors, $\overrightarrow{\boldsymbol{\mu m}}$ and $\overrightarrow{\boldsymbol{\upsilon m}}$

2) By obtaining the mean vectors, a special group of evolution rules of automaton, *h*, are applied. Such evolution rules are defined by the disjunctive normal form (DNF), used in artificial intelligence to carry out probabilistic operations or other kind of operation. The above is established in the spatial domain.

3) The mean vectors evolved in the spatial domain, $\kappa_{-p,\ldots,+p}$, can facilitate the use of evolution rules in the temporal domain, h^t. The prediction result of such vectors is converted in new membership and non−membership degrees matrices, **UT** and **VT**.

4) The desfuzzification process of **UT** and **VT** is carried out to find the concrete values, *r*, being for the OFC case, the power levels of optical spectrum. This step allows finding the prediction.

The proposed method is applied to a 2f−pulse shaper (PS) simulation, explained in section 4.5. To observe the performance of the spatio−temporal prediction, a special group of evolution rules, {27, 29, 46, 58, 78, 90, 110, 172, and 184}, are applied to identify the type of variation in the spatial spectrum.

The chapter IV is organized as follows: 4.2) Antecedents; 4.3) Cellular Automata and Fuzzy Cellular Automata; 4.4) Intuitionistic Fuzzy Cellular Automaton Based on Mean Vector (IFCA−MV); 4.5) Application of IFCA−MV: Prediction of Ultra−Short Pulse Behavior through the Mask Representation of a SLM and 4.6) Conclusions.

4.2 Antecedents

Cellular automata (CAs) are dynamical systems discrete represented in temporal and spatial domains [SET08]. Theses CAs were ideated by Von Neumann in the decades of 1940s to understand dynamical systems in biology but the development of "the game of life or Conway's game" in the decades 1970s, generated a high impact in computer sciences applications [BET12]. Nevertheless, from 1980s main concepts and the mathematical theory for CAs were described by Stephen Wolfram where the elementary cellular automata allowed analyzing the behavior of a system through a classification: *static or homogeneous fixed points, periodic configurations, chaotic or aperiodic patterns, and complex patterns*. In 2002, Wolfram suggested CAs can be defined as a universe intrinsically discrete although the rule 110 is mentioned as "universal rule" [WOL02]. The above is defined from viewpoint deterministic and a Boolean interpretation but the development of fuzzy sets theory has allowed creating other kind of CAs.

Fuzzy cellular automata (FCAs) were proposed as an extension of continuous cellular automata where the local transition rule is a disjunctive normal form (DNF) of the fuzzification for a local rule [FLO01]. FCAs were created by [CAT93] [CAT97], to find complex behaviors of a system and to understand the impact of perturbations in the dynamic through a binomial cellular automaton (BCA). These characteristics have allowed applying FCAs at different topics. [MRA00] developed a simulation of the fire spread in homogeneous nature environment. [MAJ05] and [MAJ07] used FCAs and a hybrid algorithm with radial basis function to resolve pattern recognition and clustering problems. [AHM09] introduced FCAs for carrying out a process calibration of urban dynamics in three periods of the city of Riyadh in Saudi Arabia. [MAN10] implemented an urban modeling to represent access of the multi–level urban growth dynamics in linguistic terms. [AYA12] generated a uniformly distributed random number with FCAs. [NOE12] created a technique with FCAs for removing distortions that occur in satellite and radar images and maps obtained by aerial images. In [PLA13], CAs and fuzzy numbers are combined to simulate a traffic model and compared with a model based stochastic CAs. In [HU15], an outer−inner uncertainty FCA algorithm was proposed to solve the dynamic uncertain multi−project scheduling problem in enterprise management. Recently, a FCA model was developed to simulate the decision−making process of the effect of driving behavior on traffic performance [CHAI15]. In addition, FCA transition rules are used to optimize particle swarm optimization in edge detection for image processing [UGU15].

In the study of behavior and dynamical in FCAs, several works have been developed to increase the performance of FCAs, where the temporal–spatial evolution was analyzed by [MIN06a]

[MIN06b] [BET12]. [MAJ08] introduced two operators called dependency vector and deriver complement vector to find the attractor basins of FCAs. A study about of an alternate characterization of FCAs to guarantee a generalization of an arbitrary number of variables finite or infinite fields was defined to avoid the use of a disjunctive normal form (DNF) approach in the local rule [ELY10]. Other work developed a strategy for controlling the FCA dynamics with the particular rule 90 [ELY11].

Since FCAs have the possibility for creating various configurations with fuzzy extensions, it is possible to improve its performance. The use of fuzzy extensions has been one important interesting. [LEA09] applied a fuzzy cellular models based on interval type–2 fuzzy cellular model (IT2–FCM) to simulate the dynamics of ecological systems. [ATAN11] developed an intuitionistic fuzzy estimation of Conway's Game. Recently, [CAI13] implemented a modified FCA model based on interval type–2 fuzzy logic (IT2–FL) for tasks of one–lane highway traffic. The above works indicate a tendency for developing new FCAs but it is important to consider CAs able to estimate complex behaviors with high fidelity. Moreover, CAs must adapt to other scenarios where the identification of linear or non–linear phenomena of system, as well as the interaction between them are needed.

Based on the FCAs theory and the elemental structures, a new CA is proposed in this chapter with interpretation of intuitionistic fuzzy sets and mean vectors, as explained in the following sections.

4.3 Cellular Automata and Fuzzy Cellular Automata

A cellular automaton (CA) is a dynamical system defined by binaries representation that simulates different behaviors according to a set of local and global rules. The rules describe the temporal and spatial evolution of each cell, defined as states 0 and 1. Each cell contains at least a known state. The cells are mapping in squares of D–dimensional, expressed by $\mathbb{Z}^D$. Considering C as a binary cellular automaton (BCA), being C: $\mathbb{Z}^D \rightarrow s$, the automaton is denominated as the quadruple $C = \{\mathbb{Z}^D, s, \eta, g\}$, where each subset means:

- $\mathbb{Z}^D$ is the set of cells of D–dimensional.
- s is the set of Boolean states of the cells, $s \rightarrow \{0,1\}$.
- η refers to the neighborhood of a cell (usually, the neighbor cells up to a certain radius).
- g: $s^{\eta} \rightarrow s$ is the local rule of the automaton, where η is the size of the neighborhood.

For one–dimensional BCA, cells update their Boolean states synchronously at discrete times through the local rule applied in the neighborhoods. The next state of each cell will depend on the known current states of the neighboring through the local rule updating. Defining p as a position of a cell in $\mathbb{Z}^1$ at discrete time step, $t + 1$, the local rule is updated with respect to the states of cells neighboring in the positions $p - 1$ (the left neighbor), p (the current cell), and $p + 1$ (the right neighbor) at discrete time step t. The above defines the local rule as $f : s^3 \rightarrow s$, where $\eta = 3$ is the number of neighbors. For an initial configuration of one–dimensional BCA, C^0: $\mathbb{Z}^1 \rightarrow s$, the local rule updating with neighborhood $\eta = 3$, creates a mapping, C^t: $\mathbb{Z}^1 \rightarrow s$, at any discrete time t. The above mapping is called elementary cellular automata (ECA) [COO04].

Mathematically, an BCA although set of cells is located in $X^t = \{x_1^t, ..., x_{n-1}^t\}$, for all $x^t \in \mathbb{Z}^1$, contains a set of neighbors expressed as a $x^t + x_i^t$, where I refers to one change of position for each cell, being $I = \{1, \ldots, \eta - 1\}$. Considering both sets, the global rule is expressed through an update local rule, $g(x^t) = g\left(c\left(x^t + x_1^t\right), ..., c\left(x^t + x_{n-1}^t\right)\right)$, for a configuration c in a discrete time t. Each configuration represents a BCA. The global rule, $g(x^t)$, allows mapping all BCAs in G: $\mathcal{C} \rightarrow \mathcal{C}$, being $g = G$ and $\mathcal{C}$ a general configuration of all BCAs. Based on the global rule, the global dynamics of all cells can be identified for any discrete time t.

The local rules and the global rule for BCAs allow creating two special configurations of cells, called Von Neumann and Moore [WOL02]. Von Neumann's configuration is a simple infinite array of cells, where the main characteristic is to satisfy the Manhattan norm [BRU08]. This norm is explained below: considering relative offsets, y^t, where $\left\{y^t : \left\|y_1^t, ..., y_d^t\right\|_1 = 1\right\} = \left|y_1^t\right| + \cdots + \left|y_d^t\right|$, each cell located on x^t can contain at least $2D + 1$ possible neighbors in the current cell, and therefore, the cell can move with the nearest neighbor through a coordinate unit vector, $\boldsymbol{g}_i^t = (0,\ldots,0,1,0,\ldots 0)$, expressed as $x^t \pm \boldsymbol{g}_i^t$ [KAR05]. On the other hand, Moore's configuration uses other norm called the max–norm, that generates an array of cells with three states (–1, 0, 1), such that relative offsets is expressed as: $\left\{y^t : \left\|y_1^t, ..., y_d^t\right\|_\infty = 1\right\} = max\left\{\left|y_1^t\right| + \cdots + \left|y_d^t\right|\right\}$. In Fig. 3.1 and Fig 3.2, both configurations are shown where the former has $2^{d=2}$ neighbors and the latter has $3^{d=2}$ neighbors.

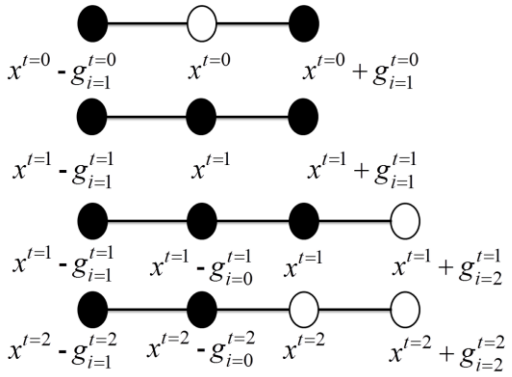

Fig. 4.1. Von Neumann's representation.

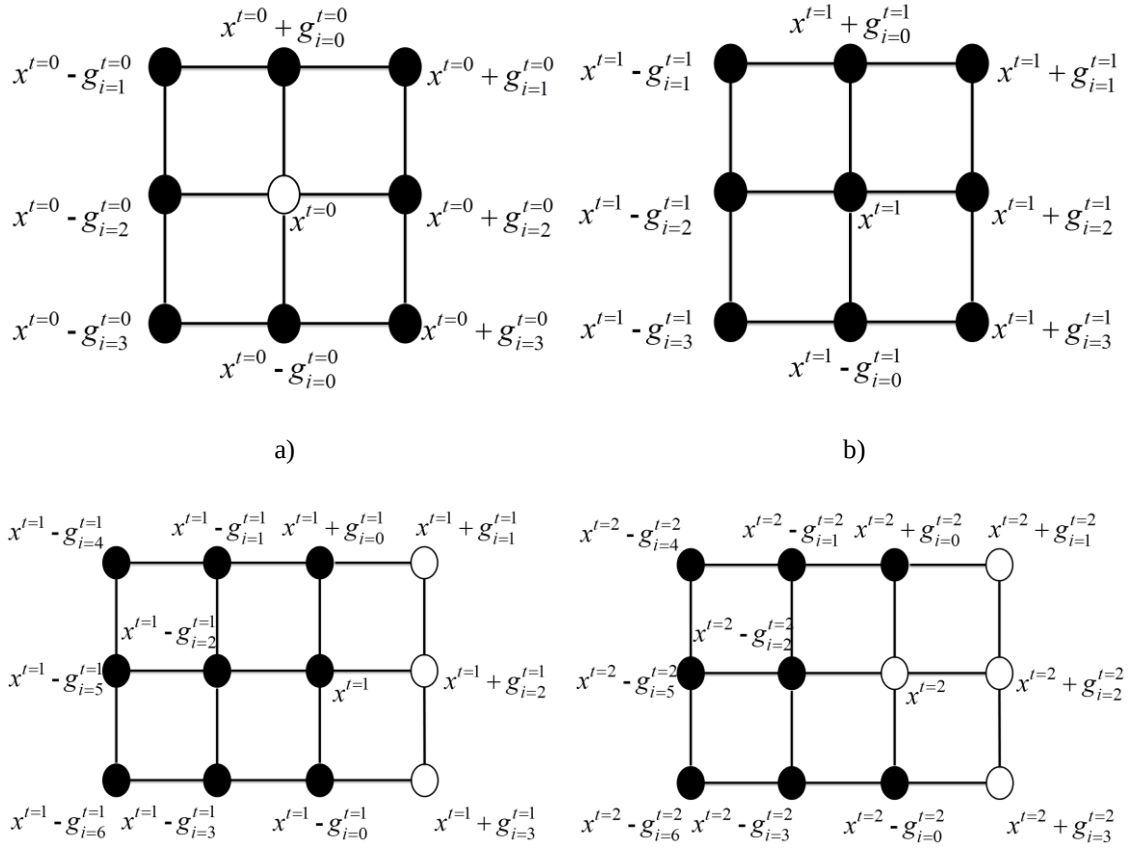

Fig. 4.2. Moore's representation for: a) $t = 0$, b) $t = 1$, c) $t = 1$ with spatial displacement, and d) $t = 2$.

Considering the BCA theory, other CA representation is the circular cellular automaton (CCA) where is a finite circular *D*–dimensional grid and the final cell is selected as the neighbor of the first cell [FLO01]. Mathematically, a CCA is mapped for any η such that G: $\{0,1\}^{\eta} \rightarrow \{0,1\}^{\eta}$, subject to two restrictions: all positions cells, $X^{t} \in \{0,1\}^{\eta}$ for all $I = \{1,\ldots, \eta - 1\}$ and the local rule is defined as $g(x_i) = g(x_{i-p},...,x_i,...,x_{i+p})$, so long as a fixed point $\mathbf{P} \in \{0,1\}^{\eta}$ such that G(**P**) = **P** [BET13]. For one–dimensional CCA, the local rule is expressed in *tabular form*, 2^{2p+1} possible local configurations and it is mapped as a Boolean value b_i, where *I* corresponds to the ranging from 0 to $2^{2p+1} - 1$ [BET09]. For example, for $p = 3$, the local rule has $2^8 - 1$ possible configurations, where b_i: $(0 \leq I \leq 2^8 - 1$: 000, 001, 010, 011, 100, 101, 110, 111) $\rightarrow (b_0,\ldots,b_{2^7-1})$. The above representation can be written as a decimal representation which is applied as the rule number (0 – 255, if $p = 3$).

To build a local rule in CCAs, Boolean operators like AND, OR, and NOT are used to update states of automaton. Such operators are expressed in disjunctive normal form (DNF), as shown in Eq. (4.1) [FLO00]:

$$g\left(x_{-p},...,x_{p}\right)=\bigvee_{i<2^{2p+1}} b_i \bigwedge_{j=-p:p} x_j^{d_{i,j+p}} \tag{4.1}$$

where $d_{i,j}$ is the *j*–th digit from left to right of d_i. The first term $\bigvee_{i<2^{2p+1}} b_i$ is the rule number (if p = 3, $I < 2^8$) and the last term $\bigwedge_{j=-p:p} x_j^{d_{i,j+p}}$ refers to binary states although values are equal to 1. If $d_{i,j}$ = 1, the binary value is equal to x_j^1, and otherwise, if $d_{i,j}$ = 0, the binary value is x_j^0 (equivalent to $\neg x_j$).

Considering CCA model and fuzzy sets (FSs), fuzzy cellular automata (FCA) are defined as a fuzzy extension of BCA, where local rules are expressed by the DNF representation. Since FCA is a fuzzy representation of a dynamical system, the local rule is expressed by a DNF–fuzzification where $(\neg\mu) = 1 - \mu, \mu_A \wedge \mu_B = \mu_A \cdot \mu_B$, and $\mu_A \vee \mu_B = \max\{1, \mu_A + \mu_B\} = \mu_A + \mu_B$ (T–norm and S–norm probabilistic representation), being *A* and *B* are two FSs. Taking into account Eq. (4.1), the DNF–fuzzification is given by[5]:

$$f\left(\mu_{-p},...,\mu_{p}\right)=\sum_{i<2^{2p+1}} g\left(d_i\right)\prod_{j=-p:p} q\left(\mu_j, d_{i,j+p}\right) \tag{4.2}$$

where $g\left(d_i\right)$ refers to the rule number for the fuzzification and $q\left(\mu_j, d_{i,j+p}\right)$ is equivalent to $q\left(\mu_j, d_{i,j+p}=0\right)=q\left(\mu_j,0\right)=1-\mu_j$ and $q\left(\mu_j, d_{i,j+p}=1\right)=q\left(\mu_j,1\right)=\mu_j$. According to [BET11], the local rule fulfills the following proportions:

(P.1) A rule is temporally periodic if for all $t>T: F\left(\mu^t\right)=F\left(\mu^{t+\tau}\right)$, being τ the period such that for all $\tau \in T$ and *F* is the global transition rule, *F*: $\{0,1\}^{\eta} \rightarrow \{0,1\}^{\eta}$.

(P.2) A rule is asymptotically periodic in time when an initial configuration fulfills for all $e > 0$, there exists for all $t>T$ such that for all $i:\left|\mu_i^t-\mu_i^{t+\tau}\right|<e$.

(P.3) A rule is asymptotically periodic in space for a period *q* in an initial configuration such that for all $e > 0$, if for all $t>T$ satisfies for all $i:\left|\mu_i^t-\mu_{i+q}^t\right|<e$.

(P.4) A rule is considered asymptotically homogeneous if it is asymptotically periodic in space for *q* = 1.

---

[5]DNF or disjunctive normal form. It is a logical formula conformed by a disjunction of conjunctive clauses, described in terms of one OR and various ANDs operation. This operation is equivalent to a sum of products of logic terms.

(P.5) A rule tends an asymptotically periodic to a fixed point $\mathbf{P} \in \{0,1\}^n$ such that $F(\mathbf{P}) = \mathbf{P}$, when $\tau = 1$.

These axioms are focused on one–dimensional. Taking into account the definitions of FCA, the next section will explain a new proposed circular CA based on mean vector obtained from intuitionistic fuzzy sets (IFSs).

4.4 Intuitionistic Fuzzy Cellular Automaton Based on Mean Vectors

To develop the proposed cellular automaton, the IFS theory and FCA are considered to define the *intuitionistic fuzzy cellular automaton based on mean vector* (IFCA–MV). This approach only uses the historical data to simulate IFCA–MV in each period τ. The automaton begins with a set of parameters: simulation period, selected rule between 1 and 255, and factor γ. Based on the above, the historical data are transformed in a membership degrees matrix (using any fuzzy clustering method) and a non–membership degree matrix (using Dombi's implication). These matrices will be the starting point of cellular automaton. For each period τ, two mean vectors (the vectors are built up with the membership and non–membership degrees) are obtained. Vectors will allow generating two matrices according to simulation period. Since the membership and non–membership degrees matrices contain the fuzzy information of historical data, a transformation of mean vectors for each period τ is required. The transformation achieves to find new membership and non–membership degrees matrices where the evolution of IFCA–MV can be analyzed. The final step is the defuzzification with the new matrices to obtain the behavior of data for each period. In Fig. 4.3, a general scheme of the proposed cellular automaton is illustrated where each one element is explained.

The proposed IFCA uses the historical data from a dynamic system (for example, data from set of optical spectra) to build up the initial configuration of cellular automaton. Let $X = \{x_{1,1},...,x_{n,d},...,x_{N,D}\}$ as a data matrix or historical data, where N refers to the number of samples and D is the number of descriptors or physical variables, the membership degrees matrix, $\boldsymbol{U}$, defined in Eq. (4.3) can be obtained by any fuzzy clustering method. Based on the matrix $\boldsymbol{U}$, the non–membership degrees matrix, $\boldsymbol{V}$, is built up, as expressed in Eq. (4.4):

$$\boldsymbol{U} = \begin{bmatrix} \mu_1(x_1) & \cdots & \mu_j(x_1) & \cdots & \mu_K(x_1) \\ \vdots & \ddots & \vdots & \cdots & \vdots \\ \mu_1(x_n) & \cdots & \mu_j(x_n) & \cdots & \mu_K(x_n) \\ \vdots & \cdots & \vdots & \ddots & \vdots \\ \mu_1(x_N) & \cdots & \mu_j(x_N) & \cdots & \mu_K(x_N) \end{bmatrix} \tag{4.3}$$

$$\boldsymbol{V}=\begin{bmatrix} \upsilon_1(x_1) & \cdots & \upsilon_j(x_1) & \cdots & \upsilon_K(x_1) \\ \vdots & \ddots & \vdots & \cdots & \vdots \\ \upsilon_1(x_n) & \cdots & \upsilon_j(x_n) & \cdots & \upsilon_K(x_n) \\ \vdots & \cdots & \vdots & \ddots & \vdots \\ \upsilon_1(x_N) & \cdots & \upsilon_j(x_N) & \cdots & \upsilon_K(x_N) \end{bmatrix} \tag{4.4}$$

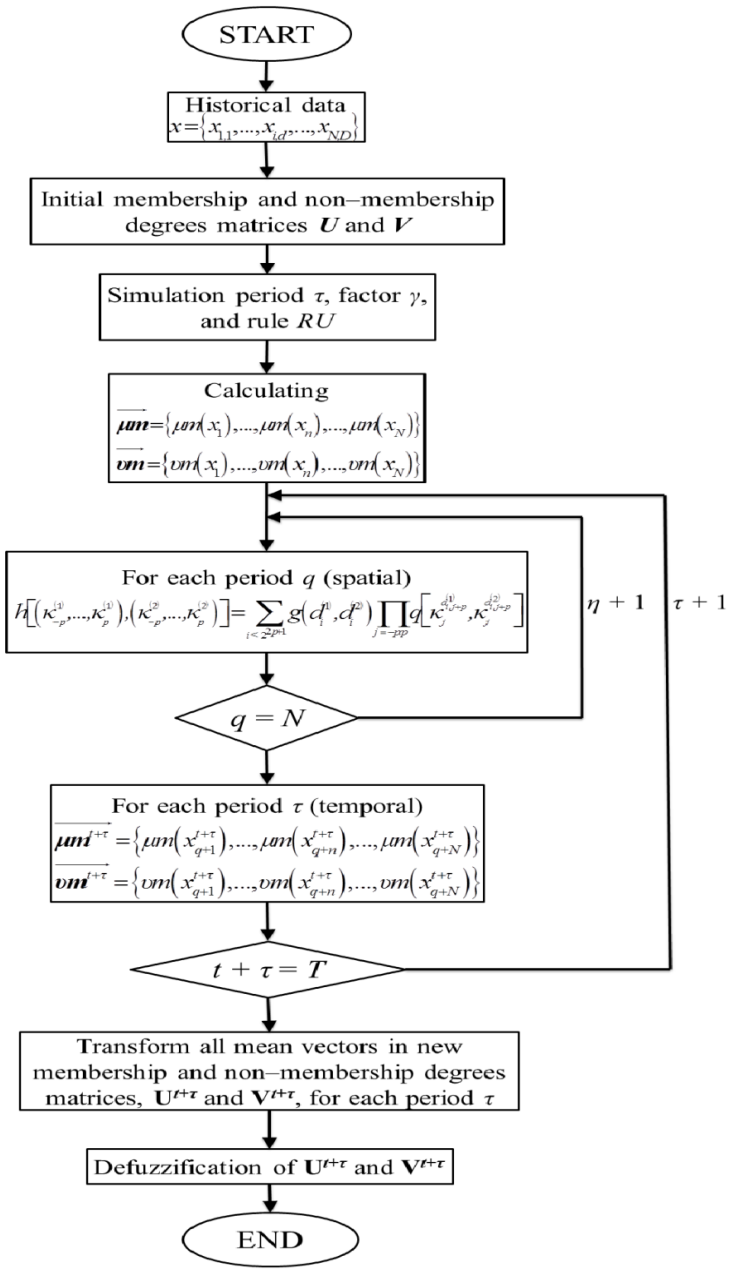

Fig. 4.3. General scheme of IFCA–MV.

Using Eq. (4.3) and Eq. (4.4), the averages of the membership degree and non–membership degree for each sample *n* are defined by Eq. (4.5) and Eq.(4.6) (in this chapter, the sample is labeled

as *n* at difference of chapter 3, where the sample is defined as *i*. This modification is realized to facilitate the explanation):

$$\mu m(x_n) = \frac{1}{K}\sum_{j=1}^{K}\mu_j(x_n) \tag{4.5}$$

$$\upsilon m(x_n) = \frac{1}{K}\sum_{j=1}^{K}\upsilon_j(x_n) \tag{4.6}$$

By using Eq. (4.5) and Eq. (4.6), two mean vectors are built–up:

$$\overrightarrow{\boldsymbol{\mu m}} = \{\mu m(x_1),...,\mu m(x_n),...,\mu m(x_N)\} \tag{4.7}$$

$$\overrightarrow{\boldsymbol{\upsilon m}} = \{\upsilon m(x_1),...,\upsilon m(x_n),...,\upsilon m(x_N)\} \tag{4.8}$$

The defined vectors are useful to obtain the initial configuration for IFCA based on mean vectors (IFCA–MV) in $\tau = 0$. Considering IFCA–MV as an intuitionistic fuzzy extension of BCA, a new *C* configuration is established. Let *C* as one–dimensional IFCA–MV (mean vector), being $C: \mathbb{Z}^1 \rightarrow q$, the automaton is represented by a quadruple $C = \{\mathbb{Z}^1, q, \eta, h\}$, where each one means:

- $\mathbb{Z}^1$ is the set of cells of one–dimensional (considering $\overrightarrow{\boldsymbol{\mu m}}$ and $\overrightarrow{\boldsymbol{\upsilon m}}$ have a size 1X*n*).
- *q* is the set of IFCA–MV states of the cells, $q \rightarrow (\{0,1\}, \{0,1\})$ or $q \rightarrow (\overrightarrow{\boldsymbol{\mu m}}, \overrightarrow{\boldsymbol{\upsilon m}})$.
- η refers to the neighborhood of a cell.
- $h: q^{\eta} \rightarrow q$ or $h: \{(0,1), (0,1)\}^{\eta} \rightarrow \{(0,1), (0,1)\}$ is the local rule of the automaton, where η is the size of the neighborhood. By default, $\eta = 3$, where the right, current, and left cell are taken into account.

Considering *h*, the local rule for IFCA–MV can be associated with a DNF representation, being:

$$h[(\mu m_{-p},...,\mu m_p),(\upsilon m_{-p},...,\upsilon m_p)] = \sum_{i<2^{2p+1}} g\left(d_i^{(1)},d_i^{(2)}\right)\prod_{j=-p:p} q\left[\left(\mu m_j,d_{i,j+p}^{(1)}\right),\left(\upsilon m_j,d_{i,j+p}^{(2)}\right)\right] \tag{4.9}$$

where $g\left(d_i^{(1)},d_i^{(2)}\right)$ is the rule number for the IFCA–MV, being $d_i^{(1)}$ the *i*–th digit (associated with the rule number) of μm and $d_i^{(2)}$ the *i*–th digit of υm. To apply the term $q\left[\left(\mu m_j,d_{i,j+p}^{(1)}\right),\left(\upsilon m_j,d_{i,j+p}^{(2)}\right)\right]$, two transformations are proposed:

- $q\left[\left(\mu m_j,d_{i,j+p}^{(1)}=0\right),\left(\upsilon m_j,d_{i,j+p}^{(2)}=1\right)\right] = q\left[\left(\mu m_j,0\right),\left(\upsilon m_j,1\right)\right] = \left(1-\mu m_j,\upsilon m_j\right)$
- $q\left[\left(\mu m_j,d_{i,j+p}^{(1)}=1\right),\left(\upsilon m_j,d_{i,j+p}^{(2)}=0\right)\right] = q\left[\left(\mu m_j,1\right),\left(\upsilon m_j,0\right)\right] = \left(1-\upsilon m_j,\mu m_j\right)$

Since the size of neighborhood is 3, the position p = 3 to create until 2^8 – 1 possible configurations for IFCA–MV. The above generates the following mapping representation for a local rule:

$$\begin{array}{llll}
(1-\mu m_{-p},\upsilon m_{-p}) & (1-\mu m_{p},\upsilon m_{p}) & (1-\mu m_{+p},\upsilon m_{+p}) & \rightarrow \quad q^{(0)} \\
(1-\mu m_{-p},\upsilon m_{-p}) & (1-\mu m_{p},\upsilon m_{p}) & (1-\upsilon m_{+p},\mu m_{+p}) & \rightarrow \quad q^{(1)} \\
(1-\mu m_{-p},\upsilon m_{-p}) & (1-\upsilon m_{p},\mu m_{p}) & (1-\mu m_{+p},\upsilon m_{+p}) & \rightarrow \quad q^{(2)} \\
(1-\mu m_{-p},\upsilon m_{-p}) & (1-\upsilon m_{p},\mu m_{p}) & (1-\upsilon m_{+p},\mu m_{+p}) & \rightarrow \quad q^{(3)} \\
(1-\upsilon m_{-p},\mu m_{-p}) & (1-\mu m_{p},\upsilon m_{p}) & (1-\mu m_{+p},\upsilon m_{+p}) & \rightarrow \quad q^{(4)} \\
(1-\upsilon m_{-p},\mu m_{-p}) & (1-\mu m_{p},\upsilon m_{p}) & (1-\upsilon m_{+p},\mu m_{+p}) & \rightarrow \quad q^{(5)} \\
(1-\upsilon m_{-p},\mu m_{-p}) & (1-\upsilon m_{p},\mu m_{p}) & (1-\mu m_{+p},\upsilon m_{+p}) & \rightarrow \quad q^{(6)} \\
(1-\upsilon m_{-p},\mu m_{-p}) & (1-\upsilon m_{p},\mu m_{p}) & (1-\upsilon m_{+p},\mu m_{+p}) & \rightarrow \quad q^{(7)}
\end{array} \tag{4.10}$$

For the function υm, it is proposed as a Dombi's complement, given by:

$$\mu m_A^c = \upsilon m_A^c = \frac{\gamma^2\left(1-\mu m_A\right)}{\gamma^2\left(1-\mu m_A\right)+\left(1-\gamma\right)^2 \mu m_A} \tag{4.11}$$

where Eq. (4.11) is the equivalent to $(\neg\mu) = 1–\mu$, in the DNF representation. In Eq. (4.10), the operator's ∧ and ∨ for IFCA–MV are expressed through IFS operators explained in chapter 2, as shown below:

$$\left(\mu m_A,\upsilon m_A\right)\wedge\left(\mu m_B,\upsilon m_B\right)=\left(\mu m_A,\upsilon m_A\right)\bullet\left(\mu m_B,\upsilon m_B\right)=\left(\mu m_A\cdot\mu m_B,\ \upsilon m_A+\upsilon m_B-\upsilon m_A\cdot\upsilon m_B\right) \tag{4.12}$$

$$\left(\mu m_A,\upsilon m_A\right)\vee\left(\mu m_B,\upsilon m_B\right)=\left(\mu m_A,\upsilon m_A\right)+\left(\mu m_B,\upsilon m_B\right)=\left(\mu m_A+\mu m_B-\mu m_A\cdot\mu m_B,\ \upsilon m_A\cdot\upsilon m_B\right) \tag{4.13}$$

To find local rules in "*general form*", Eq. (4.9) can be represented by:

$$h\left[\left(\kappa_{-p}^{(1)},\ldots,\kappa_{p}^{(1)}\right),\left(\kappa_{-p}^{(2)},\ldots,\kappa_{p}^{(2)}\right)\right]=\sum_{i<2^{2p+1}} g\left(d_i^{(1)},d_i^{(2)}\right)\prod_{j=-p:p} q\left[\kappa_j^{d_{i,j+p}^{(1)}},\kappa_j^{d_{i,j+p}^{(2)}}\right] \tag{4.14}$$

Using Eq. (4.10) – Eq. (4.14), the mapping for the general form is obtained as follows:

Table 4.1. Mathematical expressions for $q^{(0)},\ldots, q^{(7)}$ in general form.

$q^{(0)}$	$\left[\left(1-\mu m_{-p}\mu m_{p}\mu m_{+p}\right)-\mu m_{-p}\left(1-\mu m_{p}\right)-\mu m_{p}\left(1-\mu m_{+p}\right)-\mu m_{+p}\left(1-\mu m_{-p}\right),\right.$ $\left.\upsilon m_{+p}+\upsilon m_{-p}\left(1-\upsilon m_{+p}\right)+\upsilon m_{p}\left(1-\upsilon m_{+p}\right)-\upsilon m_{-p}\upsilon m_{p}\left(1-\upsilon m_{+p}\right)\right]$	$\left[\kappa_1^{(0)}\left(\mu m_{-p:+p},\upsilon m_{-p:+p}\right),\right.$ $\left.\kappa_2^{(0)}\left(\mu m_{-p:+p},\upsilon m_{-p:+p}\right)\right]$
$q^{(1)}$	$\left[\left(1-\mu m_{-p}\mu m_{p}\upsilon m_{+p}\right)-\upsilon m_{+p}\left(1-\mu m_{-p}\right)-\mu m_{p}\left(1-\upsilon m_{+p}\right)-\mu m_{-p}\left(1-\mu m_{p}\right),\right.$ $\left.\mu m_{+p}+\upsilon m_{-p}\left(1-\mu m_{+p}\right)+\upsilon m_{p}\left(1-\mu m_{+p}\right)-\upsilon m_{-p}\upsilon m_{p}\left(1-\mu m_{+p}\right)\right]$	$\left[\kappa_1^{(1)}\left(\mu m_{-p:+p},\upsilon m_{-p:+p}\right),\right.$ $\left.\kappa_2^{(1)}\left(\mu m_{-p:+p},\upsilon m_{-p:+p}\right)\right]$
$q^{(2)}$	$\left[\left(1-\mu m_{-p}\upsilon m_{p}\mu m_{+p}\right)-\mu m_{+p}\left(1-\upsilon m_{-p}\right)-\upsilon m_{p}\left(1-\mu m_{-p}\right)-\mu m_{-p}\left(1-\mu m_{+p}\right),\right.$ $\left.\upsilon m_{+p}+\upsilon m_{-p}\left(1-\upsilon m_{+p}\right)+\mu m_{p}\left(1-\upsilon m_{+p}\right)-\upsilon m_{-p}\mu m_{p}\left(1-\upsilon m_{+p}\right)\right]$	$\left[\kappa_1^{(2)}\left(\mu m_{-p:+p},\upsilon m_{-p:+p}\right),\right.$ $\left.\kappa_2^{(2)}\left(\mu m_{-p:+p},\upsilon m_{-p:+p}\right)\right]$
$q^{(3)}$	$\left[\left(1-\mu m_{-p}\upsilon m_{p}\upsilon m_{+p}\right)-\upsilon m_{+p}\left(1-\mu m_{-p}\right)-\upsilon m_{p}\left(1-\upsilon m_{+p}\right)-\mu m_{-p}\left(1-\upsilon m_{p}\right),\right.$ $\left.\mu m_{+p}+\upsilon m_{-p}\left(1-\mu m_{+p}\right)+\mu m_{p}\left(1-\mu m_{+p}\right)-\upsilon m_{-p}\mu m_{p}\left(1-\mu m_{+p}\right)\right]$	$\left[\kappa_1^{(3)}\left(\mu m_{-p:+p},\upsilon m_{-p:+p}\right),\right.$ $\left.\kappa_2^{(3)}\left(\mu m_{-p:+p},\upsilon m_{-p:+p}\right)\right]$
$q^{(4)}$	$\left[\left(1-\upsilon m_{-p}\mu m_{p}\mu m_{+p}\right)-\mu m_{+p}\left(1-\upsilon m_{-p}\right)-\mu m_{p}\left(1-\mu m_{+p}\right)-\upsilon m_{-p}\left(1-\mu m_{p}\right),\right.$ $\left.\upsilon m_{+p}+\mu m_{-p}\left(1-\upsilon m_{+p}\right)+\upsilon m_{p}\left(1-\upsilon m_{+p}\right)-\mu m_{-p}\upsilon m_{p}\left(1-\upsilon m_{+p}\right)\right]$	$\left[\kappa_1^{(4)}\left(\mu m_{-p:+p},\upsilon m_{-p:+p}\right),\right.$ $\left.\kappa_2^{(4)}\left(\mu m_{-p:+p},\upsilon m_{-p:+p}\right)\right]$
$q^{(5)}$	$\left[\left(1-\upsilon m_{-p}\mu m_{p}\upsilon m_{+p}\right)-\upsilon m_{+p}\left(1-\upsilon m_{-p}\right)-\mu m_{p}\left(1-\upsilon m_{+p}\right)-\upsilon m_{-p}\left(1-\mu m_{p}\right),\right.$ $\left.\mu m_{+p}+\mu m_{-p}\left(1-\mu m_{+p}\right)+\upsilon m_{p}\left(1-\mu m_{+p}\right)-\mu m_{-p}\upsilon m_{p}\left(1-\mu m_{+p}\right)\right]$	$\left[\kappa_1^{(5)}\left(\mu m_{-p:+p},\upsilon m_{-p:+p}\right),\right.$ $\left.\kappa_2^{(5)}\left(\mu m_{-p:+p},\upsilon m_{-p:+p}\right)\right]$
$q^{(6)}$	$\left[\left(1-\upsilon m_{-p}\upsilon m_{p}\mu m_{+p}\right)-\mu m_{+p}\left(1-\upsilon m_{-p}\right)-\upsilon m_{p}\left(1-\mu m_{+p}\right)-\upsilon m_{-p}\left(1-\upsilon m_{p}\right),\right.$ $\left.\upsilon m_{+p}+\mu m_{-p}\left(1-\upsilon m_{+p}\right)+\mu m_{p}\left(1-\upsilon m_{+p}\right)-\mu m_{-p}\mu m_{p}\left(1-\upsilon m_{+p}\right)\right]$	$\left[\kappa_1^{(6)}\left(\mu m_{-p:+p},\upsilon m_{-p:+p}\right),\right.$ $\left.\kappa_2^{(6)}\left(\mu m_{-p:+p},\upsilon m_{-p:+p}\right)\right]$
$q^{(7)}$	$\left[\left(1-\upsilon m_{-p}\upsilon m_{p}\upsilon m_{+p}\right)-\upsilon m_{+p}\left(1-\upsilon m_{-p}\right)-\upsilon m_{p}\left(1-\upsilon m_{+p}\right)-\upsilon m_{-p}\left(1-\upsilon m_{p}\right),\right.$ $\left.\mu m_{+p}+\mu m_{-p}\left(1-\mu m_{+p}\right)+\mu m_{p}\left(1-\mu m_{+p}\right)-\mu m_{-p}\mu m_{p}\left(1-\mu m_{+p}\right)\right]$	$\left[\kappa_1^{(7)}\left(\mu m_{-p:+p},\upsilon m_{-p:+p}\right),\right.$ $\left.\kappa_2^{(7)}\left(\mu m_{-p:+p},\upsilon m_{-p:+p}\right)\right]$

Since $2^8 - 1$ or 255 possible configurations can be configured in IFCA–MV, 255 rules are obtained where each on represents a unique behavior in the system. For example, the rule 15 has a tabular form: (000, 001, 010, 011, 100, 101, 110, 111) → (1, 1, 1, 1, 0, 0, 0, 0), where the DNF representation is:

$$h\left[\left(\mu m_{-p},\mu m_{p},\mu m_{+p}\right),\left(\upsilon m_{-p},\upsilon m_{p},\upsilon m_{+p}\right)\right]=\left[\kappa_1^{(0)}\left(1-\kappa_1^{(1)}\left(1-\kappa_1^{(2)}\right)\right)+\kappa_1^{(1)}\left(1-\kappa_1^{(2)}\right)\right.$$
$$\left.+\left(1-\kappa_1^{(0)}\right)\left(\kappa_1^{(2)}\left(1-\kappa_1^{(3)}\right)+\kappa_1^{(3)}\left(1-\kappa_1^{(1)}\left(1-\kappa_1^{(2)}\right)\right)\right),\ \kappa_2^{(0)}\kappa_2^{(1)}\kappa_2^{(2)}\kappa_2^{(3)}\right]$$

Due to high quantity of rules, it is difficult to apply all them in applications in real time or in databases with large number of samples and/or variables. One alternative to resolve this limitation is a special group of fuzzy rules (27, 29, 46, 58, 78, 172, and 184), analyzed by a generalized FCA with weighted average rules (GWCA) [BET09]. These rules fulfill special conditions where converge towards a fixed point and allow analyzing an elementary BCA as a simple dynamic system. Adding two rules, 90 and 110, the goal is to compare the behaviors and predictive capacity of IFCA–MV in a widely number of special rules. The rule 90 is added by its dynamical control and

aperiodic behavior for converging to a fixed point. The rule 110 is added due to that is considered as a "universal rule" for elementary CAs. In Table II, the general form for the DNF representation based on Table I is summed–up.

Table 4.2. DNF representations of IFCA–MV.

Rule	*DNF Representation*
27	$\left[\kappa_1^{(0)}\left(1-\kappa_1^{(1)}\left(1-\kappa_1^{(3)}\right)\right)+\kappa_1^{(1)}\left(1-\kappa_1^{(3)}\right)+\left(1-\kappa_1^{(0)}\right)\left(\kappa_1^{(3)}\left(1-\kappa_1^{(4)}\right)+\kappa_1^{(4)}\left(1-\kappa_1^{(1)}\left(1-\kappa_1^{(3)}\right)\right)\right)\right.$ $\left., \kappa_2^{(0)}\kappa_2^{(1)}\kappa_2^{(3)}\kappa_2^{(4)}\right]$
29	$\left[\kappa_1^{(0)}\left(1-\kappa_1^{(2)}\left(1-\kappa_1^{(3)}\right)\right)+\kappa_1^{(2)}\left(1-\kappa_1^{(3)}\right)+\left(1-\kappa_1^{(0)}\right)\left(\kappa_1^{(3)}\left(1-\kappa_1^{(4)}\right)+\kappa_1^{(4)}\left(1-\kappa_1^{(2)}\left(1-\kappa_1^{(3)}\right)\right)\right)\right.$ $\left., \kappa_2^{(0)}\kappa_2^{(2)}\kappa_2^{(3)}\kappa_2^{(4)}\right]$
46	$\left[\kappa_1^{(1)}\left(1-\kappa_1^{(2)}\left(1-\kappa_1^{(3)}\right)\right)+\kappa_1^{(2)}\left(1-\kappa_1^{(3)}\right)+\left(1-\kappa_1^{(1)}\right)\left(\kappa_1^{(3)}\left(1-\kappa_1^{(5)}\right)+\kappa_1^{(5)}\left(1-\kappa_1^{(2)}\left(1-\kappa_1^{(3)}\right)\right)\right)\right.$ $\left., \kappa_2^{(1)}\kappa_2^{(2)}\kappa_2^{(3)}\kappa_2^{(5)}\right]$
58	$\left[\kappa_1^{(1)}\left(1-\kappa_1^{(3)}\left(1-\kappa_1^{(4)}\right)\right)+\kappa_1^{(3)}\left(1-\kappa_1^{(4)}\right)+\left(1-\kappa_1^{(1)}\right)\left(\kappa_1^{(4)}\left(1-\kappa_1^{(5)}\right)+\kappa_1^{(5)}\left(1-\kappa_1^{(3)}\left(1-\kappa_1^{(4)}\right)\right)\right)\right.$ $\left., \kappa_2^{(1)}\kappa_2^{(3)}\kappa_2^{(4)}\kappa_2^{(5)}\right]$
78	$\left[\kappa_1^{(1)}\left(1-\kappa_1^{(2)}\left(1-\kappa_1^{(3)}\right)\right)+\kappa_1^{(2)}\left(1-\kappa_1^{(3)}\right)+\left(1-\kappa_1^{(1)}\right)\left(\kappa_1^{(3)}\left(1-\kappa_1^{(6)}\right)+\kappa_1^{(6)}\left(1-\kappa_1^{(2)}\left(1-\kappa_1^{(3)}\right)\right)\right)\right.$ $\left., \kappa_2^{(1)}\kappa_2^{(2)}\kappa_2^{(3)}\kappa_2^{(6)}\right]$
90	$\left[\kappa_1^{(1)}\left(1-\kappa_1^{(3)}\left(1-\kappa_1^{(4)}\right)\right)+\kappa_1^{(3)}\left(1-\kappa_1^{(4)}\right)+\left(1-\kappa_1^{(1)}\right)\left(\kappa_1^{(4)}\left(1-\kappa_1^{(6)}\right)+\kappa_1^{(6)}\left(1-\kappa_1^{(3)}\left(1-\kappa_1^{(4)}\right)\right)\right)\right.$ $\left., \kappa_2^{(1)}\kappa_2^{(3)}\kappa_2^{(4)}\kappa_2^{(6)}\right]$
110	$\left[\kappa_1^{(1)}\left(1-\kappa_1^{(2)}\right)+\kappa_1^{(2)}\left(1-\kappa_1^{(3)}\right)+\kappa_1^{(3)}\left(1-\kappa_1^{(1)}\right)+\kappa_1^{(5)}\left(1-\kappa_1^{(2)}\right)+\kappa_1^{(6)}\left(1-\kappa_1^{(1)}\right)-\kappa_1^{(1)}\kappa_1^{(3)}\left(1-\kappa_1^{(2)}\right)\right.$ $-\kappa_1^{(3)}\kappa_1^{(5)}\left(1-\kappa_1^{(1)}\right)-\kappa_1^{(2)}\kappa_1^{(6)}\left(1-\kappa_1^{(3)}\right)-\kappa_1^{(3)}\kappa_1^{(6)}\left(1-\kappa_1^{(1)}\right)-\kappa_1^{(5)}\kappa_1^{(6)}\left(1-\kappa_1^{(2)}\right)+\kappa_1^{(1)}\kappa_1^{(2)}\kappa_1^{(5)}\left(1-\kappa_1^{(6)}\right)$ $+\kappa_1^{(2)}\kappa_1^{(3)}\kappa_1^{(5)}\left(1-\kappa_1^{(6)}\right)+\kappa_1^{(1)}\kappa_1^{(2)}\kappa_1^{(6)}\left(1-\kappa_1^{(3)}\right)+\kappa_1^{(1)}\kappa_1^{(3)}\kappa_1^{(6)}\left(1-\kappa_1^{(5)}\right)-\kappa_1^{(1)}\kappa_1^{(2)}\kappa_1^{(3)}\kappa_1^{(5)}\left(1-\kappa_1^{(6)}\right)$ $\left.+\kappa_1^{(3)}\kappa_1^{(5)}\kappa_1^{(6)}, \kappa_2^{(1)}\kappa_2^{(2)}\kappa_2^{(3)}\kappa_2^{(5)}\kappa_2^{(6)}\right]$
172	$\left[\kappa_1^{(2)}\left(1-\kappa_1^{(3)}\left(1-\kappa_1^{(5)}\right)\right)+\kappa_1^{(3)}\left(1-\kappa_1^{(5)}\right)+\left(1-\kappa_1^{(2)}\right)\left(\kappa_1^{(5)}\left(1-\kappa_1^{(7)}\right)+\kappa_1^{(7)}\left(1-\kappa_1^{(3)}\left(1-\kappa_1^{(5)}\right)\right)\right)\right.$ $\left., \kappa_2^{(2)}\kappa_2^{(3)}\kappa_2^{(5)}\kappa_2^{(7)}\right]$
184	$\left[\kappa_1^{(3)}\left(1-\kappa_1^{(4)}\left(1-\kappa_1^{(5)}\right)\right)+\kappa_1^{(4)}\left(1-\kappa_1^{(5)}\right)+\left(1-\kappa_1^{(3)}\right)\left(\kappa_1^{(5)}\left(1-\kappa_1^{(7)}\right)+\kappa_1^{(7)}\left(1-\kappa_1^{(4)}\left(1-\kappa_1^{(5)}\right)\right)\right)\right.$ $\left., \kappa_2^{(3)}\kappa_2^{(4)}\kappa_2^{(5)}\kappa_2^{(7)}\right]$

The proposed IFCA–MV satisfies the following proportions:

- A rule is temporally periodic if for all $t > T : H\left(\kappa^{t^{(1)}}, \kappa^{t^{(2)}}\right) = H\left(\kappa^{(t+\tau)^{(1)}}, \kappa^{(t+\tau)^{(2)}}\right)$, where τ is the period for all $\tau \in T$ and H is the global transition rule, being H: $\{(0,1), (0,1)\}^n \rightarrow \{(0,1), (0,1)\}^n$.

- A rule is asymptotically periodic in time when an initial configuration fulfills for all $e_1 > 0$ and $e_2 > 0$, there exists for all $t > T$ such that for all $n : \left(\left| \kappa_n^{t^{(1)}} - \kappa_n^{(t+\tau)^{(1)}} \right|, \left| \kappa_n^{t^{(2)}} - \kappa_n^{(t+\tau)^{(2)}} \right| \right) < \left(e_1, e_2 \right)$.
- A rule is asymptotically periodic in space for a period q in an initial configuration if for all $e > 0$ and for all $t > T$ satisfies for all $i : \left(\left| \kappa_i^{t^{(1)}} - \kappa_{n+q}^{t^{(1)}} \right|, \left| \kappa_i^{t^{(2)}} - \kappa_{n+q}^{t^{(2)}} \right| \right) < \left(e_1, e_2 \right)$.
- A rule is asymptotically homogeneous if it is asymptotically periodic in space for $q = 1$, i.e. $n : \left(\left| \kappa_n^{t^{(1)}} - \kappa_{n+1}^{t^{(1)}} \right|, \left| \kappa_n^{t^{(2)}} - \kappa_{n+1}^{t^{(2)}} \right| \right) < \left(e_1, e_2 \right)$.
- A rule is asymptotically periodic to a fixed point when $(\boldsymbol{P_1}, \boldsymbol{P_2}) \in (\{0,1\}^n, \{0,1\}^n)$ begins as follows: $H\left(P_1, P_2 \right) = \left(P_1, P_2 \right)$, if $\tau = 1$, i.e. $n : \left(\left| \kappa_n^{t^{(1)}} - \kappa_n^{(t+1)^{(1)}} \right|, \left| \kappa_n^{t^{(2)}} - \kappa_n^{(t+1)^{(2)}} \right| \right) < \left(e_1, e_2 \right)$.

Based on the above propositions, the mean vectors can be represented for a period q, i.e. in spatial representation, as shown below:

$$\overrightarrow{\boldsymbol{\mu m}^t} = \left\{ \mu m\left(x_{q+1}^t \right), ..., \mu m\left(x_{q+n}^t \right), ..., \mu m\left(x_{q+N}^t \right) \right\} \tag{4.15}$$

$$\overrightarrow{\boldsymbol{\upsilon m}^t} = \left\{ \upsilon m\left(x_{q+1}^t \right), ..., \upsilon m\left(x_{q+n}^t \right), ..., \upsilon m\left(x_{q+N}^t \right) \right\} \tag{4.16}$$

Considering the temporal representation, expressed by a period τ, the IFCA–MV is kept in two matrices, ***UT*** and ***VT***, as defined below:

$$\boldsymbol{UT} = \begin{bmatrix} \mu m\left(x_{q+1}^{t+1} \right) & \cdots & \mu m\left(x_{q+n}^{t+1} \right) & \cdots & \mu m\left(x_{q+N}^{t+1} \right) \\ \vdots & \ddots & \vdots & \cdots & \vdots \\ \mu m\left(x_{q+1}^{t+\tau} \right) & \cdots & \mu m\left(x_{q+n}^{t+\tau} \right) & \cdots & \mu m\left(x_{q+N}^{t+\tau} \right) \\ \vdots & \cdots & \vdots & \ddots & \vdots \\ \mu m\left(x_{q+1}^{t+T} \right) & \cdots & \mu m\left(x_{q+n}^{t+T} \right) & \cdots & \mu m\left(x_{q+N}^{t+T} \right) \end{bmatrix} = \begin{bmatrix} \overrightarrow{\boldsymbol{\mu m}^{t+1}} \\ \vdots \\ \overrightarrow{\boldsymbol{\mu m}^{t+\tau}} \\ \vdots \\ \overrightarrow{\boldsymbol{\mu m}^{t+T}} \end{bmatrix} \tag{4.17}$$

$$\boldsymbol{VT} = \begin{bmatrix} \upsilon m\left(x_{q+1}^{t+1} \right) & \cdots & \upsilon m\left(x_{q+n}^{t+1} \right) & \cdots & \upsilon m\left(x_{q+N}^{t+1} \right) \\ \vdots & \ddots & \vdots & \cdots & \vdots \\ \upsilon m\left(x_{q+1}^{t+\tau} \right) & \cdots & \upsilon m\left(x_{q+n}^{t+\tau} \right) & \cdots & \upsilon m\left(x_{q+N}^{t+\tau} \right) \\ \vdots & \cdots & \vdots & \ddots & \vdots \\ \upsilon m\left(x_{q+1}^{t+T} \right) & \cdots & \upsilon m\left(x_{q+n}^{t+T} \right) & \cdots & \upsilon m\left(x_{q+N}^{t+T} \right) \end{bmatrix} = \begin{bmatrix} \overrightarrow{\boldsymbol{\upsilon m}^{t+1}} \\ \vdots \\ \overrightarrow{\boldsymbol{\upsilon m}^{t+\tau}} \\ \vdots \\ \overrightarrow{\boldsymbol{\upsilon m}^{t+T}} \end{bmatrix} \tag{4.18}$$

Eq. (4.17) and Eq. (4.18) will represent the most relevant result of IFCA–MV, where the evolution temporal–spatial of a system is observed where each instant of time shows possible future behaviors. To observe the prediction in "concrete values", i.e. spectral power, intensities, phase, etc, the defuzzification process is applied through ***UT*** and ***VT*** matrices. To carry out this task, a transformation expressed as Euclidian measure is proposed below:

$$p_j^{t+\tau}(x_n) = \frac{1}{2}\left[\left(\mu_j(x_n) - \mu m\left(x_n^{t+\tau}\right)\right)^2 + \left(\upsilon_j(x_n) - \upsilon m\left(x_n^{t+\tau}\right)\right)^2\right] \quad (4.19)$$

being $\mu m_n^{t+\tau}$ and $\upsilon m_n^{t+\tau}$ are two elements of ***UT*** and ***VT*** for all $\tau \in T$. Eq. (4.19) relates the membership and non–membership degrees matrices from the historical data with respect to the main vector for all $\tau \in T$. This relation allows observing changes in the data behavior during the prediction (each t generates a main vector for the membership degrees and other for the non–membership degrees). Considering [SZM01], distance measures should be defined in terms of membership degree, non–membership degree, and the hesitancy degree, which Eq. (4.19) can be expanded as:

$$p_j^{t+\tau}(x_n) = \frac{1}{3}\left[\left(\mu_j(x_n) - \mu m\left(x_n^{t+\tau}\right)\right)^2 + \left(\upsilon_j(x_n) - \upsilon m\left(x_n^{t+\tau}\right)\right)^2 + \left(\pi_j(x_n) - \pi m\left(x_n^{t+\tau}\right)\right)^2\right] \quad (4.20)$$

where $\pi m\left(x_n^{t+\tau}\right) = 1 - \mu m\left(x_n^{t+\tau}\right) - \upsilon m\left(x_n^{t+\tau}\right)$. Using the membership degree function used in the Fuzzy C–Means algorithm, an updating function for all $\tau \in T$ is proposed as:

$$\mu_j^{t+\tau}(x_n) = \frac{1}{\sum_{j=1}^{K}\left[\frac{p_K^{t+\tau}(x_n)}{p_j^{t+\tau}(x_n)}\right]^{\frac{2}{m-1}}} \quad (4.21)$$

Based on Eq. (4.21), the non–membership degree updating, for all $\tau \in T$, is given by:

$$\upsilon_j^{t+\tau}(x_n) = \frac{\gamma^2\left(1 - \mu_j^{t+\tau}(x_n)\right)}{\gamma^2\left(1 - \mu_j^{t+\tau}(x_n)\right) + (1-\gamma)^2\,\mu_j^{t+\tau}(x_n)} \quad (4.22)$$

To apply $\mu_j^{t+\tau}(x_n)$ and $\upsilon_j^{t+\tau}(x_n)$, a defuzzification function proposed by [YAG09] is taken into account, as expressed below:

$$r = \sum_{n=1}^{N} w_n x_n \quad (4.23)$$

being w_n a weight associated to a sample x_n. In the proposed transformation, the weight function is given by:

$$w^{t+\tau}(x_n;\gamma) = \frac{(1-\gamma)^2\left(\mu n_j^{t+\tau}(x_n) \wedge \mu n_{j+1}^{t+\tau}(x_n)\right) + \gamma^2\left[1 - \left(\upsilon n_j^{t+\tau}(x_n) \vee \upsilon n_{j+1}^{t+\tau}(x_n)\right)\right]}{(1-\gamma)^2\sum_{n=1}^{N}\left(\mu n_j^{t+\tau}(x_n) \wedge \mu n_{j+1}^{t+\tau}(x_n)\right) + \gamma^2\left[N - \sum_{n=1}^{N}\left(\upsilon n_j^{t+\tau}(x_n) \vee \upsilon n_{j+1}^{t+\tau}(x_n)\right)\right]} \quad (4.24)$$

where:

$$pn_j^{t+\tau}(x_i) = \frac{1}{3}\left[\left(\mu_j^{t+\tau}(x_i) - \hat{\mu}_j^{t+\tau}\right)^2 + \left(\upsilon_j^{t+\tau}(x_i) - \hat{\upsilon}_j^{t+\tau}\right)^2 + \left(\pi_j^{t+\tau}(x_i) - \hat{\pi}_j^{t+\tau}\right)^2\right]$$

$$\mu n_j^{t+\tau}(x_i) = \frac{1}{\sum_{j=1}^{K}\left[\frac{pn_K^{t+\tau}(x_i)}{pn_j^{t+\tau}(x_i)}\right]^{\frac{2}{m-1}}}$$

$$\upsilon n_j^{t+\tau}(x_i) = \frac{\gamma^2\left(1-\mu n_j^{t+\tau}(x_i)\right)}{\gamma^2\left(1-\mu n_j^{t+\tau}(x_i)\right)+\left(1-\gamma^2\right)\mu n_j^{t+\tau}(x_i)}$$

where $\hat{\mu}_j^{t+\tau}$, $\hat{\upsilon}_j^{t+\tau}$, and $\hat{\pi}_j^{t+\tau}$ are the mean of $\mu n_j^{t+\tau}(x)$, $\upsilon n_j^{t+\tau}(x)$, and $\pi_j^{t+\tau}(x)$, for all $x \in X$, of each set or class *j*. Considering Eq. (4.23), the defuzzification for IFCA–MV is expressed as:

$$r = \sum_{i=1}^{N} w^{t+\tau}(x_i;\gamma)\cdot x_i \tag{4.25}$$

Based on the IFCA–MV, the proposed method is applied to a case of study of ultra–short pulse behavior.

4.5 Application of IFCA–MV: Prediction of Ultra–short Pulse Behavior through the Mask Representation of a SLM

To simulate the mask representation of a SLM through the frequency components of an ultra–short pulse, a Fourier 2f–line configuration is taken into account [WEI11]. The system contains the following elements: 1 bi–convex lens, 1 mirror, 1 sinusoidal amplitude grating, 1 ultra–short pulse source based mode–locked, and 1 LC–SLM. An incident Gaussian pulse at 5.1 mm beam waist and normalized intensity (u.a.) are generated where the beam is propagated in free space at 10 cm. When the pulse is oriented directly to the grating, around 20 samples are diffracted and spanned at 10 ms (period) whether the grating holds transmission properties. Considering a set of grating parameters proposed by [VOE11], a clear display of Fresnel's diffraction pattern is maintained. The diffracted pulse is focused to bi–convex lens with a distance at 10 cm from focal length and 5 cm of curvature radius. The goal of bi–convex lens is to create an incident spherical wave into another spherical wave, considering different curvature radius. Finally, the plane waves is carried towards LC–SLM where the idea is to achieve the majority of them are located on the pixels and the main Fourier components of pulse are focused on a number particular of lines. For the simulation test, 9 lines are used to be considered as the most important information when IFCA–MV is applied. The line–to–line spacing is around 40 μm. The above description is illustrated in Fig. 4.4.

Using the configuration, the mask representation of ultra–short pulse propagation is generated as historical data, as illustrated in Fig. 4.5. The data size is 500 x 500 where each element (1 x 1) corresponds to 1 pixel of SLM and it is equivalent to 2 μm of observation plane, according to [VOE11]. By means of the historical data, the membership and non–membership degrees are

calculated, considering the value of γ (0 – 0.5). To run the IFCA–MV, a simulation time of 25 s and a special group of rules {27, 29, 46, 58, 78, 90, 110, 172, 184} are configured. For each rule, 125 membership degrees matrices and 125 non–membership degrees matrices are kept. For all the special group of rules, a total of **2250 matrices** are generated. To facilitate the observations of the mask representation behavior, the defuzzification is applied for all obtained matrices, achieving to reduce the complexity analysis to 1125 matrices that represent in "concrete values" the evolution of system. For example, Fig. 4.6 and Fig. 4.7 illustrate the particular behavior of ultra–short pulses frequency components by using rule 90 with γ = 0.1 and γ = 0.3. In that case, if γ = 0.1, the ultra–short pulses frequency components present a decrease of intensity during the simulation time. Nevertheless, if γ = 0.3, the evolution of IFCA–MV show little intensity variations but is observed important changes of phase. In both cases, two situations are predicted the IFCA–MV which the factor γ allows finding different mask representation behaviors.

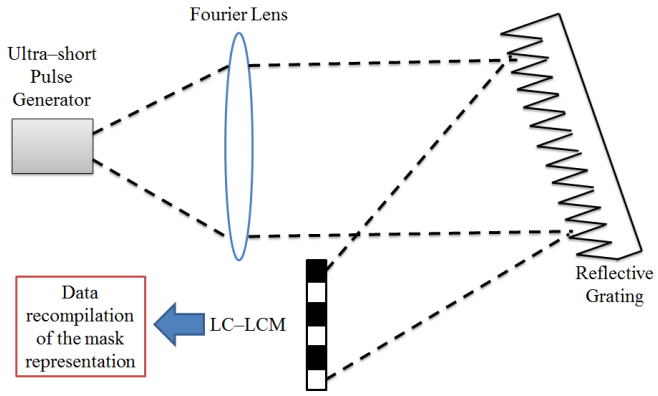

Fig. 4.4. Case of study: Fourier 2f–Configuration, considering the ultra–short pulse as carrier.

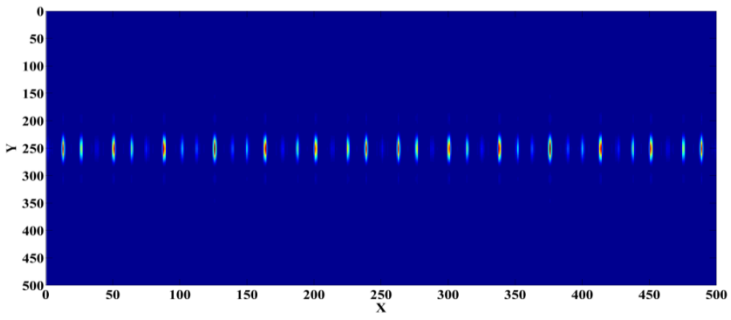

Fig. 4.5. Spectrum components obtained by the mask representation of SLM.

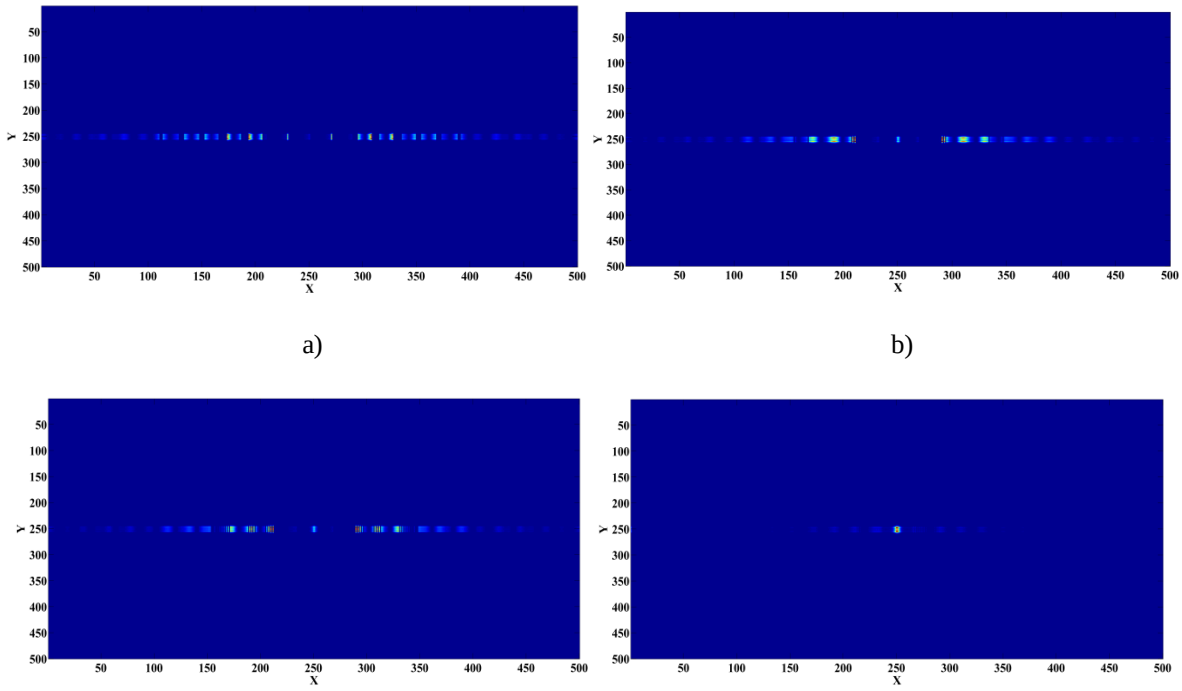

a) b)

c) d)

Fig. 4.6. Simulation of IFCA–MV, using R = 90 and γ = 0.1, for a period τ, a) τ = 5, b) τ = 15, c) τ = 20, and d) τ = 25.

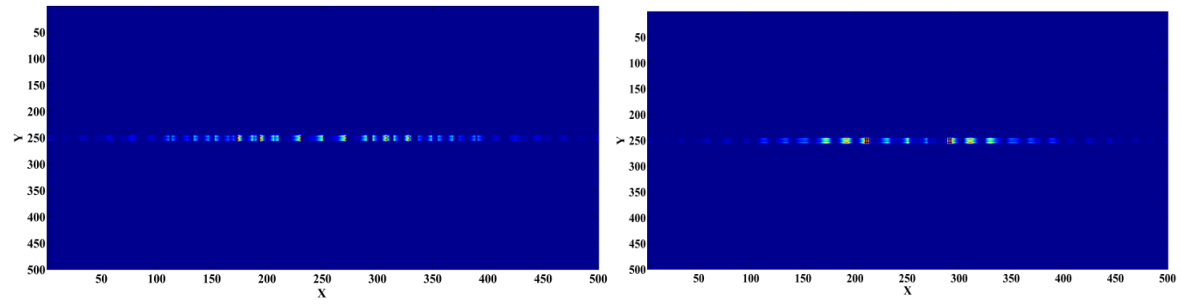

a) b)

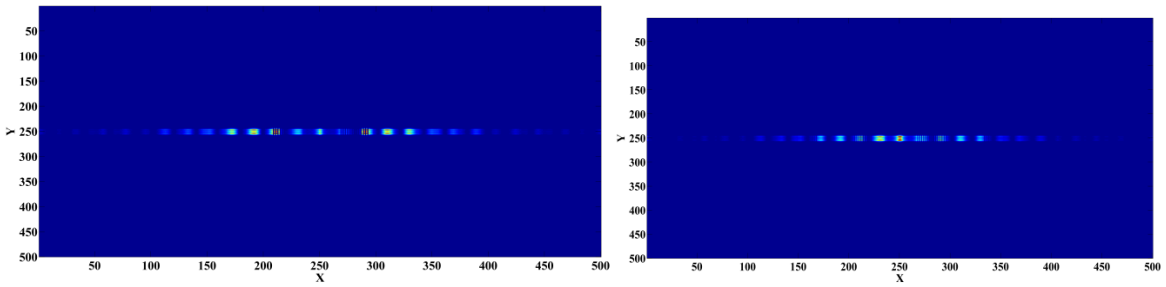

c) d)

Fig. 4.7. Simulation of IFCA–MV, using R = 90 and γ = 0.3, for a period τ, a) τ = 5, b) τ = 15, c) τ = 20, and d) τ = 25.

In order to observe a tendency in the ultra–short pulses behavior, one option is to consider the periodicity in time and space of IFCA–MV. The periodicity allows giving information about stability and behavior of any dynamical system in order to detect possible new eventualities that could present in a future time. The above is important to find a tendency in the dynamic behavior of physical variables of system and to analyze the stability when any perturbation occurs. To interpret the periodicity, the following conversion is taken into account:

- ρ **= 0.** It refers to a static dynamic of system.
- ρ **= 1.** It is a periodic behavior with a stable tendency.
- ρ **= 1 (even or odd).** It is a periodic behavior that occur in periods time and spatial even *or* odd. Normally, this periodicity is considered a stable behavior.
- ρ **= 1 (heterogeneous).** It is a periodic behavior where can conduce towards a static dynamic.
- ρ **= 2.** It refers to two periodic behaviors where system can be in a stability condition but can present a change in its dynamic in a future time.
- ρ **= 2 (even or odd).** It is two periodic behaviors when dynamic changes in even or odd periods time and spatial.
- ρ **= 4.** It refers to four periodic behaviors where a stable dynamic can become chaotic or multiple dynamics changes in a system.

In Table 4.3, the periodicity for the special group of rules obtained for a set of γ = {0.1, 0.2, 0.3, 0.4, 0.5} are summed up. Analyzing these results, rules 29 and 58 show the same periodicity (ρ = 2 or ρ = 2 even) but rule 27 generates an inverse periodicity with respect to them. These variations indicate the possibility of a linear phenomenon with rules 29 and 58 and a non–linear phenomenon with rule 27 and otherwise. On the other hand, rule 78 causes ρ = 1 and ρ = 1 (even) along γ which it represents the possible conditions of stability for an ultrashort pulse. Comparing rules 90 and 110, if γ = {0.3, 0.4} detects the same periodicity than rule 78 but γ ={0.1, 0.2, 0.5} generates important changes of the ultrashort pulses behavior. In this case, both rules can identify the presence of ρ = 1, ρ = 2 and ρ = 2 (even) which the intensity and phase variations in the ultra–short pulse are considerable. Rule 172 presents an interesting evolution of the periodicity due to the different periodicity ρ = 1 (heterogeneous), ρ = 2 (even), and ρ = 1, where the latter is the same case of rule 110 with γ = 0.5. Taking into account the above observation, rule 172 can show the likely presence of some linear and non–linear phenomena that occur in the ultrashort pulses propagation.

Nevertheless, rule 184 can also present one important evolution of the mask representation (ρ = 2 and ρ = 2 even) and it is possible to identify the interaction between linear and non–linear phenomena. If the interaction is strong, rule 46 is able of predict its impact and the possible changes of intensity and phase of frequency components of the mask representation. The above rule has ρ = 4 which indicates the presence of chaotic situation of the interaction that can affect the ultrashort pulses behavior. Relating the results for the special group of rules, IFCA–MV can predict normal and critical conditions that cause a stability condition or the linear and non–linear phenomena generation in the ultra–short pulses propagation.

Table 4.3. Periodicity of special group of rules for case of study.

RULE	**γ = 0.1**	**γ = 0.2**	**γ = 0.3**	**γ = 0.4**	**γ = 0.5**
27	ρ = 2 (even & odd)	ρ = 2 (even & odd)	ρ = 2	ρ = 2 (even & odd)	ρ = 2 (even & odd)
29	ρ = 2 (even)	ρ = 2 (even)	ρ = 2 (even)	ρ = 2 (even)	ρ = 2 (even)
46	ρ = 4	ρ = 4	ρ = 4	p = 4	ρ = 4
58	ρ = 2 (even)	ρ = 2 (even)	ρ = 2 (even)	ρ = 2 (even)	ρ = 2 (even)
78	ρ = 1	ρ = 1 (even)	ρ = 1 (even)	ρ = 1 (even)	ρ = 1 (even)
90	ρ = 2	ρ = 1	ρ = 1	ρ = 1	ρ = 2
110	ρ = 2 (even)	ρ = 2 (even)	ρ = 1	ρ = 1	ρ = 1
172	ρ = 1 (heterogeneous)	ρ = 2 (even)	ρ = 2 (even)	ρ = 1 (heterogeneous)	ρ = 1
184	ρ = 2 (even)	ρ = 2 (even)	ρ = 2 (even)	ρ = 2	ρ = 2 (even)

4.6 Summary

This chapter exhibits a new kind of CA called intuitionistic fuzzy cellular automaton based on mean vectors. The IFCA–MV carries out the evolution process in temporal and spatial conditions through average vectors for initial membership and non–membership degrees matrices (τ = 1) and new vectors are created along the simulation. The above is transformed in new membership and non–membership degrees matrices and the defuzzification step is defined for obtaining the different observations about the evolution of system. The proposed approach is applied in a case of study where the changes of the mask representation of a SLM by means of the ultrashort pulse propagation in free space are simulated. By using γ, ranging from 0.1 to 0.5, the intensity and phase variations can be observed for identifying possible linear and nonlinear phenomena present during the propagation. In order to classify those rules where detect stability, linear effect, non–linear effect or the interaction between them, a periodicity analysis is proposed to find these conditions.

According to the results, the rule 78 shows the possibility of stability for the mask representation if no changes of ultrashort pulse are conserved. On the other hand, rules 27, 29, 58, 90, and 110 achieve to find the possible conditions for generating a linear or nonlinear phenomenon. However, rules 90 and 110 are able of identify the presence of stability before the generation of any phenomenon. Rules 172 and 184 allow identify the possibility of the interaction of linear and nonlinear phenomena subject to some conditions that occur during the evolution of system. Nevertheless, if the interaction is high, the rule 46 can show the worst condition that affect the intensity and phase of Fourier components of the mask representation, as well as the changes of spectrum shaping. The last rule could determinate the possibility that the ultrashort pulse behavior handle to chaotic situation. The obtained results allow observing the potential of IFCA–MV for tasks of prediction and to evaluate the different scenarios that the system can be stable, with linear

or nonlinear condition, and the interaction of them. Moreover, the consideration of IFS inside FCA is useful to consider the credibility for the prediction which it is recommendable to guarantee an appropriated detection of abnormal situation of system.

CHAPTER 5: EXPERIMENTAL SET–UP AND RESULTS

5.1 Introduction

In chapters 3 and 4, two methods were proposed to detect relevant behaviors of OFC spectrum after propagation in SMF. Such methods were applied in four simulations: ultra–short pulses propagation in SMF, analysis of combs lines generation in MZM, propagation of combs lines spectrum in SMF, and ultra–short pulses behavior in a mask representation in a SLM. Considering the simulation results, the chapter 5 shows a general methodology based on HIFEAN and IFCA−MV. The above applies in three experimental set−up:

1. Correction of phase and spectral shape in picosecond and femtosecond pulses propagated through SMF.

2. Correction of flatness in an OFC spectrum generated by intensity modulators.

3. Prediction of noise level behavior in combs lines spectra generated microresonator rings.

To evaluate the performance, the experimental results are evaluated in the following aspects:

1. Adaptability with different scenarios in optics communications.

2. Capacity of detection of relevant situations in the OFC spectrum.

3. Computational cost in real time.

4. Statistical analysis.

In this chapter, the measurements and analysis for three experimental set−up are explained.

The chapter V is organized as follows: 5.2) HIFEAN and IFCA−MV: General Methodology for Experimental Set−up; 5.3) Application I: Propagation of Optical Spectra in SMF Generated by Picosecond and Femtosecond Pulses Sources; 5.4) Application II: Correction of Flatness of Comb Lines Spectrum Generated by Cascaded MZMs; 5.5) Application III: Prediction of Comb Lines Spectra Behaviors Generated by Microresonators ring; 5.6) General Performance of Proposed Methodology; 5.7) General Analysis of Prediction and Compensation of OFC Spectra and 5.8) Conclusions.

5.2 HIFEAN and IFCA–MV: General Methodology for Experimental Set–up

As mentioned in chapter 3, HIFEAN allows calculating the amount of information and credibility of data for IFSs. In chapter 4, IFCA−MV achieves to identify possible significant

behaviors in OFC spectrum generated by one ultra−short pulse. To use both proposals, a general methodology is developed for OFC spectrum. The explanation of methodology is given as follows:

1) To apply the methodology, a database measured by one OSA (Optical Spectrum Analyzer), must be stored in any format (.cvs, .dat, among others). The database is re−called *historical data*, being the normalized data matrix. This condition is required by any fuzzy clustering method such as Fuzzy C−Means, GK−Means or LAMDA.

2) Fuzzy clustering methods generate a membership degrees matrix which is the FSs representation from historical data. To obtain the best classification, validation index of classes finds the best parameters (number of classes and other values) in the fuzzy classifier.

3) The non−membership degrees are calculated through the membership degrees, using Eq. (2.72). After, both degrees allow establishing the hesitancy degrees for IFSs. Some works presented by [PEL08] [XU08] [VIS10] [CHU11] [LIN14], show alternatives for obtaining the hesitancy degree.

4) The membership, non−membership and hesitancy degrees will be used as the initial information in the general methodology. Considering $t = 1$, IFCA−MV requests the rule number $\{0 – 255\}$, the value of γ $\{0.1 – 0.5\}$ and initial information. By default, the algorithm is configured at least 10 seconds of operation in real time. For offline applications, a prediction time over 60 seconds is recommendable to identify multiple relevant behaviors (this step avoids the presence of false detection).

5) By obtaining the prediction results, HIFEAN can be used as a validation measure. By default, a threshold of 0.25 is defined for those classes or IFSs with the most relevant information. If HIFEAN value is under threshold, the class is stored. Otherwise, if HIFEAN value is over threshold, the class is removed. The use of HIFEAN allows reducing the number of classes with little information for prediction. Other useful of HIFEAN is focused on the reduction of computational cost during desfuzzification process (to convert IFSs in concrete values).

6) As soon as the prediction results were obtained, the analysis of stability and detection of relevant behaviors can be realized for multiple proposes, according to the conditions and knowledge of physical variables of system. To find relevant predictions, the special group of rules mentioned in chapter 4 is used.

In optics communications, the methodology can be applied to detect chromatic dispersion, high–order dispersion, non–lineal phenomena, PMD, and the most critical situation, the interaction among them. The goal is to observe the impact of mentioned phenomena through optical spectra and other kind of measurements such as RMSE (Root Mean Square Error), analysis of periodicity according to prediction results, and the presence of dynamic chaos.

In Fig. 5.1, a general scheme of the proposed methodology is shown.

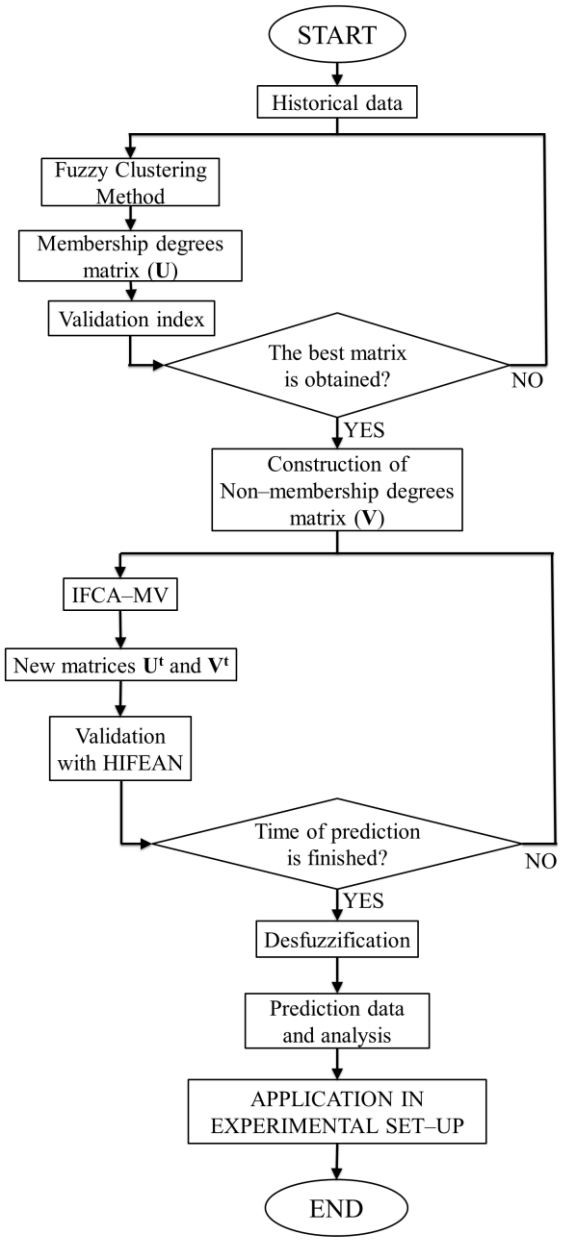

Fig. 5.1. General scheme of proposed methodology.

5.3 Application I: Propagation of Optical Spectra in SMF Generated by Picosecond and Femtosecond Pulses Sources

The first experimental set–up is focused on the analysis of OFC spectra generated by two pulsed sources: picosecond and femtosecond pulses generator. To observe the performance for both spectra, they are propagated through SMF and a pulse shaper (PS) is put at SMF output. The PS recovers the initial characteristics of spectrum generated by source, such as spectrum shape, phase, and/or intensity levels. Through spectra measurements in OSA, the methodology is applied to

predict possible changes of spectrum in a future time. If a critical variation in spectrum is detected, a correction in phase and/or intensity is made in spectrum through PS. A computer or laptop is connected towards PS, where the SLM parameters are set up. The changes of phase and/or intensity are sent towards PS as a vector of 1 x *NR* samples, where *NR* refers to the number of samples. It is important to clarify that the number of samples is associated with the number of pixels from SLM. Depending on the resolution of SLM, the number of samples can be adjusted where *a large number of samples are recommendable to reach the best correction in the spectrum*.

Based on the above explanation, two experiments are planned as explained below:

In Fig. 5.2, a picosecond pulsed laser is connected to a FPC (Fiber Polarization Controller, PolaRite, General Photonics Corporation) and it is linked to a SMF (Single–Mode Fiber, SMF−28E Corning) at 25 km and 0.20 dB of attenuation at 1550 nm. A second FPC is connected at the SMF output and a PS (Wave Shaper 1000s, Finisar, C–band) is implemented for correcting possible changes of phase and/or pulse shaping in the spectrum. As the PS generates an insertion loss at 4.5 dB, an EDFA (SPFA24, Pritel) is linked at the PS output. The above increases the OFC spectrum gain until an average power similar to the pulsed laser. The characteristics of picosecond pulsed laser (ERGO, Time–Bandwidth Products) are: repetition rate around of 9.888060 GHz (~10 GHz), operation wavelength at 1535–1565 nm, –11.2 dBm of average power, pulse duration between 1.8 ps/sech^2 and 2 ps/sech^2, and the current pump is tuned at 0.35 A. The last configuration is designed as an open–loop control to reduce the normal dispersion, as explained [WEI11].

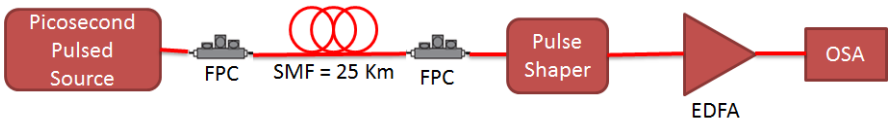

Fig. 5.2. Experimental set–up using a picosecond pulsed laser.

Using the same strategy for an open loop control in the PS, the source is replaced by a femtosecond pulsed laser. The source is connected a FPC and an EDFA and the pulse is propagated through a SMF at 25 km. A second FPC is linked at the SMF output and a DCF (Dispersion Compensation Fiber, DCF 28, Thorlabs) at 48 m and –49 ps/nm^{2}km of abnormal dispersion to reduce the normal dispersion. A second EDFA (SPFA18, Pritel) is linked between the DCF output and the PS output due to the insertion loss of the latter. Unlike picosecond pulsed laser, the femtosecond pulsed laser (FPL–03CFT, Calmar Optcom) has two output: low and high power. To analyze the impact of linear and nonlinear phenomena, the low power is selected. The low power output generates an average power at –20.4575 dBm, less than ERGO, –9.586 dBm. Other characteristics are: pulse duration at 600 fs sech^2, repetition rate around of 20 MHz, and center wavelength at 1548 nm. This experiment is illustrated in Fig. 5.3.

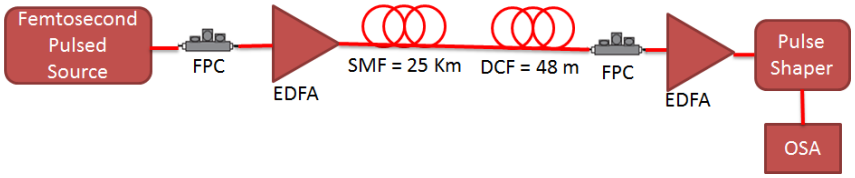

Fig. 5.3. Experimental set–up using a femtosecond pulsed laser.

Using the proposed methodology (Fig. 5.1), the measurements of optical spectra for both matrices are organized on two groups of historical data. Each one contains the original spectrum and the spectrum after its propagation in SMF. In Fig. 5.4 and Fig. 5.5, the original spectra for both source lasers are shown. Since both spectra must be tuned through of current emission control, the best picosecond and femtosecond pulses spectra are obtained to 350 mA and 433 mA. In Fig. 5.6 and Fig. 5.7, the spectra after propagation in SMF are illustrated.

According with the measurements, the femtosecond pulse spectrum is affected by the fiber attenuation, chromatic dispersion, non–linear phenomena, and the interaction among them. By contrast, the picosecond pulse spectrum is attenuated 5 dBm but the characteristics of spectrum are conserved. Due to the high repetition rate and used power average, the picosecond pulse spectrum can avoid the presence of non–linear phenomena.

On the other hand, the low repetition rate and average power in the femtosecond pulse laser are little appropriated for optics communications applications. The main reasons are the fiber losses and the possible presence of chromatic dispersion and non–linear phenomena. Considering the former, the attenuation level is critic to recover the original spectrum when the average power is low. Although two EDFAs were linked at SMF input and output, the average power is low. Using PS at the EDFA output, it could recover at least part of spectrum shape.

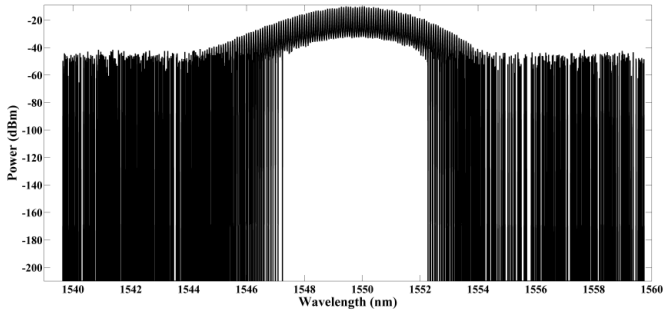

Fig. 5.4. Spectrum of picosecond pulsed laser source.

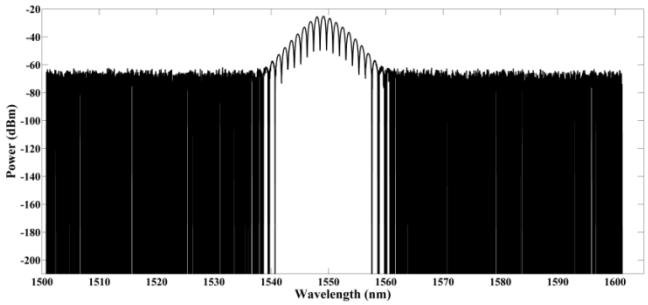

Fig. 5.5. Spectrum of femtosecond pulsed laser source.

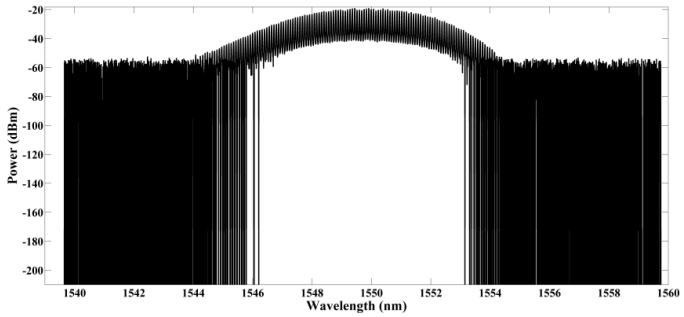

Fig. 5.6. Spectrum at the SMF output using the picosecond pulsed laser source.

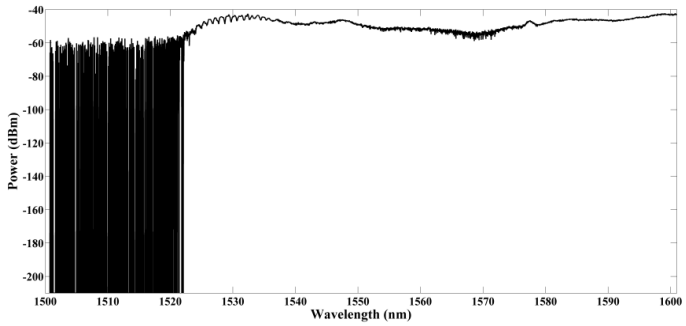

Fig. 5.7. Spectrum at the DCF output using the femtosecond pulsed laser source.

To find the vectors of phase and intensity, the methodology is applied in the historical data to identify the most relevant range of wavelength (in that case, each wavelength is associated to a sample to facilitate the use of method). Through historical data, the membership and non–membership degrees are calculated with γ = {0.1, 0.2, 0.3, 0.4, 0.5}. To begin the IFCA–MV, a special group of rules {27, 29, 46, 58, 78, 90, 110, 172, 184} and 10 iterations are configured. For each rule, 50 membership degrees matrices and 50 non–membership degrees matrices are stored. For all the special group of rules, a total of 900 matrices are generated. To simplify the observations of the spectrum behavior, the defuzzification is applied for all obtained matrices, achieving to reduce the complexity analysis to 450 matrices, represented in "power (dBm) vs wavelength (nm)". The used pulse shaper works in D–1 vector of intensity and phase of 5025 samples which the data historical must has a size 2 x 5025. The new generated spectrum is compared with the pulsed laser source spectrum, in three aspects: recuperation of phase and intensity after propagation in SMF,

spectrum stability, and performance of IFCA–MV. If the spectrum is partially recovered, a new measurement at the PS output is carried out. In that case, the historical data is replaced by new information (the new historical data are the original spectrum and the spectrum measured after PS). This procedure is replied until to obtain the best spectrum shape.

Considering the original spectrum and the spectrum at the SMF output, the results of prediction are shown in Fig. 5.8 and Fig. 5.9. In the picosecond pulse spectrum case, the rules 27 and 29 (Fig. 5.8a and 5.8b) show an optimal stability in the spectrum where the Gaussian shapes is maintained constant. The rules 46, 58, 78, 90, and 110 (Fig. 5.8c, 5.8d, 5.8e, 5.8f, and 5.8g) indicate some likely changes of phases and powers are probable but the Gaussian shape is conserved. The above is interesting due to that if some little changes in the spectrum occur, the spectrum shape will be Gaussian and tolerant front the chromatic dispersion and nonlinear phenomena during its propagation in SMF. The rules 172 and 184 (Fig. 5.8h and 5.8i) show the best stability and the presence of some changes of phase in the OFC spectrum. The former shows the changes of phase and power are depreciable and the spectral shape is stable; in contrast, the latter indicates the possibility that some slight changes of spectral shape can be presented. Nevertheless, the found predictions suggest that the picosecond pulsed source at high repetition rate can become robust and applicable in optics communications.

In the femtosecond pulse spectrum case, all rules predict critical changes of spectrum shape. The rules 27, 29, 46, 78, 110, 172, and 184 (Fig. 5.9a, 5.9b, 5.9e, 5.9g, 5.9h, and 5.9i) indicate a tendency in the spectrum behavior where the chromatic dispersion and the non–linear phenomena generate a high impact in the propagation in SMF. Rule 90 (Fig. 5.9f) shows the worst behavior of OFC spectrum where the impact of the linear and non–linear phenomena can become considerable in the propagation. Therefore, the changes of phase are wide and this kind of spectrum would not be recommendable in optics communications.

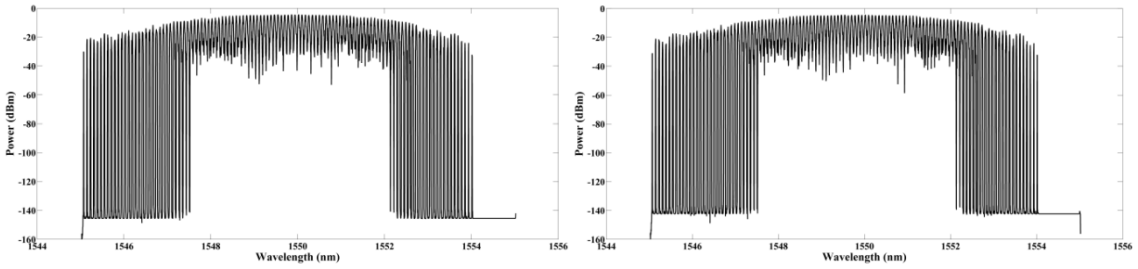

a) b)

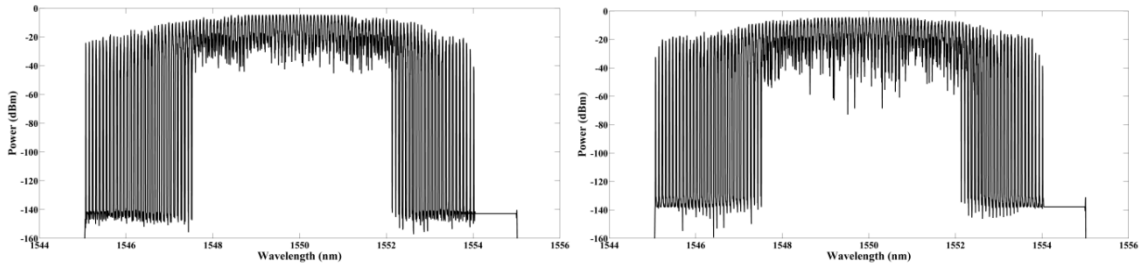

c) d)

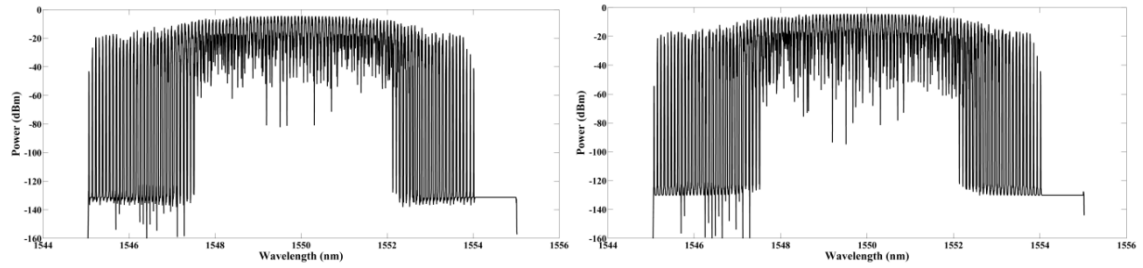

e) f)

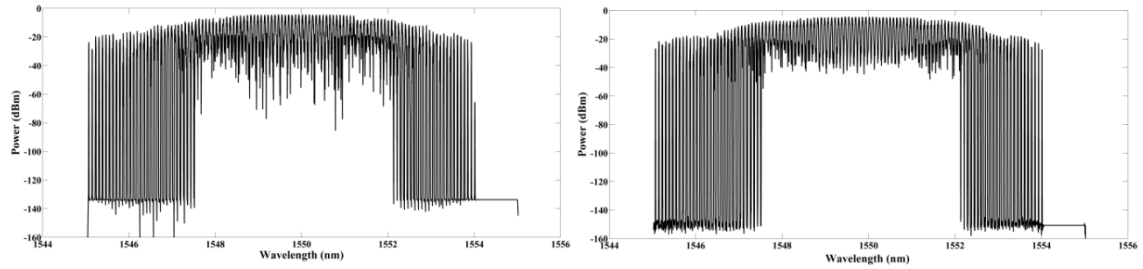

g) h)

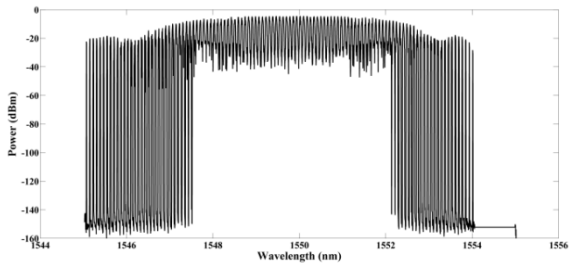

i)

Fig. 5.8. Prediction of picosecond pulses spectrum, using a) Rule 27, b) Rule 29, c) Rule 46, d) Rule 58, e) Rule 78, f) Rule 90, g) Rule 110, h) Rule 172, and i) Rule 184.

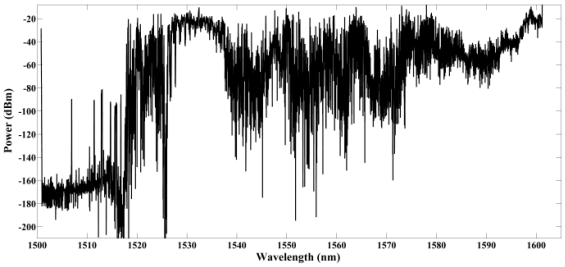
Power (dBm)
Wavelength (nm)

a)

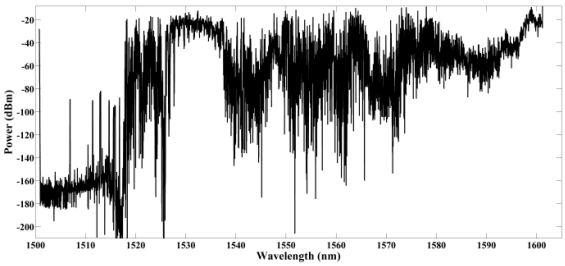
Power (dBm)
Wavelength (nm)

b)

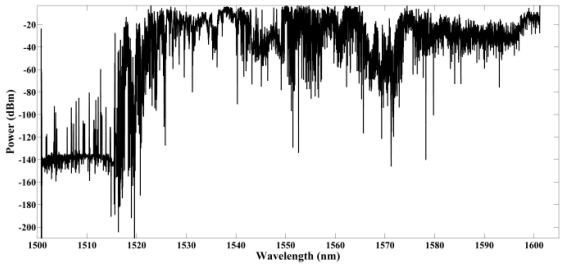
Power (dBm)
Wavelength (nm)

c)

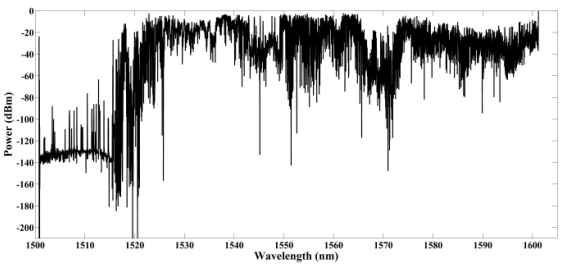
Power (dBm)
Wavelength (nm)

d)

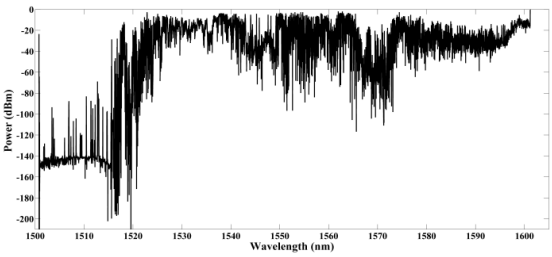
Power (dBm)
Wavelength (nm)

e)

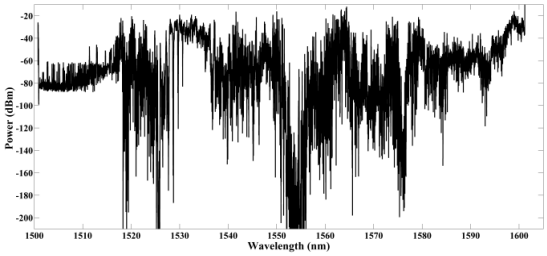
Power (dBm)
Wavelength (nm)

f)

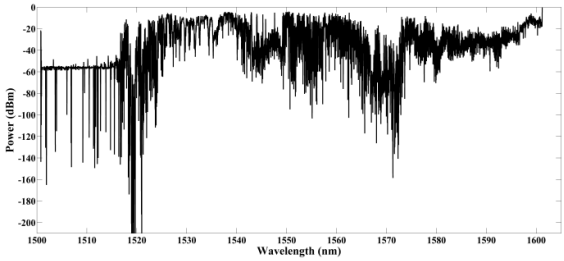
Power (dBm)
Wavelength (nm)

g)

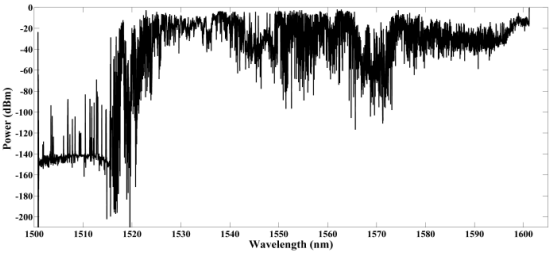
Power (dBm)
Wavelength (nm)

h)

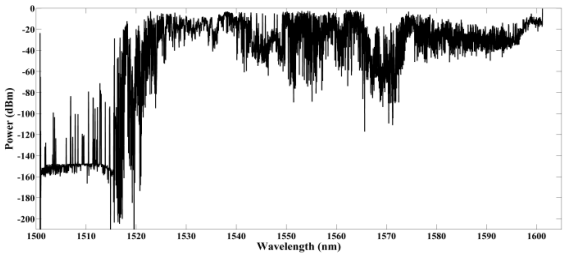

i)

Fig. 5.9. Prediction of femtosecond pulses spectrum, using a) Rule 27, b) Rule 29, c) Rule 46, d) Rule 58, e) Rule 78, f) Rule 90, g) Rule 110, h) Rule 172, and i) Rule 184.

Comparing the prediction results and the measurements at the SMF output, the tendency in the spectrum behavior is pretty close. In the picosecond pulse spectrum case, the good stability of spectrum after its propagation allows evidencing the optimal prediction of IFCA–MV which the analysis of its behavior based on evolution of rules is useful. On the other hand, the critical spectrum shapes variation for the femtosecond pulses source are evident and IFCA–MV carried out a prediction close. Nevertheless, the effect of attenuation in SMF is difficult to add in this kind of prediction but the changes of spectrum present in the experimental set–up are simulated with optimal approaching.

By means of the obtained predictions and the analysis of stability, the next step is the use of PS to improve the spectrum shape. By analyzing the picosecond pulses spectrum, the phase correction is the best option where it is done between 0 and 2π. The vector of phase is created through the original spectrum, the spectra obtained by IFCA–MV, and the spectrum at the SMF output. According to the resultant vector, the changes of phase are small (calculating root mean square error of phase, the phase error is 5.9048×10^{-18} rad) which the good stability predicted by IFCA–MV is verified although an EDFA is used to recover the power average lost due to the SMF attenuation. The above is achieved with the rule 184. To build–up the femtosecond pulse spectrum, the phase and attenuation vectors are required to obtain the best spectrum possible. In that case, the linear and non–linear phenomena and the SMF attenuation at 25 km affect the spectrum shape which an EDFA is used before the PS. The attenuation levels are normalized between 0 to 1 where the former is the highest and the latter is the smallest. By applying several changes of the attenuation and phase, it is difficult to obtain one reconstructed spectrum similar to the original spectrum. Considering the high impact of chromatic dispersion, nonlinear effects, the SMF attenuation, and the analysis of stability based on IFCA–MV, not all the femtosecond pulses spectrum can be recovered. This limitation is due to the difficult for obtaining the Gaussian shape and the low resolution of the PS. Calculating the root mean square error of spectrum, the power error is high, −8.337 dBm but by comparing with the spectrum illustrated in Fig. 5.7, with an error at −9.46087 dBm, the proposed methodology achieves to reduce an error at −11.2387 dBm. Despite of this result, the used femtosecond pulse source has disadvantages for optics communication applications. The above is carried out with rule 90 where is achieved the best result as possible.

In Fig. 5.10 and Fig. 5.11, the reconstructed spectra of both cases are illustrated.

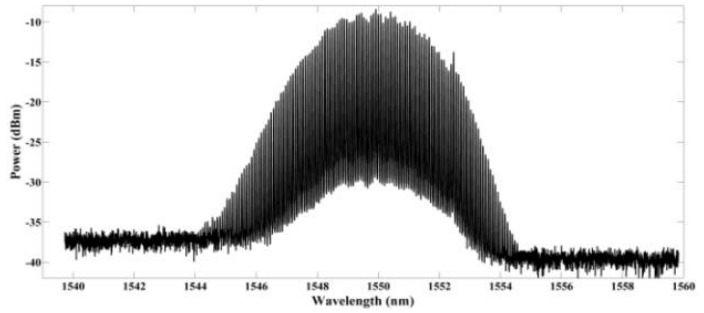

a)

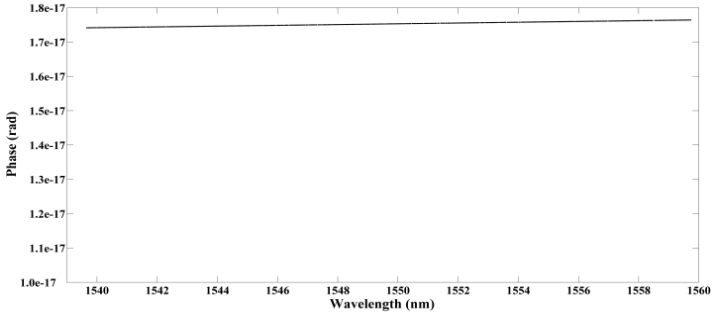

b)

Fig. 5.10. OFC spectrum and phase applied with PS for the picosecond pulsed laser: a) Improved spectrum of the picosecond pulses laser after its propagation at 25 km of SMF; b) changes of phase applied in the spectrum, using the pulse shaper.

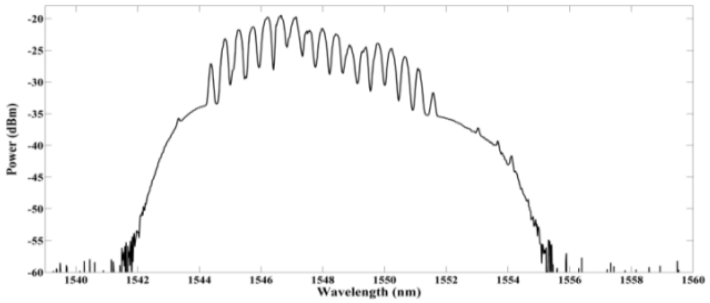

a)

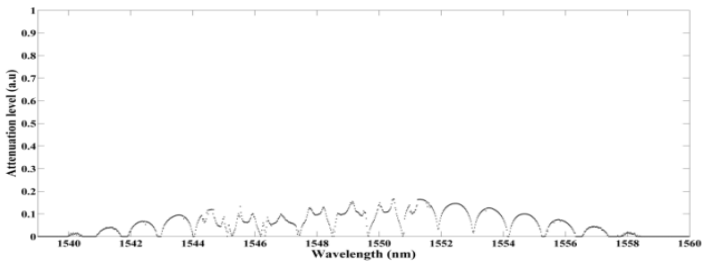

b)

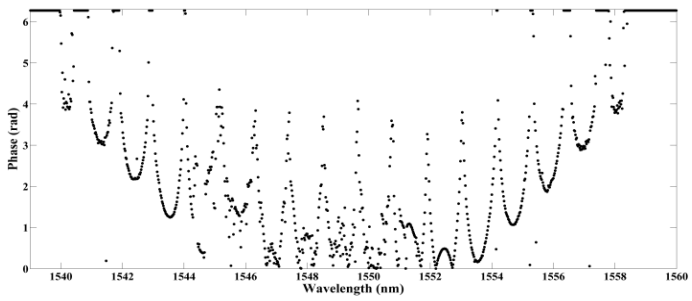

c)

Fig. 5.11. OFC spectrum and attenuation and phase applied with PS for the femtosecond pulsed laser: a) Spectrum reconstruction of the femtosecond pulsed laser after its propagation at 25 km of SMF; b) attenuation levels applied in the spectrum, using the pulse shaper; c) changes of phase applied in the spectrum, using the pulse shaper.

Considering the obtained results, the prediction can be analyzed through the periodicity in time and space. The periodicity allows giving information about behavior of any dynamical system and detecting possible eventualities in a future time. In addition, the periodicity shows the tendency in the behavior of system and stability with perturbation. To understand the periodicity information, the following conversion is used:

- ρ **= 0.** It refers to one physical system that is at rest.
- ρ **= 1.** It is a periodic behavior with stable tendency.
- ρ **= 1 (even or odd).** It is a periodic behavior in time and spatial (even *or* odd). This periodicity is a stable behavior.
- ρ **= 1 (heterogeneous).** It is a periodic behavior when a static dynamic is generated.
- ρ **= 2.** It refers to two periodic behaviors where system can be in a stability condition but can generate one change of its dynamic in a future time.
- ρ **= 2 (even or odd).** It is two periodic behaviors when dynamic contains even or odd periods in time and spatial.
- ρ **= 4.** It refers to four periodic behaviors where a stable dynamic can become chaotic or multiple dynamics changes in a system. This periodicity is called *strange attractors.*

Based on Fig. 5.8 and Fig. 5.9, the periodicity for the special group of rules for a set of $\gamma = \{0.1, 0.2, 0.3, 0.4, 0.5\}$ are summed–up in Table 5.1.

Table 5.1. Results of periodicity for the application I.

RULE	γ = 0.1	γ = 0.2	γ = 0.3	γ = 0.4	γ = 0.5
27	ρ = 2 (even & odd)	ρ = 2 (even & odd)	ρ = 2	ρ = 2 (even & odd)	ρ = 2 (even & odd)
29	ρ = 2 (even)	ρ = 2 (even)	ρ = 2 (even)	ρ = 2 (even)	ρ = 2 (even)
46	ρ = 2 (even)	ρ = 2 (even)	ρ = 2 (even)	ρ = 2	ρ = 2 (even)
58	ρ = 2 (even)	ρ = 2 (even)	ρ = 2 (even)	ρ = 2 (even)	ρ = 2 (even)
78	ρ = 1	ρ = 1 (even)	ρ = 1 (even)	ρ = 1 (even)	ρ = 1 (even)
90	ρ = 2	ρ = 1	ρ = 1	ρ = 1	ρ = 2
110	ρ = 2 (even)	ρ = 2 (even)	ρ = 1	ρ = 1	ρ = 1
172	ρ = 4	ρ = 4	ρ = 2 (even)	ρ = 1 (heterogeneous)	ρ = 1
184	ρ = 4	ρ = 4	ρ = 4	ρ = 2	ρ = 2 (even)

Rules 29 and 58 show the same periodicity (ρ = 2 or ρ = 2 even) but the rule 27 generates an inverse periodicity with respect to them. These variations indicate two behaviors: rules 29 and 58 identify the presence of one linear phenomenon and the rule 27 detects one non–linear phenomenon. Therefore, the IFCA−MV is capable of finding difference between one linear phenomenon and one non−linear phenomenon.

On the other hand, the rule 78 detected ρ = 1 and ρ = 1 (even) along γ which it represents the possible conditions of stability for a picosecond pulse. Comparing rules 90 (γ = {0.3, 0.4}) and 110 (γ = {0.3, 0.4}), these rules detected the same periodicity than rule 78. However, if γ = {0.1, 0.2, 0.5} then the behavior of femtosecond pulse spectrum may change. Based on this observation, rules 90 and 110 can identify critical variations of peak power and phase for both pulsed sources (i.e., ρ = 1, ρ = 2 and ρ = 2 (even)).

The rule 172 presented an interesting evolution of the periodicity when ρ = 1 (heterogeneous), ρ = 2 (even), ρ = 4, and ρ = 1 (it is the same case for the rule 110 with γ = 0.5). This rule can show the likely presence of linear and non–linear phenomena for the femtosecond pulse spectrum.

The rule 184 found relevant behaviors of spectrum when ρ = 4, ρ = 2, and ρ = 2 (even). This rule was capable of detecting the possible interaction between linear phenomenon and non−linear phenomenon. Analyzing ρ = 4 (γ = 0.1, 0.2, and 0.3), the rule can predict the possibility of one chaotic situation in the interaction of both phenomena. Such case could occur in the spectrum of femtosecond pulsed source. Comparing rules 184 (ρ = 4) and 172 (ρ = 4), the latter identified possible chaotic situation whether γ = 0.1 and 0.2.

Relating the results for the special group of rules, IFCA–MV can predict normal and critical behaviors for spectra of picosecond and femtosecond pulsed sources after their propagation in SMF.

5.4 Application II: Correction of Flatness of Combs Lines Spectrum Generated by Cascaded MZMs

The second application is the flatness correction of one spectrum generated by a cascaded configuration of MZMs after its propagation in SMF. Unlike of first application, this experiment required several iterations of IFCA–MV until to obtain the desired spectrum. Each iteration updates attenuation and phase vectors to be sent to PS. When the PS receives the new data, the

reconstructed spectrum is observed in OSA. If one change is needed, the data vectors are modified through the comparison among original spectrum, the obtained spectrum in OSA and one reference spectrum (it is the desire spectrum). During the updating, the vectors size must be the same (mentioned in section 5.3). Using the proposed method, the goal is to verify when the flatness is stable in a future time. For the experiment, the special group of rules is used.

The experiment is explained below: a CW Laser fixed at 1550 nm (Agilent Technologies, 438A Power Meter – includes CW source) is connected to two MZMs (JDS Uniphase, 12.3G: Xcut LN Intensity modulator, insertion loss < 5 dB, including polarizer). The output of the cascaded MZMs is connected to one FPC (PLC−003, General Photonics Corporation) to maintain the polarization states at +45°. The FPC output is linked to one EDFA amplifier (Pritel, SPFA 24) which increases the average power before the spectrum propagation in one SMF at 25 km (SMF−28E Corning). The SMF output is linked to other FPC to maintain the linear polarization. At the FPC output, one PS (Wave Shaper 1000s, Finisar, C–band) is used to reduce the positive chromatic dispersion and to improve the flatness of comb lines spectrum. To correct the flatness, the proposed approach is applied but the wavelengths location with one comb line is required. The above allows correcting the peak power and phase in the points of interest. For the experiment, two spectra are necessaries: the comb lines spectrum after the EDFA and the comb lines spectrum at the second FPC output (after SMF). The general scheme is shown in Fig. 5.12.

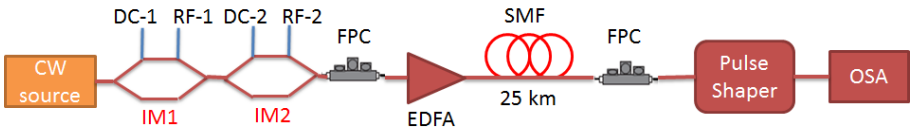

Fig. 5.12. Experimental set–up of cascaded MZMs.

The experiment was configured with 3 V (IM1) and 3.28 V (IM2), using two DC sources (BK precision). RF sources (HMC–T2100, Hittite) were adjusted with 21 dBm (IM1) and 23 dBm (IM2). RF1 and RF2 were fixed in 20 GHz (IM1) and 6 GHz (IM2). The average power for CW source is 5 mW (central wavelength = 1550 nm) and the pumping current is adjusted to 192 mA. The configured values allowed obtaining the best combs lines spectrum as possible with 9 combs lines in a span of 0.5 nm and one separation of 0.046 nm among comb lines. In Fig. 5.13, the comb lines spectrum generated for MZMs configuration is shown.

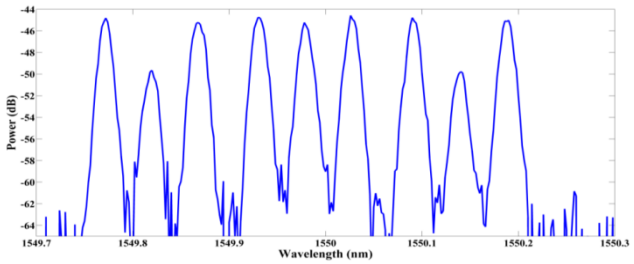

Fig. 5.13. Comb lines spectrum at the MZMs output.

Due to the insertion loss of MZMs, one EDFA amplifies the average power of combs lines spectrum before its propagation in SMF. In addition, the FPC is connected before SMF to guarantee

a linear polarization and stable power. The spectrum at the SMF input is illustrated in Fig. 5.14. In Fig. 5.15, the combs lines spectrum at the SMF output is shown. In that case, the influence of normal chromatic dispersion and the possible non–linear phenomena are detected.

According to [YOU09], GVD and SPM are the most influent phenomena in the propagation of optical signal in SMF. Considering the above, the proposed method must predict the effects in combs lines spectrum after the flatness correction, guaranteeing a good stability. Using the spectrum data (Fig. 5.14 and Fig. 5.15), rules 27, 29, 46, 58, 78, 90, 110, 172, and 184 were used in the experiment. In that case, the main goal of experiment is to identify the set of rules or at least one rule which the flatness correction is stable, In addition, one comb lines spectrum as reference is generated through the spectrum data (Fig. 5.14) where it is the desire spectrum at the PS output (see Fig. 5.16).

By using all special groups of rules, several comb lines spectra are obtained at the PS output (see Fig. 5.17).

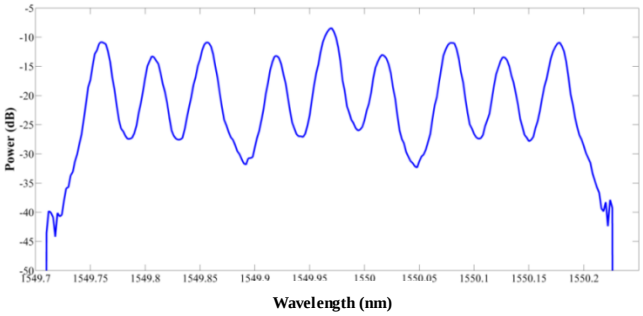

Fig. 5.14. Comb lines spectrum at the EDFA output.

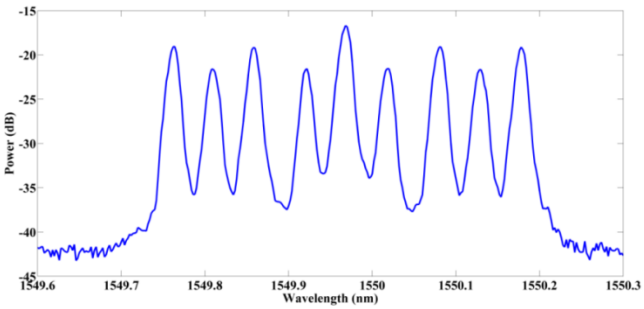

Fig. 5.15. Comb lines spectrum at the SMF output.

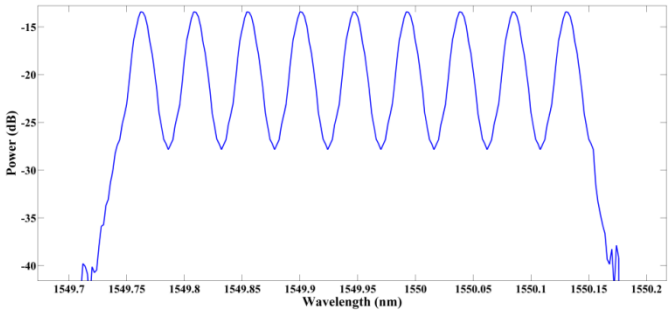

Fig. 5.16. Comb lines spectrum as point of reference.

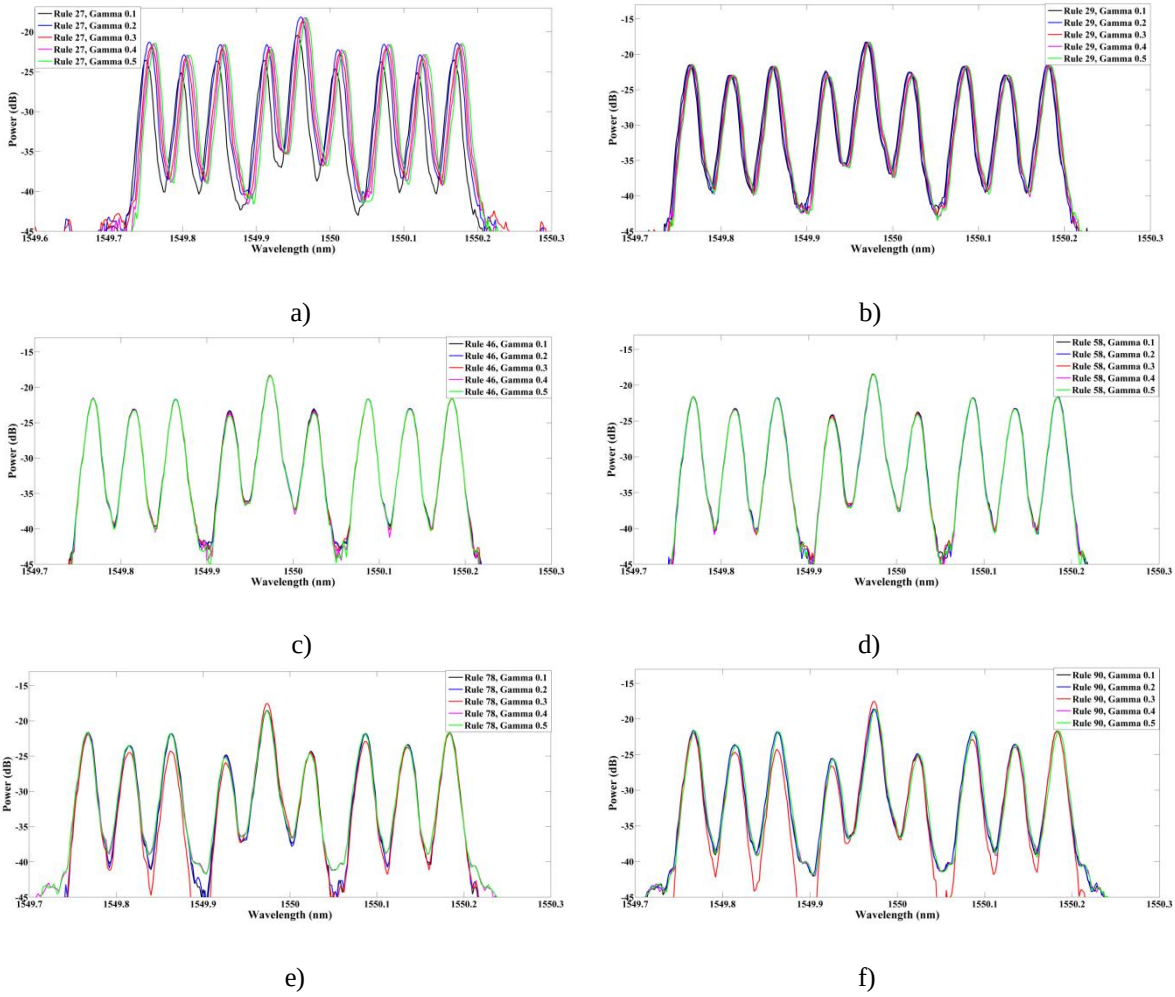

a) b)

c) d)

e) f)

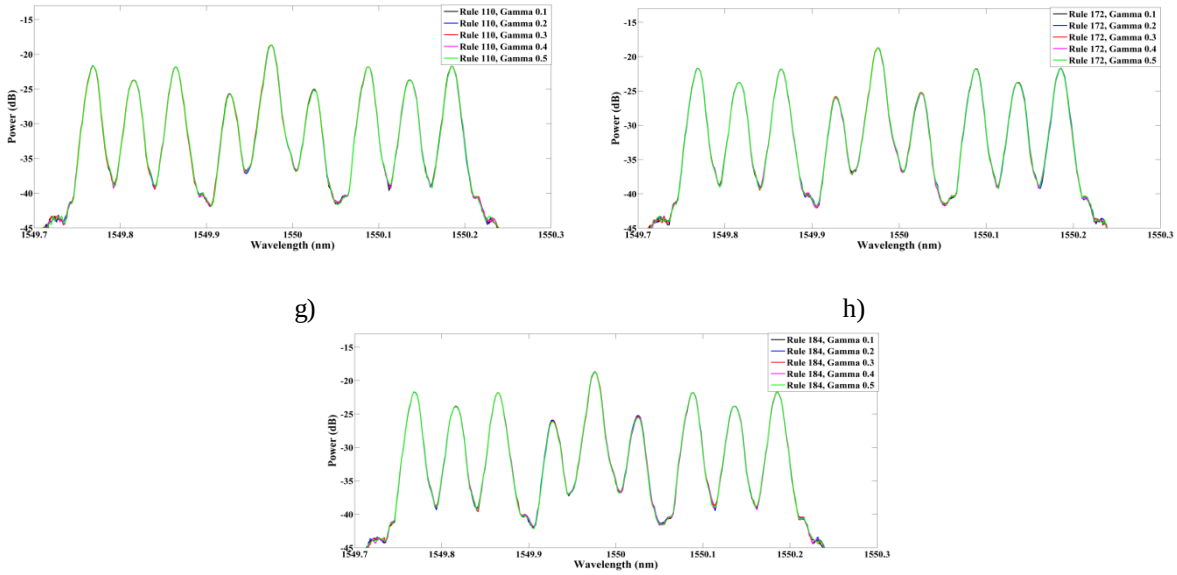

g) h)

i)

Fig. 5.17. Results of comb lines spectra using the proposed methodology for: a) rule 27, b) rule 29, c) rule 46, d) rule 58, e) rule 78, f) rule 90, g) rule 110, h) rule 172, and i) rule 184.

The results of comb lines spectra show an acceptable flatness but around 4 iterations are required in the proposed method. By analyzing of results, rules 27, 29, 78 and 90 predicted several changes of phase and peak power in the comb lines. The remaining rules predicted a stable spectrum. The comb line with the highest peak power (1549.968 nm, –16.69 dBm) is difficult to reduce due to that the emission current of CW laser generates such peak power. To reduce the power of this comb line, a strategy is implemented. Considering the attenuation vectors for each rule, the calculation of attenuation average is required to obtain the best flatness as possible. The phase vector is calculated through the change of spectral phase in each comb line and it is compared with the original spectrum. For this experiment, the *rule 27* generated the best result in the correction process. The average power of comb lines spectrum is little reduced but the spectrum shape is conserved, as shown in Fig. 5.18a. Comparing Fig. 5.15 and Fig. 5.18, the attenuation average level is adjusted in 24.1036 dBm and the phase correction is fixed in 6.23 rad. The vectors of phase and attenuation are visualized in Fig. 5.18b and Fig. 5.18c.

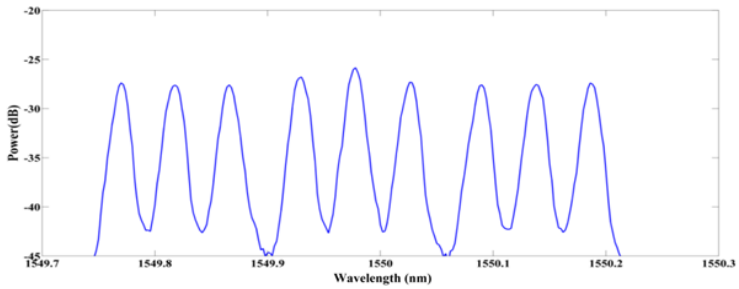

a)

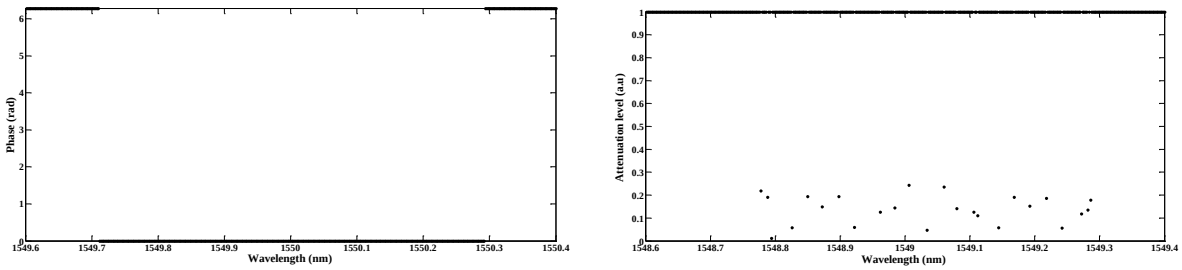

b) c)

Fig. 5.18. Comb lines improved with rule 27: a) Combs lines spectrum improved with the attenuation average vector and the vector of phase for rule 27, b) Vector of phase for rule 27, and c) Vector of attenuation for rule 27 (Normalized units).

Based on the results obtained in Fig. 5.17, the analysis of periodicity is explained below. Like in section 5.3, the stability of spectrum with perturbations is analyzed in time and space. Rules 27 and 29 detected changes of phase may become critic in a future time. This observation generates the same periodicity found in Table 5.1 with $\rho = 2$ or $\rho = 2$ (even) for rule 27 and $\rho = 2$ (even) for rule 29. Rules 46, 58, 110, 172, and 184 predicted an optimal stability of spectrum in a future time. In that case, $\rho = 1$ and $\rho = 1$ (heterogeneous) indicate a stable behavior in the combs lines spectrum. Rules 78 and 90 identified changes of intensity with $\rho = 1$, $\rho = 2$ and $\rho = 2$ (even). The above indicates one stable spectrum may vary its behavior in a future time, modifying the spectral shape. Such case could be generated by the interaction of GVD and SPM whether average power of CW source and EDFA gain increase (the non–linear length of SMF would become minor than the effective length). *Other possibility is the bias drifting in MZMs which can change peak power of comb lines,* explained by [SHA14].

The analysis of periodicity is summed–up in Table 5.2.

Table 5.2. Results of periodicity for the application II.

RULE	**γ = 0.1**	**γ = 0.2**	**γ = 0.3**	**γ = 0.4**	**γ = 0.5**
27	$\rho = 2$ (even & odd)	$\rho = 2$ (even & odd)	$\rho = 2$	$\rho = 2$ (even & odd)	$\rho = 2$ (even & odd)
29	$\rho = 2$ (even)	$\rho = 2$ (even)	$\rho = 2$ (even)	$\rho = 2$ (even)	$\rho = 2$ (even)
46	$\rho = 1$	$\rho = 1$	$\rho = 1$	$\rho = 1$	$\rho = 1$
58	$\rho = 1$	$\rho = 1$	$\rho = 1$	$\rho = 1$	$\rho = 1$
78	$\rho = 1$	$\rho = 1$	$\rho = 1$	$\rho = 2$	$\rho = 2$ (even)
90	$\rho = 2$	$\rho = 1$	$\rho = 1$	$\rho = 1$	$\rho = 2$
110	$\rho = 1$	$\rho = 1$	$\rho = 1$	$\rho = 1$	$\rho = 1$
172	$\rho = 1$	$\rho = 1$	$\rho = 1$ (heterogeneous)	$\rho = 1$ (heterogeneous)	$\rho = 1$
184	$\rho = 1$	$\rho = 1$	$\rho = 1$	$\rho = 1$	$\rho = 1$

Through the analysis of rules, the proposed methodology is able to predict the flatness behavior when a critical variation in power and/or phase is present. It is important to mention that rules 27, 29, 78, and 90 allowed finding the most relevant changes of comb lines. Such rules predicted phase and power variations after an initial stability condition of spectrum.

The FCA theory mentions a chaotic behavior with the rule 46 [BET12]. However, if a good stability of physical variables is defined, the possibility of chaos is null. Thus, the stability of comb lines spectrum could be guaranteed.

5.5 Application III: Prediction of Combs Lines Spectra Behaviors Generated by Microresonators Ring

The third experimental set–up is the analysis of noise intensity and stability of combs lines spectrum produced by a microresonator ring (a complete explanation was shown in section 2.2.3). Using the same strategy mentioned in section 5.3 and 5.4, a number of iterations are applied to observe the possible changes of noise intensity and peak power in a future time, identifying the frequencies where the noise level can rise. Unlike the above experiments, two predictions are obtained: the combs lines spectrum and intensity levels. To obtain the latter, a PIN photodiode is used to convert one optical signal in one electrical signal. Considering the analysis of periodicity, the detection of possible abnormal behaviors will be obtained through special group of rules with $\rho = 4$, where the presence of chaos can occur in a future time.

The experimental set–up is described below: a CW tunable laser (TLB–6728, Newport) was connected to an EDFA (SPFA33, Pritel) to amplify the main component of high power (located in 1550 nm). To maintain a linear polarization, one FPC (PLC–003, General Photonics Corporation) was used. The above appointment allows controlling fluctuations in the flatness of combs lines spectrum. Others points of experiment are the external causes such as mechanical vibrations, fluorescent light, and perturbations as well as internal causes, e.g. the increase of temperature when microresonator ring is in resonance state. Such causes can modify the peak power of comb lines and the spectral shape can vary. To avoid a deformed spectral, the experiment must be carried out in dark space with environment temperature and minimum vibration of desk. However, a high increase of average power of CW tunable laser can generate an increase of temperature inside of ring.

Continuing with the explanation, the FPC output is connected with an EDFA. The EDFA is connected towards the microresonator ring where the comb lines spectrum is generated. According to the central wavelength shift in CW tunable laser, the flatness changes and the peak power of some comb lines decreases. The above happens for the resonance wavelength in the microresonator ring due to that the tuning is difficult of adjusting. Therefore, the changes of peak power can become critic and some comb lines can lose, reducing its spectral width. To observe the impact of flatness variation in spectrum, one strategy is to obtain the electrical spectrum through a PIN photodiode (DET01CFC, Thorlabs). Using one spectrum analyzer, the electrical spectrum shows the behavior of noise with respect to the changes of central wavelength (influenced by linewidth of CW tunable laser). The noise measurement is carried out by a beam divider, where 95% of signal is sent to OSA and 5% of signal is sent to PIN photodector. Others factors like the microresonator size or thermic conditions can influence in the behavior of noise which they will be taken into account in analysis.

In Fig. 5.19, a general scheme of experiment is illustrated.

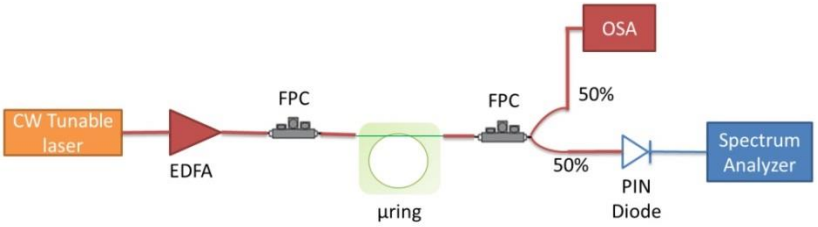

Fig. 5.19. Experimental set–up for the microresonator ring.

In order to generate a spectra database, several microresonator diameters were considered: 0.6, 0.8, 7, 9, 26, 45, 55, 62, 63, 72, 83, 85, 93, 98, 123, 288, and 395 µm. The CW tunable laser was tuned between 1532 nm to 1558 nm and the average power was adjusted between 1 mW to 8 mW. The pump current for the EDFA was fixed in 200 mA. During the experimental tests, the tuning of microresonator is carried out below: a microresonator (with a fixed size) is selected and the tuning is configured each 0.2 nm (1532 nm − 1558 nm), by using a CW tunable laser. When the best flatness is obtained during the tuning process, then the spectrum is stored. When the best comb lines spectrum is achieved, the information about the central wavelength, average power and pump current of EDFA are noted.

In Fig. 5.20, the historical data of the best comb lines spectra are shown below.

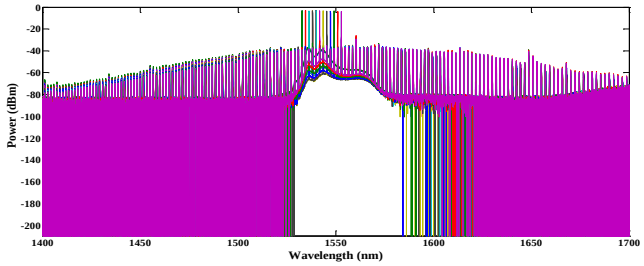

Fig. 5.20. Optical combs lines spectra generated by microresonators ring.

In Fig. 5.21, the noise intensity data are shown below:

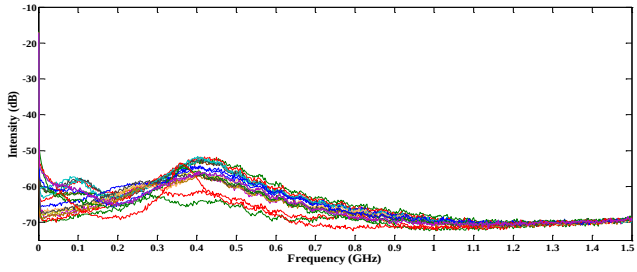

Fig. 5.21. Noise intensity of the generated comb lines spectra.

Around of 19 optical spectra (15001 samples) and 19 noise signals (601 samples) were stored as historical data. By means of historical data, two types of prediction are considered to analyze the impact of noise intensity:

- Prediction of abnormal behavior in the comb lines spectra, detecting range of frequency with the highest noise intensity in a future time.
- Prediction of the most stable and the most unstable comb lines spectra in a future time.

Based on the methodology explained in section 5.2, the application of fuzzy clustering method and its validation index were used. In that case, the LAMDA method is selected, where the results are shown in Annex A.8. According to the results, the Min–Max connectivity with exigency value = 0.7 and a MAD fuzzy binomial allowed finding the best classification for the comb lines spectra. The optimal parameters in the intensity noise data were: Min–Max connectivity, exigency value = 0.9, and a kind of MAD Gaussian. The membership degrees representations for both cases are shown in Fig. 5.22.

By extracting the vector of classes (applying the strategy mentioned in section 3.5, 3.6, and 3.7), several behavior were identified (see Fig. 5.23). Comparing the classes' representation (Fig. 5.23a) with respect to Fig. 5.21a, the class 26 is the most relevant due to that contains the main behavior of comb lines. In that case, the class 26 detected the comb lines with high peak power generated by the CW tunable laser (located in the tuned central wavelength).

In Fig. 5.21b and Fig. 5.23b, classes 4 and 5 represent the most critical variation of comb lines spectra where an increase of noise is possible. To verify such observation, the HIFEAN and HVS calculation were carried out, as shown in Annex A.9. HIFEAN results showed a better performance than HVS.

Taking into account the entropy results, the IFCA–MV is applied with 10 iterations (each iteration is equal one second of prediction time) in order to observe if the most relevant class(es) identify(es) for HIFEAN are stables or could lead towards chaotic environments. If the latter situation will be presented, it is possible to find the worst scenario of combs generation using microresonator ring where the laboratory conditions, possible vibrations, and changes of temperature when the device is in resonance with center wavelength of CW tunable laser can become critics. Other possible situation is the change of polarization states which can generate some power variations and to modify the quality of flatness. Despite FPC is used to guarantee the most possible linear polarization ever, not all polarization states can maintain stables in a real experiment of optics communications. In case of the best stability condition is detected with these mentioned possible situations, the optimal condition of combs generation could be found.

In Fig. 5.24 and Fig. 5.25, the prediction results are illustrated.

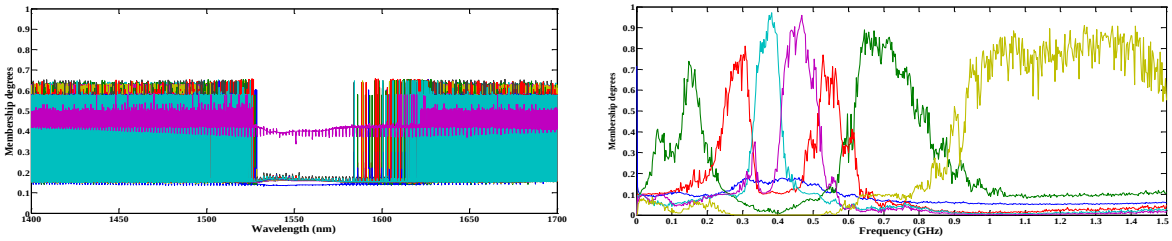

a) b)

Fig. 5.22. Membership degrees representation of microresonator ring data, for: a) comb lines spectra and b) noise intensity.

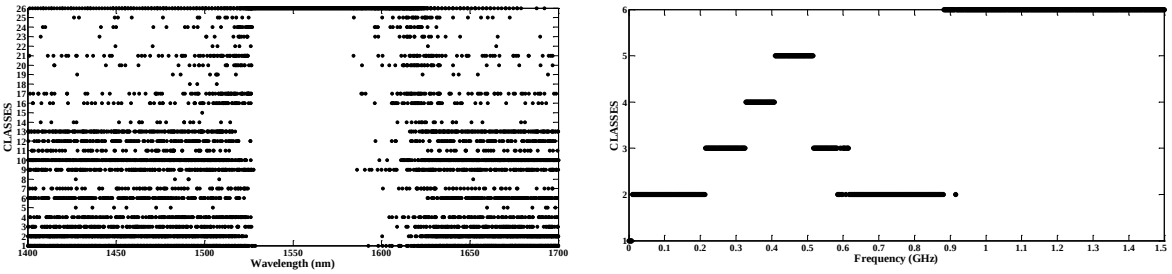

a) b)

Fig. 5.23. Classification of the microresonator ring data, for: a) combs lines spectra and b) noise intensities.

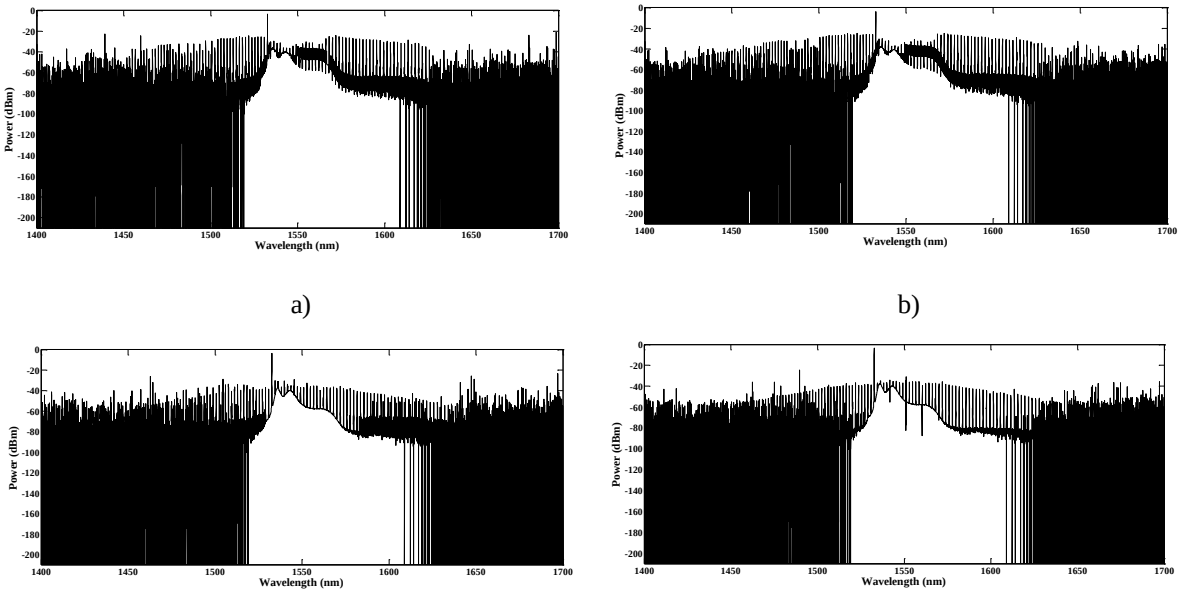

a) b)

c) d)

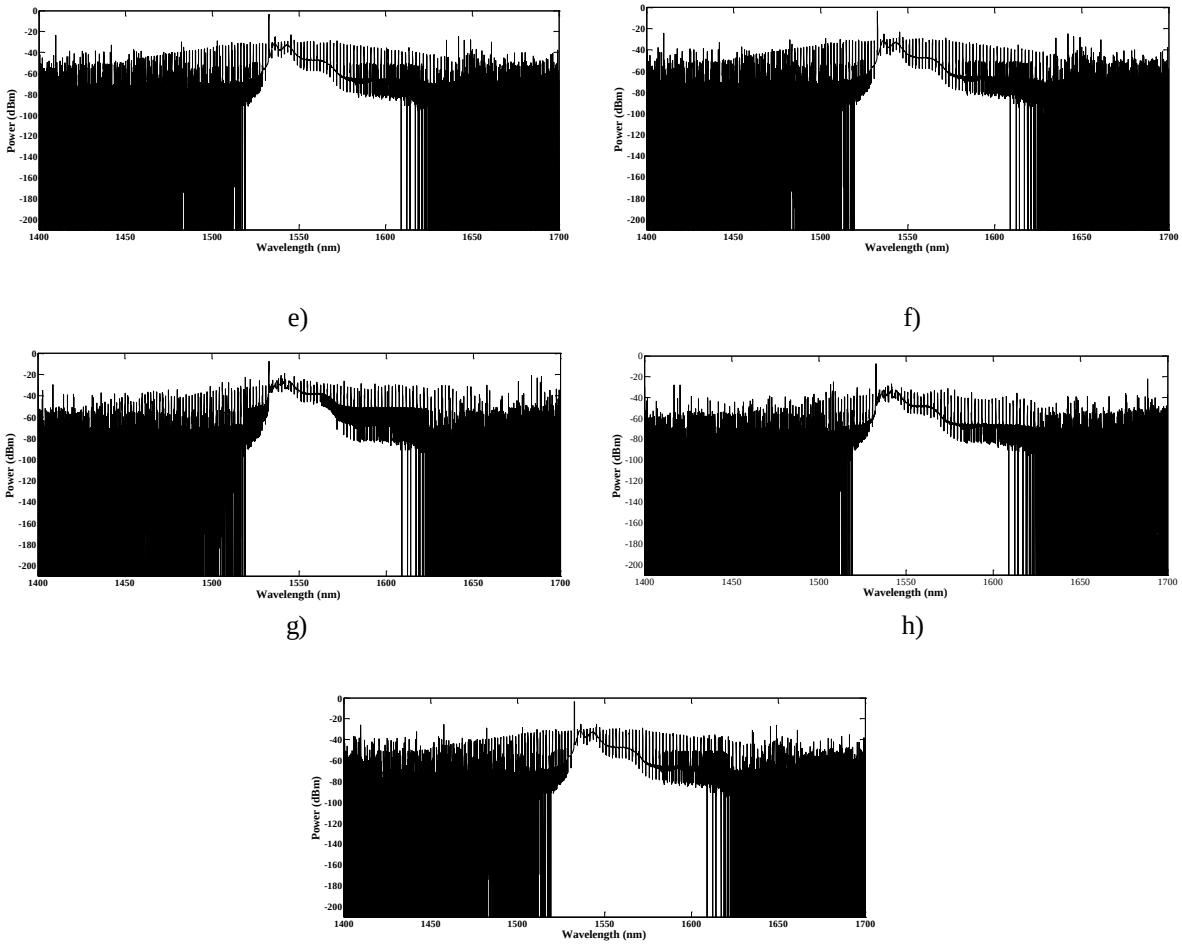

Fig. 5.24. Prediction of the combs lines spectrum (microresonator ring), for: a) rule 27, b) rule 29, c) rule 46, d) rule 58, e) rule 78, f) rule 90, g) rule 110, h) rule 172, and i) rule 184.

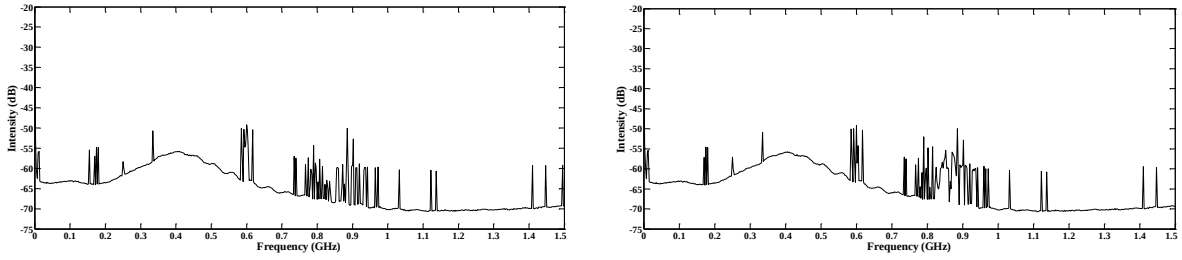

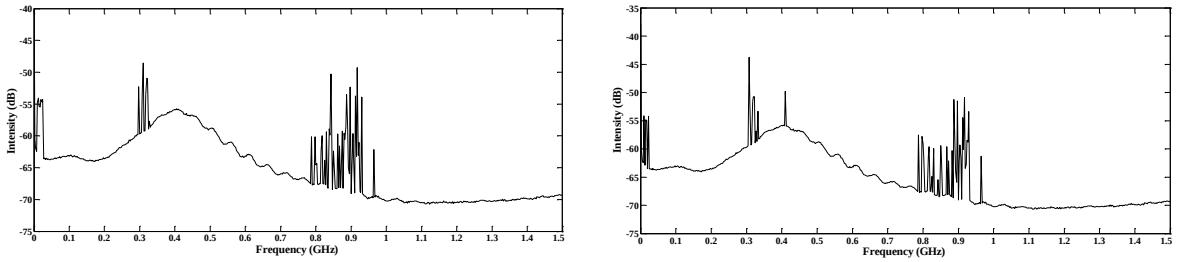

c)

d)

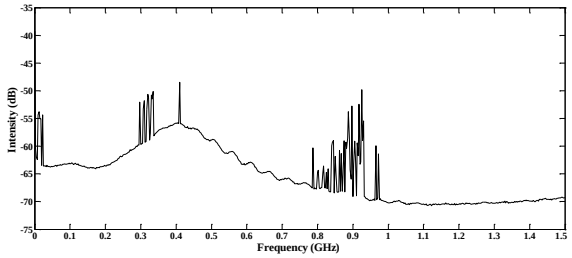

e)

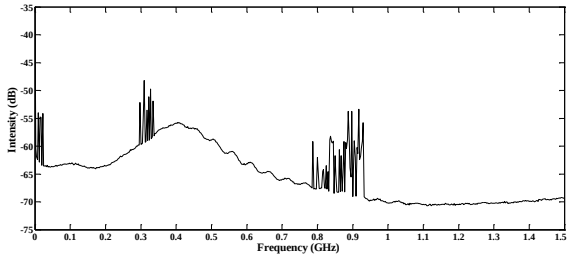

f)

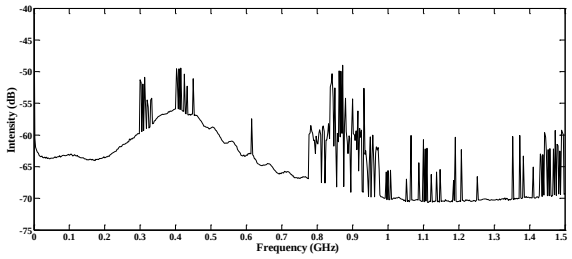

g)

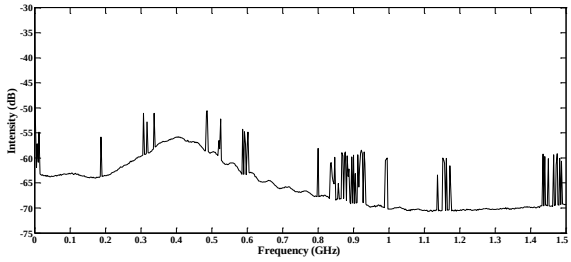

h)

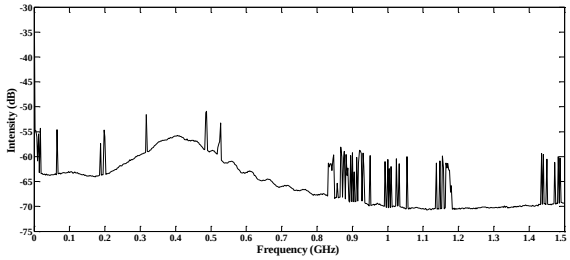

i)

Fig. 5.25. Prediction of the noise intensity (microresonator ring), for: a) rule 27, b) rule 29, c) rule 46, d) rule 58, e) rule 78, f) rule 90, g) rule 110, h) rule 172, and i) rule 184.

Analyzing Fig. 5.24, the comb lines spectrum can become unstable due to external events like temperature variation or mechanical vibrations. In Fig, 5.24a and Fig 5.24b, the closest comb lines to 1550 nm can attenuate and to affect the flatness. Others ranges of wavelength in spectrum can generate changes of peak power and a reduction of spectral width. Among Fig. 5.24c to Fig. 5.24h,

high fluctuations of peak power affect the performance of comb generation. The above could indicate chaos in the comb lines spectrum. Some mechanisms such as heat, polarization or mechanical stability control methods can improve the comb generation in the microresonator ring but they are not robust, the chaos can be present. This kind of spectrum could be unstable with respect to critical environment conditions. Due to this possible situation, it is required to identify the most relevant rules that allow identifying critical condition of spectrum. Using the prediction of the noise intensity, it is possible to detect the influence of spectral dynamic with respect to electrical spectrum noise. Since a PIN detector is used to obtain the electrical spectrum, the changes of thermal noise of device can be an alternative in the analysis of comb lines generation.

In Fig. 5.25a and Fig. 5.25b, the prediction detected several peaks at different ranges of frequency. The range between 600 MHz to 1 GHz generated the most critical changes of noise intensity. Peaks close to 600 MHz indicate the biggest noise intensities and this behavior is related with comb lines close to 1550 nm (indicated in Fig. 5.24a and Fig. 5.24b). An explanation is a critical variation of any external variable which the noise level is increased. Thus, comb lines close to 1550 nm will be attenuated due to the OSNR (Optical Signal Noise Ratio) decreases and the quality of flatness can be deteriorated. The increase of thermal noise inside PIN detector is an "intrinsic consequence" of the performance of microresonator ring which any external variable is not controlled. In Fig. 5.25c – Fig. 5.25f, the range between 800 MHz to 1 GHz shows high noise intensity but the highest noise intensity is observed close to 300 MHz. The above explains the flatness fluctuations viewed in Fig. 5.24c – Fig. 5.24f, where the increase of noise can attenuate the peak power of some comb lines. A similar situation was observed in Fig. 5.25h and Fig. 5.25i, where the range between 0 to 600 MHz shows high noise intensity. An exceptional behavior of noise was identified in Fig 5.25g. In that case, the noise peaks are higher than in others noise peaks observed in the above predictions. If this condition becomes critic, i.e. the noise level is increased in a future time, a critical variation of flatness could happen. Scrutinizing Fig. 5.24g, the flatness is conserved between 1550 nm to1600 nm but its quality is altered between 1400 nm to 1500 nm. Comparing this observation with Fig. 5.24i for the same range, the latter predicts better stability of flatness. Therefore, the rule 110 showed the worst situation of combs lines generation with microresonator ring.

To complete the last interpretation of combs lines spectrum prediction and the influence of noise, the RMSE (Root Mean Square Error) is calculated between the predicted spectra and the historical data from Fig. 5.20. *The main goal is to detect the rule(s) with the highest variation of power and noise intensity, as well as the lowest variation of them*. The results are shown in Table 5.3 and Table 5.4.

Table 5.3. RMSE applied to the optical combs lines spectra generated by microresonator ring.

RULE	Spectrum 1 (dBm)	Spectrum 2 (dBm)	Spectrum 3 (dBm)	Spectrum 4 (dBm)	Spectrum 5 (dBm)
27	–32,4356	–26,4104	–20,7462	–20,8198	–20,7695
29	**–45,3946**	–25,842	–20,6409	–20,7093	–20,6642
46	**–42,6804**	–25,8413	–20,6441	–20,7095	–20,6641
58	–24,5554	–23,5669	–21,6897	–21,8022	–21,731
78	–35,228	–26,0375	–20,6471	–20,7177	–20,668
90	–35,2304	–26,0342	–20,6451	–20,7156	–20,666
110	–30,7247	–26,1771	–20,8363	–20,9103	–20,8585
172	–35,0255	–26,1264	–20,6428	–20,7132	–20,6637
184	–24,6257	–23,6706	–21,6671	–21,7821	–21,7193
RULE	**Spectrum 6 (dBm)**	**Spectrum 7 (dBm)**	**Spectrum 8 (dBm)**	**Spectrum 9 (dBm)**	**Spectrum 10 (dBm)**
27	–20,9645	–20,8556	–20,7984	–20,8162	–20,8845
29	–20,8496	–20,7454	–20,6917	–20,7094	–20,7744
46	–20,8495	–20,7453	–20,6916	–20,7106	–20,7745
58	–22,0425	–21,8646	–21,775	–21,8063	–21,9152
78	–20,8537	–20,7504	–20,6957	–20,7132	–20,7775
90	–20,8515	–20,7483	–20,6937	–20,7111	–20,7753
110	–21,062	–20,9481	–20,8886	–20,9074	–20,9787
172	–20,849	–20,7459	–20,6913	–20,7088	–20,7729
184	–22,0274	–21,8502	–21,7632	–21,8028	–21,9137
RULE	**Spectrum 11 (dBm)**	**Spectrum 12 (dBm)**	**Spectrum 13 (dBm)**	**Spectrum 14 (dBm)**	**Spectrum 15 (dBm)**
27	–20,6751	–20,9496	–20,8309	–21,0908	–21,0317
29	**–20,5728**	–20,836	–20,7235	–20,9711	–20,9141
46	**–20,5727**	–20,8378	–20,7234	–20,9701	–20,9142
58	–21,5854	–22,023	–21,8262	–22,2528	–22,1528
78	–20,5783	–20,8403	–20,7259	–20,9729	–20,9187
90	–20,5764	–20,8381	–20,7238	–20,9706	–20,9164
110	–20,7599	–21,0467	–20,9227	–21,1946	–21,1327
172	–20,5742	–20,8356	–20,7215	–20,968	–20,9139
184	–21,5816	–22,0369	–21,8029	–22,2219	–22,1302
RULE	**Spectrum 16 (dBm)**	**Spectrum 17 (dBm)**	**Spectrum 18 (dBm)**	**Spectrum 19 (dBm)**	**Average (dBm)**
27	–20,9339	–21,1855	–21,3186	–21,3186	–21,330
29	–20,8214	–21,0594	–21,1849	–21,1849	–21,225
46	–20,8213	–21,0593	–21,1851	–21,1851	–21,225
58	–21,9908	–22,4163	–22,6566	–22,6566	**–22,174**
78	–20,8239	–21,0634	–21,1881	–21,1881	–21,224
90	–20,8217	–21,0609	–21,1855	–21,1855	–21,222
110	–21,0304	–21,2941	–21,4343	–21,4343	**–21,412**
172	–20,8193	–21,0582	–21,1826	–21,1826	–21,221
184	–21,9604	–22,3786	–22,6138	–22,6138	–22,163

Table 5.4. RMSE applied to the noise intensities generated by microresonator ring.

RULE	Noise 1 (dB)	Noise 2 (dB)	Noise 3 (dB)	Noise 4 (dB)	Noise 5 (dB)
27	–32,0803	–32,0789	–32,0811	–32,0857	–32,0623
29	–31,1957	–31,1946	–31,1964	–31,2001	–31,1810
46	–31,1794	–31,1783	–31,1801	–31,1838	–31,1648
58	–32,0803	–32,0789	–32,0811	–32,0857	–32,0623
78	–31,1853	–31,1842	–31,1860	–31,1897	–31,1706
90	–31,1863	–31,1852	–31,1870	–31,1907	–31,1716
110	–31,1737	–31,1725	–31,1743	–31,1780	–31,1590
172	–31,3814	–31,3802	–31,3821	–31,3860	–31,3660
184	–31,3292	–31,3280	–31,3299	–31,3337	–31,3141
RULE	**Noise 6 (dB)**	**Noise 7 (dB)**	**Noise 8 (dB)**	**Noise 9 (dB)**	**Noise 10 (dB)**
27	**–32,0884**	–32,0876	–32,0684	–31,4371	–31,6176
29	–31,2023	–31,2017	–31,1860	–30,6642	–30,8146
46	–31,1860	–31,1854	–31,1697	–30,6497	–30,7997
58	**–32,0882**	–32,0877	–32,0684	–31,4371	–31,6176
78	–31,1919	–31,1913	–31,1756	–30,6549	–30,8051
90	–31,1929	–31,1923	–31,1766	–30,6558	–30,8060
110	–31,1802	–31,1796	–31,1640	**–30,6446**	–30,7944
172	–31,3883	–31,3877	–31,3712	–30,8280	–30,9844
184	–31,3360	–31,3354	–31,3192	–30,7821	–30,9368
RULE	**Noise 11 (dB)**	**Noise 12 (dB)**	**Noise 13 (dB)**	**Noise 14 (dB)**	**Noise 15 (dB)**
27	–32,0712	–31,7528	–31,8216	–31,8876	–31,9376
29	–31,1883	–30,9267	–30,9836	–31,0379	–31,0790
46	–31,1721	–30,9114	–30,9681	–31,0222	–31,0631
58	–32,0712	–31,7528	–31,8216	–31,8876	–31,9376
78	–31,1779	–30,9169	–30,9736	–31,0278	–31,0688
90	–31,1789	–30,9179	–30,9746	–31,0288	–31,0698
110	–31,1663	–30,9060	–30,9626	–31,0166	–31,0575
172	–31,3736	–31,1010	–31,1602	–31,2168	–31,2596
184	–31,3216	–31,0521	–31,1106	–31,1665	–31,2089
RULE	**Noise 16 (dB)**	**Noise 17 (dB)**	**Noise 18 (dB)**	**Noise 19 (dB)**	**Average (dB)**
27	–31,9901	–32,0212	–32,0347	–32,0347	–31,95621003
29	–31,1220	–31,1475	–31,1585	–31,1585	–31,09425617
46	–31,1060	–31,1314	–31,1424	–31,1424	–31,0783419
58	–31,9901	–32,0212	–32,0347	–32,0347	**–31,95621174**
78	–31,1118	–31,1372	–31,1482	–31,1482	–31,08405856
90	–31,1128	–31,1382	–31,1492	–31,1492	–31,08506071
110	–31,1003	–31,1256	–31,1367	–31,1367	**–31,07269316**
172	–31,3045	–31,3310	–31,3426	–31,3426	–31,27552829
184	–31,2532	–31,2795	–31,2909	–31,2909	–31,22460809

According to results from Table 5.3, the spectrum 1 and noise 1 show the lowest variations of power in comb lines and the lowest noise intensity. the former case shows that rules 29 and 46 predicted a stable condition of spectrum with RMSE values of −45.3946 dBm and −42.6804 dBm. This possible power fluctuation can be generated by the comb lines attenuation close at 1550 nm, observed in Fig. 5.24a and Fig. 5.24c. Despite of a possible stability of combs spectrum, a critical change of spectrum shape can occur in a future time. In the spectrum 11, the same rules detected the highest RMSE values, −20.5728 dBm and −20.5727 dBm. The above shows that the power fluctuations could increase in a future time. The most possible causes could be the influence of external physical variables which can affect the OFC generation. Calculating the RMSE average for all rules, the rules 58 and 110 present the lowest and the highest RMSE value, −22.174 dBm and

−21.412 dBm. These rules can provide the most generalized predictions for all analyzed spectra of microresonator ring. In the Table 5.4, the noise 6 shows the lowest RMSE values detected by rules 27 and 58, −32.0884 dB and −32.0882 dB. The noise 9 presents the highest RMSE values identified by rules 46 and 110, −30.6497 dB and −30.6446 dB. These results are showing critical changes in the microresonator dynamic with respect to thermal and external noises (laboratory environment where measurements were obtained). Therefore, the frequency offset and the normal dispersion can generate several changes of spectral phase (in section 5.7, the analysis of this observations will be explained). Calculating the RMSE average, rules 58 and 110 predict the lowest and the highest RMSE values, −31.9562 dBm and −31.0726 dBm, verifying a good performance of these rules in the task of prediction.

Like applications I and II, the analysis of periodicity for application III is used to verify the importance of rules 58 and 110 in the tasks of prediction, oriented to the microresonator ring behavior. In rules 27 and 29, the periodicity is $\rho = 2$ and $\rho = 2$ (even or odd), which the changes of flatness and noise are periodic in a future time. In that case, the spectrum behavior can become stable as long as the polarization is lineal and the external conditions will be constants. Similar observations were identified in rules 46, 78, 90, 172, and 184. Such rules indicated that the peak power of comb lines and noise levels can generate little fluctuations in a future time. The little fluctuations might tend to a chaotic disorder in spectrum. Despite that the above rules show little chaos, rules 58 and 110 predicted the opposite. In some values of γ, the noise level and spectrum behaviors are periodic but the periodicity changes to $\rho = 4$. This critic variation establishes the presence of chaos for both cases. Then, the spectrum could not maintain stable in any instant of time and the influence of noise may create critical fluctuations in flatness. *Based on the results of periodicity, rules 58 and 110 are selected.*

In Table 5.5, the analysis of periodicity is shown.

Table 5.5. Results of periodicity for the application III.

RULE	**$\gamma = 0.1$**	**$\gamma = 0.2$**	**$\gamma = 0.3$**	**$\gamma = 0.4$**	**$\gamma = 0.5$**
27	$\rho = 2$	$\rho = 2$	$\rho = 2$	$\rho = 2$	$\rho = 2$ (even & odd)
29	$\rho = 2$ (even)	$\rho = 2$ (even)	$\rho = 2$ (even)	$\rho = 2$ (even)	$\rho = 2$ (even)
46	$\rho = 2$ (even & odd)	$\rho = 2$ (even & odd)	$\rho = 2$ (even & odd)	$\rho = 2$ (even & odd)	$\rho = 2$
58	$\rho = 4$	$\rho = 4$	$\rho = 2$ (even)	$\rho = 2$ (even)	$\rho = 4$
78	$\rho = 1$	$\rho = 1$	$\rho = 2$	$\rho = 1$	$\rho = 1$
90	$\rho = 2$	$\rho = 2$	$\rho = 2$	$\rho = 2$	$\rho = 2$
110	$\rho = 1$	$\rho = 2$ (even)	$\rho = 2$ (even)	$\rho = 4$	$\rho = 4$
172	$\rho = 2$ (even)	$\rho = 2$ (even)	$\rho = 1$	$\rho = 1$	$\rho = 1$
184	$\rho = 1$	$\rho = 2$ (even & odd)	$\rho = 2$ (even& odd)	$\rho = 1$	$\rho = 1$

5.6 General Performance of Proposed Methodology

According to the results mentioned until now, the proposed methodology presented a good performance in the three real laboratory experiments. During the analysis of results, the stability of spectrum and its flatness were predicted by special group of rules. In each experiment, one rule or a specific set of rules allows improving the main characteristics of spectrum or predicting the stability

condition in a future time. Nevertheless, a general question is asked: What is the most dominant rule for real applications in optical communications based on the analyzed results for the three experiments? To find an answer, several analyses are carried out for each rule.

Initially, the computational cost is considered in the three laboratory experiments whose computations time are calculated for each parameter γ (ranging from 0.1 to 0.5). All experiments were made with a laptop Sony VAIO VPCSA, processor Intel Core i5–2410M CPU @ 2.30 GHz, RAM Memory 6 GB, Hard Disk 750 GB, Video card AMD RadeonI HD 6630M @ 1 GB, Operative system Windows 7, and Matlab 2011a^{TM}. In Table 5.6, the computational costs for the spectra of ultra–short and ultrafast pulses are shown. Identifying the relevant data, all rules with γ = 0.1 and γ = 0.5 present the highest and the lowest computation cost in real time for ultra–short pulses spectrum. By using the ultrafast pulses spectrum, γ = 0.1 and γ = 0.4 generate the lowest and the highest computation cost. Analyzing for each rule, the rule 184 gives the best efficiency *(saving 2.0466 s of computation time*) with respect to rule 27 when ultra–short pulses spectrum is applied. Nevertheless, the condition improves by the ultrafast pulses spectrum where *rule 184 saves 28.9316 s with respect to rule 58*. According to these observations, the rule 184 has an optimal behavior for both kinds of spectra and with the same number of samples (5025). In addition, the computational performance depends on the characteristics of data.

Table 5.6. Computational costs for application I.

Picosecond pulsed laser						
RULE	**γ = 0.1 (s)**	**γ = 0.2 (s)**	**γ = 0.3 (s)**	**γ = 0.4 (s)**	**γ = 0.5 (s)**	**Average (s)**
27	100,2573	88,1140	90,1431	88,6350	89,4880	**91,3274**
29	99,3735	87,4782	87,2490	88,0145	90,3347	90,4899
46	91,6834	90,4178	91,7655	88,9816	87,7158	90,1128
58	89,1140	88,3974	92,0406	88,8039	88,2851	89,3282
78	88,2028	88,3507	87,3094	97,8929	88,1590	89,9829
90	89,8676	95,5995	88,7177	93,0530	85,8541	90,6183
110	88,1139	89,9582	92,8818	88,6634	92,4513	90,4137
172	89,5006	90,1976	88,3895	91,2192	88,2823	89,5178
184	88,8758	88,2722	90,0849	88,6066	90,5647	**89,2808**
Average (s)	**91,6654**	89,6428	89,8423	90,4300	**89,0150**	-
Femtosecond pulsed laser						
RULE	**γ = 0.1 (s)**	**γ = 0.2 (s)**	**γ = 0.3 (s)**	**γ = 0.4 (s)**	**γ = 0.5 (s)**	**Average (s)**
27	152,9091	161,7353	159,2423	154,4374	152,7725	156,2193
29	146,7104	152,8252	177,3548	184,5881	180,7349	168,4427
46	166,3007	173,2300	164,4807	173,1368	200,0782	175,4453
58	210,2436	171,2758	167,7771	170,1791	169,3326	**177,7616**
78	163,8276	165,7837	160,8114	167,0992	163,8406	164,2725
90	158,1997	164,4141	164,1732	173,3548	159,3031	163,8890
110	151,5202	158,3384	168,5328	181,8995	155,7342	163,2050
172	146,8274	152,8705	150,2512	151,5841	149,4640	150,1994
184	143,8388	149,7602	149,6978	149,2516	151,6015	**148,8300**
Average (s)	**160,0419**	161,1370	162,4802	**167,2812**	164,7624	-

In Table 5.7, γ = 0.2 and γ = 0.3 showed the highest and the lowest computation cost for the cascaded MZM. For all rules, *the rule 27 presents a better computational performance than rule 46 where the former saves a computation time at 88.2609 s*. Recovering the analysis of results exposed in section 5.4, the rule 27 was the most appropriated choice to correct the flatness of comb lines spectrum. The above allowed corroborating the good throughput for the application II.

Table 5.7. Computational costs for application II.

IM−MZMs						
RULE	**γ = 0.1 (s)**	**γ = 0.2 (s)**	**γ = 0.3 (s)**	**γ = 0.4 (s)**	**γ = 0.5 (s)**	**Average (s)**
27	87,7588	92,7736	86,6451	84,5952	89,5316	**88,2609**
29	89,092	92,3214	86,6560	84,9951	88,3365	88,28044
46	145,5665	305,6970	145,6684	145,3532	157,1167	**179,8804**
58	159,3963	145,6073	149,3702	148,5098	154,9224	151,5612
78	160,4257	147,6259	148,0371	150,1810	157,8805	152,8300
90	162,5813	147,9225	149,7187	161,0594	153,1172	154,8798
110	152,7886	151,9128	150,0879	154,4602	160,5139	153,9527
172	84,3245	89,48558	82,3849	95,5168	91,6152	88,6654
184	89,8347	90,58761	88,5412	90,5447	93,5978	90,6212
Average (s)	130,5012	**140,4370**	**120,7899**	123,9128	127,4035	-

In Table 5.8, the value $\gamma = 0.1$ presents the lowest computational cost and the value $\gamma = 0.4$ has the highest computation cost for both cases analyzed in the microresonator ring. Independent of γ, the first case shows that the rule 46 is more efficient than the rule 184; the second case indicates otherwise. *Whilst the rule 184 allows saving 1.4853 s with respect to the rule 46* in the noise intensity case, the difference is increased for the comb lines spectra case where the *rule 46 saves 189.0485 s with respect to the rule 184.*

Table 5.8. Computational costs for application III.

Microresonator ring – OFC spectra						
RULE	**γ = 0.1 (s)**	**γ = 0.2 (s)**	**γ = 0.3 (s)**	**γ = 0.4 (s)**	**γ = 0.5 (s)**	**Average (s)**
27	210,0520	242,1512	267,5893	320,5958	282,4916	264,5759
29	232,7327	338,3043	256,2249	251,9891	248,3026	265,5107
46	248,2192	252,4136	255,0846	262,5474	249,6311	**253,5791**
58	247,7099	256,6338	266,6138	264,7319	266,0930	260,3564
78	255,7709	269,8252	266,6544	263,1832	313,9945	273,8856
90	312,0796	334,3602	336,8919	351,4637	346,7901	336,3171
110	332,1838	393,2726	362,6791	401,5690	370,1171	371,9643
172	416,7108	409,2464	473,7421	430,9204	466,1495	439,3538
184	404,8102	403,0902	453,1542	482,7760	469,2625	**442,6186**
Average (s)	**295,5854**	322,1441	326,5149	**336,6418**	334,7591	-
Microresonator ring – Noise intensities						
RULE	**γ = 0.1 (s)**	**γ = 0.2 (s)**	**γ = 0.3 (s)**	**γ = 0.4 (s)**	**γ = 0.5 (s)**	**Average (s)**
27	9,5893	11,1130	11,0475	10,7893	10,8487	10,6775
29	9,4333	10,6866	10,9443	10,9958	10,9255	10,5971
46	11,0336	10,6232	11,5207	11,4619	11,0313	**11,1341**
58	9,9020	10,2133	10,4106	10,1440	10,2620	10,1863
78	10,2536	9,8961	10,0621	10,6444	10,6293	10,2971
90	9,7116	10,2383	10,1352	10,2982	10,2975	10,1361
110	10,7371	10,3894	10,3705	11,0113	10,2598	10,5536
172	10,3523	10,0682	9,8154	10,2666	10,4279	10,1860
184	8,3839	10,0061	10,2881	9,5500	10,0159	**9,6488**
Average (s)	**9,9329**	10,3593	10,5104	**10,5735**	10,5219	-

Other analysis is a *statistical study* to find a set of rules that predict the stability and instability conditions of optical spectra. The above allows showing the maximum capacity of the proposed methodology for correcting the spectral shape or for recovering the phase and power level of comb lines. In Tables 5.9, 5.10, 5.11, 5.12, and 5.13, the calculation of correlation for three experiment results is shown. According to the analysis, the best correlations are obtained by different rule as well as the worst correlations.

For the picosecond and femtosecond pulse spectra, rules 172 and 184 have the maximum correlation values, predicting the best stability of spectrum. Rules 184 (Table 5.9) and 90 (Table 5.10) generated the lowest correlations which indicate critical behaviors of spectrum. The results of Table 5.9 show similar correlations for all rules, suggesting that *the changes of phase for picosecond pulse spectrum are little which the use of one rule with respect to other does not affect the performance of proposed methodology for reconstructing the original spectrum*. However, the wide differences of correlation among rules (Table 5.10) indicate that rules 90 and 184 are the best options to predict a possible stability and instability of spectrum.

Table 5.9. Analysis of correlation for picosecond pulse spectrum.

RULE	27	29	46	58	78	90	110	172	184
Correlation	0,74390	0,732984	0,733735	0,736091	0,732876	0,735632	0,739301	**0,746417**	**0,726107**

Table 5.10. Analysis of correlation for femtosecond pulse spectrum.

RULE	27	29	46	58	78	90	110	172	184
Correlation	0,72090	0,713967	0,741888	0,738305	0,745849	**0,133768**	0,450856	0,219968	**0,748584**

In the cascaded MZMs case, the rule 110 (Table 5.11) presents the best correlation, 0.9631, than rule 27 (Table 5.11). However, the rule 27 allowed optimizing the power of each comb line with respect to the original spectrum before its propagation in SMF. By adjusting the phase and attenuation levels with selected rule, a spectrum shift is produced with the PS. The above generates a change of location in the central wavelength but the spectral shape is conserved and the quality of flatness is increased. With others rules, *the capacity for optimizing the spectral shape was not efficient than rule 27 during the experimental tests due to that it is able to predict the most critical changes of phase*. Based on this explanation, the analysis of correlation for cascaded MZMs does not allow verifying the impact of rules to correct the power of comb lines.

Table 5.11. Analysis of correlation for comb lines spectra – cascaded MZMs

RULE	27	29	46	58	78	90	110	172	184
Correlation	**0,5414**	0,9257	0,8640	0,6855	0,7048	0,8567	**0,9631**	0,9542	0,9505

Observing the correlation of rules for the microresonator ring case, the rules 58 and 110 have the maximum and minimum correlation values in both cases exposed in Table 5.12 and 5.13. Comparing such observations with respect to Tables 5.3 and 5.4, the generalization of such rules is verified again.

Table 5.12. Analysis of correlation for optical comb lines spectra – microresonator ring.

RULE	Spectrum 1	Spectrum 2	Spectrum 3	Spectrum 4	Spectrum 5
27	0,953262	0,372838	0,368923	0,359179	0,349988
29	0,952321	0,3679	0,363285	0,355663	0,349861
46	0,953885	0,349467	0,335757	0,322515	0,284784
58	0,95193	0,37338	0,382797	0,369135	0,363157
78	0,944909	0,367374	0,346481	0,342024	0,310226
90	0,944777	0,366938	0,34625	0,34191	0,310101
110	0,951451	0,321852	0,32873	0,311392	0,292966
172	0,961271	0,353737	0,36242	0,348376	0,335596
184	0,944028	0,366164	0,345432	0,34047	0,310385
RULE	**Spectrum 6**	**Spectrum 7**	**Spectrum 8**	**Spectrum 9**	**Spectrum 10**
27	0,346726	0,330475	0,326138	0,322518	0,32536
29	0,344618	0,330517	0,32564	0,317909	0,322314
46	0,277087	0,299826	0,287006	0,284992	0,30431
58	0,359693	0,33598	0,328801	0,34677	0,328687
78	0,291919	0,321756	0,307965	0,302825	0,330547
90	0,292345	0,32197	0,307766	0,302592	0,33095
110	0,298144	0,308195	0,292102	0,277215	0,27782
172	0,333748	0,312601	0,304309	0,321697	0,310885
184	0,290673	0,320613	0,307597	0,305293	0,329304
RULE	**Spectrum 11**	**Spectrum 12**	**Spectrum 13**	**Spectrum 14**	**Spectrum 15**
27	0,350017	0,313342	0,299915	0,279784	0,322636
29	0,352334	0,312919	0,299213	0,275126	0,318969
46	0,330282	0,260487	0,269034	0,255778	0,278969
58	0,350239	0,325777	0,325476	0,321503	0,342474
78	0,348281	0,273447	0,283525	0,281191	0,294966
90	0,34806	0,271207	0,283799	0,281297	0,293747
110	0,313204	0,25838	0,259836	0,24996	0,281995
172	0,333858	0,308116	0,305603	0,299992	0,322243
184	0,346835	0,274325	0,283364	0,280797	0,296221
RULE	**Spectrum 16**	**Spectrum 17**	**Spectrum 18**	**Spectrum 19**	**Average**
27	0,305214	0,292286	0,3358	0,3358	0,362642181
29	0,30544	0,288054	0,332951	0,332951	0,360420323
46	0,262841	0,307373	0,300545	0,300545	0,329762335
58	0,318133	0,375134	0,351513	0,351513	**0,379057495**
78	0,271288	0,319786	0,318233	0,318233	0,346051322
90	0,271201	0,319061	0,318655	0,318655	0,345856868
110	0,272885	0,28373	0,288682	0,288682	**0,324064344**
172	0,292221	0,350607	0,323977	0,323977	0,358170153
184	0,27177	0,319763	0,318442	0,318442	0,345785179

Table 5.13. Analysis of correlation for noise intensities – microresonator ring.

RULE	Noise 1	Noise 2	Noise 3	Noise 4	Noise 5
27	0,856756	0,859543	0,850103	0,844051	0,827434
29	0,822447	0,826977	0,815979	0,804265	0,796688
46	0,872227	0,866067	0,860251	0,853876	0,825134
58	0,889411	0,882888	0,880836	0,872947	0,851188
78	0,879952	0,872086	0,869077	0,861828	0,839275
90	0,881495	0,874319	0,872393	0,865697	0,844798
110	0,746757	0,743824	0,743646	0,72793	0,729198
172	0,87787	0,874708	0,868705	0,863847	0,847858
184	0,868807	0,862132	0,857042	0,853672	0,832518
RULE	**Noise 6**	**Noise 7**	**Noise 8**	**Noise 9**	**Noise 10**
27	0,826808	0,844761	0,845537	0,744255	0,781398
29	0,79366	0,807397	0,811934	0,710514	0,748424
46	0,829397	0,859956	0,84467	0,715623	0,768761
58	0,854271	0,877824	0,867484	0,740524	0,792708
78	0,841888	0,866858	0,855106	0,726326	0,77982
90	0,846298	0,870632	0,860439	0,736187	0,78688
110	0,728348	0,730657	0,733209	0,636557	0,681969
172	0,848535	0,866153	0,856958	0,757079	0,795727
184	0,833879	0,857318	0,845638	0,742413	0,779634
RULE	**Noise 11**	**Noise 12**	**Noise 13**	**Noise 14**	**Noise 15**
27	0,840697	0,839525	0,82977	0,832977	0,839585
29	0,80136	0,807986	0,797332	0,796385	0,797618
46	0,860526	0,83039	0,821033	0,827681	0,853537
58	0,877133	0,854138	0,845499	0,851785	0,86741
78	0,866612	0,840093	0,832861	0,839855	0,85931
90	0,869059	0,846929	0,839039	0,844583	0,861464
110	0,72881	0,730705	0,732458	0,719373	0,71331
172	0,86284	0,851597	0,846116	0,849168	0,865059
184	0,856142	0,836349	0,827793	0,833544	0,857142
RULE	**Noise 16**	**Noise 17**	**Noise 18**	**Noise 19**	**Average**
27	0,8193	0,686674	0,813391	0,813391	0,820839776
29	0,771278	0,644922	0,768991	0,768991	0,783849708
46	0,834756	0,723997	0,837092	0,837092	0,827477083
58	0,847873	0,728978	0,847513	0,847513	**0,846206509**
78	0,843879	0,730811	0,840128	0,840128	0,836099566
90	0,842586	0,724652	0,840005	0,840005	0,839340075
110	0,683278	0,575557	0,675565	0,675565	**0,707195526**
172	0,852411	0,729407	0,845981	0,845981	0,842421121
184	0,849174	0,73399	0,842418	0,842418	0,832211873

To complete the statistical analysis, the calculation of ANOVA (Analysis of Variance) is applied. For all three experiments, two hypotheses are defined as:

$$H_0: \text{mean}_{rule\_27} = \text{mean}_{rule\_29} = \text{mean}_{rule\_46} = \text{mean}_{rule\_58} = \text{mean}_{rule\_78} = \text{mean}_{rule\_90} = \text{mean}_{rule\_110} = \text{mean}_{rule\_172} = \text{mean}_{rule\_184}$$

$$H_1: \text{at least one of the means is different.}$$

In Tables 5.14 and 5.15, the ANOVA analysis for the picosecond and femtosecond pulse spectra case is shown. For both cases, F > F–critic. The above indicates that all means of rules are not equal and the null hypothesis is rejected. If F ≈ F–critic, it is possible that some means for H_0 can be equal. Considering the standard deviation, the rule 172 (Table 5.14) has minor deviation than the rule 184 (Table 5.14). Comparing such rules with other rules, 110 and 46, the differences are little with values of 0.121 dBm and 0.006 dBm. The little difference is indicating a similar prediction and performance. Given this case, *the rule 184 presented the best throughput for improving the spectral phase of picosecond pulse spectrum after its propagation in SMF, as explained in section 5.3*.

Comparing the rule 184 with respect to rules 27, 29, 46, and 90, their differences in standard deviation are low and the performance might be similar.

Table 5.14. ANOVA – Picosecond pulses spectrum.

RULE	27	29	46	58	78	90	110	172	184
Average (dBm)	–13.91	–13.87	–14.315	–14.318	–14.415	–14.234	–14.581	–14.413	–14.067
Variance (dBm)	–21.922	–21.843	–21.970	–22.111	–22.14	–21.948	–22.163	–22.404	–21.982
Standard deviation (dBm)	–10.961	–10.921	–10.985	–11.055	–11.07	–10.974	–11.081	**–11.202**	**–10.991**
F and F–critic					2.382291 > 1.938869				
P–value					0.014583				

In Table 5.15, the rule 184 has minor deviation than the rule 90 with a wide difference at 4.97 dBm. The above is presented by F > F–critic, 3.357791 > 1.038861. For hence, two or more means can be larger than others means. Comparing rules 90 and 58, the difference is 0.27 dBm, pretty close than the differences between rules 90 and 78, 0.36 dBm, and rules 90 and 46, 0.6 dBm. Therefore, rules 46, 58, and 78 could have a similar performance than rule 90. Despite of these similarities, *rule 90 allows recovering part of the femtosecond pulse spectrum after its propagation in SMF, as shown in section 5.3.*

Table 5.15. ANOVA – Femtosecond pulses spectrum.

RULE	27	29	46	58	78	90	110	172	184
Average (dBm)	−26.43	−26.25	−15.63	−15.37	−15.31	−14.79	−17.04	−29.12	−29.92
Variance (dBm)	−31.64	−31.60	−23.15	−22.49	−22.67	−21.95	−25.33	−31.86	−31.88
Standard deviation (dBm)	−15.82	−15.80	−11.57	−11.24	−11.33	**−10.97**	−12.66	−15.93	**−15.94**
F and F–critic					3.357791 > 1.038861				
P–value					0				

Analyzing the results of Table 5.16, the rule 27 presents the lowest standard deviation and its difference with the rule 46 is 2.99 dBm. Since the standard deviation of rule 27 is widely differentiable with the rest of rules, it can have a great potential to predict relevant behaviors. In section 5.4, this rule allowed correcting the flatness and phase of spectrum after its propagation in SMF. By using the rule 46 in the experiment II, the performance was lower than rule 27, as verified in section 5.4. *Therefore, the rule 27 is considered as the best alternative for compensating the spectral shape generated by IMs − MZM.*

Table 5.16. ANOVA – Cascaded MZMs.

RULE	27	29	46	58	78	90	110	172	184
Average (dBm)	–29.49	–27.18	–27.23	–27.39	–27.56	–27.64	–27.55	–27.59	–27.60
Variance (dBm)	–57.76	–51.90	–51.79	–51.98	–52.10	–52.29	–52.35	–52.41	–52.42
Standard deviation (dBm)	**–28.88**	–25.95	**–25.89**	–25.99	–26.05	–26.14	–26.17	–26.20	–26.21
F and F–critic					2.3956 > 1.883				
P–value					0.014293				

In Table 5.17, means are similar (0.3365 < 1.9384). Analyzing the standard deviation, the rule 58 has minor deviation than the rule 110 and its difference is 3.98 dBm. *Although rules 46, 78, 90, and 172 have standard deviations similar than the rule 110, the latter showed a better throughput to find the most instable OFC spectrum, as shown in section 5.5*.

Table 5.17. ANOVA – Comb lines spectrum generated by microresonator ring.

RULE	27	29	46	58	78	90	110	172	184
Average (dBm)	–39.24	–39.51	–40.04	–42.63	–39.05	–39.05	–39.06	–40.11	–38.66
Variance (dBm)	–45.15	–45.57	–44.68	–52.60	–44.69	–44.68	–44.67	–44.69	–52.14
Standard deviation (dBm)	–22.57	–22.78	–22.34	**–26.30**	–22.34	–22.34	**–22.32**	–22.34	–26.07
F and F–critic					0.3365 < 1.9384				
P–value					$2.67x10^{-5}$				

In Table 5.18, *rules 58 and 110 have the minimum and maximum standard deviation, −54 dB and −38.341 dB.* Although rules 110 and 27 have similar standard deviations, the calculating shown in Tables 5.4 and 5.13 determined that the former can predict critical intensity noise for OFC spectrum.

Table 5.18. ANOVA – Noise intensities measured in microresonator ring.

RULE	27	29	46	58	78	90	110	172	184
Average (dB)	−51.73	−60.071	−59.98	−60.71	−60.41	−60.62	−51.71	−56.52	−57.33
Variance (dB)	−76.67	−109.969	−103.17	−108	−106.05	−105.81	−76.67	−88.30	−90.56
Standard deviation (dB)	**−38.341**	−54.98	−51.58	**−54**	−53.02	−52.90	**−38.34**	−44.15	−45.28
F and F–critic					0.723 < 1.9401				
P–value					0.6711				

5.7 General Analysis of Prediction and Compensation of OFC spectra

In section 5.6, an analysis for a special group of rules allowed finding the most relevant rules in tasks of prediction. In Table 5.19, the most important rules are summed−up. Based on the selected rules, an analysis of phase shifts, changes of peak power for each comb line, and SCSR are carried out for each case.

Table 5.19. Relevant rules for three experiments set−up.

Experiment	**Rule(s)**
Picosecond pulsed laser	172 and 184
Femtosecond pulsed laser	90 and 184
Two cascaded Ims−MZM	27
Microresonator ring	58 and 110

5.7.1 Analysis of Picosecond and Femtosecond Pulse Lasers

The analysis of mode−locked lasers (picosecond and femtosecond pulsed sources) is carried out through the best rules found to improve the spectral shape, phase, and peak power for each comb line. In section 5.3, the rule 184 allowed correcting little changes of phase and peak power of spectrum generated by picosecond pulsed source laser. Based on the above, three kinds of

comparison are shown for observing the performance of rule 184: original spectrum vs predicted spectrum, original spectrum vs spectrum after its propagation in SMF, and original spectrum vs corrected spectrum using PS. *It is important to mention that the corrected spectrum was obtained through the predicted spectrum and the original spectrum*.

In Fig. 5.26, the phase shifts for three cases are shown below:

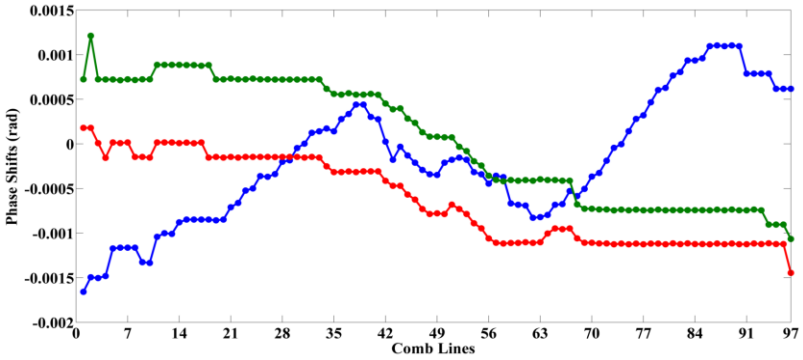

Fig. 5.26. Phase shifts calculated between the original OFC spectrum generated by picosecond pulse laser and the OFC spectrum predicted by the rule 184 (blue color); between the original OFC spectrum and the spectrum after its propagation in SMF (green color); and between the original OFC spectrum and the OFC spectrum corrected by pulse shaper (red color).

In Table 5.20, averages and standard deviations for three cases are indicated.

Table 5.20. Averages and standard deviations of phase shifts – picosecond pulse laser.

Case	**Mean (rad)**	**Standard deviation (rad)**	**Delay time – Estimated (fs)**
1) Original OFC spectrum vs predicted OFC spectrum	−0.0001945	0.00069709	2.584
2) Original OFC spectrum vs Spectrum after SMF	4.06×10^{-5}	0.000667	0.10284
3) Original OFC spectrum vs Corrected spectrum	−0.00063	**0.000471**	**0.0375**

Analyzing Table 5.20 and Fig. 5.26, the prediction is showing the most critical phase shift with respect to the original OFC spectrum, which the standard deviation is high. This is relevant to carry out an optimal correction in phase. By comparing the original spectrum with respect to spectrum after SMF and the corrected spectrum, the latter contains a standard deviation lower than the former. The mean for the case 2 indicates a positive phase shift of comb lines, influenced by the normal dispersion and possible non−linear phenomena (in that case, SPM and XPM could be the most representatives). To achieve a better phase correction, the use of LC−SLM with high spectral resolution is recommendable. By using this kind of SLM, a higher quantity of wavelength components can be manipulated in the PS and a fine correction of phase could be reached in the experiment.

In Fig. 5.27, the peak power of original spectrum, the spectrum after its propagation in SMF, the predicted spectrum, and the corrected spectrum are illustrated. Calculating the changes of power for the four spectra, 22.13 dBm (green color), 23.08 dBm (blue color), 13.16 dBm (black color), and

19.89 dBm (red color), the rule 184 predicts that the flatness can become low in a future time. By using the original and predicted spectra, the changes of power are reduced by the PS (its difference with respect to original spectrum is 2.24 dBm). This result shows that the prediction data are useful for correcting power peaks of comb lines and achieving flat lines.

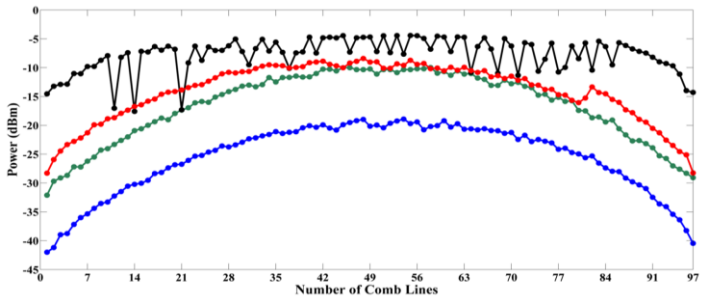

Fig. 5.27. Peak powers measured for the original spectrum generated by picosecond pulse laser (green color), the spectrum after its propagation in SMF (blue color), the predicted spectrum (black color), and the corrected spectrum (red color).

Another calculation realized in the four spectra is the side−comb suppression ratio (SCSR). For definition, the SCSR is the relation of power between comb lines at the central wavelength with the nearest higher–order comb line. From Fig. 5.27, SCSRs values are: 23.2 dBm (green color), 22.7 dBm (blue color), 22.819 dBm (black color), and 22.49 dBm (red color). Comparing SCSRs values, the suppression comb has little changes significant and the Gaussian shape will be conserved in a future time. This indicative allows verifying the good stability of spectrum generated by picosecond pulsed laser.

By means of the above calculation, the analysis is focused on OFC spectrum generated by femtosecond pulsed laser. To remember, the rule 90 allowed recovering part of spectrum of femtosecond pulsed laser after its propagation in SMF (see section 5.3). In addition, the spectrum measured at the SMF output and the found predictions presented critical changes of spectral shape (see Fig. 5.7 and Fig. 5.9) and therefore, the number of comb lines is difficult to find. Thus, the phase shift is calculated between the original and corrected spectrum, as illustrated in Fig. 5.28. Calculating the mean and standard deviation, 1.5345 rad and 0.8716 rad (delay time of 3.1603 ρs), these values are higher than means and standard deviations shown in Table 5.20. In that case, the frequency offset fluctuations are considerable and the phase shift is critic. *However, the rule 90 allows reducing the phase shifts in the comb lines 3, 6, 9, 10, and 11.*

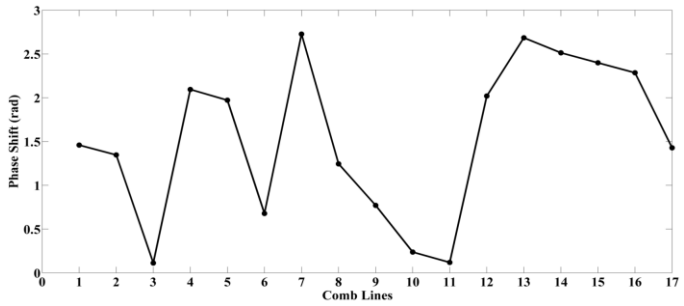

Fig. 5.28. Phase shifts calculated between the original OFC spectrum generated by femtosecond pulse laser and the OFC spectrum corrected by pulse shaper.

A relevant result of spectral shape correction is illustrated in Fig. 5.29. Calculating the changes of power for the original and corrected spectrum, 20.87 dBm and 9.04 dBm, the latter shows an important improving of flatness. *This result shows a good performance of rule 90 for correcting the peak power*. Although the Gaussian shape is modified with respect to the original spectrum, flat comb lines are required for optical communication networks. The reduction of peal powers variation is necessary for avoiding a instability condition of spectrum.

On the other hand, the SCSR for the original and corrected spectrum were 24.47 dBm and 11.25 dBm. Comparing these values, the PS generated a high suppression comb which device tries to improve the spectral shape. Although phase shifts and peak power variations for some comb lines were corrected by the rule 90, the SCSR is reduced. Therefore, the increase of SCSR is required to avoid losses of comb lines.

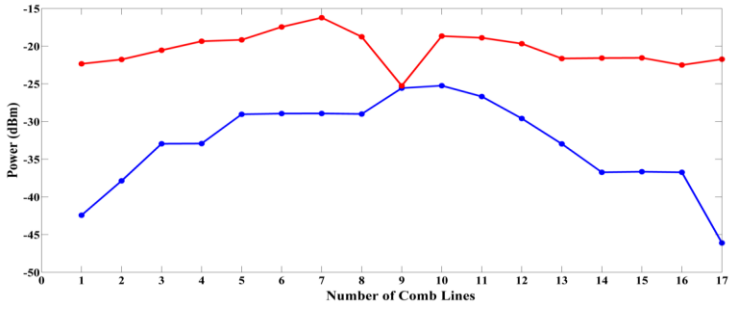

Fig. 5.29. Peak powers measured for the original spectrum generated by femtosecond pulsed laser (green color) and the corrected spectrum (red color).

5.7.2 Analysis of Two Cascaded IMS − MZM

OFC spectrum measured at the SMF input is compared with the OFC spectrum predicted by rule 27, as illustrated in Fig. 5.30. Observing this comparison, a phase shift at −1.41161 rad (with a delay time of 40.139 ρs) and a change of power in the flatness at 4.97 dBm are detected by the prediction approach. In Fig. 5.31, the OFC spectrum measured at the PS input is compared with the OFC spectrum corrected by PS through the prediction information. In that case, the flatness and the frequency variation are corrected. Due to the insertion loss of PS (~4.5 dB), the average power is reduced a little. Nevertheless, *the main characteristics of corrected OFC spectrum are conserved*.

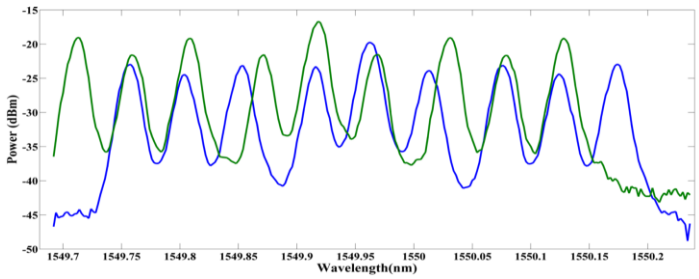

Fig. 5.30. Comparing between the original OFC spectrum generated by two cascaded IMS − MZM (green line) and the OFC spectrum predicted by rule 27 (blue line).

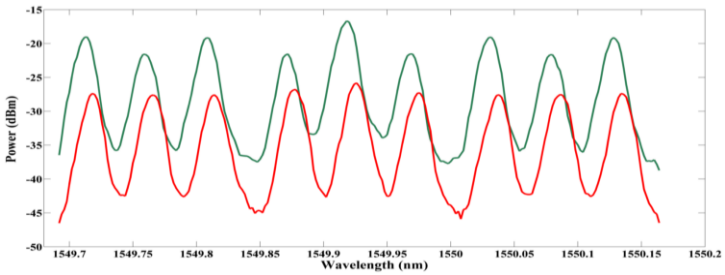

Fig. 5.31. Comparing between the original OFC spectrum generated by two cascaded IMS − MZM (green line) and the OFC spectrum corrected by pulse shaper, through predicted spectrum (red line).

In Table 5.21, the phase shift for 9 comb lines is shown. By using the prediction and the original spectrum, the corrected spectrum shows a reduction of phase shift, −0.2618 rad (with a delay time 4.519 ρs). Nevertheless, the phase shifts among comb lines are changing both the original spectrum to the corrected spectrum. This behavior is generated by frequency offset during the OFCG [SON12]. Considering linear and non–linear phenomena during the OFC propagation in SMF, the phase shift can change and the frequency offset can become critic for an optical communication link. However, *the prediction was satisfactory due to that the vector of phase allowed a reduction of phase shift.*

Table 5.21. Phase shifts of comb lines generated by two cascaded IMS − MZM.

Comb Line	**Δθ Between the Original and Predicted Spectrum (rad)**	**Δθ Between the Original and Corrected Spectrum (rad)**
1	−1.5708	−0.1428
2	−1.44513	−0.25133
3	−1.122901	−0.14726
4	−1.5025	−0.20489
5	−1.3823	−0.25133
6	−1.12901	−0.14726
7	−1.4399	−0.19635
8	−1.4399	−0.19635
9	−1.6659	−0.2618
Average	**−1.41161**	**−0.2618**
Standard deviation	**0.180839**	**0.04739**

In Table 5.22, the peak powers for 9 comb lines are specified. According to the results, the changes of power for the original and the predicted spectrum were 4.724 dBm and 4.97 dBm. The above indicates that the changes of power may increase around 0.246 dBm. Such variation occurs for the bias drifting of IM–MZM which affects the stability of flat comb lines [SHA14]. In the IM−MZM case, the main disadvantage is the bias voltage fluctuation. This instability generates a complex combination of pyroelectric, photorefractive, and photoconductive phenomena in the Lithium Niobate [ŠVA10]. Such physical phenomena are responsible of comb lines power variation when MZM is operated by long periods. Some solutions were proposed by [HUAN11] [ŠVA14] [ZHU14], but the automatic control is not enough for maintaining the stability of bias drifting in long periods. These proposals require a manual control of the operation point (curves of V_{BIAS} vs V_{π}), avoiding that the point is located in a non−linear region. This kind of research is active in the present day.

By correcting the OFC spectrum, changes of power is reduced until 1.78 dBm which the flatness of comb lines is improved. The standard deviation of power variation for the original OFC spectrum and the OFC predicted are −23.4748 dBm and −26.9687 dBm (its difference is 3.49 dBm). Analyzing this result, the prediction approach detected a slight reduction of standard deviation which the spectrum can reach a point of stability. By applying the power correction with the PS, the standard deviation is reduced until −35.69 dBm, indicating that the power stability is improved.

Table 5.22. Peak powers of comb lines generated by two cascaded Ims−MZM.

Comb Line	Original OFC Spectrum (dBm)	Predicted OFC Spectrum (dBm)	Corrected OFC Spectrum (dBm)
1	–19.05	–22.976	–27.38
2	–21.61	–24.454	–27.61
3	–19.16	–23.14	–27.58
4	–21.55	–23.28	–26.78
5	–16.69	–19.73	–25.83
6	–21.55	–23.91	–27.31
7	–19.09	–23.1	–27.58
8	–21.66	–24.358	–27.54
9	–19.12	–22.936	–27.39
Average	**–19.942**	**–23.098**	**–27.2222**
Standard Deviation	**–23.4748**	**–26.9687**	**–35.6986**

Other calculation carried out for three OFC spectra is SCSR. The SCSR for the original spectrum is 21.36 dBm and the SCSR for the predicted spectrum is 21.03 dBm (its difference is 0.33 dBm). This result shows that the suppression comb lines may reduce in a future time and therefore, the spectral shape can change. Establishing the SCSR for the corrected spectrum, 20.07 dBm, a slight increase of suppression comb lines is generated (its difference with respect to the SCSR for the original spectrum is 1.29 dBm). Notwithstanding these results, the power and the phase correction configured by the PS allowed obtaining flat comb lines.

In Table 5.23, a comparison of the flatness correction for 2 IMs– MZM with respect to others research works is shown. Analyzing the OFCG systems, the maximum number of comb lines was

generated by [SUP12] (75 comb lines) and the most stable spectrum was obtained by [CHEN14] (flatness < 0.5 dB). Such mentioned works required of phase modulators and IMs – MZM as well as an electrical system to guarantee stability, as explained [TOR14]. Although their results are relevant, the number of electrical components is big and the complexity of system is considerable. Comparing these results and the proposed method, the addition of one PS can avoid the increase of electrical components to find the stability of spectrum. The above represents one advantage due to the task of compensation is carried out through a control algorithm (as was shown in Fig. 5.1) which the flatness variation was corrected until 1.78 dBm. If the resolution of PS is high, the flatness variation could be lower but the best PS used in Purdue University has 10 GHz. Nevertheless, this aspect can be explored as a future work. *Other advantage of the proposed method is the phase shift correction where the mentioned works are not considered it. Thus, the method can improve the flatness and phase shift at the same time.*

Table 5.23. Comparison of the flatness variation between the results of experiment II and others research works

Research Work	**OFCG**	**Result**
[SHA14]	2 IMs – MZM with 20 GHz	15 comb lines, flatness correction= 0.6 dB
[DOU11]	1 phase modulator and 1 IM−MZM with 10 GHz	15 comb lines, flatness correction = 1 dB
[SUP12]	4 phase modulators MZM	75 comb lines, flatness correction = 1 dB
[SAK07b]	DD−MZM with 2 RF source − 10 GHz	11 comb lines, flatness correction = 1.1 dB 19 comb lines, flatness correction < 4.3 dB
[CHEN14]	Three systems: 1 phase modulator MZM. 1 phase modulator and 1 IM – MZM. 1 phase modulator and 2 IM – MZM. All optical systems were adjusted with 20 GHz.	7 comb lines, flatness correction < 0.5 dB 17 comb lines, flatness correction < 0.5 dB 29 comb lines, flatness correction < 0.5 dB
The proposed method	2 IMs−MZM where, IM1 was configured with 20 GHz IM2 was configured with 6 GHz	9 comb lines, flatness correction = 1.78 dBm **Phase shift = −0.2618 rad**

5.7.3 Analysis of Microresonator Ring

Using the prediction approach, the most stable and instable OFC spectra were found by rules 58 and 110. In Fig. 5.32, the original OFC spectrum is compared with the OFC spectrum predicted by rule 58, where the latter shows the best stability in peak power and phase. This case is identified with one μring at 7 μm. In Fig. 5.33, the original OFC spectrum is compared with the OFC spectrum predicted by rule 110, being the latter the most instable OFC spectrum. The above is detected with one μring at 0.6 μm.

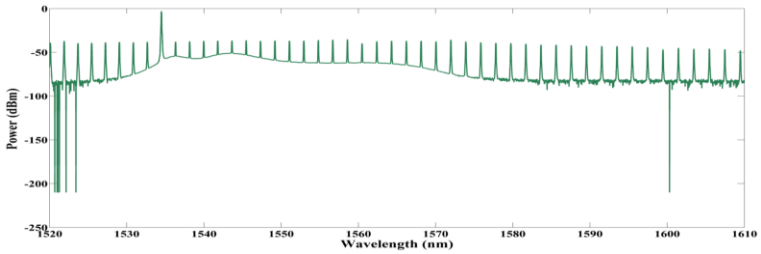

(a)

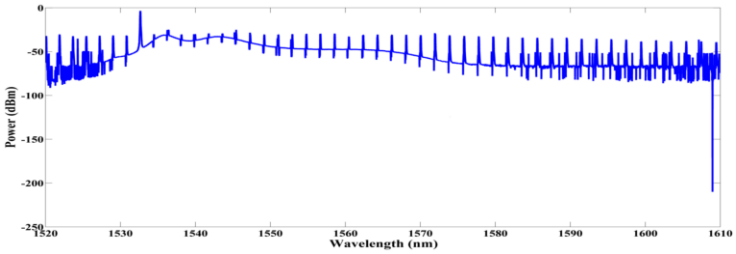

(b)

Fig. 5.32. Comparing between the original spectrum and the spectrum predicted by the rule 58: a) the original OFC spectrum generated by a μring at 7 μm (green line), and b) the OFC spectrum predicted by rule 58 (blue line).

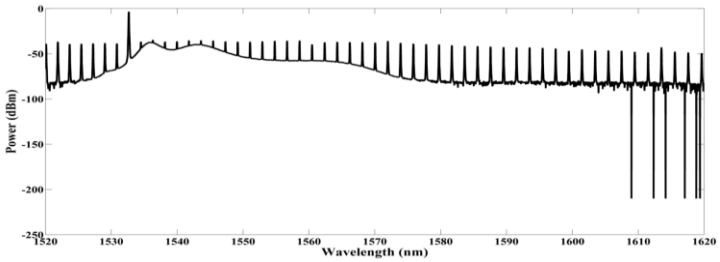

(a)

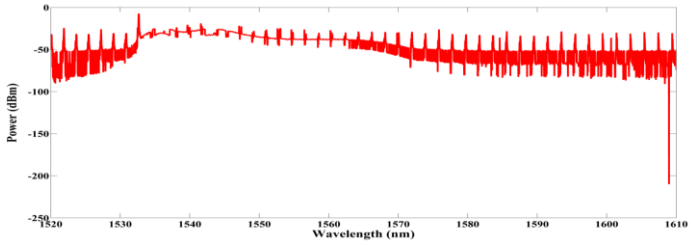

(b)

Fig. 5.33. Comparing between the original spectrum and the spectrum predicted by the rule 110: a) the original OFC spectrum generated by a μring at 0.6 μm (black line), and b) the OFC spectrum predicted by rule 110 (red line).

Using OFC spectra (Fig. 5.32 and Fig. 5.33), phase shifts are calculated for both cases. In Fig.

5.34, phase shifts between the original spectrum for a μring at 7 μm and the OFC spectrum predicted by rule 58 are illustrated. Analyzing this result, maximum phase shifts are observed in the comb lines 1 (1.572 rad) and 2 (0.5471 rad). In Fig. 5.35, the frequency variation between the original OFC spectrum for a μring at 7 μm and the OFC spectrum predicted by rule 110 are shown. Maximum phase shifts are identified in the comb lines 3 (−2.862 rad), 5 (−2.737 rad), 15 (1,772 rad), 38 (−3.174 rad), 44 (2.752 rad), 48 (1.538 rad), 50 (3.157 rad), and 51 (1.539 rad). Comparing these results, the instable OFC spectrum detected by rule 110 predicted critical phase shifts due to a possible increase of frequency offset. Calculating the standard deviation (Fig. 5.34 and Fig. 5.35), although values are 0.018706 rad and 0.027501 rad, the latter has a high phase shift.

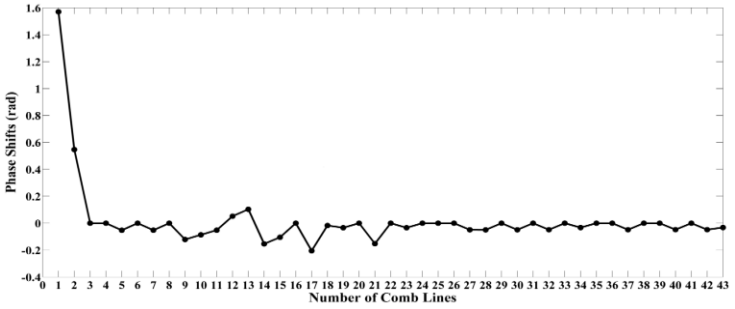

Fig. 5.34. Phase shifts calculated between the original OFC spectrum generated by a μring at 7 μm and the OFC spectrum predicted by rule 58.

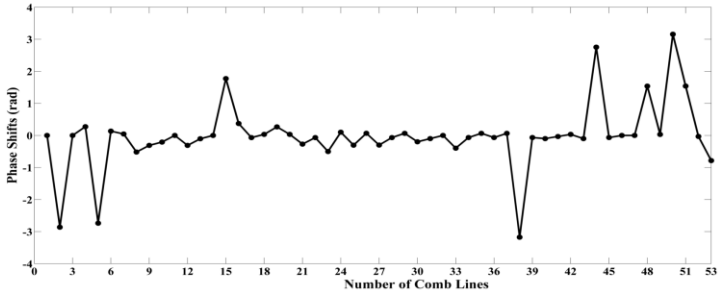

Fig. 5.35. Phase shifts calculated between the original OFC spectrum generated by a μring at 0.6 μm and the OFC spectrum predicted by rule 110.

The prediction approach identified critical phase shifts in a future time which several points support such observations. In optical microresonators, the normal dispersion can be generated due to changes of temperature or mechanical vibrations. This behavior can influence that some high optical frequencies propagate slower than low frequencies [KIP11]. The main is free spectral range (FSR) which the cascaded four waves mixing (FWM) is weak and the bandwidth is limited (in that case, several comb lines are attenuated). Another point is a large intensity noise in the FSR and a poor temporal coherence in microresonators. Both behaviors can contribute in an increase of frequency offset [WANG14]. Considering the frequency offset, the bandwidth is limited by instability of repletion rate when microresonators are dependent of intensity round–trip time inside ring cavity.

Peak powers measured and calculated through OFC spectra are illustrated in Fig. 5.36 and Fig.

5.37. Analyzing Fig. 5.36, changes of power and standard deviations for the original OFC spectrum (μring of 7 μm) and the predicted OFC spectrum (rule 58) are 43.65 dBm (stdv −11.3198 dBm) and 32.19 dBm (stdv −11.8577 dBm). These results indicate that OFC spectrum can stabilize whether the linear polarization is constant.

In the calculation of SCSR, the predicted spectrum has a high suppression comb than the original spectrum (43.807 dBm < 77.21 dBm). If a high suppression comb occurs in a future time, the spectral shape can modify. Such situation could increase phase shifts among comb lines.

Changes of power and standard deviations for the original spectrum (μring of 0.6 μm) and the predicted spectrum (rule 110) are 37.68 dBm (stdv −11.7902 dBm) and 51.82 dBm (stdv −9.611 dBm). Such calculations (obtained from Fig 5.37) show the relation between the microresonator size and the flatness spectrum. In that case, a small size of ring may cause changes of peak power in each comb line. Considering SCSRs values, 78.24 dBm and 43.59 dBm, the latter indicates a high power variation which could suppress some comb lines. One cause is the thermal noise and Kerr nonlinearity. Since these physical phenomena occur inside of the CW tunable laser, the peak power variations can change the mode spacing of the frequency comb and to reduce the effective path length of resonator [KIP11]. In contrast, the thermal effects cause a refractive index fluctuation, converting the optical energy in heat energy. For any microresonator, changes of temperature can reduce the number of flat comb lines.

Other limitation of the OFC spectrum generated by microresonators is high peak power of the frequency comb (CW tunable laser) and its amplification with an EDFA. This unique comb line can influence in the power variation which its suppression is required. In [FER11], the use of line−by−line pulse shaping allowed compressing stably to nearly bandwidth−limited pulses, improving the flatness and the spectral shape. Nevertheless, this research is focused in the performance of prediction approach for detecting relevant behaviors of OFC spectrum.

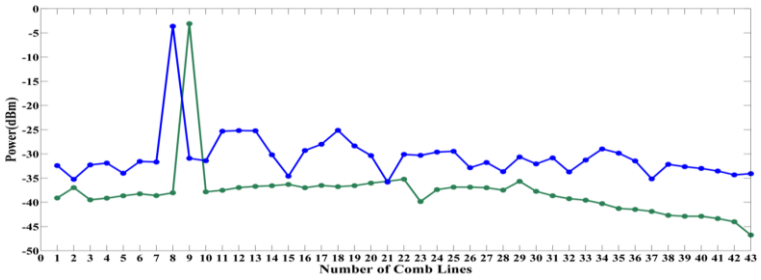

Fig. 5.36. Peak powers calculated between the original OFC spectrum generated by an μring at 7 μm (green line) and the OFC spectrum predicted by rule 58 (blue line).

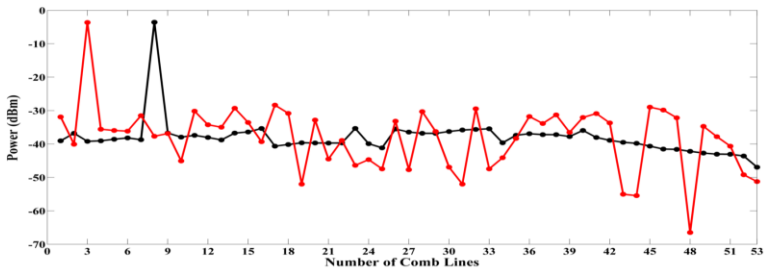

Fig. 5.37. Peak power calculated between the original OFC spectrum generated by an μring at 0.6 μm (black line) and the OFC spectrum predicted by rule 110 (red line).

5.8 Summary

In this chapter, a general methodology for predicting the behavior of an optical spectrum is proposed through IFCA–MV and HIFEAN. The IFCA–MV is used to predict the most relevant changes of phase, spectral shape, flatness, and others physical variables, considering a special group of evolution rules {27, 29, 46, 58, 78, 90, 110, 172, and 184}. The HIFEAN allowed verifying the quality of prediction through of the IFCA–MV results (membership and non–membership degrees matrices in a defined future time). To corroborate the performance of proposed method, three experiments set–up were selected because generate a comb lines spectrum.

In the application I, the rule 184 corrected the phase and spectral shape generated by a picosecond pulsed laser. The rule 90 allowed predicting possible chaotic dynamics in a future time when the interaction between chromatic dispersion and non–linear phenomena is increased. This case is observed in the femtosecond pulse spectrum where a part of spectrum was recovered. Comparing both results, the femtosecond pulse laser has more disadvantage than the picosecond pulse laser in optical communications links with SMF. In that case, phase shifts after the PS is higher in femtosecond pulsed laser (mean = 1.5345 rad and std = 0.8716 rad) than picosecond pulsed laser (mean = −0.00063 rad and std = 0.000471 rad). The SCSR after PS is larger in the picosecond pulse laser (22.49 dBm) than femtosecond pulse laser (11.25 dBm) which the low suppression comb is presented. The peak power variation corrected by PS is lower in femtosecond pulsed laser (9.04 dBm) than picosecond pulsed laser (19.09 dBm), but the latter has the highest SCSR.

In the application II, the rule 27 produced the best correction of flatness for the comb lines spectrum. During the experiment, bias drifting affected the flatness of comb lines which the tuning of DC Bias and RF amplitude must be adjusted several times until to obtain the best spectrum. Propagating the comb lines spectrum through SMF, the characteristics of spectrum are conserved but the average power is attenuated. By using the mentioned rule, phase and power corrections generated by the PS allowed obtaining an optimal spectrum after its propagation. In that case, changes of peak power were reduced until 1.78 dBm and the SCSR was maintained in 20.07 dBm. In addition, the phase shift was reduced until −0.2618 rad (std = 0.04739 rad). Nevertheless, it is required to propose new strategies based on pulse shaping and the prediction approach for mitigating more frequency offset. On the other hand, the comparison of these results with respect to other works shows that the proposed method can compensate phase shift and power peak variation at the same time.

In the application III, rules 58 and 110 allow predicting the best and the worst changes of OFC spectrum. For both cases, the phase shifts were higher than phase shifts observed in the experiment II. During the analysis, phase shifts averages were 0.018706 rad (the most stable OFC spectrum) and 0.027501 rad (the most instable OFC spectrum). Such averages indicated considerable noise intensities in FSRs, affecting the stability of phase. Therefore, a strategy of control like feedback control is required. SCSRs and peak power variation for the microresonator have values larger than in MZMs. The comparison shows that the OFC generation based on electro−optic modulators can guarantee an optimal stability. However, bandwidth−limited spectrum for MZM is minor than microresonator.

Considering the computational cost measured for the three experiments, rules 27, 46, and 184 presented the minimum exigency in CPU and memory. These rules were used in tasks of real time. The rule 184 had the best throughput in the applications I and III which its capacity for online optics systems can become benefic. Comparing with rules 27, 58, 90, and 110, the throughput of rule 184 was not similar. Thus, there is not a relation between the computational cost and the mentioned applications to mention minor machine exigency, better capacity of prediction and optimal performance to correct the spectrum. However, there is an exception. In the application II, the rule 27 presented the best results to correct the flatness of comb lines spectrum generated by cascaded MZMs, and the ANOVA analysis verified its good performance. Therefore, the rule 27 is useful for the application II or other kind of configuration based on MZM.

Based on the analysis, *rules 27, 58, 90, 110, and 184 are the useful for optical communications,* applied in tasks of flatness correction and stability analysis of OFC spectrum.

In Table 5.24, a general review of the performance of special group of rules is shown through a score (1 = deficient, 2 = regular, 3 = acceptable, 4 = good, and 5 = excellent).

Table 5.24. Review of the performance for the special group of rules.

RULE	Computational cost	Capacity of prediction	Correlation	ANOVA	RMSE	General evaluation
27	4.0	5.0	3.0	4.0	4.0	**4.0**
29	3.0	4.0	3.0	3.0	2.0	3.0
46	4.0	3.0	3.0	2.0	2.0	2.8
58	2.0	5.0	3.0	3.0	4.0	3.4
78	2.0	4.0	2.0	3.0	3.0	2.8
90	3.0	5.0	4.0	4.0	4.0	**4.0**
110	3.0	5.0	4.0	5.0	5.0	**4.4**
172	2.0	3.0	4.0	3.0	4.0	3.2
184	5.0	5.0	4.0	4.0	4.0	**4.4**

In Table 5.25, main results of analysis for the three experiments set−up are summed−up below:

Table 5.25. Summary of analysis for the three experiments set−up.

Experiment	Std – Phase shift	Change of power – Comb Lines	SCSR	Number of Comb Lines
Picosecond Pulse Laser –OFC spectrum after pulse shaper	**0.000471 rad**	19.89 dBm	22.49 dBm	97
Femtosecond Pulse Laser –OFC spectrum after pulse shaper	0.8716 rad	9.04 dBm	11.25 dBm	17
Two cascaded Ims−MZM –OFC spectrum after pulse shaper	0.04739 rad	**1.78 dBm**	20.07 dBm	9
Microresonator ring – the best OFC spectrum (rule 58)	0.018706 rad	32.19 dBm	**78.24 dBm**	43 (part of spectral width)
Microresonator ring – the worst OFC spectrum (rule 110)	0.027501 rad	51.19 dBm	43.59 dBm	53 (part of spectral width)

CONCLUSIONS AND REMARKS

In this research, the characteristics of OFC spectrum and its propagation in SMF were explained where the impact for the scientific community was justified. The study of state−of−the−art is focused on the OFC techniques and the compensation methods. During the searching, the optic microresonator has been a high influence in OFC generation due to a high peak power for each comb line, a large spectral width, and cents of comb lines. Such characteristics have boosted a new development of OFC spectrum in different fields since 2011. One limitation of microresonator is the stability with respect to the thermal noise, normal dispersion, mechanical vibrations, and non−linear polarization. Some topics such as nonlinear dynamic of microresonator, the development of thermal control or the reduction of average power variation have been focused by researchers of different disciplines. Due to the microresonator limitations, the different configurations with MZMs and the advance of mode−locked laser at low intensity noise levels are still working in the present day. The main reasons are the facilities for controlling the flatness of OFC spectrum and creating control systems to reduce the phase shift. Nevertheless, researchers are seeking the increase of spectral width for MZMs until 100 GHz and to improve the tuning control of mode−locked lasers to obtain the best Gaussian shape or other shaping with low frequency offset.

Since the frequency offset, the power variation, and the effects of linear and non−linear phenomena can affect the OFC spectrum during the propagation in SMF, the research has been seek new mathematical models or methods. Considering the influence of uncertainly in dynamic of OFC spectrum and the random behaviors of frequency offset among comb lines, the fuzzy sets theory is the best alternative to propose a new methodology. The first contribution is a new uncertainly measure called the general intuitionistic fuzzy entropy by adequacy and non−adequacy (HIFEAN). HIFEAN showed an efficiency of 76.42% and comparing with other measure well−known Vlachos and Sergiadis's entropy (HVS), the efficiency decreased around 44.91%. The above indicates a high throughput of HIFEAN in the analysis of OFC spectrum.

Defining HIFEAN, the next step of research was the development of prediction approach. This step allowed proposing a new kind of automaton called intuitionistic fuzzy cellular automaton based on means vector (IFCA−MV). Unlike FCA, the IFCA−MV built the geometrical representation of cells through the feature vector obtained by membership and non−membership degrees matrices. Such matrices allowed generating one−dimensional cellular automaton. The use of intuitionistic fuzzy sets (IFSs) in IFCA−MV increased the capacity of prediction due to that γ−parameter adjusted the prediction for detecting abnormal behaviors.

In a simulation of the mask representation for an ultra−short pulse spectrum, the HIFEAN generated relevant results. The rule 78 identified the possibility of stability for the mask representation whether no changes of ultra−short pulse are conserved. Rules 27, 29, 58, 90, and 110 found the possible conditions for generating a linear or a non−linear phenomenon. Analyzing rules 90 and 110, they identified a likely stability before the generation of any linear or non−linear phenomenon. Rules 172 and 184 detected the possibility of an interaction of linear and non−linear phenomena, subjected to some conditions of average power. Such interaction can become high whether the intensity and phase of Fourier components change their magnitudes in a future time.

This observation was found by the rule 46. If the intensity variation and phase shift are high, rule 46 determined the possibility of chaotic situation in the OFC spectrum. For this reason, the prediction suggested that the average power of laser must maintain a moderate magnitude. In summary, the simulation results indicated that the IFCA–MV can analysis the dynamic of system in stable and instable conditions.

In the research, a general methodology based on fuzzy clustering methods, IFCA−MV, and HIFEAN is defined for applications in real environment of laboratory. The LAMDA method was used to obtain a membership degree matrix. The IFCA−MV carried out the prediction of OFC spectrum according to the fuzzy clustering data, the evolution time of automaton, the selected rule, and γ−parameter. The HIFEAN was implemented to verify the quality of the prediction data (membership and non−membership degrees matrices after IFCA−MV). Such measures and methods were applied for tasks of analysis and/or compensation using the pulse shaper. Analyzing the main results, the proposed method is adapted in the spectrum prediction in real−time through OSA data and it was able to identify the best and the worst behavior of OFC.

The adjustment of γ−parameter for the three experiments showed relevant points, explained below:

- Unlike FSs, the use of γ−parameter for IFSs allows observing minimal changes of peak power and phase in each comb line. The above evidenced that the γ−value shows all possible variation in power and phase and its stability or instability.
- Since the intuitionistic fuzzy entropy measure analyzes the amount of information for an IFS, the measure also showed the credibility of data. By using the γ−parameter in HIFEAN, several entropy measures for each γ−value demonstrated whether the predicted data are validated or not. Such analysis reduced the number of spurious classes generated by IFCA−MV and conserved the most relevant classes with useful information about dynamical of spectrum. This procedure was required for three experiments, achieving to observe the credibility of prediction.
- The γ−parameter reached to show more information about the prediction for each evolution rule, which IFSs are most efficient in tasks of prediction than FSs.

For the experiment I, rules 90 and 184 allowed correcting the phase shift and spectral shape of picosecond and femtosecond pulsed lasers after its propagation in SMF. Comparing both spectra, the picosecond pulsed laser is more stable than the femtosecond pulsed laser. The former has a phase shift of −0.00063 rad (average) and 0.000417 rad (standard deviation) and the latter has 1.5345 rad (average) and 0.8716 rad (standard deviation). Comparing the peak power variation, the picosecond pulsed laser is maintained in 22.49 dBm but the femtosecond pulsed laser decreased its average power until 11.25 dBm. This decrease of average power can affect the spectral shape and therefore, various pre−amplification stages along SMF are required. The solution with pre−amplifiers can avoid the effects of SMF attenuation but the financial investment could be expensive in real engineering applications for optical links. Other limitation of pre−amplifiers is the noise due to the frequency offset variation of comb lines.

For the experiment II, the rule 27 was the most appropriated for correcting the phase and peak powers in a OFC spectrum with 9 comb lines. The phase shift is reduced until −0.2618 rad and *the change of power is the lowest among the OFC generation techniques used in the laboratory*, 1.78 dBm. Other potential of OFC spectrum is the stability of SCSR, which was maintained in 20.07

dBm. The above avoids high comb suppression and its spectral shape is conserved stable. Comparing these results with respect to others works, the former can correct peak power variation and phase shift using the PS and the proposed method, avoiding the use of many electrical components in different MZM configuration to obtain a flat comb spectrum.

For the experiment III, rules 58 and 110 detected the best and the worst behaviors of OFC spectrum. These rules were able to identify the highest frequency variations in the two spectra, 7.87 THz and 7.91 THz, and the highest power variation, 32.19 dBm and 51.19 dBm. The prediction is shown that the highest comb peak power generated by CW tunable laser can have a magnitude larger than the neighbors comb lines. Keeping in mind the highest peak power is amplified, this condition can excite degenerative and non−degenerative states of FWM. In that case, the neighbor's comb lines could attenuate along spectrum and the flatness is affected. One reason of this behavior is the thermal noise and the normal dispersion during comb lines generation, producing high fluctuations of frequency offset among lines. Due to these limitations, the bandwidth of microresonator can be limited by the repetition rate variation and its dependence with respect to the intensity round−trip time of ring. One advantage of microresonator with respect to the others OFC generation techniques is to contain *the highest SCSR value* (78.24 dBm), avoiding comb suppression whether the spectrum is propagated inside SMF or during the flatness correction through pulse shaper. Other advantage is a large spectral width (> 300 nm) which could be the next point of research in multi−channel optical and optical elastic networks.

For the three experiments of laboratory, the most relevant rules were *27, 90, 110, and 184*. These rules allowed analyzing and/or compensating OFC spectrum. For each experiment, one or more rules generated the best results but the research did not find a general rule to analyze the flatness variation and phase shift. However, the methodology offered some advantages for real experiments of OFC such as:

- Analysis of OFC spectra based on historical data.
- Prediction of OFC behavior in the spatio−temporal domain useful for identifying normal and abnormal phase shifts and peak power.
- Capacity for compensating the flatness variation and phase shift using open loop control and pulse shaper.

In the general methodology, the spectrum can be analyzed and/or compensated by using IFSs, IFCA−MV, and HIFEAN. The method could be considered as a novel analysis technique for OFC because spectra data are the unique requirement for detecting normal and abnormal behaviors in a future time. Based on the information given by the method, known mathematical models of comb generation and propagation in SMF could be complemented through prediction data. Other relevant contribution of method is the capacity for correcting the OFC spectrum. For the three experiments, the global average of computational cost is 142.88 seconds (see Annex A.11), which it is calculated through the function "clock" from Matlab, established as: the acquisition time from OSA to computer, the response time of pulse shaper, the acquisition time from computer to pulse shaper, and the algorithmic time for the prediction. Such factors must be considered in real experiments when the pulse shaper is programed through the proposed method. Since the proposed method was developed to predict linear and non−linear behaviors of OFC spectrum propagated through SMF, several new fields of research might be focused such as:

- *Monitoring system of OFCG in microresonator ring*: due to the normal dispersion generated by microresonator ring and the linewidth of CW tunable laser, comb lines can change the wavelength position. This change generates phase shift in a future time. One alternative to observe the behavior of OFC spectrum is the use of fuzzy clustering method and the IFCA−MV as a monitoring system. The goal is to train the monitoring system with historical data of OFC spectra, noise intensity and wavelength (using a wavelength meter). Afterwards, new data of microresonator are sent to monitoring system to identify the abnormal behaviors such as decrease of power peak in each comb line, increase phase shift, and SCSR. Each behavior must be recognized in the monitoring system as functional state, i.e. actual behavior of system. Such functional states are detected by the IFCA−MV. The monitoring is shown as a graphical representation of functional states vs time, where each state is identified as a representative color to facilitate the observation.

- *Strategy of surveillance of OFC spectrum propagated through long−haul transmission*: To construct a surveillance system, the fault detection step, the diagnostic step, and the control action are required [BOT11]. To monitor an OFC spectrum propagated in long−haul transmission optical networks, the fault detection can be established as a fuzzy automaton system based on fuzzy clustering [BOT13]. This automaton contains all functional states (associated with classes) where each one describes normal, abnormal, critical or alert situation of the OFC spectrum behavior. The detection system based on this kind of automaton is static which the dynamical behavior must be considered in real−time. The above could be added in a diagnostic system based on fuzzy transition probabilities and weights of fuzzy transition presented by [ISA14]. Using the results of prediction states from diagnostic system, the action control could be defined by the IFCA−MV and HIFEAN. Both could be proposed as a predictor for sending a control signal in the CW laser or mode−locked laser when a linear or non−linear phenomenon is identified. The control signal can be the average power or a percentage of wavelength adjustment to maintain the central wavelength (it is carried out by a piezoelectric device inside laser. For more information, go to TLB–6728 user manual). Such control signals could avoid the interaction between linear and non−linear phenomena mentioned in section 2.2.4.

- *Feedback control of bias drifting for two IMS − MZMs or other configuration illustrated* by [TOR14]: Comb lines change the peak power due to bias drifting generated by DC source, phase desynchronizations of RF source and physical behaviors of Lithium Niobate (mentioned by he[ŠVA10]). This behavior can modify the spectral shape in a future time. One alternative to reduce the bias drifting is ABC controller [HUAN11]. This controller compares an electrical signal obtained by a photodetector (the optical signal before photodetector have 10% of power with respect to the original spectrum) and a dither signal. When a peak is generated, the controller sent a voltage signal at DC input of MZM and a phase correction to RF source. Although this solution exists, the main limitation is its mismatch in the dither signal for a long operation time. To correct the mismatch, the IFCA−MV can be added as a support mechanism for ABC controller. The goal is to send alert data when the dither signal changes offset level. To achieve the detection, the IFCA−MV must compare the dither signal with possible prediction

obtained in the training. Such comparison is validated by HIFEAN.

- *Temperature control of a microresonator ring based on IFCA−MV and fuzzy control*: one limitation of microresonator ring is the decrease of peak power in each comb line when the operation temperature begins to increase. This behavior generates phase and power peak variations which the spectral width is reduced. In addition, the spectral shape is not conserved. Due to this problem, a temperature control could stabilize the operation temperature using as sensor a thermocouple and a microheater as actuator connects with the microresonator. The microheater allows changing the heating power through an applied voltage and tuning the resonance wavelength with CW tunable laser wavelength [XUE15]. The temperature control can be designed by a fuzzy control or a proportional−integral−derivative (PID) fuzzy control, where the IFCA−MV could be used as a monitoring system. This idea will increase the control efficient when the fuzzy controller cannot observe any abnormal behavior. In that case, the IFCA−MV analyzes the controller behavior and an alert signal is sent to fuzzy control to compensate the temperature offset level.

- *Optimal equalization of high optical modulation formats (m−ary QPSK or m−ary QAM) in the reception step of an optical communications network*: The goal is to use the IFCA−MV and HIFEAN as a decision method about the best optical modulation format according to several parameters such as: transmission rate, BER, and delay time generated by PMD. The method obtains parameter data in the reception step to analyze the stability of modulation format with respect to linear and non−linear phenomena in SMF. Using a strategy similar to group−decision making or multiatribute decision making [FEN09], the method could be adapted as an expert system. This adaptation could be an alternative in the flexible optical networks to select the best optical modulation format.

On the other hand, the IFCA−MV and HIFEAN can be improved in the following future works:

- *Optimization of IFCA−MV*: one alternative to increase its efficient in real−time is the analysis of computation complexity based on average−case complexity and Big−O notation (also called Banchmann−Landau notation). Big−O notation allows classifying algorithms according to input and output sizes and the processing time, defining as order−*n* function. Such function can be logarithmic, constant, polynomial, among others. The result of complexity analysis could be useful to propose a new local transition rule of IFCA−MV based on another structure based on form normal, possibility form, weights of transition fuzzy, or other function.

- *Amount of knowledge in HIFEAN*: since 2013, the topic about amount of knowledge has been relevance in the IFSs and entropy measures [PAL13]. Such measure adds in HIFEAN could increase its performance in tasks of data analysis whether the knowledge information about a system is added as qualitative data. Although HIFEAN uses quantitative data obtained by IFSs, the form normal prenex (widely used on mathematical logical) could be an option for converting qualitative data in quantitative data. Considering this strategy, the full or partial knowledge of system can be applied as an extension of HIFEAN.

REFERENCES

[ABR14] Abrams, D. M., Slawik, A., and Srinivasan, K. Nonlinear oscillations and bifurcations in silicon photonic microresonators. Phys. Rev. Lett. 112, 123901, 2014.

[AGR05] Agrawal, G.P. Lightwave Technologies: Telecommunications Systems. Wiley–Interscience, pp. 30, 2005.

[AGU82] Aguilar–Martín, J., and López de Mantaras, R. The process of classification and learning the meaning of linguistic descriptors of concepts. Approximate reasoning in decision analysis, North Holland, pp. 165–175, 1982.

[AGU07a] Aguilar–Martín, J. Inteligencia Artificial para la Supervisión de Procesos Industriales. ULA, Mérida, Venezuela, 2007.

[AGU07b] Aguilar–Martin J., Isaza C., Diez–Lledo E., LeLann M.V., Waissman–Vilanova J. Process Monitoring Using Residuals and Fuzzy Classification with Learning Capabilities, Advances in Soft Computing–Theoretical Advances and Applications of Fuzzy Logic and Soft Computing, ISSN 1615–3871, Springer Berlin Heidelberg, New York, 2007b.

[AHD02] Ahderom, S., Raisi, M., Lo, K., Alameh, K. E., and Mavaddat, R. Applications of liquid crystal modulators in optical communications. High Speed Networks and Multimedia Communications 5th IEEE Int. Conf. on, pp. 239–242, 2002.

[AHM09] Al–Ahmadi, K., See, L., Heppenstall, A., and Hogg, J. Calibration of a fuzzy cellular automata model of urban dynamics in Saudi Arabia. Ecolo. Complex. 6(2), pp. 80–101, 2009.

[AKH95] Akhmediev, N. and Karisson. Cherenkov radiation by solitons in optical fibers. Physic. Rev. A 51(3), pp. 2602–2607, 1995.

[AKT06] Akturk, S., Gu, X., Kimmel, M., and Trebino, R. Extremely simple single–prism ultrashort–pulse compressor. Opt. Exp. 14, pp. 10101–10108, 2006.

[ANT06] Antonicini, C. Ultrashort Laser Pulses. University of Reading, Department of Physics, 2006.

[ATA86] Atanassov, K. Intuitionistic fuzzy sets, Fuzzy Sets and Systems 20, pp. 87–96, 1986.

[ATA12] Atanassov, K. On intuitionistic fuzzy sets theory, Springer–Verlarg, Berlin, Germany, 2012.

[ATAN11] Atanassova, L. and Atanassov, K. Intuitionistic Fuzzy Interpretation of Conway's Game of Life. Lecture Notes on Comp. Sci. 6046, pp. 232–239, 2011.

[AVI13] Avino, S., Giorgini, A., Malara, P., Gagliardi, G., and de Natale, P. Investigating the resonance spectrum of optical frequency combs in fiber–optic cavities. Opt. Exp. 21(11), pp. 13785–13793, 2013.

[AYA12] Ayanzadeh, R., Zavar Mousavi, A. S., and Shahamatnia, E. Fuzzy Cellular Automata Based Random Numbers Generation. Trends in Appl. Sci. Resear. 7(1), pp. 96–102, 2012.

[BET09] Betel, H., and Flochinni, P. On the Asymptotic Behavior of Fuzzy Cellular Automata, Electr. Notes in Theor. Compt. Sci. 252, pp. 23–40, 2009.

[BET11] Betel, H. and Flocchini, P. On the Relationship Between Boolean and Fuzzy Cellular Automata, Theor. Compt. Sci. 412, pp. 703–713, 2011.

[BET12] Betel, H. Properties and behaviors of fuzzy cellular automata. PhD These, School of Electrical Engineering and Computer Science, Faculty of Engineering, University of Ottawa, 2012.

[BET13] Betel, H., de Oliviera, P.P.B, and Flocchini, P. Solving the Parity Problem in one–Dimensional Cellular Automata. Natural Comp. 12(3), pp. 323–337, 2013.

[BOT11] Botia, J.F. Metodología para las conexiones automáticas entre estados funcionales a partir de clustering difuso. M.S. Thesis. Universidad de Antioquia, 2011.

[BOT13] Botía, J.F., Isaza, C., Kempowsky, T., Le Lann, M.V., and Aguilar−Martin, J. Automaton based on fuzzy clustering methods for monitoring industrial processes. Eng. Appl. Artif. Intell. 26(4), pp. 1211−1220, 2013.

[BETH05] Beth, T. and Leuchs, G. Quantum Information Processing. Second Edition, Wiley–VCH, Weinheim, Germany, ch. 30, 2005.

[BEZ81] Bezdek, J.C. Pattern Recognition with Fuzzy Objective Function Algorithms. Edit Plenum Publishing Corporation, New York, USA, 1981.

[BIN09] Binh, Le N. Uncertainty aspects of coherent and direct detection of amplitude shift keying and continuous phase frequency shift keying in optical fiber transmission. Optic. Eng. 48(5), 055005, 2009.

[BLO88] Blow, K. J., and Wood, D. Mode–Locked Laserswith Nonlinear External Cavities. J. Opt. Soc. Am. B **5,** pp. 629–632, 1988.

[BOT13] Botía, J.F., Isaza, C., Kempowsky, T., Le Lann, M. V., and Aguilar–Martín, J. Automaton based on fuzzy clustering methods for monitoring industrial processes, Eng. Appl. Artif. Intell. 26(4), pp. 1211–1220, 2013.

[BRA14] Brasch, V., Herr, T., Geiselmann, M., Lihachev, G., Pfeiffer, M. H. P., Gorodetsky, M. L., and Kippenberg, T. J. Photonic chip based optical frequency comb using soliton induced Cherenkov radiation. Phys. Opt. 14(10), pp. 1–14, 2014.

[BRO75] Brouwer, L. E. J. Collected Works, vol. 1. North Holland, Amsterdam, 1975.

[BRU08] Brummitt, C. D., Delventhal, H., and Retzlaff, M. Packard Snowflackes on the von Neumann Neighborhood. J. of Cellular Automata 3(1), pp. 57–79, 2008.

[BUC02] Buckley, J. J. and Eslami, E. An introduction to fuzzy logic and fuzzy sets. Physica–Verlag GmbH & Co, Heidelberg, 2002.

[BUR96] Burillo, P. and Bustince, H. Entropy on intuitionistic fuzzy sets and on interval–valued fuzzy sets, Fuzzy Sets and Systems 78(3), pp. 305–316, 1996.

[CAI13] Cai, S. Z. and Zhang, Q. F. An interval type–2 fuzzy cellular automaton model for traffic flow. Adv. Mater. Resea. 4423, pp. 756–759, 2013.

[CAT93] Cattaneo, G., Flocchini, P., Mauri, G., and Santoro, N. Fuzzy cellular automata and their chaotic behavior. Proc. Int. Symp. on Nonlinear Theory and its Appl. 4, IEICE, 1993.

[CAT97] Cattaneo, G., Flocchini, P., Mauri, G., Quaranta–Vogliotti, C., and Santoro, N. Cellular automata in fuzzy backgrounds, Physica D 105, pp. 105–120, 1997.

[CHA98] Chang, C. C., Sardesai, H. P., and Weiner, A. M. Dispersion–free fiber transmission for femtosecond pulses by use of a dispersion–compensating fiber and a programmable pulse shaper. Opt. Lett. 23(4), pp. 283–285, 1998.

[CHAI15] Chai, C. and Wong, Y. D. Fuzzy cellular automata model for signalized intersections, Computer–Aided Civil and Infrastructure Eng. 30 (12), pp. 951–964, 2015

[CHE10] Chen, T–Y. and Li, C–H. Determining objective weights with intuitionistic fuzzy entropy measures: A comparative analysis. Inf. Sci. 180, pp. 4207–4222, 2010.

[CHEN14] Chen, C., Zhang, C., Zhang, W., Zhang, W., Jin, W. and Qiu, K. Scalable and reconfigurable generation of flat optical comb for WDM–based next–generation broadband optical access networks. Opt. Comm. 321, pp. 16–22, 2014.

[CHEM10] Chembo Y. K. and Yu, N. Modal expansion approach to optical–frequency–comb generation with monolithic whispering–gallery–mode resonators. Phys. Rev. A 82, 033801, 2010.

[CHI14] Chitgarha, M. R., Khaleghi, S., Ziyadi, M., Almaiman, A., Mohajerin–Ariaei, A., Gerstel, O., Paraschis, L., Langrock, C., Fejer, M. M., Touch, J., and Willner, A. E. Demonstration of tunable optical generation of higher–order modulation formats using nonlinearities and coherent frequency comb. Opt. Lett. 39(16), pp. 4915–4918, 2014.

[CHO08] Chong, A., Renninger, W. H., and Wise, F. W. Properties of normal–dispersion femtosecond fiber lasers. J. Opt. Soc. Am. B 25, 140, 2008.

[CHU11] Liu, H. –Chaun, Yu, Y. –K, Tsai, H. –C, Liu, T. –S., and Jeng, B. –C. An extensional fuzzy C–means clustering algorithm based on intuitionistic extension index, Procc. of Machine Learn. And Cyber., 2011 Int. Conf. on, pp. 199–203, 2011.

[COE13] Coen, S. and Erkintalo, M. Universal scaling laws of Kerr frequency combs. Opt. Lett. 38(11), pp. 1790–1792, 2013.

[COO04] Cook, M. Universality in Elementary Cellular Automata, Complex Syst. 15, pp. 1–40, 2004.

[COR03] Cornelis, C. and Kerre, E.E. Inclusion measures in intuitionistic fuzzy set theory. ECSQARU 2003, Lecture Notes in Artif. Intell. 2711, pp. 345–356, 2003.

[CORK07] Corkun, P. B., and Krausz, F. Attosecond science, Nature Phys. 3, pp. 381–387, 2007.

[DAN89] Danailov, M. B. and Christov, I. P. Time–space shaping of light pulses by Fourier optical processing, J. Mod. Opt. 36, pp. 725 731, 1989.

[DAI13] Dai, B., Gao, Z., Wang, X., Chen, H., Kataoka, N., and Wada, N. Generation of versatile waveforms from CW light using a dual–drive Mach–Zehnder modulator and employing chromatic dispersion, J. Lightwave Tech. 31(1), pp. 145–151, 2013.

[DIE06] Diez–Lledo, E. and Aguilar–Martín, J. Proposition of NON–probabilistic entropy as reliability index for decision making. CCIA, pp. 137–144, 2006.

[DIE08] Diez–Lledo, E. Diagnostic et prognostic de défaillances dans des composants d'un moteur d'avion. Ph.D. Thèse, LAAS–CNRS, Toulouse, France, 2008.

[DOM99] Dombi, J. DeMorgan class and negations. In: Proceedings of EUROFUSE–SIC'99: The fourth meet. of the EURO Working Group on Fuzzy Sets and The Second Inter. Conf. on Soft and Intell. Comp., pp. 335–344, 1999.

[DOR05] Dorrer, C. and Walmsley, I.A. Concepts for the temporal characterization of short optical pulses. J. on Appl. Signal Process. 10, pp. 1541–1553, 2005.

[DRI96] Driankov, D., Hellendoorn, H., and Reinfrank, M. An Introduction to Fuzzy Control. Heidelberg: Springer, 1996.

[DUO11] Dou, Y., Zhang, H., and Yao, M. Improvement of flatness of optical frequency comb based on nonlinear effect of intensity modulator, Opt. Lett. 36(14), pp. 2749–2751, 2011.

[DU13] Du, J., Dai, Y., Lei, G. K. P., and Shu, C. Using SBS loop for extinction ratio enhancement and flatness imrpovement in optical comb generation. IEEE–OFC/NFOEC, pp. 1–3, 2013.

[DUA09] Duarte, F. J. Generalized multiple–prism dispersion theory for laser pulse compression: higher order

phase derivatives. Appl. Phys B 96, pp. 809–814, 2009.

[DUG97] Dugan, M. A., Tull, J. X., and Warren, W. S. High–resolution acousto–optic shaping of unamplified and amplified femtosecond laser pulses. J. Opt. Soc. Of Ame. B: Opt. Phys. 14, pp. 2348–2358, 1997.

[DUN73] Dunn, J. C. A fuzzy relative of the ISODATA process and its use in detecting compact well–separated clusters. J. Cyber. 3, pp. 32–57, 1973.

[ELL01] Ell, R., Morgner, U., Kartner, F. X., Fujimoto, J. G., Ippen, E. P., Scheuer, V., Angelow, G., Tsuchudi T., Lederer M. J., Boiko, A. and Luther–Davies, B. Generation of 5–fs pulses and octave–spanning spectra directly from a Ti:sapphire laser. Opt. Lett. 26**,** pp. 373–375, 2001.

[ELY10] ElYacoubi, S. and Mingarelli, A. B. An algebraic characterization of fuzzy cellular automata. J. Cellular Automata 6(1), pp. 195–206, 2010.

[ELY11] ElYacoubi, S. and Mingarelli, A. B. Controlling the dynamics of FCA rule 90 in [0,1]T. J. Cellular Automata 6(2), pp. 163–180, 2011.

[ERI14] Erickson, R.P., Vissers, M. R., Sandberg, M., Jefferts, S. R., and Pappas, D. P. Frequency comb generation in superconducting resonators. Phys. Rev. Lett. 113(18), pp. 187002–187007, 2014.

[ERK14] Erkintalo, M. and Coen, S. Coherence properties of Kerr frequency combs. Opt. Lett. 39(2), pp. 283–286, 2014.

[FAT11] Fatemi, A. Entropy of stochastic intuitionistic fuzzy sets. J. Appl. Sci. 11(4), pp. 748–751, 2011.

[FEN09] Li, D.−F., Wang, Y.−C., Liu, S., and Shan, F. Fractional programming methodology for multi−attribute group decision−making using IFS. Appl. Soft Comp. 9, pp. 219−225, 2009.

[FER05] Fermann, M. E., Galvanauskas, A., and Sucha, G. Ultrafast lasers: Technology and applications. Marcel Dekker Inc., part II: Applications, 2005.

[FERD11] Ferdous, F., Miao, H., Leaird, D. E., Srinivasan, K., Wang, J., Chen, L., Varghese, L. T., and Weiner, A. M. Spectral line–by–line pulse shaping of on–chip microresonator frequency combs. Nature Photonics 5(12), pp. 770–776, 2011.

[FLO00] Flocchini, P., Geurts, F., Mingarelli, A., and Santoro, N. Convergence and Aperiodicity in Fuzzy Cellular Automata: Revisiting Rule 90, J. Physica D 142(1), pp. 20–28, 2000.

[FLO01] Flocchini, P. and Cezar, V. Radial View of Continuous Cellular Automata, Fundamenta Informaticae XXI, pp. 1001–1018, 2001.

[FOM05] Fomundam, L. Modeling uncertainty in optical communication systems. Undergraduate Honors Thesis, Department of Mathematics and Statistics, University of Maryland, Baltimore County, USA, 2005.

[FRE09] Frei, F., Galler, A., and Feurer, T. Space–time coupling in femtosecond pulse shaping and its effects on coherent control. J. Chem. Phys.130, 034302, 2009.

[GAR70] Gardner, M. Mathematical games – the fantastic combinations of joining Conway's new solitaire game 'life'. Scientific American, 223: 120–123, 1970.

[GEN07] Gentil, Sylviane. Supervision des procédés complexes. Hermes science publications, France, 2007.

[GOH05] Ghole, C., Udem, T., Herrmann, M., Rauschenberger, J., Holzwarth, R., Schuessler, H. A., Krausz, F., and Hansch, T. W. A Frequency Comb in the Extreme Ultraviolet. Nature 436, pp. 234–237, 2005.

[GOL08] Gollub, C. Femtosecond quantum control studies on vibrational quantum information processing. Ph.D. thesis. Ludwig–Maximilians Univ., Munich, Germany, 2008.

[GON12] Gong, Z., Lin, Y., and Yao, T. Uncertain fuzzy preference relations and their applications. Springer–Verlag Berlin and Heidelberg GmbH & Co.K. Berlin, Germany, 2012.

[GUS79] Gustafson, D.E. and Kessel, W.C. Fuzzy Clustering with a Fuzzy Covariance Matrix. Proc. IEEE CDC 17, pp. 761–766, 1979.

[GUS92] Gustafson, D. and Kessel, W. Fuzzy Clustering with a Fuzzy Covariance Matrix. IEEE on FMPR, 1992 reprinted from Proc. IEEE CDC 1979.

[HAA80] Haavisto, J. and Pajer, G. A. Resonance effects in low–loss ring waveguides. Opt. Lett. 5, pp. 510–512, 1980.

[HAG97] Hagness, S. C., Rafizadeh, D., Ho, S. T., and Taflove, A. FDTD microcavity simulations: design and experimental realization of waveguide–coupled single–mode ring and whispering–gallery–mode disk resonators. J. Light. Tech. 15, pp. 2154–2165, 1997.

[HAY07] Del' Haye, P., Schliesser, A., Arcizet, O., Wilken, T., Holzwarth, R., and Kippenberg, T. J. Optical frequency comb generation from a monolithic microresonator. Nature 450, pp. 1214–1217, 2007.

[HAY08] Del' Haye, Arcizet, O., Schliesser, A., Holzwarth, R., and Kippenberg, T. J. Full stabilization of a microresonator–based optical frequency comb. Phys. Rev. Lett. 101, 053903, 2008.

[HAY09] Del' Haye, Herr, T., Gavartin, E., Holzwarth, R., and Kippenberg, T. J. Octave spanning frequency comb on a chip. DOI: http://arxiv.org/abs/0912.4890, pp. 1–6, 2009.

[HAY11] Del' Haye, T. Herr, E. Gavartin, M. L. Gorodetsky, R. Holzwarth, and T. J. Kippenberg. Octave spanning tunable frequency comb from a microresonator. Phys. Rev. Lett. 107, 063901, 2011.

[HEE08] Heebner, J., Grover, R., and Ibrahim, T. A. Optical microresonator. Springer–Verlag, London, UK, 2008.

[HER14] Herr, T., Brash, V., Jost, J. D., Wang, C. Y., Kondratiev, N. M., Gorodetskky, M. L., and Kippenberg, T. J. Temporal solitons in optical microresonator, Nature Photo. 8, pp. 145–152, 2014.

[HERN06] Hernández de León, H. R. Supervision et diagnostic des procédés de production d'eau potable. Ph.D. Thèse, LAAS–CNRS, Toulouse, France, 2006.

[HRA14] Hraghi, A., Menif, M., and Ben Abid, S. Optimization of optical flat comb source based on Dual–Arm Mach–Zehnder modulator for flexgrid terabit superchannel WDM–Nyquist systems, Transparent Optical Networks (ICTON), 2014 16th Int. Conf. on, p. 1–4, 2014.

[HU15] Hu, W., Wang, H., Peng, C., Wang, H., Liang, H., Du, B. An outer–inner fuzzy cellular automata algorithm for dynamic uncertainty multi–project scheduling problem, Soft Comput. 19 (8), p. 2111–2132, 2015.

[HUA08] Huang, C.–B. Control and characterization of phase–modulated continuous–wave laser frequency combs, P. D. Thesis, Purdue University, USA, p. 2, 2008.

[HUAN11] Huang, Z., Xianmin, Z., Zheng, S., Jin, X., and Chi, H. Any bias point control Mach−Zehnder electrooptic modulator and its applications in optimization of radio−over−fiber links. Micro. Photo. 2011, Int. Tropical Meet. on & Micro. Photo. Conf. Asia−Pacific MWP/APMP, pp. 218−221, 2011.

[HUN03] Hung, W–L. A note on entropy of intuitionistic fuzzy sets. Int. J. Uncertainly, Fuzziness and Knowledge–Based Syst. 10(1), pp. 725–736, 2003.

[HUN06] Hung, W–L. and Yang, M–S. Fuzzy entropy on intuitionistic fuzzy sets. Int. J. Intell. Syst. 21(4), pp. 443–451, 2006.

[IPP75] Ippen, E. P. and Shank, C.V. Dynamic spectroscopy and subpicosecond pulse compression. Appl. Phys. Lett. 27(9), pp. 488–490, 1975.

[ISA07] Isaza, C. Thèse Diagnostic Par Techniques D'Apprentissage Floues : Conception D'Une Méthode de Validation et D'Optimisation dans Partitions. Ph.D. Thèse, LAAS–CNRS, Toulouse, France, 2007.

[ISA08] Isaza, C., Le Lann, M.V., and Aguilar–Martín, J. Diagnosis of chemical processes by fuzzy clustering methods: New optimization method of partitions. 18th European Symp. on Comp. Aided Process Eng.–ESCAPE 18, pp. 1–6, 2008.

[ISA14] Isaza, C., Sarmiento, H. O., Kempowsky−Hamon, T., and LeLann, M.−V. Situation prediction based on fuzzy clustering for industrial complex processes. Inf. Sci. 279, pp. 785−804, 2014.

[JIA05] Jiang, Z., Yang, S. D., Leaird, D. E., and Weiner, A. M., Fully dispersion–compensated ~500 fs pulse transmission over 50 Km single–mode fiber. Opt. Lett. 30, pp. 1449–1451, 2005.

[JIA07] Jiang, Z. Huang, C.–B., Leaird, D. E., and Weiner, A. M. Optical arbitrary waveform processing of more than 100 spectral comb lines, Nature Photo. 1, pp. 463–467, 2007.

[JOH14] Johnson, A. R., Okawachi, Y., Lamont, M. R. E., Levy, J. S., Lipson, M., and Gaeta, A. L. Microresonator–based comb generation without an external laser source. Opt. Exp. 22(2), pp. 1394–1401, 2014.

[JON00] Jones, D. J., Diddams, S. A., Ranka, J. K., Stentz, A., Windeler, R. S., Hall, J. L., and Cundiff, S. T. Carrier–envelope phase control of femtosecond mode–locked lasers and direct optical frequency synthesis. Science 288, pp. 635–639, 2000.

[KAR05] Kari, J. Theory of Cellular Automata: A survey, Theoretical Computer Science 334(3), pp. 3–33, 2005.

[KARN96] Karna, S. and Yeates, A. (ed.). Nonlinear Optical Materials: Theory and Modeling. Washington, DC: American Chemical Society, 1996.

[KAS98] Kasabov, N. K. Foundations of Neural Networks, Fuzzy Systems, and Knowledge Engineering. The MIT Press, Cambridge, Massachusetts, 1998.

[KEL94] Keller, U. Ultrafast All–Solid–State Laser Technology. Appl. Phys. B 58, pp. 347–363, 1994.

[KEM04] Kempowsky, T. Thèse Surveillance de Procèdes à Base de Méthodes de Classification : Conception d'un Outil d'Aide Pour la Détection et le Diagnostic des Défaillances. LAAS – CNRS, Toulouse, France, 2004.

[KEM06] Kempowsky, T., Subias, A. and Aguilar–Martin, J. Process Situation Assessment: From a Fuzzy Partition to a Finite State Machine. Eng. Appl. Art. Intell.19(5), pp. 461–477, 2006.

[KIP04] Kippenberg, T. J., Spillane, S. M., and Vahala, K. J. Kerr–nonlinearity optical parametric oscillation in an ultrahigh–Q toroid microcavity. Phys. Rev. Lett. 93(8), 083904, 2004.

[KIP11] Kippenberg, T. J., Holzwarth, R., and Diddams, S. A. Microresonator–Based Optical Frequency Combs. Science 332, pp. 555–559, 2011.

[KOS86] Kosko, B. Fuzzy Entropy and Conditioning. Inf. Sci. 40, pp. 165–174, 1986.

[KRY72] Kryukov, P. G. and Letokhov, V. S. Fluctuation mechanism of ultrashort pulse generation by laser with saturable absorber. IEEE J. Quan. Electron. 8(766), 1972.

[KUN14] Kundermann, S., Portuondo–Campa, E., and Lecomte, S. Ultra–low–noise 1 μm optical frequency comb. IEEE Electr. Lett. 50(17), pp. 1231–1232, 2014.

[LAV11] Lavocat–Dubuis, X., Vidal, F., Matte, J. P., Kieffer, J. C. and Ozaki, T. Multiple attosecond pulse generation in relativistically laser–driven overdense plasmas. New J. Phys. 13 023039, 2011.

[LEA09] Leal–Ramirez, C., Castillo, O., and Rodriguez–Diaz, A. Interval type–2 fuzzy cellular model applied to the dynamics of a uni–specific population induced by environment variations. Studies in Comp. Intell., Bio–Inspired Hybrid Intel. Syst. for Image Anal. and Patt. Recog. 256, pp. 33–47, 2009.

[LEAI07] Leaird, D., Jiang, Z., Huang, C. B., Miao, H., Kourogi, M., Imai, K. and Weiner, A. M. Spectral line–by–

line pulse shaping on an optical frequency comb generator. IEEE J. Quan. Electron. 43, pp. 1163–1174, 2007.

[LEE06] Lee, G.–H., Jiang, Z., Xiao, S., and Weiner, A. M. 1700 ps/nm tunable dispersion compensation for 10 Gbit/s RZ lightwave transmission. Electro. Lett. 42(13), pp. 768–769, 2006.

[LEV10] Levy, J. S., Gondarenko, A., Foster, M. A., Turner–Foster, A. C., Gaeta, A. L., and Lipson, M. CMOS–compatible multiple–wavelength oscillator for on–chip optical interconnects. Nature Photo. 4, pp. 37–40, 2010.

[LI12] Li, J., Deng, G., Li, H., and Zeng, W. The relationship between similarity measure and entropy of intuitionistic fuzzy sets. Inf. Sci. 188, pp. 314–321, 2012.

[Li14] Li, W., Wang, W. T., Sun, W. H., Wang, L. X., Liu, J. G., and Zhu, N. H. Generation of flat optical frequency comb using a single polarization modulator and a Brillouin–assisted power equalizer. IEEE Photo. J. 6(2), 1943–0655, 2014.

[LIN14] Lin, K.–P. A novel evolutionary kernel intuitionistic fuzzy C –means clustering algorithm, Fuzzy Systems 22(5), pp. 1074–1087, 2014.

[LIND72] Von der Linde, D. Experimental study of single picosecond light pulses. IEEE J. Quan. Electron. QE–8, 3, pp. 328 –338, 1972.

[LIU05] Liu, X–D., Zheng, S., and Xiong, F–I. Entropy and subsethood for general interval–valued intuitionistic fuzzy sets. FSKD'05, Lecture Notes in Comp, Sci, 3613, pp. 42–52, 2005.

[LUC72] De Luca, A. and Termini, S. A definition of a non–probabilistic entropy in the setting of fuzzy sets theory. Inf. and Control 20, pp. 301–312, 1972.

[MAC12] Macano, J., Yao, P., Shi, S., Zablocki, A., Hamty, C., Martin, R. D., Schuetz, C. A., and Prather, D. W. Full milimiter–wave modulation. Opt. Exp. 20(21), pp. 23623–23629, 2012.

[MAH12] Mahalati, R. N., Askarov, D., Wilde, J. P., and Kahn, J. M. Adaptive control of input field to achieve desired output intensity profile in multimode fiber with random mode coupling. Opt. Exp. 20(13), pp. 14321–14337, 2012.

[MAHA86] Mahapatra, A. and Connors, J. M. High finesse ring resonators fabrication and analysis. In: Integrated Opt. Circu. Eng., Innsbruck, Austria, 1986.

[MAJ05] Maji, P. and Chaudhuri, P. P. Fuzzy Cellular Automata for Modeling Pattern Classifier. IEICE Trans. Inf. & Syst. 88(4), pp. 691–702, 2005.

[MAJ07] Maji, P. and Chaudhuri, P. P. RBFFCA: A hybrid pattern classifier using radial basis function and fuzzy cellular automata. Fundamenta Informaticae 78(3), pp. 369–396, 2007.

[MAJ08] Maji, P. On characterization of attractor basins of fuzzy multiple attractor cellular automata. Fundamenta Informaticae 86(1), pp. 143–168, 2008.

[MAL11] Malykin, G.B. and Pozdnyakova, V.I. Influence of the polarization mode dispersion on the propagation of ultrashort optical pulses in single–mode fiber light guides with very weak linear birefringence and random inhomogeneities. Radiophysics and Quantum Electronics 54(4), pp. 274–283, 2011.

[MAN10] Mantelas, L. A., Hatzichristos, T., and Prastacos, P. A fuzzy cellular automata modeling approach – Accessing urban growth dynamics in linguistic terms. Lect. Notes in Comp. Sci., Theore. Comp. Sci. and General Issues, Comput. Sci. and Its Appl, Springer–Verlag Berlin Heidelberg 6016, pp. 140–151, 2010.

[MAR66] De Maria, A. J., Stetser, D. A., and Heynau, H. Self mode–locking of lasers with saturable absorbers. Appl. Phys. Lett. 8, 174, 1966.

[MAR69] De Maria, A. J., Glenn, W. H., Brienza, M. J., and Mack, M. E. Picosecond laser pulses. Proc. IEEE 57, 2, 1969.

[MARC69] Marcatili, E. A. J. Bends in optical dielectric guides. The Bell System Tech. J. 48, pp. 2103–2132, 1969.

[MART08] Martin, M. J., Foreman, S. M., Schibli, T. R., and Ye, J. Testing ultrafast mode–locking at microhertz relative optical linewidth. Opt. Exp. 17(2), pp. 558–568, 2008.

[MEN06] Menyuk, C. R. and Marks, B. S. Interaction of Polarization Mode Dispersion and Nonlinearity in Optical Fiber Transmission Systems, J. Light. Tech. 24(7), pp. 2806–2826, 2006.

[MIN06a] Mingarelli, A. B. The global evolution of general fuzzy cellular automata. J. Cellular Automata 1(2), pp. 141–164, 2006.

[MIN06b] Mingarelli, A. B. and ElYacoubi, S. On the decidability of the evolution of the fuzzy cellular automaton, FCA 184, V. N. Alexandrov et al. (Eds): ICCS 2006, Part III, LNCS 3993, Springer–Verlag Berlin Heidelberg, pp. 360–366, 2006.

[MON10] Monmayrant, A., Weber, S., and Chatel, B.A. A newcomer's guide to ultrashort pulse shaping and characterization, J. Phys. B: Atomic, Molecular and Opt. Phys. 43(10), pp. 1–34, 2010.

[MOR11] Morohashi, I., Sakamoto, T., Kawanishi, T., and Hosako, I. Frequency Tunable Millimeter Wave Pulse Generation Using Mach–Zehnder–Modulator–Based Flat Comb Generator. Micro. Photo., 2011 Inter. Topical Meet. on & Micro. Photo. Conf., Asia–Pacific MWP/APMP, pp. 89–92, 2011.

[MRA00] Mraz, M., Zimic, N., Lapanja, I., and Bajec, I. Fuzzy cellular automata: from theory to applications. Tools with Artificial Intelligence, 2000. ICTAI 2000. Proc. 12th IEEE Int. Conf. on , pp. 320–323, 2000.

[MUR12] Murphy, M. T., Locke, C. R., Light, P. S., Luiten, A. N., and Lawrence, J. S. Laser frequency combs technique for precise astronomical spectroscopy, Mon. Not. R. Astron. Soc. 000, pp. 1–11, 2012.

[NEL97] Nelson, L. E., Jones, D. J., Tamura, K., Haus, H. A., Ippen, E. P. Ultrashort–pulse fiber ring lasers. Appl. Phys. B 65 275, 1997.

[NEW11] Newbury, N. R. Searching for applications with a fine–tooth comb. Nature Photo. 5, pp. 186–188, 2011.

[NOE12] Noei, Sh., Sargolzaei, S., Ramezanpour, H., and Sargolzaei, A. Fuzzy–cellular automata method for noise cancelation of satellite and radar images and maps. Int. J. of Emerging Tech. & Advan. Eng. 2(7), pp. 404–408, 2012.

[NOH08] Nohadani, O., Birge, J. R., Kartner, F. X., and Bertsimas, D. J. Robust chirped mirrors. Appl. Opt. 47(14), pp. 2630–2636, 2008.

[NUE09] Nuemberger, P., Selle, R., Langhojer, F., Dimier, F., Fechner, S., Gerber, G., and Brixner, T. Polarization–shaped femtosecond laser pulses in the ultraviolet. J. of Opt. A: Pure Appl. Opt. 11(8), pp. 1–8, 2009.

[OHA06] Ohara, T., Takara, H., Yamamoto, T., Masuda, H., Morioka, T., Abe, M., and Takahashi, H. Over–1000–channel ultradense WDM transmission with supercontinuum multicarrier source. J. Ligh. Tech. 24(6), pp. 2311–2317, 2006.

[OME02] Omenetto, F. G., Reitze, D. H., Luce, B. P., Moores, M. D., and Taylor, A. J. Adaptive control methods for ultrafast pulse propagation in optical fibers. J. Selec. Top. in Quan. Elec. 8(3), pp. 690–698, 2002.

[PAL13] Pal, N.R., Bustince, H., Pagola, M., Mukherjee, U.K., Goswami, D.P., and Beliakov, G. Uncertainties with Atanassov's intuitionistic fuzzy sets: Fuzziness and lack of knowledge. Inf. Sci. 228, pp. 61–74, 2013.

[PALM08] Palma Méndez, J. and Marín Morales, R. Inteligencia Artificial: Técnicas, Métodos y Aplicaciones. Edit McGraw – Hill, Madrid, España, 2008.

[PAY89] Payne, S. A., Chase, L. I., Smith, L. R., Kway, W. L., Newkirk, H. W. Laser performance of $LiSrAlF_6:Cr^{3+}$. J. Appl. Phys. 66, pp. 1051–1056, 1989.

[PEL08] Pelekis, N., Iakovidis, D. K., Kotsifakos, E. E., and Kopanakis, I. Fuzzy clustering of intuitionistic fuzzy data, Int. J. of Business Intell. and Data Mining 3(1), pp. 45–65, 2008.

[PER11] Peretti, R., Jacquier, B., Boivin, D., Burov, E., and Jurdyc, A.–M. Inhomogeneous Gain Saturation in EDF: Experiment and Modeling. J. of Light. Tech. 29(10), pp. 1445–1452, 2011.

[PFE14] Pfeifle, J., Brasch, V., Lauermann, M., Yu, Y., Wegner, D., Herr, T., Hartinger, K., Schindler, P., Li, J., Hillerkuss, D., Schmogrow, R., Weimann, C., Holzwarth, R., Freude, W., Leuthold, J., Kippenberg, T. J., and Koos, C. Coherent terabit communications with microresonator Kerr frequency combs. Nature Photo. 8, pp. 375–380, 2014.

[PIE89] Piera, N., Deroches, P. and Aguilar−Martin, J. LAMDA: An Incremental Conceptual Clustering Method. LAAS –CNRS, report (89420), Toulouse, France, 1989.

[PIE91] Piera, N. and Aguilar–Martín, J. Controlling Selectivity in Non–Standard Pattern Recognition Algorithms. IEEE Trans. On Sys., Man and Cyber. 21, 1991.

[PLA13] Placzek, B. A traffic model based on fuzzy cellular automata, J. Cellular Automata 8(4), pp. 261–282, 2013.

[POP10] Popmintchev, T., Chen, M.–C. Arpin, P., Murnane, M. M., and Kapteyn, H. C. The Attosecond Nonlinear Optics of Bright Coherent X–Ray Generation, Nature Photo. 4, pp. 822–832, 2010.

[PRE14] Preussler, S., Wenzel, N., and Schneider, T. Flat, rectangular frequency comb generation with tunable bandwidth and frequency spacing. Opt. Lett. 39(6), pp. 1637–1640, 2014.

[QUE10] Quevedo, J., Puig, V., Cembrano, G., Blanch, J., Aguilar, J., Saporta, D., Benito, G., Hedo, M., and Molina, A. Validation and reconstruction of flow meter data in the Barcelona water distribution network. Control Eng. Prac. 18(6), pp. 640–651, 2010.

[RAJ11] Rajurkar, H.V. Simulated design and analysis of PMD–induced broadening of ultrashort pulses in optical fiber communication system. Int. J. of Eng. Sci. and Tech., NCICT February Special Issue, pp. 128–132, 2011.

[RAM10] Ramaswami, R., Sivarajan, K N., and Sasaki, G. H. Optical Networks: A Practical Perspective. Third Edition, Morgan Kaufman Publishers, USA, 2010.

[REX00] Rex, N. B., Chang, R. K., and Guido, L. J. Threshold minimization and directional laser emission from GaN microdisks. In: Laser Resonators, San Jose, CA, 2000.

[RÜT12] Rützel, S., Krischke, A., and Brixner, T. The von Neumann representation as a joint time–frequency parameterization for polarization–shaped femtosecond laser pulses. Applied Physics B 107, pp.1–9, 2012.

[SAK07a] Sakamoto, T., Kawanishi, T., and Izutsu, M. Widely wavelength–tunable ultra–flat frequency comb generation using conventional dual–drive Mach−Zehnder modulator. Electr. Lett. 43(19), pp. 1039–1040, 2007.

[SAK07b] Sakamoto, T., Kawanishi, T., and Izutsu, M. Optimization of Electro–Optic Comb Generation Using Conventional Mach–Zehnder Modulator. Micro. Photo., Int. Topi. Meet. On, pp. 50–53, 2007.

[SAM08] Samá Monosonis, A. Tesis: Estudio y Desarrollo de Sistema LAMDA Para Aprendizaje Automático y Toma de Decisiones, MA2, Universitat Politécnica de Catalunya, Barcelona, España, 2008.

[SAN03] Sano, T., Iwashima, T., Katayama, M., Kanie, T., Harumoto, M., Shigehara, M., Suganuma, H., and

Nishimura, M. Novel multichannel tunable chromatic dispersion compensator based on MEMS and diffraction grating. IEEE Photo. Tech. Lett. 15(8), pp.1109–1110, 2003.
[SAR00] Sarkar, P. A brief history of cellular automata. ACM Computing Surveys 32(1), pp. 80–107, 2000.
[SCH14] Schratwieser, T. C., Balskus, K., McCracken, R. A., Farrell, C., Leburn, C. G., Zhang, Z., Lamour, T. P., Ferreiro, T. I., Marandi, A., Arnold, A. S., and Reid, D. T. ^{87}Rb–stabilized 375–MHz Yb:fiber femtosecond frequency comb. Opt. Exp. 22(9), pp. 10494–10499, 2014.
[SET08] Seth, A., Bandyopadhyay, S., and Maulik, U. Probabilistic analysis of cellular automata rules and its application in pseudo random pattern generation. Int. J. of Appl. Math. 38(4), pp. 205–213, 2008.
[SHA14] Shang, L., Wen, A., Lin, G., and Gao, Y. A flat and broadband optical frequency comb with tunable bandwidth and frequency spacing. Opt. Comm. 311, pp. 262–266, 2014.
[SHAP93] Shapiro, J. H. Composition Operators and Classical Function Theory. Springer Science+Business Media, New York, USA, 1993.
[SHE10] Shemirani, M. B., Wilde, J. P., and Kahn, J. M. Adaptive compensation of multimode fiber dispersion by control of launched amplitude, phase, and polarization. J. Ligh. Tech. 28(18), pp. 2627–2639, 2010.
[SMI70] Smith, P. W. Mode–locking of lasers, Proc. IEEE 58(9), pp. 1342–1357, 1970.
[SON12] Song, M. Microwave Photonic Filter Design Via Optical Frequency Comb Shaping. Ph.D. Thesis, School of Materials and Electrical Engineering, Faculty of Engineering, Purdue University, 2012.
[STO82] Stokes, L. F., Chodorow, M., and Shaw, H. J. All–single–mode fiber resonator. Opt. Lett. 7, pp. 288–290, 1982.
[SUG97] Sugeno, M. Fuzzy Measures and Fuzzy Integrals. North Holland, 1997.
[SUP12] Supradeepa V. R. and Weiner, A. M. Bandwidth scaling and spectral flatness enhancement of optical frequency combs from phase–modulated continuous–wave lasers using cascaded four–wave mixing, Opt. Lett. 37(15), pp. 3066–3068, 2012.
[ŠVA10] Švarný, J. Analysis of quadrature bias-point drift of Mach−Zehnder electro−optic modulator, 12th Bienal Baltic Electr. Conf. BEC, pp. 231−234, 2010.
[ŠVA14] Švarný, J. Bias driver of the Mach−Zehnder intensity electro−optic modulator, based on harmonic analysis. Procc. of Adv. In Robotics, Mechatronics and Circuits pp. 184−189, 2014.
[SZM01] Szmidt, E. and Kacprzyk, J. Entropy for intuitionistic fuzzy sets. Fuzzy Sets and Syst. 118, pp. 467–477, 2001.
[SZM14a] Szmidt, E. Kacprzyk, J., and Bujnowski, P. How to measure the amount of knowledge conveyed by Atanassov's intuitionistic fuzzy sets. Inf. Sci. 257, pp. 276–285, 2014.
[SZM14b] Szmidt, E. Distances and Similarities in Intuitionistic Fuzzy Sets. Springer Science+Business Media, 2014.
[TOR14] Torres–Company, V. and Weiner, A. M. Optical frequency comb technology for ultra–broadband radio–frequency photonics. Laser Photo. Rev. 8(3), pp. 368–393, 2014.
[UDE02] Udem, T., Holzwarth, R., and Hansch, T. W. Optical frequency metrology. Nature 416(14), pp. 233–237, 2002.
[UGU15] Ugu, S., Sahin U., and Sahin, F. Edge detection with fuzzy cellular automata transition function optimized by PSO, Computers & Electrical Eng. 43, pp. 180 –192, 2015.
[ULR72] Ulrich, R. and Weber, H. P. Solution–deposited thin films as passive and active light–guides. Appl. Opt. 11, pp. 428–434, 1972.
[URI10] Uribe, C., Isaza, C., Gualdron, O., Duran, C., and Carvajal, A. A wrapper approach based on clustering for sensors selection of industrial monitoring systems. BWCCA, 2010 Inter. Conf. on, pp. 482−487, 2010.
[VER13] Verma, R. and Sharma, B.D. Exponential entropy on intuitionistic fuzzy sets. Kybernetika 49(1), pp. 114–127, 2013.
[VIS10] Visalakshi, N. K., Thangavel, K., and Parvathi, R. An intuitionistic fuzzy approach to distributed fuzzy clustering, Int. J. of Comp. Theo. And Eng. 2(2), pp. 295–302, 2010.
[VLA07] Vlachos, I.K. and Sergiadis, G.D. Intuitionistic fuzzy information–Application to pattern recognition, Patt. Recog. Lett. 28, pp. 197–206, 2007.
[VOE11] Voelz, D. Computational Fourier Optics: A Matlab tutorial. USA: SPIE Press, 2011.
[WAF09] Wafula Waswa, D. Compensation for polarization mode dispersion and nonlinear birefringence in a multichannel optical fibre system. Ph.D Thesis, Faculty of Sci., Nelson Mandela Metropolitan Univ., 2009.
[WAL83] Walker, R. G. and Wilkinson, C. D. W. Integrated optical ring resonators made by silver ion–exchange in glass. Appl. Opt. 22, pp. 1029–1035, 1983.
[WAN14] Wang, Q., Huo, L., Xing, Y., and Zhou, B. Ultra–flat optical frequency comb generator using a single–driven dual–parallel Mach–Zehnder modulator. Opt. Lett. 39(10), pp. 3050–3053, 2014.
[WANG14] Wang, P.−H., Xuan, Y., Wang, J., Xue, X., Leaird, D. E., Qi, M., and Weiner, A. M. Coherent Frequency Comb Generation in a Silicon Nitride Microresonator with Anomalous Dispersion, in CLEO: OSA Technical Digest (Online), paper SF2E.3, 2014.
[WEI95] Weiner, A. M. Femtosecond optical pulse shaping and processing. Prog. Quantum Electron. 19(3), pp.

161–237, 1995.

[WEI00] Weiner, A. M. Femtosecond pulse shaping using spatial light modulators. Rev. Sci. Instr. 71(5), pp. 1929–1960, 2000.

[WEI09] Weiner, A. M. Ultrafast Optics. First Edition, Wiley & Sons, USA, 2009.

[WEI11] Weiner, A. M. Ultrafast optical pulse shaping: A tutorial review. Opt. Comm. 284, pp. 3669–3692, 2011.

[WEN14] Wen, L., Chao, G., Yun–Yun, W., Yi, T., Qi, L., Hong–Mei, L., and Xin–Yang, L. Experimental demonstration of single–mode fiber coupling using adaptive fiber coupler. Chin. Phys. B 23(1), pp. 1–7, 2014.

[WOL02] Wolfram, S. A New Kind of Science. Champaing: Wolfram Media, 2002.

[WU14] Wu, S., Li, Y., Fei, Y., and Hu, F. Z. Generation of flat optical frequency comb based on Mach–Zehnder Modulator and recirculating frequency shifter loop. Opt. Comm. 35(2), pp. 101–107, 2014.

[XU08] Xu, Z., Chen, J., and Wu, J. Clustering algorithm for intuitionistic fuzzy sets, Inf. Sci. 178, pp. 3775–3790, 2008.

[XUE15] Xue, X., Xuan, Y., Liu, Y., Wang, P.−H., Chen, S., Wang, J., Leaird, D. E., Qi, M., and Weiner, A. M. Mode−locked dark pulse Kerr combs in normal−dispersion microresonators. Nature Photo. 9, pp. 594−600, 2015.

[YAG80] Yager, R.R. On the measure of fuzziness and negation. part II. lattices. Inf. and Control 44, pp. 236–260, 1980.

[YAG93] Yager, R. R. Counting the number of classes in a fuzzy set. IEEE Trans. On Syst., Man, and Cyber. 23(1), pp. 257−264, 1993.

[YAG09] Yager, R. R. Some aspects of intuitionistic fuzzy sets, Fuzzy Optim. Decis. Mak. 8(1), pp. 67–90, 2009.

[YE10] Ye, J. Two effective measures of intuitionistic fuzzy entropy. Comp. 87, pp. 55–62, 2010.

[YEP12] Yepes, H. and Cardenas, A. M. Optical Combs configuration for WDM and OFDM access networks. 4th IEEE Latin–Amercan Conf. on Comm. 2012 (Latincom 2012), 2012.

[YOS11] Yost, D. C., Cingöz, A., Allison, T. K., Ruehl, A., Fermann, M. E., Hartl, I., and Ye, J. Power optimization of XUV frequency combs for spectroscopy applications, Opt. Exp. 19(23), pp. 23483 – 23493, 2011.

[YOU09] Yousaf Hamza, M. Mitigation of SPM and GVD Effects in Fiber Optic Communications by Dispersion–and Power–Map Co–Optimization Using Genetic Algorithm, Ph.D. thesis. Dept. Comp. Science, Univ. of Man. Sciences, Lahore, Pakistan, 2009.

[ZAD65] Zadeh, L. Fuzzy sets. Information and Control 8, pp. 338–353, 1965.

[ZAP12] Zapata, J. D. Estudio del PMD desde un punto de vista clásico en fibras ópticas mono–modo. M.S. Tesis, Instituto de Física, Universidad de Antioquía, Medellín, Colombia, 2012.

[ZEE00] Zeek, E. Pulse shaping for high–harmonic generation. P. D. Thesis, University of Michigan, 2000.

[ZHU14] Zhu, X., Zheng, Z., Zhang, C., Zhu, L., Tao, Z., and Chen, Z. Coherent detection−based automatic bias control of Mach−Zehnder modulators for various modulation formats. J. Light. Tech. 32(14), pp. 2502−2509, 2014.

[ZIM01] Zimmermann, H.–J. Fuzzy set theory–and its applications. Springer Netherlands, 2001.

[ZOU13] Zou, X., Li, W., Pan,W., Yan, L., and Yao, J. Photonic–Assisted Microwave Channelizer with Improved Channel Characteristics Based on Spectrum–Controlled Stimulated Brillouin Scattering. Microw. Theory Tech. 61(9), pp. 3470–3478, 2013.

VITA

Javier Fernando Botía Valderrama was born in Sogamoso, Colombia in 1985. He received his B.S. in Electronic Engineering from "Universidad Santo Tomás − USTA", Tunja, Colombia, in 2008. He has a specialization degree in Electronic Instrumentation from "Universidad Santo Tomás − USTA", Tunja, Colombia, in 2008. The M. S. degree in Engineering – Emphasis on Automatic was received in 2011 at the "Universidad de Antioquia − UdeA", Medellin, Colombia. Since 2011, he has been pursuing his Ph.D degree on Electronic Engineering at the "Universidad de Antioquia − UdeA", Medellin, Colombia. Currently, he is professorship in the department of electronic and telecommunications engineering, and the department of computer science at the UdeA. He has achieved researches in the Research Group on Applied Telecommunications (GITA – acronym in Spanish) on prediction approaches based on fuzzy sets theory, fuzzy expansions, intuitionistic fuzzy sets, fuzzy entropy, and fuzzy cellular automata, for analysis and compensation of OFC spectra generated by mode−locked lasers, IMs−MZM, and microresonator rings.

During his Ph.D studies, Javier has authored and co−authored over 7 publications in conferences and journals (3 publications during the M.S. studies and 4 publications in the PhD studies). He has been assessor of two M.S. theses developed in GITA and reviewer of one final work of undergraduate from Department of Telecommunications Engineering. He has been reviewer for Journal of Applied Mathematics and Computing, Journal of Applied Computer Communication & Collaboration, Optics Communications, IEEE Latin−American Transactions, and "Revista Politécnica − Colombia". In addition, He has been reviewer of several international conferences, congress, and workshops such as IEEE−STSIVA 2012−2015, COMTEL 2013−2015, IEEE−CIICT 2011, 2013, and 2015, and CICIC 2011 – 2015. Since 2009, he is an active member of "Sociedad Colombiana de Física".

ANNEX

A.1 Demonstration Eq. (3.5)

From Eq. (3.5):

$$E_A^{(2)} = \frac{RET\left(A \cap A^c\right)}{RET\left(A \cup A^c\right)}$$

where:

$$RET\left(A \cap A^c\right) = \sum_{n=1}^{N}\left[\delta_A\left(x_n\right) \wedge \delta_A^c\left(x_n\right)\right];\ RET\left(A \cup A^c\right) = \sum_{n=1}^{N}\left[\delta_A\left(x_n\right) \vee \delta_A^c\left(x_n\right)\right]$$

Taking into account the propositions (P.1)–(P.4), defining for Eq. (3.3), it is obtained:

Proof:

(P.1) If $\delta_A(x)$ and $\delta_A^c(x) = 1 - \delta_A(x) = \mu_A(x)$ (when $\mu m_A = 1$, for FS(A)) are Singleton function, then there exists one sample x_i such that $\mu_A(x_n) = \mu m_A = 1$ (if FS(A) is normal) and therefore, $[\delta_A(x_n) = 0 \wedge \delta_A^c(x_n) = 1] = 0$ and $[\delta_A(x_n) = 0 \vee \delta_A^c(x_i) = 1] = 1$. Considering the above case and for the rest samples of universe of discourse $\mu_A(x) = 0$, then it is sufficient to obtain $E_A^{(2)} = 0$.

(P.2) If $\delta_A(x) = \delta_A^c(x)$ for all $x \in X$, then $E_A^{(2)} = 1$.

(P.3) Considering $FS(A^*)$, then:

$$E_{A^*}^{(2)} = \frac{RET\left(A^* \cap A^{*c}\right)}{RET\left(A^* \cup A^{*c}\right)}$$

Then, if it is considered:

$$E_A^{(2)} - E_{A^*}^{(2)} = \frac{RET\left(A \cap A^c\right)}{RET\left(A \cup A^c\right)} - \frac{RET\left(A^* \cap A^{*c}\right)}{RET\left(A^* \cup A^{*c}\right)}$$

If $\delta_A^c(x) > \delta_A(x)$ and $\delta_{A^*}^c(x) > \delta_A^*(x)$, then $\delta_A^c(x) > \delta_A(x) > \delta_{A^*}^c(x) > \delta_A^*(x)$, for all $x \in X$:

$$\frac{\sum_{n=1}^{N}\delta_A(x_n)}{\sum_{n=1}^{N}\delta_A^c(x_n)}-\frac{\sum_{n=1}^{N}\delta_{A^*}(x_n)}{\sum_{n=1}^{N}\delta_{A^*}^c(x_n)}=0$$

$$\frac{\sum_{n=1}^{N}\delta_A(x_n)}{\sum_{n=1}^{N}\delta_A^c(x_n)}\geq\frac{\sum_{i=1}^{N}\delta_{A^*}(x_n)}{\sum_{n=1}^{N}\delta_{A^*}^c(x_n)}$$

And therefore:

$$\frac{\sum_{n=1}^{N}\left[\delta_A(x_n)\wedge\delta_A^c(x_n)\right]}{\sum_{n=1}^{N}\left[\delta_A(x_n)\vee\delta_A^c(x_n)\right]}\geq\frac{\sum_{n=1}^{N}\left[\delta_{A^*}(x_n)\wedge\delta_{A^*}^c(x_n)\right]}{\sum_{n=1}^{N}\left[\delta_{A^*}(x_n)\vee\delta_{A^*}^c(x_n)\right]}$$

To sum up, if $\delta_A{}^c(x) > \delta_A(x) > \delta_{A^*}{}^c(x) > \delta_A{}^*(x)$, for all $x \in X$, it is sufficient condition for $E_A{}^{(2)} \geq E_{A^*}{}^{(2)}$.

(P.4) If the complement of A, $A^c(\delta_A{}^c(x), \delta_A(x))$ for all $x \in X$, then $E_A{}^{(2)} = E_A{}^{c\,(2)}$.□

A.2 Demonstration Eq. (3.6)

From Eq. (3.6):

$$E_A^{(3)} = \frac{\sum_{n=1}^{N} Q_A(x_n)\exp\left(Q_A(x_n)\right)}{\sum_{n=1}^{N} L_A(x_n)\exp\left(L_A(x_n)\right)}$$

where $Q_A(x_n) = 1-\delta_A(x_n) \wedge 1-\delta_A^c(x_n)$ and $L_A(x_n) = 1-\delta_A(x_n) \vee 1-\delta_A^c(x_n)$.

Taking into account the propositions (P.1)–(P.4), defining for Eq. (3.3), it is obtained:

Proof:

(P.1) If $\mu_A(x) = 1$ (when $\mu m_A = 1$, for FS(A)) for all $x \in X$, then $E_A^{(3)} = 0$.

(P.2) If $\delta_A(x) = \delta_A^c(x)$ for all $x \in X$, then $E_A^{(3)} = 1$.

(P.3) Considering $FS(A^*)$, then:

$$E_{A^*}^{(3)} = \frac{\sum_{n=1}^{N} Q_{A^*}(x_n)\exp\left(Q_{A^*}(x_n)\right)}{\sum_{n=1}^{N} L_{A^*}(x_n)\exp\left(L_{A^*}(x_n)\right)}$$

And:

$$E_A^{(3)} - E_{A^*}^{(3)} = \frac{\sum_{n=1}^{N} Q_A(x_n)\exp\left(Q_A(x_n)\right)}{\sum_{n=1}^{N} L_A(x_n)\exp\left(L_A(x_n)\right)} - \frac{\sum_{n=1}^{N} Q_{A^*}(x_n)\exp\left(Q_{A^*}(x_n)\right)}{\sum_{n=1}^{N} L_{A^*}(x_n)\exp\left(L_{A^*}(x_n)\right)}$$

As $\delta_A^c(x) > \delta_A(x) > \delta_{A^*}^c(x) > \delta_A^*(x)$, for all $x \in X$, then $Q_A(x) = 1-\delta_A(x) \wedge 1-\delta_A^c(x) = 1-\delta_A^c(x)$, $L_A(x) = 1-\delta_A(x) \vee 1-\delta_A^c(x) = 1-\delta_A(x)$, $Q_A^*(x) = 1-\delta_A^*(x) \wedge 1-\delta_A^{*\,c}(x) = 1-\delta_A^{*\,c}(x)$, and $L_A^*(x) = 1-\delta_A^*(x) \vee 1-\delta_A^{*\,c}(x) = 1-\delta_A^*(x)$. Therefore:

$$\frac{\sum_{n=1}^{N}\left[1-\delta_A^c(x_n)\right]\exp\left(1-\delta_A^c(x_n)\right)}{\sum_{n=1}^{N}\left[1-\delta_A(x_n)\right]\exp\left(1-\delta_A(x_n)\right)} - \frac{\sum_{n=1}^{N}\left[1-\delta_{A^*}^c(x_n)\right]\exp\left(1-\delta_{A^*}^c(x_n)\right)}{\sum_{n=1}^{N}\left[1-\delta_{A^*}(x_n)\right]\exp\left(1-\delta_{A^*}(x_n)\right)} = 0$$

$$\frac{\sum_{n=1}^{N}\left[1-\delta_A^c(x_n)\right]\exp\left(1-\delta_A^c(x_n)\right)}{\sum_{n=1}^{N}\left[1-\delta_A(x_n)\right]\exp\left(1-\delta_A(x_n)\right)} \geq \frac{\sum_{n=1}^{N}\left[1-\delta_{A^*}^c(x_n)\right]\exp\left(1-\delta_{A^*}^c(x_n)\right)}{\sum_{n=1}^{N}\left[1-\delta_{A^*}(x_n)\right]\exp\left(1-\delta_{A^*}(x_n)\right)}$$

Therefore, if $\delta_A{}^c(x) > \delta_A(x) > \delta_{A^*}{}^c(x) > \delta_A{}^*(x)$, for all $x \in X$, it is sufficient condition for $E_A{}^{(3)} \geq E_{A^*}{}^{(3)}$.

(P.4) The preposition is fulfilled if the complement of A, $A^c(\delta_A{}^c(x), \delta_A(x))$ for all $x \in X$, then $E_A{}^{(3)} = E_A{}^{c\,(3)}$.□

A.3 Demonstration Eq. (3.12) and (3.13)

From Eq. (3.12) and Eq. (3.13):

$$H_{R1}(A)=\frac{1}{N}\sum_{n=1}^{N}\left[1-\left|\mu_A(x_n)-\upsilon_A(x_n)\right|\right]$$

$$H^{*}_{R1}(A)=\frac{1}{N}\sum_{n=1}^{N}\left[\frac{\gamma^2\left(1-\left|\mu_A(x_n)-\upsilon_A(x_n)\right|\right)}{\gamma^2\left(1-\left|\mu_A(x_n)-\upsilon_A(x_n)\right|\right)+(1-\gamma)^2\left|\mu_A(x_n)-\upsilon_A(x_n)\right|}\right]$$

Taking into account the propositions (P.1)–(P.4), defining for Eq. (3.12) and Eq. (3.13), it is shown that:

Proof:

(P.1) If $\upsilon_A(x) = 0$ and $\mu_A(x) = 1$, for all $x \in X$, then $H_{R1}(A) = H^{*}_{R1}(A) = 0$ for any value of γ in $\pi_A^{*}(x)$. On the other hand, when $\upsilon_A(x) = 1$ and $\mu_A(x) = 0$, for all $x \in X$, the condition is also fulfilled.

(P.2) For all $x \in X$, if $\mu_A(x) = \upsilon_A(x)$, $H_{R1}(A) = H^{*}_{R1}(A) = 1$.

(P.3) Considering IFS(B), $B = \langle (x, \mu_B(x), \upsilon_B(x)) | \; x \in X \rangle$, the goal is shown that $H_{R1}(A) < H_{R1}(B)$, and $H^{*}_{R1}(A) < H^{*}_{R1}(B)$. Initially, $H_{R1}(A) < H_{R1}(B)$ will be demonstrated. From Eq. (3.12), it can be written as follows:

$$H_{R1}(A)=1-\frac{1}{N}\sum_{n=1}^{N}\left|\mu_A(x_n)-\upsilon_A(x_n)\right| \text{ and } H_{R1}(B)=1-\frac{1}{N}\sum_{n=1}^{N}\left|\mu_B(x_n)-\upsilon_B(x_n)\right|$$

Taking into account $\mu_A(x) \le \mu_B(x) \le \upsilon_B(x) \le \upsilon_A(x)$, for all $x \in X$, $H_{R1}(A)$ and $H_{R1}(B)$ are rewritten as:

$$H_{R1}(A)=1+\frac{1}{N}\sum_{n=1}^{N}\left(\mu_A(x_n)-\upsilon_A(x_n)\right) \text{ and } H_{R1}(B)=1+\frac{1}{N}\sum_{n=1}^{N}\left(\mu_B(x_n)-\upsilon_B(x_n)\right)$$

If $H_{R1}(B) - H_{R1}(A)$ is used as a condition for finding $H_{R1}(A) < H_{R1}(B)$, then:

$$H_{R1}(B)-H_{R1}(A)=1+\frac{1}{N}\sum_{n=1}^{N}\left(\mu_B(x_n)-\upsilon_B(x_n)\right)-\left(1+\frac{1}{N}\sum_{n=1}^{N}\left(\mu_A(x_n)-\upsilon_A(x_n)\right)\right)$$

$$H_{R1}(B)-H_{R1}(A)=\frac{1}{N}\left(\sum_{n=1}^{N}\left(\mu_B(x_n)-\mu_A(x_n)\right)\right)+\frac{1}{N}\left(\sum_{i=1}^{N}\left(\upsilon_A(x_n)-\upsilon_B(x_n)\right)\right)$$

As the cardinalities $\sum_{n=1}^{N}\mu_A(x_n)\leq\sum_{n=1}^{N}\mu_B(x_n)$ and $\sum_{n=1}^{N}\upsilon_B(x_n)\leq\sum_{n=1}^{N}\upsilon_A(x_n)$, then the terms from $H_{R1}(B) - H_{R1}(A)$ are positive, and therefore, $H_{R1}(A) < H_{R1}(B)$. If $\mu_A(x) \geq \mu_B(x) \geq \upsilon_B(x) \geq \upsilon_A(x)$, $H_{R1}(A)$ and $H_{R1}(B)$ are written as:

$$H_{R1}(A)=1+\frac{1}{N}\sum_{n=1}^{N}\left(\upsilon_A(x_n)-\mu_A(x_n)\right) \text{ and } H_{R1}(B)=1+\frac{1}{N}\sum_{n=1}^{N}\left(\upsilon_B(x_n)-\mu_B(x_n)\right)$$

Carrying out $H_{R1}(B) - H_{R1}(A)$, it is obtained:

$$H_{R1}(B)-H_{R1}(A)=\frac{1}{N}\left(\sum_{n=1}^{N}\left(\mu_A(x_n)-\mu_B(x_n)\right)\right)+\frac{1}{N}\left(\sum_{n=1}^{N}\left(\upsilon_B(x_n)-\upsilon_A(x_n)\right)\right)$$

In that case, $\sum_{n=1}^{N}\mu_A(x_n)\geq\sum_{n=1}^{N}\mu_B(x_n)$ and $\sum_{n=1}^{N}\upsilon_B(x_n)\geq\sum_{n=1}^{N}\upsilon_A(x_n)$, and therefore, $H_{R1}(A) < H_{R1}(B)$.

On the other hand, to show that $H^*_{R1}(A) < H^*_{R1}(B)$, both are defined as:

$$H_{R1}^{*}(A)=\frac{1}{N}\sum_{n=1}^{N}\left[\frac{\gamma^2\left(1-\left|\mu_A(x_n)-\upsilon_A(x_n)\right|\right)}{\gamma^2\left(1-\left|\mu_A(x_n)-\upsilon_A(x_n)\right|\right)+(1-\gamma)^2\left|\mu_A(x_n)-\upsilon_A(x_n)\right|}\right]$$

$$H_{R1}^{*}(B)=\frac{1}{N}\sum_{n=1}^{N}\left[\frac{\gamma^2\left(1-\left|\mu_B(x_n)-\upsilon_B(x_n)\right|\right)}{\gamma^2\left(1-\left|\mu_B(x_n)-\upsilon_B(x_n)\right|\right)+(1-\gamma)^2\left|\mu_B(x_n)-\upsilon_B(x_n)\right|}\right]$$

Taking into account $H^*_{R1}(A)$ and $H^*_{R1}(B)$, we indicate that $H^*_{R1}(B) - H^*_{R1}(A) > 0$, in order to show that $H^*_{R1}(A) < H^*_{R1}(B)$, as follows:

$$H_{R1}^{*}(B)-H_{R1}^{*}(A)=\frac{1}{N}\left[\sum_{n=1}^{N}\left[\frac{\gamma^2\left(1-\left|\mu_A(x_n)-\upsilon_A(x_n)\right|\right)}{\gamma^2\left(1-\left|\mu_A(x_n)-\upsilon_A(x_n)\right|\right)+(1-\gamma)^2\left|\mu_A(x_n)-\upsilon_A(x_n)\right|}\right]-\sum_{n=1}^{N}\left[\frac{\gamma^2\left(1-\left|\mu_B(x_n)-\upsilon_B(x_n)\right|\right)}{\gamma^2\left(1-\left|\mu_B(x_n)-\upsilon_B(x_n)\right|\right)+(1-\gamma)^2\left|\mu_B(x_n)-\upsilon_B(x_n)\right|}\right]\right]$$

Since $0 \leq \gamma \leq 1/2$, the last equation can be rewritten for $\gamma = 1/2$, as shown below:

$$H_{R1}^{*}(B)-H_{R1}^{*}(A)=\frac{1}{N}\left[\sum_{n=1}^{N}\left[\frac{1-\left|\mu_A(x_n)-\upsilon_A(x_n)\right|}{1-\left|\mu_A(x_n)-\upsilon_A(x_n)\right|+\left|\mu_A(x_n)-\upsilon_A(x_n)\right|}\right]-\sum_{n=1}^{N}\left[\frac{1-\left|\mu_B(x_n)-\upsilon_B(x_n)\right|}{1-\left|\mu_B(x_n)-\upsilon_B(x_n)\right|+\left|\mu_B(x_n)-\upsilon_B(x_n)\right|}\right]\right]$$

$$H_{R1}^{*}(B)-H_{R1}^{*}(A)=\frac{1}{N}\left[\sum_{n=1}^{N}\left[1-\left|\mu_A(x_n)-\upsilon_A(x_n)\right|\right]-\sum_{n=1}^{N}\left[1-\left|\mu_B(x_n)-\upsilon_B(x_n)\right|\right]\right]$$

$$H_{R1}^{*}(B)-H_{R1}^{*}(A)=\frac{1}{N}\sum_{n=1}^{N}1-\frac{1}{N}\sum_{n=1}^{N}\left|\mu_B(x_n)-\upsilon_B(x_n)\right|-\frac{1}{N}\sum_{n=1}^{N}1+\frac{1}{N}\sum_{n=1}^{N}\left|\mu_A(x_n)-\upsilon_A(x_n)\right|$$

$$H_{R1}^{*}(B)-H_{R1}^{*}(A)=\frac{1}{N}\sum_{n=1}^{N}\left|\mu_A(x_n)-\upsilon_A(x_n)\right|-\frac{1}{N}\sum_{n=1}^{N}\left|\mu_B(x_n)-\upsilon_B(x_n)\right|$$

Considering $\mu_A(x) \le \mu_B(x) \le \upsilon_B(x) \le \upsilon_A(x)$, for all $x \in X$, then:

$$H_{R1}^{*}(B)-H_{R1}^{*}(A)=-\frac{1}{N}\sum_{n=1}^{N}\left[\mu_A(x_n)-\upsilon_A(x_n)\right]+\frac{1}{N}\sum_{n=1}^{N}\left[\mu_B(x_n)-\upsilon_B(x_n)\right]$$

$$H_{R1}^{*}(B)-H_{R1}^{*}(A)=\frac{1}{N}\sum_{n=1}^{N}\left[\mu_B(x_n)-\mu_A(x_n)\right]+\frac{1}{N}\sum_{n=1}^{N}\left[\upsilon_A(x_n)-\upsilon_B(x_n)\right]$$

In that case, $\sum_{n=1}^{N}\mu_B(x_n) \ge \sum_{n=1}^{N}\mu_A(x_n)$ and $\sum_{n=1}^{N}\upsilon_A(x_n) \ge \sum_{n=1}^{N}\upsilon_B(x_n)$, and therefore, $H^{*}_{R1}(A) \le H^{*}_{R1}(B)$. By considering the second condition, $\mu_A(x) \ge \mu_B(x) \ge \upsilon_B(x) \ge \upsilon_A(x)$, for all $x \in X$, it is obtained:

$$H_{R1}^{*}(B)-H_{R1}^{*}(A)=\frac{1}{N}\sum_{n=1}^{N}\left[\mu_A(x_n)-\upsilon_A(x_n)\right]-\frac{1}{N}\sum_{n=1}^{N}\left[\mu_B(x_n)-\upsilon_B(x_n)\right]$$

$$H_{R1}^{*}(B)-H_{R1}^{*}(A)=\frac{1}{N}\sum_{n=1}^{N}\left[\mu_A(x_n)-\mu_B(x_n)\right]+\frac{1}{N}\sum_{n=1}^{N}\left[\upsilon_B(x_n)-\upsilon_A(x_n)\right]$$

From the last equation, $\sum_{n=1}^{N}\mu_A(x_n) \ge \sum_{n=1}^{N}\mu_B(x_n)$ and $\sum_{n=1}^{N}\upsilon_B(x_n) \ge \sum_{n=1}^{N}\upsilon_A(x_n)$, which $H^{*}_{R1}(A) \le H^{*}_{R1}(B)$ is fulfilled. Since both conditions were evaluated for $\gamma = 1/2$, $H^{*}_{R1}(A) = H_{R1}(A)$ and $H^{*}_{R1}(B) = H_{R1}(B)$, and for $\gamma = 0$, $H^{*}_{R1}(A) = H^{*}_{R1}(B) = 0$, being the minimum value of intuitionistic fuzzy entropy.

For any γ–value ($0 \le \gamma \le 1/2$), we rewritten $H^{*}_{R1}(B) - H^{*}_{R1}(A)$, as follow:

$$H_{R1}^{*}(B)-H_{R1}^{*}(A)=\frac{1}{N}\sum_{n=1}^{N}\left[\frac{\gamma^2\left(1-\left|\mu_A(x_n)-\upsilon_A(x_n)\right|\right)}{\gamma^2\left(1-\left|\mu_A(x_n)-\upsilon_A(x_n)\right|\right)+(1-\gamma)^2\left|\mu_A(x_n)-\upsilon_A(x_n)\right|}-\frac{\gamma^2\left(1-\left|\mu_B(x_n)-\upsilon_B(x_n)\right|\right)}{\gamma^2\left(1-\left|\mu_B(x_n)-\upsilon_B(x_n)\right|\right)+(1-\gamma)^2\left|\mu_B(x_n)-\upsilon_B(x_n)\right|}\right]$$

Carrying out an algebraic operation, $H^{*}_{R1}(B) - H^{*}_{R1}(A)$ is defined as:

$$H_{R1}^{*}(B)-H_{R1}^{*}(A)=\frac{1}{N}\sum_{n=1}^{N}\left[\frac{\gamma^2(1-\gamma)^2\left[\left|\mu_A(x_n)-\upsilon_A(x_n)\right|+\left|\mu_B(x_n)-\upsilon_B(x_n)\right|\right]}{DEM_{|A,B|}(x_n)}\right]$$

Being $DEM_{|A,B|}(x_n)$:

$$DEM_{|A,B|}(x_n)=\gamma^4+(2\gamma+1)^2\left[\left|\mu_A(x_n)-\upsilon_A(x_n)\right|\cdot\left|\mu_B(x_n)-\upsilon_B(x_n)\right|\right]+\gamma^2(1-2\gamma)\left[\left|\mu_A(x_n)-\upsilon_A(x_n)\right|+\left|\mu_B(x_n)-\upsilon_B(x_n)\right|\right]$$

Considering $\mu_A(x) \le \mu_B(x) \le \upsilon_B(x) \le \upsilon_A(x)$, for all $x \in X$, it is obtained:

$$H_{R1}^{*}(B)-H_{R1}^{*}(A)=\frac{1}{N}\sum_{n=1}^{N}\left[\frac{\gamma^2(1-\gamma)^2\left[\left(\mu_B(x_n)-\mu_A(x_n)\right)+\left(\upsilon_A(x_n)-\upsilon_B(x_n)\right)\right]}{DEM^{(1)}_{(A,B)}(x_n)}\right]$$

where:

$$DEM^{(1)}_{(A,B)}(x_n)=\gamma^4+(2\gamma+1)^2\left[\left(\upsilon_A(x_n)-\mu_A(x_n)\right)\cdot\left(\mu_B(x_n)-\upsilon_B(x_n)\right)\right]+\gamma^2(1-2\gamma)\left[\left(\mu_B(x_n)-\mu_A(x_n)\right)+\left(\upsilon_A(x_n)-\upsilon_B(x_n)\right)\right]$$

The relation $H^{*}_{R1}(B) - H^{*}_{R1}(A)$ can be redefined as follow:

$$H_{R1}^{*}(B)-H_{R1}^{*}(A)=\frac{1}{N}\sum_{n=1}^{N}\left[\frac{\gamma^2(1-\gamma)^2\left(\mu_B(x_n)-\mu_A(x_n)\right)}{DEM^{(1)}_{(A,B)}(x_n)}\right]+\frac{1}{N}\sum_{n=1}^{N}\left[\frac{\gamma^2(1-\gamma)^2\left(\upsilon_A(x_n)-\upsilon_B(x_n)\right)}{DEM^{(1)}_{(A,B)}(x_n)}\right]$$

For that case:

$$\frac{1}{N}\sum_{n=1}^{N}\left[\frac{\gamma^2(1-\gamma)^2\mu_B(x_n)}{DEM^{(1)}_{(A,B)}(x_n)}\right]\ge\frac{1}{N}\sum_{n=1}^{N}\left[\frac{\gamma^2(1-\gamma)^2\mu_A(x_n)}{DEM^{(1)}_{(A,B)}(x_n)}\right]$$

$$\text{and } \frac{1}{N}\sum_{n=1}^{N}\left[\frac{\gamma^2(1-\gamma)^2\upsilon_A(x_n)}{DEM^{(1)}_{(A,B)}(x_n)}\right]\geq\frac{1}{N}\sum_{n=1}^{N}\left[\frac{\gamma^2(1-\gamma)^2\upsilon_B(x_n)}{DEM^{(1)}_{(A,B)}(x_n)}\right]$$

Being $DEM^{(1)}_{(A,B)}(x)>0$ if $\mu_A(x) \leq \mu_B(x) \leq \upsilon_B(x) \leq \upsilon_A(x)$, for all $x \in X$. Such conditions allow establishing $H^*_{R1}(A) < H^*_{R1}(B)$ for any γ–value.

Taking into account $\mu_A(x) \geq \mu_B(x) \geq \upsilon_B(x) \geq \upsilon_A(x)$, for all $x \in X$, it is obtained:

$$H_{R1}{}^*(B)-H_{R1}{}^*(A)=\frac{1}{N}\sum_{n=1}^{N}\left[\frac{\gamma^2(1-\gamma)^2\left[\left(\mu_A(x_n)-\mu_B(x_n)\right)+\left(\upsilon_B(x_n)-\upsilon_A(x_n)\right)\right]}{DEM^{(2)}_{(A,B)}(x_n)}\right]$$

where:

$$\begin{aligned}DEM^{(2)}_{(A,B)}(x_n)=\gamma^4+(2\gamma+1)^2\left[\left(\mu_A(x_n)-\upsilon_A(x_n)\right)\cdot\left(\upsilon_B(x_n)-\mu_B(x_n)\right)\right]\\ +\ \gamma^2(1-2\gamma)\left[\left(\mu_A(x_n)-\mu_B(x_n)\right)+\left(\upsilon_B(x_n)-\upsilon_A(x_n)\right)\right]\end{aligned}$$

Organizing $H^*_{R1}(B) - H^*_{R1}(A)$, then:

$$H_{R1}{}^*(B)-H_{R1}{}^*(A)=\frac{1}{N}\sum_{n=1}^{N}\left[\frac{\gamma^2(1-\gamma)^2\left(\mu_A(x_n)-\mu_B(x_n)\right)}{DEM^{(2)}_{(A,B)}(x_n)}\right]+\frac{1}{N}\sum_{n=1}^{N}\left[\frac{\gamma^2(1-\gamma)^2\left(\upsilon_B(x_n)-\upsilon_A(x_n)\right)}{DEM^{(2)}_{(A,B)}(x_n)}\right]$$

And therefore:

$$\frac{1}{N}\sum_{n=1}^{N}\left[\frac{\gamma^2(1-\gamma)^2\mu_A(x_n)}{DEM^{(2)}_{(A,B)}(x_n)}\right]\geq\frac{1}{N}\sum_{n=1}^{N}\left[\frac{\gamma^2(1-\gamma)^2\mu_B(x_n)}{DEM^{(2)}_{(A,B)}(x_n)}\right]$$

$$\text{and } \frac{1}{N}\sum_{n=1}^{N}\left[\frac{\gamma^2(1-\gamma)^2\upsilon_B(x_n)}{DEM^{(2)}_{(A,B)}(x_n)}\right]\geq\frac{1}{N}\sum_{n=1}^{N}\left[\frac{\gamma^2(1-\gamma)^2\upsilon_A(x_n)}{DEM^{(2)}_{(A,B)}(x_n)}\right]$$

Being $DEM^{(2)}_{(A,B)}(x)>0$ if $\mu_A(x) \geq \mu_B(x) \geq \upsilon_B(x) \geq \upsilon_A(x)$, for all $x \in X$. Based on the above, the condition $H^*_{R1}(A) < H^*_{R1}(B)$ fulfills for any γ–value.

(P.4) For $A^c = \langle(x,, \upsilon_A(x), \mu_A(x))| x \in X\rangle$, $H_{R1}(A) = H_{R1}(A^c)$ and $H^*_{R1}(A) = H^*_{R1}(A^c)$ are fulfilled. □

A.4 Demonstration Eq. (3.15)

From Eq. (3.15):

$$H_{AN}(A)=1-\left[\frac{Q+W}{N\cdot\exp(1)}\right]$$

where:

$$Q=\left|\sum_{i=1}^{N}\left(1-\mu_A(x_i)\right)\exp\left(1-\mu_A(x_i)\right)-\sum_{i=1}^{N}\left(1-\upsilon_A(x_i)\right)\exp\left(1-\upsilon_A(x_i)\right)\right|$$

$$W=\left|\sum_{i=1}^{N}\left|\mu_A(x_i)-\upsilon_A(x_i)\right|\exp\left(\left|\mu_A(x_i)-\upsilon_A(x_i)\right|\right)-\right.$$

$$\sum_{i=1}^{N}\left(1-\frac{\gamma^2\left(1-\left|\mu_A(x_i)-\upsilon_A(x_i)\right|\right)}{\gamma^2\left(1-\left|\mu_A(x_i)-\upsilon_A(x_i)\right|\right)+(1-\gamma)^2\left|\mu_A(x_i)-\upsilon_A(x_i)\right|}\right)$$

$$\left.\exp\left(1-\frac{\gamma^2\left(1-\left|\mu_A(x_i)-\upsilon_A(x_i)\right|\right)}{\gamma^2\left(1-\left|\mu_A(x_i)-\upsilon_A(x_i)\right|\right)+(1-\gamma)^2\left|\mu_A(x_i)-\upsilon_A(x_i)\right|}\right)\right|$$

Taking into account the propositions (P.1)–(P.4) where it is the same defines for Eq. (3.12) and Eq. (3.13), it is shown that:

Proof:

(P.1) Considering $\mu_A(x) = 1$ and $\upsilon_A(x) = 0$, for all $x \in X$, it is shown that:

$$Q=\left\|\left[\sum_{n=1}^{N}\delta_A(x_n)\exp\left(\delta_A(x_n)\right)=0\right]-\left[\sum_{n=1}^{N}\xi_A(x_n)\exp\left(\xi_A(x_n)\right)=N\cdot\exp(1)\right]\right\|=N\cdot\exp(1)$$

$$W=\left|N\cdot\exp(1)-N\cdot\exp(1)\right|=0$$

$$H_{AN}(A)=1-\left[\frac{N\cdot\exp(1)}{N\cdot\exp(1)}\right]=0$$

The above allows demonstrating $H_{AN}(A) = 0$, for all $x \in X$. When $\mu_A(x) = 0$ and $\upsilon_A(x) = 1$, the condition is fulfilled.

(P.2) If $\mu_A(x) = \upsilon_A(x)$, for all $x \in X$, $W = Q = 0$, and therefore, $H_{AN}(A) = 1$.

(P.3) Taking into account $B = \langle (x, \mu_B(x), \upsilon_B(x)) | \; x \in X \rangle$, the goal is demonstrated $H_{AN}(A) < H_{AN}(B)$ through $H_{AN}(B) - H_{AN}(A)$, as shown below:

$$H_{AN}(B) - H_{AN}(A) = 1 - \frac{W_B + Q_B}{N \cdot \exp(1)} - \left[1 - \frac{W_A + Q_A}{N \cdot \exp(1)}\right] =$$

$$\frac{1}{N \cdot \exp(1)}\left[Q_A - Q_B\right] + \frac{1}{N \cdot \exp(1)}\left[W_A - W_B\right]$$

Analyzing the first term of $H_{AN}(B) - H_{AN}(A)$:

$$\frac{1}{N \cdot \exp(1)}\left[Q_A - Q_B\right] =$$

$$\frac{1}{N \cdot \exp(1)}\left[\left|\sum_{n=1}^{N}\left(1-\mu_A(x_n)\right)\exp\left(1-\mu_A(x_n)\right) - \sum_{n=1}^{N}\left(1-\upsilon_A(x_n)\right)\exp\left(1-\upsilon_A(x_n)\right)\right| - \right.$$

$$\left.\left|\sum_{n=1}^{N}\left(1-\mu_B(x_n)\right)\exp\left(1-\mu_B(x_n)\right) - \sum_{n=1}^{N}\left(1-\upsilon_B(x_n)\right)\exp\left(1-\upsilon_B(x_n)\right)\right|\right]$$

From the first definition, $\mu_A(x) \leq \mu_B(x) \leq \upsilon_B(x) \leq \upsilon_A(x)$, for all $x \in X$:

$$\frac{1}{N \cdot \exp(1)}\left[Q_A - Q_B\right] = \frac{1}{N \cdot \exp(1)}\left[\left(\sum_{n=1}^{N}\left(1-\mu_A(x_n)\right)\exp\left(1-\mu_A(x_n)\right) - \sum_{n=1}^{N}\left(1-\mu_B(x_n)\right)\exp\left(1-\mu_B(x_n)\right)\right) + \right.$$

$$\left.\left(\sum_{n=1}^{N}\left(1-\upsilon_B(x_n)\right)\exp\left(1-\upsilon_B(x_n)\right) - \sum_{n=1}^{N}\left(1-\upsilon_A(x_n)\right)\exp\left(1-\upsilon_A(x_n)\right)\right)\right]$$

If $\mu_A(x) \leq \mu_B(x)$, then $1 - \mu_A(x) \geq 1 - \mu_B(x)$, for all $x \in X$; on the other hand, if $\upsilon_B(x) \leq \upsilon_A(x)$, then $1 - \upsilon_B(x) \geq 1 - \upsilon_A(x)$. The above show that the terms from $\frac{1}{N \cdot \exp(1)}\left[Q_A - Q_B\right]$ are positives. From the second definition, $\mu_A(x) \geq \mu_B(x) \geq \upsilon_B(x) \geq \upsilon_A(x)$, for all $x \in X$:

$$\frac{1}{N \cdot \exp(1)}\left[Q_A - Q_B\right] =$$

$$\frac{1}{N \cdot \exp(1)}\left[\left(\sum_{n=1}^{N}\left(1-\mu_B(x_n)\right)\exp\left(1-\mu_B(x_n)\right) - \sum_{n=1}^{N}\left(1-\mu_A(x_n)\right)\exp\left(1-\mu_B(x_n)\right)\right) + \right.$$

$$\left.\left(\sum_{n=1}^{N}\left(1-\upsilon_A(x_n)\right)\exp\left(1-\upsilon_A(x_n)\right) - \sum_{n=1}^{N}\left(1-\upsilon_B(x_n)\right)\exp\left(1-\upsilon_B(x_n)\right)\right)\right]$$

If $\mu_A(x) \geq \mu_B(x)$, then $1 - \mu_B(x) \geq 1 - \mu_A(x)$, for all $x \in X$; when $\upsilon_B(x) \geq \upsilon_A(x)$, then $1 - \upsilon_A(x) \geq 1 - \upsilon_B(x)$. The above indicates that the terms from $\frac{1}{N \cdot \exp(1)}\left[Q_A - Q_B\right]$ are positives. Now, considering the second term of $H_{AN}(B) - H_{AN}(A)$:

$$\frac{1}{N \cdot \exp(1)}\left[W_A - W_B\right] = \frac{1}{N \cdot \exp(1)} \cdot$$

$$\left[\left|\sum_{n=1}^{N}\left|\mu_A(x_n) - \upsilon_A(x_n)\right|\exp\left(\left|\mu_A(x_n) - \upsilon_A(x_n)\right|\right) - \right.$$

$$\sum_{n=1}^{N}\left(1 - \frac{\gamma^2\left(1 - \left|\mu_A(x_n) - \upsilon_A(x_n)\right|\right)}{\gamma^2\left(1 - \left|\mu_A(x_n) - \upsilon_A(x_n)\right|\right) + (1-\gamma)^2\left|\mu_A(x_n) - \upsilon_A(x_n)\right|}\right) \cdot$$

$$\left.\exp\left(1 - \frac{\gamma^2\left(1 - \left|\mu_A(x_n) - \upsilon_A(x_n)\right|\right)}{\gamma^2\left(1 - \left|\mu_A(x_n) - \upsilon_A(x_n)\right|\right) + (1-\gamma)^2\left|\mu_A(x_n) - \upsilon_A(x_n)\right|}\right)\right| -$$

$$\left|\sum_{n=1}^{N}\left|\mu_B(x_n) - \upsilon_B(x_n)\right|\exp\left(\left|\mu_B(x_n) - \upsilon_B(x_n)\right|\right) - \right.$$

$$\sum_{n=1}^{N}\left(1 - \frac{\gamma^2\left(1 - \left|\mu_B(x_n) - \upsilon_B(x_n)\right|\right)}{\gamma^2\left(1 - \left|\mu_B(x_n) - \upsilon_B(x_n)\right|\right) + (1-\gamma)^2\left|\mu_B(x_n) - \upsilon_B(x_n)\right|}\right) \cdot$$

$$\left.\left.\exp\left(1 - \frac{\gamma^2\left(1 - \left|\mu_B(x_n) - \upsilon_B(x_n)\right|\right)}{\gamma^2\left(1 - \left|\mu_B(x_n) - \upsilon_B(x_n)\right|\right) + (1-\gamma)^2\left|\mu_B(x_n) - \upsilon_B(x_n)\right|}\right)\right|\right]$$

If $\mu_A(x) \leq \mu_B(x) \leq \upsilon_B(x) \leq \upsilon_A(x)$, for all $x \in X$:

$$\frac{1}{N \cdot \exp(1)}\left[W_A - W_B\right] = \frac{1}{N \cdot \exp(1)} \cdot$$

$$\left[\sum_{n=1}^{N}\left|\mu_B(x_n) - \upsilon_B(x_n)\right|\exp\left(\left|\mu_B(x_n) - \upsilon_B(x_n)\right|\right) - \sum_{n=1}^{N}\left|\mu_A(x_n) - \upsilon_A(x_n)\right|\exp\left|\mu_A(x_n) - \upsilon_A(x_n)\right|\right] +$$

$$\frac{1}{N \cdot \exp(1)} \cdot \left[\sum_{n=1}^{N}\left(1 - \frac{\gamma^2\left(1 - \left|\mu_A(x_n) - \upsilon_A(x_n)\right|\right)}{\gamma^2\left(1 - \left|\mu_A(x_n) - \upsilon_A(x_n)\right|\right) + (1-\gamma)^2\left|\mu_A(x_n) - \upsilon_A(x_n)\right|}\right) \cdot \right.$$

$$\exp\left(1 - \frac{\gamma^2\left(1 - \left|\mu_A(x_n) - \upsilon_A(x_n)\right|\right)}{\gamma^2\left(1 - \left|\mu_A(x_n) - \upsilon_A(x_n)\right|\right) + (1-\gamma)^2\left|\mu_A(x_n) - \upsilon_A(x_n)\right|}\right) -$$

$$\sum_{n=1}^{N}\left(1 - \frac{\gamma^2\left(1 - \left|\mu_B(x_n) - \upsilon_B(x_n)\right|\right)}{\gamma^2\left(1 - \left|\mu_B(x_n) - \upsilon_B(x_n)\right|\right) + (1-\gamma)^2\left|\mu_B(x_n) - \upsilon_B(x_n)\right|}\right) \cdot$$

$$\left.\exp\left(1 - \frac{\gamma^2\left(1 - \left|\mu_B(x_n) - \upsilon_B(x_n)\right|\right)}{\gamma^2\left(1 - \left|\mu_B(x_n) - \upsilon_B(x_n)\right|\right) + (1-\gamma)^2\left|\mu_B(x_n) - \upsilon_B(x_n)\right|}\right)\right]$$

If $|\mu_A(x) - \upsilon_A(x)| = (\upsilon_A(x) - \mu_A(x))$, when $\mu_A(x) \leq \upsilon_A(x)$, for all $x \in X$, and $|\mu_B(x) - \upsilon_B(x)| = (\upsilon_B(x) - \mu_B(x))$, when $\mu_B(x) \leq \upsilon_B(x)$, for all $x \in X$, then:

$$\sum_{n=1}^{N}\left(\upsilon_B(x_n)-\mu_B(x_n)\right)\exp\left(\upsilon_B(x_n)-\mu_B(x_n)\right)\geq\sum_{n=1}^{N}\left(\upsilon_A(x_n)-\mu_A(x_n)\right)\exp\left(\upsilon_A(x_n)-\mu_A(x_n)\right)$$

and

$$\sum_{n=1}^{N}\left(1-\frac{\gamma^2\left(1-\left(\upsilon_A(x_n)-\mu_A(x_n)\right)\right)}{\gamma^2\left(1-\left(\upsilon_A(x_n)-\mu_A(x_n)\right)\right)+(1-\gamma)^2\left(\upsilon_A(x_n)-\mu_A(x_n)\right)}\right)\cdot \exp\left(1-\frac{\gamma^2\left(1-\left(\upsilon_A(x_n)-\mu_A(x_n)\right)\right)}{\gamma^2\left(1-\left(\upsilon_A(x_n)-\mu_A(x_n)\right)\right)+(1-\gamma)^2\left(\upsilon_A(x_n)-\mu_A(x_n)\right)}\right)$$

$$\leq\sum_{n=1}^{N}\left(1-\frac{\gamma^2\left(1-\left(\upsilon_B(x_n)-\mu_B(x_n)\right)\right)}{\gamma^2\left(1-\left(\upsilon_B(x_n)-\mu_B(x_n)\right)\right)+(1-\gamma)^2\left(\upsilon_B(x_n)-\mu_B(x_n)\right)}\right)\cdot \exp\left(1-\frac{\gamma^2\left(1-\left(\upsilon_B(x_n)-\mu_B(x_n)\right)\right)}{\gamma^2\left(1-\left(\upsilon_B(x_n)-\mu_B(x_n)\right)\right)+(1-\gamma)^2\left(\upsilon_B(x_n)-\mu_B(x_n)\right)}\right)$$

Therefore, the two terms of $\frac{1}{N\cdot\exp(1)}\left[W_A - W_B\right]$ are positives, if $\mu_A(x) \leq \mu_B(x) \leq \upsilon_B(x) \leq \upsilon_A(x)$.

On the other hand, if $\mu_A(x) \geq \mu_B(x) \geq \upsilon_B(x) \geq \upsilon_A(x)$, for all $x \in X$, it is obtained:

$$\frac{1}{N\cdot\exp(1)}\left[W_A - W_B\right]=\frac{1}{N\cdot\exp(1)}\cdot \left[\sum_{n=1}^{N}\left|\mu_B(x_n)-\upsilon_B(x_n)\right|\exp\left(\left|\mu_B(x_n)-\upsilon_B(x_n)\right|\right)-\sum_{n=1}^{N}\left|\mu_A(x_n)-\upsilon_A(x_n)\right|\exp\left(\left|\mu_A(x_n)-\upsilon_A(x_n)\right|\right)\right]+$$

$$\left[\sum_{n=1}^{N}\left(1-\frac{\gamma^2\left(1-\left|\mu_A(x_n)-\upsilon_A(x_n)\right|\right)}{\gamma^2\left(1-\left|\mu_A(x_n)-\upsilon_A(x_n)\right|\right)+(1-\gamma)^2\left|\mu_A(x_n)-\upsilon_A(x_n)\right|}\right)\cdot \exp\left(1-\frac{\gamma^2\left(1-\left|\mu_A(x_n)-\upsilon_A(x_n)\right|\right)}{\gamma^2\left(1-\left|\mu_A(x_n)-\upsilon_A(x_n)\right|\right)+(1-\gamma)^2\left|\mu_A(x_n)-\upsilon_A(x_n)\right|}\right)-\right.$$

$$\left.\sum_{i=1}^{N}\left(1-\frac{\gamma^2\left(1-\left|\mu_B(x_n)-\upsilon_B(x_n)\right|\right)}{\gamma^2\left(1-\left|\mu_B(x_n)-\upsilon_B(x_n)\right|\right)+(1-\gamma)^2\left|\mu_B(x_n)-\upsilon_B(x_n)\right|}\right)\cdot \exp\left(1-\frac{\gamma^2\left(1-\left|\mu_B(x_n)-\upsilon_B(x_n)\right|\right)}{\gamma^2\left(1-\left|\mu_B(x_n)-\upsilon_B(x_n)\right|\right)+(1-\gamma)^2\left|\mu_B(x_n)-\upsilon_B(x_n)\right|}\right)\right]$$

If $|\mu_A(x) - \upsilon_A(x)| \rightarrow (\upsilon_A(x) - \mu_A(x))$, when $\mu_A(x) \geq \upsilon_A(x)$, for all $x \in X$, and $|\mu_B(x) - \upsilon_B(x)| \rightarrow (\upsilon_B(x) - \mu_B(x))$, when $\mu_B(x) \geq \upsilon_B(x)$, for all $x \in X$, then:

$$\sum_{n=1}^{N}\left(\mu_A(x_n)-\upsilon_A(x_n)\right)\exp\left(\mu_A(x_n)-\upsilon_A(x_n)\right)\geq\sum_{n=1}^{N}\left(\mu_B(x_n)-\upsilon_B(x_n)\right)\exp\left(\mu_B(x_n)-\upsilon_B(x_n)\right)$$

and

$$\sum_{n=1}^{N}\left(1-\frac{\gamma^2\left(1-\left(\mu_A(x_n)-\upsilon_A(x_n)\right)\right)}{\gamma^2\left(1-\left(\mu_A(x_n)-\upsilon_A(x_n)\right)\right)+(1-\gamma)^2\left(\mu_A(x_n)-\upsilon_A(x_n)\right)}\right)\cdot$$
$$\exp\left(1-\frac{\gamma^2\left(1-\left(\mu_A(x_n)-\upsilon_A(x_n)\right)\right)}{\gamma^2\left(1-\left(\mu_A(x_n)-\upsilon_A(x_n)\right)\right)+(1-\gamma)^2\left(\mu_A(x_n)-\upsilon_A(x_n)\right)}\right)$$
$$\geq\sum_{n=1}^{N}\left(1-\frac{\gamma^2\left(1-\left(\mu_B(x_n)-\upsilon_B(x_n)\right)\right)}{\gamma^2\left(1-\left(\mu_B(x_n)-\upsilon_B(x_n)\right)\right)+(1-\gamma)^2\left(\mu_B(x_n)-\upsilon_B(x_n)\right)}\right)\cdot$$
$$\exp\left(1-\frac{\gamma^2\left(1-\left(\mu_B(x_n)-\upsilon_B(x_n)\right)\right)}{\gamma^2\left(1-\left(\mu_B(x_n)-\upsilon_B(x_n)\right)\right)+(1-\gamma)^2\left(\mu_B(x_n)-\upsilon_B(x_n)\right)}\right)$$

Two terms of $\frac{1}{N\cdot\exp(1)}\left[W_A - W_B\right]$ are positives, if $\mu_A(x) \geq \mu_B(x) \geq \upsilon_B(x) \geq \upsilon_A(x)$.

According to the demonstrations for $\frac{1}{N\cdot\exp(1)}\left[Q_A - Q_B\right]$ and $\frac{1}{N\cdot\exp(1)}\left[W_A - W_B\right]$, all terms are positives, and therefore, $H_{AN}(A) < H_{AN}(B)$ is satisficed the axiom (P.3).

(P.4) Considering $A^c = \langle(x, \upsilon_A(x), \mu_A(x))| x \in X\rangle$, then $H_{AN}(A) = H_{AN}(A^c)$; therefore, this condition is fulfilled. □

A.5 Validation Indexes Applied to Optical Combs Spectra (Section 3.5)

For the case 1:

V_1 = 6.5 V; $\boldsymbol{V_2}$ **= 6.5 V**; $\Theta_1 = 0°$; $\Theta_2 = 180°$; f_1 = 10 GHz; f_2 = 10 GHz.

Min–Max				Probabilistic			
Exigency Value	**MAD Binomial**	**MAD Centered Binomial**	**MAD Gaussian**	**Exigency Value**	**MAD Binomial**	**MAD Centered Binomial**	**MAD Gaussian**
0.1	$5.94x10^{-5}$	0.00013386	0.0177879	0.1	$5.16x10^{-6}$	$9.15x10^{-5}$	0.00303585
0.2	$5.93x10^{-5}$	0.00012617	0.02381005	0.2	$5.36\ x10^{-6}$	$9.43x10^{-5}$	0.00478542
0.3	0.000105071	0.00012351	0.03126871	0.3	$5.57\ x10^{-6}$	$9.76x10^{-5}$	0.00648804
0.4	0.000207726	0.00012161	0.03441636	0.4	$5.73\ x10^{-6}$	$9.90x10^{-5}$	0.00801142
0.5	0.000304263	0.00010473	0.03616461	0.5	$5.82\ x10^{-6}$	0.00010067	0.00979667
0.6	0.000411643	0.00012261	0.03805218	0.6	$5.84\ x10^{-6}$	0.00010106	0.01240867
0.7	0.000800059	0.00010377	0.03954078	0.7	$5.87\ x10^{-6}$	0.00010106	0.0168014
0.8	0.000919562	$4.78x10^{-5}$	0.02243753	0.8	$5.89\ x10^{-6}$	0.00010107	0.01583607
0.9	0.001502177	$8.74x10^{-5}$	0.03440969	0.9	$5.92\ x10^{-6}$	0.00010107	0.0134375
1	0.004264948	$9.96x10^{-5}$	0.02511624	1	$5.94\ x10^{-6}$	0.00010108	0.0082916

V_1 = 6.5 V; $\boldsymbol{V_2}$ **= 6 V**; $\Theta_1 = 0°$; $\Theta_2 = 180°$; f_1 = 10 GHz; f_2 = 10 GHz.

Min–Max				Probabilistic			
Exigency Value	**MAD Binomial**	**MAD Centered Binomial**	**MAD Gaussian**	**Exigency Value**	**MAD Binomial**	**MAD Centered Binomial**	**MAD Gaussian**
0.1	$2.89x10^{-5}$	0.00011481	0.02859394	0.1	$6.80x10^{-6}$	$7.46x10^{-5}$	0.00187344
0.2	$9.70x10^{-5}$	0.00011363	0.02859485	0.2	$7.06x10^{-6}$	$7.70x10^{-5}$	0.00296102
0.3	0.00014385	0.00011278	0.02626427	0.3	$7.33x10^{-6}$	$7.97x10^{-5}$	0.00340552
0.4	0.0002001	0.00011087	0.03159604	0.4	$7.56x10^{-6}$	$8.27x10^{-5}$	0.0042988
0.5	0.00032056	0.0001028	0.0308016	0.5	$7.66x10^{-6}$	$8.41x10^{-5}$	0.00589469
0.6	0.00038605	$9.56x10^{-5}$	0.03451986	0.6	$7.67x10^{-6}$	$8.44x10^{-5}$	0.00745871
0.7	0.00056467	$8.94x10^{-5}$	0.03583089	0.7	$7.67x10^{-6}$	$8.44x10^{-5}$	0.00840648
0.8	0.00106376	$2.36x10^{-5}$	0.03210929	0.8	$7.68x10^{-6}$	$8.44x10^{-5}$	0.00974983
0.9	0.0017584	$8.04x10^{-5}$	0.02667179	0.9	$7.68x10^{-6}$	$8.44x10^{-5}$	0.0110478
1	0.00178849	$1.88x10^{-4}$	0.02332391	1	$7.69x10^{-6}$	$8.44x10^{-5}$	0.00642846

V_1 = 6.5 V; $\boldsymbol{V_2}$ **= 5.5 V**; $\Theta_1 = 0°$; $\Theta_2 = 180°$; f_1 = 10 GHz; f_2 = 10 GHz.

Min–Max				Probabilistic			
Exigency Value	**MAD Binomial**	**MAD Centered Binomial**	**MAD Gaussian**	**Exigency Value**	**MAD Binomial**	**MAD Centered Binomial**	**MAD Gaussian**
0.1	$3.84x10^{-5}$	0.00010579	0.01740237	0.1	$8.50x10^{-7}$	$8.51x10^{-5}$	0.00457438
0.2	$8.15x10^{-5}$	0.00011096	0.02162157	0.2	$8.86x10^{-7}$	$8.77x10^{-5}$	0.00669576
0.3	0.00011224	0.00010994	0.0188449	0.3	$9.22x10^{-7}$	$9.03x10^{-5}$	0.00894921
0.4	0.00016272	0.00011319	0.01899331	0.4	$9.51x10^{-7}$	$9.18x10^{-5}$	0.01110219
0.5	0.00020996	0.00011842	0.02015762	0.5	$9.66x10^{-7}$	$9.35x10^{-5}$	0.01237502
0.6	0.00021539	$1.38x10^{-4}$	0.02055407	0.6	$9.72x10^{-7}$	$9.39x10^{-5}$	0.01339888
0.7	0.00032948	$7.73x10^{-5}$	0.02181905	0.7	$9.77x10^{-7}$	$9.39x10^{-5}$	0.01540926
0.8	0.00058756	$7.49x10^{-5}$	0.02110009	0.8	$9.82x10^{-7}$	$9.39x10^{-5}$	0.01648141
0.9	0.00054897	$2.77x10^{-5}$	0.02041157	0.9	$9.87x10^{-7}$	$9.40x10^{-5}$	0.01230667
1	0.00313358	$9.27x10^{-5}$	0.01680814	1	$9.93x10^{-7}$	$9.40x10^{-5}$	0.00631471

$V_1 = 6.5$ V; $\boldsymbol{V_2 = 5}$ **V**; $\Theta_1 = 0°$; $\Theta_2 = 180°$; $f_1 = 10$ GHz; $f_2 = 10$ GHz.

Min–Max				Probabilistic			
Exigency Value	**MAD Binomial**	**MAD Centered Binomial**	**MAD Gaussian**	**Exigency Value**	**MAD Binomial**	**MAD Centered Binomial**	**MAD Gaussian**
0.1	$6.42\text{x}10^{-5}$	0.00016802	0.02099761	0.1	$5.04\text{x}10^{-6}$	$5.94\text{x}10^{-5}$	0.00138142
0.2	$7.15\text{x}10^{-5}$	0.00019634	0.02471317	0.2	$5.24\text{x}10^{-6}$	$6.12\text{x}10^{-5}$	0.00201909
0.3	$8.49\text{x}10^{-5}$	0.00018776	0.03041895	0.3	$5.44\text{x}10^{-6}$	$6.33\text{x}10^{-5}$	0.00255741
0.4	0.00017871	0.00012756	0.02024896	0.4	$5.62\text{x}10^{-6}$	$6.47\text{x}10^{-5}$	0.00335992
0.5	0.00012667	0.00013687	0.02227782	0.5	$5.69\text{x}10^{-6}$	$6.58\text{x}10^{-5}$	0.00473474
0.6	0.00033686	$1.34\text{x}10^{-4}$	0.03121889	0.6	$5.70\text{x}10^{-6}$	$6.69\text{x}10^{-5}$	0.00696943
0.7	0.00071223	$1.09\text{x}10^{-4}$	0.0397167	0.7	$5.70\text{x}10^{-6}$	$6.72\text{x}10^{-5}$	0.00994416
0.8	0.00057375	$1.09\text{x}10^{-4}$	0.03140213	0.8	$5.71\text{x}10^{-6}$	$6.72\text{x}10^{-5}$	0.01348377
0.9	0.00207318	$6.97\text{x}10^{-5}$	0.02295808	0.9	$5.71\text{x}10^{-6}$	$6.72\text{x}10^{-5}$	0.01394118
1	0.00286623	$8.02\text{x}10^{-5}$	0.02048063	1	$5.71\text{x}10^{-6}$	$6.72\text{x}10^{-5}$	0.00858307

$V_1 = 6.5$ V; $\boldsymbol{V_2 = 4.5}$ **V**; $\Theta_1 = 0°$; $\Theta_2 = 180°$; $f_1 = 10$ GHz; $f_2 = 10$ GHz.

Min–Max				Probabilistic			
Exigency Value	**MAD Binomial**	**MAD Centered Binomial**	**MAD Gaussian**	**Exigency Value**	**MAD Binomial**	**MAD Centered Binomial**	**MAD Gaussian**
0.1	$6.18\text{x}10^{-5}$	0.00013646	0.01565433	0.1	$8.86\text{x}10^{-6}$	$6.23\text{x}10^{-5}$	0.00318693
0.2	$6.82\text{x}10^{-5}$	0.00016712	0.01193876	0.2	$9.18\text{x}10^{-6}$	$6.43\text{x}10^{-5}$	0.00395512
0.3	$9.99\text{x}10^{-5}$	0.00016178	0.01134516	0.3	$9.53\text{x}10^{-6}$	$6.54\text{x}10^{-5}$	0.00483369
0.4	0.00017419	0.00015815	0.01114055	0.4	$9.81\text{x}10^{-6}$	$6.65\text{x}10^{-5}$	0.00590232
0.5	0.00019713	0.00012026	0.01178869	0.5	$9.90\text{x}10^{-6}$	$6.77\text{x}10^{-5}$	0.007087
0.6	0.00039694	$1.07\text{x}10^{-4}$	0.01203914	0.6	$9.91\text{x}10^{-6}$	$6.81\text{x}10^{-5}$	0.00868784
0.7	0.00046502	$4.54\text{x}10^{-5}$	0.01229167	0.7	$9.93\text{x}10^{-6}$	$6.81\text{x}10^{-5}$	0.01070046
0.8	0.00093235	$5.02\text{x}10^{-5}$	0.01242161	0.8	$9.94\text{x}10^{-6}$	$6.81\text{x}10^{-5}$	0.01306697
0.9	0.00123205	$9.08\text{x}10^{-5}$	0.03124823	0.9	$9.95\text{x}10^{-6}$	$6.81\text{x}10^{-5}$	0.0146491
1	0.00375941	$1.93\text{x}10^{-4}$	0.02004851	1	$9.97\text{x}10^{-6}$	$6.81\text{x}10^{-5}$	0.00996339

$V_1 = 6.5$ V; $\boldsymbol{V_2 = 4}$ **V**; $\Theta_1 = 0°$; $\Theta_2 = 180°$; $f_1 = 10$ GHz; $f_2 = 10$ GHz.

Min–Max				Probabilistic			
Exigency Value	**MAD Binomial**	**MAD Centered Binomial**	**MAD Gaussian**	**Exigency Value**	**MAD Binomial**	**MAD Centered Binomial**	**MAD Gaussian**
0.1	$4.53\text{x}10^{-5}$	0.00013512	0.01584567	0.1	$9.91\text{x}10^{-6}$	$1.46\text{x}10^{-4}$	0.00126869
0.2	$5.36\text{x}10^{-5}$	0.00012994	0.02020086	0.2	$1.03\text{x}10^{-5}$	$1.51\text{x}10^{-4}$	0.00226909
0.3	$6.83\text{x}10^{-5}$	0.00012361	0.02520678	0.3	$1.06\text{x}10^{-5}$	$1.56\text{x}10^{-4}$	0.00352032
0.4	0.00013175	0.00015711	0.03029121	0.4	$1.09\text{x}10^{-5}$	$1.62\text{x}10^{-4}$	0.00512801
0.5	0.00020783	0.00010033	0.03559723	0.5	$1.09\text{x}10^{-5}$	$1.64\text{x}10^{-4}$	0.00673561
0.6	0.0002443	$8.95\text{x}10^{-5}$	0.03632737	0.6	$1.09\text{x}10^{-5}$	$1.64\text{x}10^{-4}$	0.00832396
0.7	0.00041227	$1.02\text{x}10^{-4}$	0.0355428	0.7	$1.10\text{x}10^{-5}$	$1.64\text{x}10^{-4}$	0.00961862
0.8	0.00068605	$2.69\text{x}10^{-5}$	0.03587997	0.8	$1.10\text{x}10^{-5}$	$1.64\text{x}10^{-4}$	0.01082376
0.9	0.00056506	$1.30\text{x}10^{-4}$	0.0333477	0.9	$1.10\text{x}10^{-5}$	$1.64\text{x}10^{-4}$	0.01098158
1	0.00282209	$1.01\text{x}10^{-4}$	0.02585669	1	$1.10\text{x}10^{-5}$	$1.64\text{x}10^{-4}$	0.00651106

$V_1 = 6.5$ V; $\boldsymbol{V_2 = 3.5}$ **V**; $\Theta_1 = 0°$; $\Theta_2 = 180°$; $f_1 = 10$ GHz; $f_2 = 10$ GHz.

Min–Max				Probabilistic			
Exigency Value	**MAD Binomial**	**MAD Centered Binomial**	**MAD Gaussian**	**Exigency Value**	**MAD Binomial**	**MAD Centered Binomial**	**MAD Gaussian**
0.1	$5.18\text{x}10^{-5}$	0.00011077	0.01820164	0.1	$1.76\text{x}10^{-5}$	$1.40\text{x}10^{-4}$	0.00177918
0.2	$1.59\text{x}10^{-5}$	0.00010633	0.01629633	0.2	$1.82\text{x}10^{-5}$	$1.44\text{x}10^{-4}$	0.0025725
0.3	$6.80\text{x}10^{-5}$	0.00010341	0.02281152	0.3	$1.88\text{x}10^{-5}$	$1.47\text{x}10^{-4}$	0.00358456
0.4	0.00010854	$9.87\text{x}10^{-5}$	0.02403769	0.4	$1.93\text{x}10^{-5}$	$1.49\text{x}10^{-4}$	0.00489602
0.5	0.00016732	0.00011196	0.02337731	0.5	$1.95\text{x}10^{-5}$	$1.50\text{x}10^{-4}$	0.00640845
0.6	0.0002827	$6.60\text{x}10^{-5}$	0.02334809	0.6	$1.95\text{x}10^{-5}$	$1.50\text{x}10^{-4}$	0.00861315
0.7	0.00022738	$8.65\text{x}10^{-5}$	0.02236427	0.7	$1.95\text{x}10^{-5}$	$1.50\text{x}10^{-4}$	0.00987609
0.8	0.00055111	$1.10\text{x}10^{-5}$	0.02106784	0.8	$1.95\text{x}10^{-5}$	$1.50\text{x}10^{-4}$	0.00952968
0.9	0.00133944	$4.38\text{x}10^{-5}$	0.01835139	0.9	$1.95\text{x}10^{-5}$	$1.50\text{x}10^{-4}$	0.00878334
1	0.00089244	$4.93\text{x}10^{-5}$	0.01236689	1	$1.95\text{x}10^{-5}$	$1.50\text{x}10^{-4}$	0.00627363

$V_1 = 6.5$ V; $\boldsymbol{V_2 = 3}$ **V**; $\Theta_1 = 0°$; $\Theta_2 = 180°$; $f_1 = 10$ GHz; $f_2 = 10$ GHz.

Min–Max				Probabilistic			
Exigency Value	**MAD Binomial**	**MAD Centered Binomial**	**MAD Gaussian**	**Exigency Value**	**MAD Binomial**	**MAD Centered Binomial**	**MAD Gaussian**
0.1	$4.72\text{x}10^{-5}$	0.0001048	0.01387736	0.1	$8.57\text{x}10^{-6}$	$2.89\text{x}10^{-5}$	0.00313472
0.2	$6.28\text{x}10^{-5}$	$9.84\text{x}10^{-5}$	0.0160715	0.2	$8.88\text{x}10^{-6}$	$2.98\text{x}10^{-5}$	0.00450639
0.3	$1.19\text{x}10^{-4}$	$9.36\text{x}10^{-5}$	0.02220753	0.3	$9.23\text{x}10^{-6}$	$3.09\text{x}10^{-5}$	0.00594489
0.4	0.00010695	$9.00\text{x}10^{-5}$	0.02482912	0.4	$9.55\text{x}10^{-6}$	$3.19\text{x}10^{-5}$	0.00735064
0.5	0.00017725	$8.68\text{x}10^{-5}$	0.02544407	0.5	$9.68\text{x}10^{-6}$	$3.26\text{x}10^{-5}$	0.00877405
0.6	0.00037212	$6.49\text{x}10^{-5}$	0.03273787	0.6	$9.69\text{x}10^{-6}$	$3.29\text{x}10^{-5}$	0.01033875
0.7	0.00060001	$5.39\text{x}10^{-5}$	0.03612239	0.7	$9.70\text{x}10^{-6}$	$3.29\text{x}10^{-5}$	0.0116124
0.8	0.0008967	$3.54\text{x}10^{-5}$	0.03393183	0.8	$9.70\text{x}10^{-6}$	$3.29\text{x}10^{-5}$	0.012735
0.9	0.00215839	$4.40\text{x}10^{-5}$	0.02938098	0.9	$9.71\text{x}10^{-6}$	$3.29\text{x}10^{-5}$	0.01288501
1	0.00286776	$5.96\text{x}10^{-5}$	0.02787283	1	$9.71\ \text{x}10^{-6}$	$3.29\text{x}10^{-5}$	0.00747932

For the case 2:

$V_1 = 6.5$ V; $V_2 = 6.5$ V; $\Theta_1 = 0°$; $\boldsymbol{\Theta_2 = 180°}$; $f_1 = 10$ GHz; $f_2 = 10$ GHz.

Min–Max				Probabilistic			
Exigency Value	**MAD Binomial**	**MAD Centered Binomial**	**MAD Gaussian**	**Exigency Value**	**MAD Binomial**	**MAD Centered Binomial**	**MAD Gaussian**
0.1	$8.31\text{x}10^{-5}$	$1.36\text{x}10^{-4}$	0.009922	0.1	$9.76\text{x}10^{-6}$	$5.66\text{x}10^{-5}$	0.002877
0.2	$8.25\text{x}10^{-5}$	$1.30\text{x}10^{-4}$	0.004994	0.2	$1.01\text{x}10^{-5}$	$5.84\text{x}10^{-5}$	0.0037
0.3	$6.51\text{x}10^{-5}$	$1.23\text{x}10^{-4}$	0.009877	0.3	$1.05\text{x}10^{-5}$	$5.97\text{x}10^{-5}$	0.003187
0.4	$4.33\text{x}10^{-5}$	$1.15\text{x}10^{-4}$	0.010945	0.4	$1.09\text{x}10^{-5}$	$6.06\text{x}10^{-5}$	0.002381
0.5	$4.97\text{x}10^{-5}$	$1.08\text{x}10^{-4}$	0.008207	0.5	$1.10\text{x}10^{-5}$	$6.17\text{x}10^{-5}$	0.001836
0.6	$7.27\text{x}10^{-5}$	$1.01\text{x}10^{-4}$	0.008552	0.6	$1.10\text{x}10^{-5}$	$6.28\text{x}10^{-5}$	0.002625
0.7	$7.51\text{x}10^{-5}$	$9.32\text{x}10^{-5}$	0.009101	0.7	$1.10\text{x}10^{-5}$	$6.30\text{x}10^{-5}$	0.003821
0.8	0.000111	$8.58\text{x}10^{-5}$	0.009108	0.8	$1.10\text{x}10^{-5}$	$6.30\text{x}10^{-5}$	0.005367
0.9	0.000173	$9.05\text{x}10^{-5}$	0.009251	0.9	$1.10\text{x}10^{-5}$	$6.30\text{x}10^{-5}$	0.005742
1	0.000165	$6.25\text{x}10^{-5}$	0.011459	1	$1.10\text{x}10^{-5}$	$6.30\text{x}10^{-5}$	0.001866

$V_1 = 6.5$ V; $V_2 = 6.5$ V; $\Theta_1 = 0°$; $\mathbf{\Theta_2 = 150°}$; $f_1 = 10$ GHz; $f_2 = 10$ GHz.

Min–Max				Probabilistic			
Exigency Value	**MAD Binomial**	**MAD Centered Binomial**	**MAD Gaussian**	**Exigency Value**	**MAD Binomial**	**MAD Centered Binomial**	**MAD Gaussian**
0.1	$7.85\text{x}10^{-5}$	$8.53\text{x}10^{-5}$	0.004687	0.1	$9.90\text{x}10^{-6}$	$3.54\text{x}10^{-5}$	0.000908
0.2	$6.95\text{x}10^{-5}$	$8.25\text{x}10^{-5}$	0.004392	0.2	$1.03\text{x}10^{-5}$	$3.66\text{x}10^{-5}$	0.001292
0.3	$2.87\text{x}10^{-5}$	$6.9\text{x}10^{-5}$	0.014829	0.3	$1.07\text{x}10^{-5}$	$3.79\text{x}10^{-5}$	0.001347
0.4	$2.40\text{x}10^{-5}$	$6.70\text{x}10^{-5}$	0.002974	0.4	$1.11\text{x}10^{-5}$	$3.88\text{x}10^{-5}$	0.001365
0.5	$6.74\text{x}10^{-5}$	$6.40\text{x}10^{-5}$	0.008774	0.5	$1.13\text{x}10^{-5}$	$3.95\text{x}10^{-5}$	0.001418
0.6	$8.10\text{x}10^{-5}$	$6.17\text{x}10^{-5}$	0.011219	0.6	$1.14\text{x}10^{-5}$	$3.99\text{x}10^{-5}$	0.00158
0.7	$7.55\text{x}10^{-5}$	$5.91\text{x}10^{-5}$	0.004003	0.7	$1.14\text{x}10^{-5}$	$3.99\text{x}10^{-5}$	0.001997
0.8	0.000139	$5.66\text{x}10^{-5}$	0.006418	0.8	$1.14\text{x}10^{-5}$	$3.99\text{x}10^{-5}$	0.002074
0.9	$9.27\text{x}10^{-5}$	$5.97\text{x}10^{-5}$	0.008991	0.9	$1.14\text{x}10^{-5}$	$3.9\text{x}10^{-5}$	0.002366
1	0.000128	$4.74\text{x}10^{-5}$	0.006103	1	$1.14\text{x}10^{-5}$	$3.99\text{x}10^{-5}$	0.001915

$V_1 = 6.5$ V; $V_2 = 6.5$ V; $\Theta_1 = 0°$; $\mathbf{\Theta_2 = 120°}$; $f_1 = 10$ GHz; $f_2 = 10$ GHz.

Min–Max				Probabilistic			
Exigency Value	**MAD Binomial**	**MAD Centered Binomial**	**MAD Gaussian**	**Exigency Value**	**MAD Binomial**	**MAD Centered Binomial**	**MAD Gaussian**
0.1	$8.11\text{x}10^{-5}$	$7.21\text{x}10^{-5}$	0.008179	0.1	$6.49\text{x}10^{-6}$	$7.21\text{x}10^{-5}$	0.000502
0.2	$6.94\text{x}10^{-5}$	$5.94\text{x}10^{-5}$	0.00717	0.2	$6.73\text{x}10^{-6}$	$7.45\text{x}10^{-5}$	0.000816
0.3	$6.79\text{x}10^{-5}$	$5.61\text{x}10^{-5}$	0.007642	0.3	$6.96\text{x}10^{-6}$	$7.73\text{x}10^{-5}$	0.001211
0.4	$4.83\text{x}10^{-5}$	$5.26\text{x}10^{-5}$	0.009216	0.4	$7.18\text{x}10^{-6}$	$8.04\text{x}10^{-5}$	0.001638
0.5	$2.45\text{x}10^{-5}$	$4.90\text{x}10^{-5}$	0.014124	0.5	$7.33\text{x}10^{-6}$	$8.12\text{x}10^{-5}$	0.00205
0.6	$5.66\text{x}10^{-5}$	$4.53\text{x}10^{-5}$	0.00729	0.6	$7.34\text{x}10^{-6}$	$8.12\text{x}10^{-5}$	0.002455
0.7	$6.47\text{x}10^{-5}$	$5.96\text{x}10^{-5}$	0.010386	0.7	$7.34\text{x}10^{-6}$	$8.12\text{x}10^{-5}$	0.002759
0.8	0.000139	$4.33\text{x}10^{-5}$	0.010615	0.8	$7.34\text{x}10^{-6}$	$8.12\text{x}10^{-5}$	0.003162
0.9	$1.96\text{x}10^{-4}$	$4.22\text{x}10^{-5}$	0.012528	0.9	$7.34\text{x}10^{-6}$	$8.12\text{x}10^{-5}$	0.00366
1	0.000105	$3.54\text{x}10^{-5}$	0.011891	1	$7.34\text{x}10^{-6}$	$8.12\text{x}10^{-5}$	0.001809

$V_1 = 6.5$ V; $V_2 = 6.5$ V; $\Theta_1 = 0°$; $\mathbf{\Theta_2 = 90°}$; $f_1 = 10$ GHz; $f_2 = 10$ GHz.

Min–Max				Probabilistic			
Exigency Value	**MAD Binomial**	**MAD Centered Binomial**	**MAD Gaussian**	**Exigency Value**	**MAD Binomial**	**MAD Centered Binomial**	**MAD Gaussian**
0.1	$3.82\text{x}10^{-5}$	$8.97\text{x}10^{-5}$	0.005133	0.1	$8.45\text{x}10^{-6}$	$8.54\text{x}10^{-5}$	0.000891
0.2	$6.86\text{x}10^{-5}$	$8.74\text{x}10^{-5}$	0.005164	0.2	$8.75\text{x}10^{-6}$	$8.82\text{x}10^{-5}$	0.000972
0.3	$2.48\text{x}10^{-5}$	$8.49\text{x}10^{-5}$	0.007055	0.3	$9.09\text{x}10^{-6}$	$9.14\text{x}10^{-5}$	0.000907
0.4	$6.60\text{x}10^{-5}$	$7.92\text{x}10^{-5}$	0.008445	0.4	$9.44\text{x}10^{-6}$	$9.34\text{x}10^{-5}$	0.000844
0.5	$1.10\text{x}10^{-4}$	$7.67\text{x}10^{-5}$	0.008954	0.5	$9.72\text{x}10^{-6}$	$9.36\text{x}10^{-5}$	0.000649
0.6	$1.30\text{x}10^{-4}$	$7.44\text{x}10^{-5}$	0.00921	0.6	$9.76\text{x}10^{-6}$	$9.36\text{x}10^{-5}$	0.00066
0.7	$1.57\text{x}10^{-4}$	$7.71\text{x}10^{-5}$	0.00874	0.7	$9.76\text{x}10^{-6}$	$9.36\text{x}10^{-5}$	0.00106
0.8	0.000205	$6.20\text{x}10^{-5}$	0.008512	0.8	$9.75\text{x}10^{-6}$	$9.36\text{x}10^{-5}$	0.00159
0.9	$4.22\text{x}10^{-4}$	$6.12\text{x}10^{-5}$	0.009173	0.9	$9.75\text{x}10^{-6}$	$9.37\text{x}10^{-5}$	0.001348
1	0.000576	$6.00\text{x}10^{-5}$	0.008953	1	$9.75\text{x}10^{-6}$	$9.37\text{x}10^{-5}$	0.001469

$V_1 = 6.5$ V; $V_2 = 6.5$ V; $\Theta_1 = 0°$; $\mathbf{\Theta_2 = 60°}$; $f_1 = 10$ GHz; $f_2 = 10$ GHz.

Min–Max				Probabilistic			
Exigency Value	**MAD Binomial**	**MAD Centered Binomial**	**MAD Gaussian**	**Exigency Value**	**MAD Binomial**	**MAD Centered Binomial**	**MAD Gaussian**
0.1	$7.13\text{x}10^{-5}$	$9.25\text{x}10^{-5}$	0.008608	0.1	$3.31\text{x}10^{-6}$	$7.45\text{x}10^{-5}$	0.001051
0.2	$2.99\text{x}10^{-5}$	$8.03\text{x}10^{-5}$	0.00964	0.2	$3.43\text{x}10^{-6}$	$7.69\text{x}10^{-5}$	0.001165
0.3	$3.72\text{x}10^{-5}$	$7.94\text{x}10^{-5}$	0.010694	0.3	$3.56\text{x}10^{-6}$	$7.96\text{x}10^{-5}$	0.001291
0.4	$5.08\text{x}10^{-5}$	$7.85\text{x}10^{-5}$	0.011021	0.4	$3.70\text{x}10^{-6}$	$8.15\text{x}10^{-5}$	0.001508
0.5	$1.02\text{x}10^{-4}$	$7.75\text{x}10^{-5}$	0.008474	0.5	$3.78\text{x}10^{-6}$	$8.23\text{x}10^{-5}$	0.001671
0.6	$9.88\text{x}10^{-5}$	$7.65\text{x}10^{-5}$	0.011613	0.6	$3.79\text{x}10^{-6}$	$8.23\text{x}10^{-5}$	0.001677
0.7	$1.27\text{x}10^{-4}$	$7.54\text{x}10^{-5}$	0.013605	0.7	$3.78\text{x}10^{-6}$	$8.23\text{x}10^{-5}$	0.001828
0.8	0.000176	$7.45\text{x}10^{-5}$	0.013032	0.8	$3.78\text{x}10^{-6}$	$8.23\text{x}10^{-5}$	0.002052
0.9	$3.57\text{x}10^{-4}$	$5.72\text{x}10^{-5}$	0.013101	0.9	$3.78\text{x}10^{-6}$	$8.23\text{x}10^{-5}$	0.003145
1	0.000383	$5.85\text{x}10^{-5}$	0.011201	1	$3.78\text{x}10^{-6}$	$8.23\text{x}10^{-5}$	0.003495

$V_1 = 6.5$ V; $V_2 = 6.5$ V; $\Theta_1 = 0°$; $\mathbf{\Theta_2 = 45°}$; $f_1 = 10$ GHz; $f_2 = 10$ GHz.

Min–Max				Probabilistic			
Exigency Value	**MAD Binomial**	**MAD Centered Binomial**	**MAD Gaussian**	**Exigency Value**	**MAD Binomial**	**MAD Centered Binomial**	**MAD Gaussian**
0.1	$3.58\text{x}10^{-5}$	$1.15\text{x}10^{-4}$	0.002832	0.1	$1.11\text{x}10^{-5}$	$8.12\text{x}10^{-5}$	0.000446
0.2	$6.88\text{x}10^{-5}$	$1.12\text{x}10^{-4}$	0.003591	0.2	$1.15\text{x}10^{-5}$	$8.38\text{x}10^{-5}$	0.000368
0.3	$3.80\text{x}10^{-5}$	$1.08\text{x}10^{-4}$	0.006158	0.3	$1.19\text{x}10^{-5}$	$8.67\text{x}10^{-5}$	0.000382
0.4	$5.9\text{x}10^{-5}$	$1.05\text{x}10^{-4}$	0.00435	0.4	$1.24\text{x}10^{-5}$	$8.81\text{x}10^{-5}$	0.000782
0.5	$4.42\text{x}10^{-5}$	$1.02\text{x}10^{-4}$	0.005225	0.5	$1.28\text{x}10^{-5}$	$8.94\text{x}10^{-5}$	0.000909
0.6	$5.61\text{x}10^{-5}$	$9.86\text{x}10^{-5}$	0.005166	0.6	$1.28\text{x}10^{-5}$	$8.94\text{x}10^{-5}$	0.000471
0.7	$1.19\text{x}10^{-4}$	$6.14\text{x}10^{-5}$	0.009188	0.7	$1.28\text{x}10^{-5}$	$8.94\text{x}10^{-5}$	0.000495
0.8	0.000133	$5.95\text{x}10^{-5}$	0.006022	0.8	$1.28\text{x}10^{-5}$	$8.94\text{x}10^{-5}$	0.000587
0.9	$1.11\text{x}10^{-4}$	$5.75\text{x}10^{-5}$	0.007839	0.9	$1.28\text{x}10^{-5}$	$8.94\text{x}10^{-5}$	0.000801
1	0.000221	$5.65\text{x}10^{-5}$	0.00662	1	$1.28\text{x}10^{-5}$	$8.94\text{x}10^{-5}$	0.000919

$V_1 = 6.5$ V; $V_2 = 6.5$ V; $\Theta_1 = 0°$; $\mathbf{\Theta_2 = 30°}$; $f_1 = 10$ GHz; $f_2 = 10$ GHz.

Min–Max				Probabilistic			
Exigency Value	**MAD Binomial**	**MAD Centered Binomial**	**MAD Gaussian**	**Exigency Value**	**MAD Binomial**	**MAD Centered Binomial**	**MAD Gaussian**
0.1	$8.47\text{x}10^{-5}$	$7.63\text{x}10^{-5}$	0.010222	0.1	$1.22\text{x}10^{-5}$	$6.97\text{x}10^{-5}$	0.000968
0.2	$4.15\text{x}10^{-5}$	$7.44\text{x}10^{-5}$	0.005345	0.2	$1.26\text{x}10^{-5}$	$7.21\text{x}10^{-5}$	0.001464
0.3	$3.52\text{x}10^{-5}$	$7.28\text{x}10^{-5}$	0.006374	0.3	$1.31\text{x}10^{-5}$	$7.48\text{x}10^{-5}$	0.001684
0.4	$4.03\text{x}10^{-5}$	$7.10\text{x}10^{-5}$	0.008224	0.4	$1.35\text{x}10^{-5}$	$7.68\text{x}10^{-5}$	0.001667
0.5	$5.43\text{x}10^{-5}$	$6.93\text{x}10^{-5}$	0.006421	0.5	$1.38\text{x}10^{-5}$	$7.70\text{x}10^{-5}$	0.001301
0.6	$7.39\text{x}10^{-5}$	$6.74\text{x}10^{-5}$	0.007946	0.6	$1.38\text{x}10^{-5}$	$7.70\text{x}10^{-5}$	0.001508
0.7	$5.31\text{x}10^{-5}$	$6.54\text{x}10^{-5}$	0.010052	0.7	$1.38\text{x}10^{-5}$	$7.70\text{x}10^{-5}$	0.001732
0.8	0.00016	$6.35\text{x}10^{-5}$	0.011243	0.8	$1.37\text{x}10^{-5}$	$7.70\text{x}10^{-5}$	0.002035
0.9	$1.45\text{x}10^{-4}$	$5.64\text{x}10^{-5}$	0.008603	0.9	$1.37\text{x}10^{-5}$	$7.70\text{x}10^{-5}$	0.002399
1	$8.02\text{x}10^{-5}$	$4.56\text{x}10^{-5}$	0.01116	1	$1.37\text{x}10^{-5}$	$7.70\text{x}10^{-5}$	0.002189

V_1 = 6.5 V; V_2 = 6.5 V; Θ_1 = 0°; **Θ_2 = 0°**; f_1 = 10 GHz; f_2 = 10 GHz.

Min–Max				Probabilistic			
Exigency Value	**MAD Binomial**	**MAD Centered Binomial**	**MAD Gaussian**	**Exigency Value**	**MAD Binomial**	**MAD Centered Binomial**	**MAD Gaussian**
0.1	$7.10x10^{-5}$	$6.35x10^{-5}$	0.003355	0.1	$5.14x10^{-6}$	$6.38x10^{-5}$	0.00143
0.2	$7.21x10^{-5}$	$6.05x10^{-5}$	0.006784	0.2	$5.32x10^{-6}$	$6.59x10^{-5}$	0.001988
0.3	$4.66x10^{-5}$	$5.73x10^{-5}$	0.004463	0.3	$5.52x10^{-6}$	$6.84x10^{-5}$	0.002327
0.4	$6.18x10^{-5}$	$5.42x10^{-5}$	0.004537	0.4	$5.71x10^{-6}$	$6.99x10^{-5}$	0.001695
0.5	$4.72x10^{-5}$	$5.08x10^{-5}$	0.005122	0.5	$5.82x10^{-6}$	$7.01 x10^{-5}$	0.001325
0.6	$4.75x10^{-5}$	$4.76x10^{-5}$	0.007374	0.6	$5.84x10^{-6}$	$7.01 x10^{-5}$	0.001484
0.7	$8.05x10^{-5}$	$4.17x10^{-5}$	0.005505	0.7	$5.84x10^{-6}$	$7.01 x10^{-5}$	0.00218
0.8	0.000185	$4.21x10^{-5}$	0.005775	0.8	$5.84x10^{-6}$	$7.01 x10^{-5}$	0.003524
0.9	$1.11x10^{-4}$	$4.16x10^{-5}$	0.008555	0.9	$5.83x10^{-6}$	$7.01 x10^{-5}$	0.003686
1	$3.92x10^{-4}$	$3.99x10^{-5}$	0.005187	1	$5.83x10^{-6}$	$7.01 x10^{-5}$	0.002823

For the case 3:

V_1 = 3–6.5 V; V_2 = 6.5 V; Θ_1 = 0°–180°; Θ_2 = 0°; **f_1 = 1 GHz**; f_2 = 10 GHz.

Min–Max				Probabilistic			
Exigency Value	**MAD Binomial**	**MAD Centered Binomial**	**MAD Gaussian**	**Exigency Value**	**MAD Binomial**	**MAD Centered Binomial**	**MAD Gaussian**
0.1	$3,36x10^{-5}$	0,000122	0,027004	0.1	$6,34x10^{-6}$	$7,49x10^{-5}$	0,002913
0.2	$7,70x10^{-5}$	0,000119	0,032552	0.2	$6,57x10^{-6}$	$7,73x10^{-5}$	0,004901
0.3	0,000153	0,000118	0,02036	0.3	$6,81x10^{-6}$	$8,01x10^{-5}$	0,007616
0.4	0,000185	0,000109	0,031188	0.4	$7,02x10^{-6}$	$8,33x10^{-5}$	0,010184
0.5	0,000278	$9,84x10^{-5}$	0,036547	0.5	$7,11x10^{-6}$	$8,51x10^{-5}$	0,011278
0.6	0,000414	$9,67x10^{-5}$	0,033131	0.6	$7,13x10^{-6}$	$8,57x10^{-5}$	0,012433
0.7	0,000461	0,000107	0,042069	0.7	$7,13x10^{-6}$	$8,57x10^{-5}$	0,013691
0.8	0,001061	$3,08x10^{-5}$	0,025439	0.8	$7,14x10^{-6}$	$8,57x10^{-5}$	0,013128
0.9	0,00134	$9,68x10^{-5}$	0,042048	0.9	$7,15x10^{-6}$	$8,57x10^{-5}$	0,011958
1	0,003402	$1,71x10^{-4}$	0,016352	1	$7,16x10^{-6}$	$8,58x10^{-5}$	0,007694

V_1 = 3–6.5 V; V_2 = 6.5 V; Θ_1 = 0°–180°; Θ_2 = 0°; **f_1 = 5 GHz**; f_2 = 10 GHz.

Min–Max				Probabilistic			
Exigency Value	**MAD Binomial**	**MAD Centered Binomial**	**MAD Gaussian**	**Exigency Value**	**MAD Binomial**	**MAD Centered Binomial**	**MAD Gaussian**
0.1	$5,90x10^{-5}$	0,000121	0,024707	0.1	$3,94x10^{-6}$	$5,95x10^{-5}$	0,001443
0.2	$5,53x10^{-5}$	0,000116	0,018199	0.2	$4,09x10^{-6}$	$6,14x10^{-5}$	0,002144
0.3	0,000115	0,000109	0,017625	0.3	$4,25x10^{-6}$	$6,35x10^{-5}$	0,00287
0.4	0,000248	0,000101	0,027832	0.4	$4,44x10^{-6}$	$6,60x10^{-5}$	0,003864
0.5	0,000373	$7,03x10^{-5}$	0,025707	0.5	$4,55x10^{-6}$	$6,76x10^{-5}$	0,004928
0.6	0,00066	$1,04x10^{-4}$	0,025336	0.6	$4,56x10^{-6}$	$6,87x10^{-5}$	0,006199
0.7	0,000919	$8,29x10^{-5}$	0,035144	0.7	$4,57x10^{-6}$	$6,87x10^{-5}$	0,007585
0.8	0,000762	$6,06x10^{-5}$	0,033901	0.8	$4,58x10^{-6}$	$6,87x10^{-5}$	0,00894
0.9	0,001318	$9,57x10^{-5}$	0,026803	0.9	$4,59x10^{-6}$	$6,87x10^{-5}$	0,00966
1	0,002588	$1,27x10^{-4}$	0,019597	1	$4,60x10^{-6}$	$6,87x10^{-5}$	0,005141

V_1 = 3–6.5 V; V_2 = 6.5 V; Θ_1 = 0°–180°; Θ_2 = 0°; $\boldsymbol{f_1}$ **= 10 GHz**; f_2 = 10 GHz.

Min–Max				Probabilistic			
Exigency Value	**MAD Binomial**	**MAD Centered Binomial**	**MAD Gaussian**	**Exigency Value**	**MAD Binomial**	**MAD Centered Binomial**	**MAD Gaussian**
0.1	$3{,}50\text{x}10^{-5}$	0,000109	0,015995	0.1	$5{,}24\text{x}10^{-6}$	$9{,}44\text{x}10^{-5}$	0,002774
0.2	$4{,}40\text{x}10^{-5}$	0,000103	0,017884	0.2	$5{,}43\text{x}10^{-6}$	$9{,}75\text{x}10^{-5}$	0,003867
0.3	0,00013	0,0001	0,019977	0.3	$5{,}63\text{x}10^{-6}$	$9{,}99\text{x}10^{-5}$	0,005573
0.4	0,0002	$9{,}27\text{x}10^{-5}$	0,022607	0.4	$5{,}81\text{x}10^{-6}$	$1{,}01\text{x}10^{-4}$	0,007538
0.5	0,000315	$8{,}95\text{x}10^{-5}$	0,025016	0.5	$5{,}92\text{x}10^{-6}$	$1{,}03\text{x}10^{-4}$	0,009225
0.6	0,000434	$8{,}99\text{x}10^{-5}$	0,026336	0.6	$5{,}92\text{x}10^{-6}$	$1{,}04\text{x}10^{-4}$	0,010762
0.7	0,000364	$7{,}34\text{x}10^{-5}$	0,029084	0.7	$5{,}92\text{x}10^{-6}$	$1{,}04\text{x}10^{-4}$	0,012001
0.8	0,000746	$6{,}83\text{x}10^{-5}$	0,028679	0.8	$5{,}92\text{x}10^{-6}$	$1{,}04\text{x}10^{-4}$	0,012521
0.9	0,001375	$6{,}47\text{x}10^{-5}$	0,025323	0.9	$5{,}92\text{x}10^{-6}$	$1{,}04\text{x}10^{-4}$	0,011654
1	0,001809	$5{,}93\text{x}10^{-5}$	0,020366	1	$5{,}92\text{x}10^{-6}$	$1{,}04\text{x}10^{-4}$	0,007258

V_1 = 3–6.5 V; V_2 = 6.5 V; Θ_1 = 0°–180°; Θ_2 = 0°; $\boldsymbol{f_1}$ **= 12.5 GHz**; f_2 = 10 GHz.

Min–Max				Probabilistic			
Exigency Value	**MAD Binomial**	**MAD Centered Binomial**	**MAD Gaussian**	**Exigency Value**	**MAD Binomial**	**MAD Centered Binomial**	**MAD Gaussian**
0.1	$4{,}58\text{x}10^{-5}$	0,000137	0,015504	0.1	$1{,}22\text{x}10^{-5}$	$2{,}20\text{x}10^{-5}$	0,002887
0.2	$8{,}78\text{x}10^{-5}$	0,000173	0,021228	0.2	$1{,}27\text{x}10^{-5}$	$2{,}27\text{x}10^{-5}$	0,004623
0.3	0,00019	0,000164	0,022757	0.3	$1{,}32\text{x}10^{-5}$	$2{,}35\text{x}10^{-5}$	0,006264
0.4	0,000208	$4{,}76\text{x}10^{-5}$	0,023993	0.4	$1{,}38\text{x}10^{-5}$	$2{,}40\text{x}10^{-5}$	0,007603
0.5	0,00028	$8{,}31\text{x}10^{-5}$	0,026942	0.5	$1{,}42\text{x}10^{-5}$	$2{,}44\text{x}10^{-5}$	0,00872
0.6	0,00045	$7{,}92\text{x}10^{-5}$	0,027901	0.6	$1{,}42\text{x}10^{-5}$	$2{,}49\text{x}10^{-5}$	0,009992
0.7	0,00045	0,000102	0,036866	0.7	$1{,}43\text{x}10^{-5}$	$2{,}52\text{x}10^{-5}$	0,011437
0.8	0,001146	$3{,}87\text{x}10^{-5}$	0,028836	0.8	$1{,}43\text{x}10^{-5}$	$2{,}52\text{x}10^{-5}$	0,011564
0.9	0,001797	$3{,}42\text{x}10^{-5}$	0,023502	0.9	$1{,}43\text{x}10^{-5}$	$2{,}52\text{x}10^{-5}$	0,01056
1	0,003781	$5{,}91\text{x}10^{-5}$	0,019394	1	$1{,}43\text{x}10^{-5}$	$2{,}52\text{x}10^{-5}$	0,007392

V_1 = 3–6.5 V; V_2 = 6.5 V; Θ_1 = 0°–180°; Θ_2 = 0°; $\boldsymbol{f_1}$ **= 20 GHz**; f_2 = 10 GHz.

Min–Max				Probabilistic			
Exigency Value	**MAD Binomial**	**MAD Centered Binomial**	**MAD Gaussian**	**Exigency Value**	**MAD Binomial**	**MAD Centered Binomial**	**MAD Gaussian**
0.1	$5{,}11\text{x}10^{-5}$	0,00015	0,018368	0.1	$1{,}26\text{x}10^{-6}$	$4{,}20\text{x}10^{-5}$	0,001331
0.2	$6{,}37\text{x}10^{-5}$	0,000142	0,020164	0.2	$1{,}33\text{x}10^{-6}$	$4{,}33\text{x}10^{-5}$	0,002133
0.3	$3{,}96\text{x}10^{-5}$	0,000175	0,024556	0.3	$1{,}39\text{x}10^{-6}$	$4{,}48\text{x}10^{-5}$	0,003066
0.4	0,000138	0,000109	0,033792	0.4	$1{,}44\text{x}10^{-6}$	$4{,}56\text{x}10^{-5}$	0,004518
0.5	0,000229	$9{,}09\text{x}10^{-5}$	0,036485	0.5	$1{,}48\text{x}10^{-6}$	$4{,}64\text{x}10^{-5}$	0,005841
0.6	0,000338	$1{,}07\text{x}10^{-4}$	0,022924	0.6	$1{,}50\text{x}10^{-6}$	$4{,}73\text{x}10^{-5}$	0,007222
0.7	0,00037	$6{,}18\text{x}10^{-5}$	0,023474	0.7	$1{,}51\text{x}10^{-6}$	$4{,}77\text{x}10^{-5}$	0,008809
0.8	0,000577	$1{,}42\text{x}10^{-4}$	0,030571	0.8	$1{,}53\text{x}10^{-6}$	$4{,}77\text{x}10^{-5}$	0,010793
0.9	0,001096	$1{,}39\text{x}10^{-4}$	0,016903	0.9	$1{,}54\text{x}10^{-6}$	$4{,}77\text{x}10^{-5}$	0,012622
1	0,001489	$4{,}71\text{x}10^{-5}$	0,021893	1	$1{,}56\text{x}10^{-6}$	$4{,}77\text{x}10^{-5}$	0,010579

For the case 4:

V_1 = 6.5 V; V_2 = 3–6.5 V; Θ_1 = 0°; Θ_2 = 0°–180°; f_1 = 10 GHz; $\boldsymbol{f_2}$ **= 1 GHz.**

Min–Max				Probabilistic			
Exigency Value	**MAD Binomial**	**MAD Centered Binomial**	**MAD Gaussian**	**Exigency Value**	**MAD Binomial**	**MAD Centered Binomial**	**MAD Gaussian**
0.1	$6{,}19\text{x}10^{-5}$	$9{,}25\text{x}10^{-5}$	0,008625	0.1	$1{,}10\text{x}10^{-6}$	$5{,}42\text{x}10^{-5}$	0,000822
0.2	$4{,}87\text{x}10^{-5}$	$7{,}87\text{x}10^{-5}$	0,012276	0.2	$1{,}13\text{x}10^{-6}$	$5{,}61\text{x}10^{-5}$	0,001365
0.3	$6{,}81\text{x}10^{-5}$	$7{,}66\text{x}10^{-5}$	0,011888	0.3	$1{,}15\text{x}10^{-6}$	$5{,}79\text{x}10^{-5}$	0,00179
0.4	$7{,}33\text{x}10^{-5}$	$7{,}46\text{x}10^{-5}$	0,013693	0.4	$1{,}17\text{x}10^{-6}$	$5{,}90\text{x}10^{-5}$	0,002019
0.5	0,000111	$7{,}24\text{x}10^{-5}$	0,018802	0.5	$1{,}17\text{x}10^{-6}$	$5{,}97\text{x}10^{-5}$	0,002265
0.6	0,000184	$6{,}41\text{x}10^{-5}$	0,024183	0.6	$1{,}15\text{x}10^{-6}$	$5{,}97\text{x}10^{-5}$	0,002493
0.7	0,000381	$6{,}22\text{x}10^{-5}$	0,020293	0.7	$1{,}13\text{x}10^{-6}$	$5{,}97\text{x}10^{-5}$	0,003128
0.8	0,000571	$6{,}05\text{x}10^{-5}$	0,023749	0.8	$1{,}11\text{x}10^{-6}$	$5{,}97\text{x}10^{-5}$	0,004589
0.9	0,001176	$5{,}22\text{x}10^{-5}$	0,022567	0.9	$1{,}10\text{x}10^{-6}$	$5{,}97\text{x}10^{-5}$	0,006116
1	0,001863	$5{,}23\text{x}10^{-5}$	0,021418	1	$1{,}08\text{x}10^{-6}$	$5{,}97\text{x}10^{-5}$	0,00425

V_1 = 6.5 V; V_2 = 3–6.5 V; Θ_1 = 0°; Θ_2 = 0°–180°; f_1 = 10 GHz; $\boldsymbol{f_2}$ **= 5 GHz.**

Min–Max				Probabilistic			
Exigency Value	**MAD Binomial**	**MAD Centered Binomial**	**MAD Gaussian**	**Exigency Value**	**MAD Binomial**	**MAD Centered Binomial**	**MAD Gaussian**
0.1	$7{,}31\text{x}10^{-5}$	$8{,}69\text{x}10^{-5}$	0,01195002	0.1	$1{,}98\text{x}10^{-6}$	$7{,}96\text{x}10^{-5}$	0,00070331
0.2	$4{,}36\text{x}10^{-5}$	$8{,}54\text{x}10^{-5}$	0,0117253	0.2	$2{,}05\text{x}10^{-6}$	$8{,}21\text{x}10^{-5}$	0,00085776
0.3	$3{,}95\text{x}10^{-5}$	$8{,}41\text{x}10^{-5}$	0,01442527	0.3	$2{,}12\text{x}10^{-6}$	$8{,}48\text{x}10^{-5}$	0,00093276
0.4	$8{,}22\text{x}10^{-5}$	$8{,}30\text{x}10^{-5}$	0,01398517	0.4	$2{,}20\text{x}10^{-6}$	$8{,}62\text{x}10^{-5}$	0,00095349
0.5	$8{,}88\text{x}10^{-5}$	$8{,}14\text{x}10^{-5}$	0,0194141	0.5	$2{,}26\text{x}10^{-6}$	$8{,}70\text{x}10^{-5}$	0,0009887
0.6	0,0001878	$8{,}00\text{x}10^{-5}$	0,01611007	0.6	$2{,}26\text{x}10^{-6}$	$8{,}70\text{x}10^{-5}$	0,00116261
0.7	0,0002982	$7{,}86\text{x}10^{-5}$	0,02797933	0.7	$2{,}26\text{x}10^{-6}$	$8{,}70\text{x}10^{-5}$	0,00196631
0.8	0,0005987	$7{,}59\text{x}10^{-5}$	0,01761338	0.8	$2{,}25\text{x}10^{-6}$	$8{,}70\text{x}10^{-5}$	0,00336002
0.9	0,0005676	$5{,}33\text{x}10^{-5}$	0,01878977	0.9	$2{,}25\text{x}10^{-6}$	$8{,}70\text{x}10^{-5}$	0,00468699
1	0,001067	$4{,}63\text{x}10^{-5}$	0,01608255	1	$2{,}24\text{x}10^{-6}$	$8{,}70\text{x}10^{-5}$	0,00417544

V_1 = 6.5 V; V_2 = 3–6.5 V; Θ_1 = 0°; Θ_2 = 0°–180°; f_1 = 10 GHz; $\boldsymbol{f_2}$ **= 10 GHz.**

Min–Max				Probabilistic			
Exigency Value	**MAD Binomial**	**MAD Centered Binomial**	**MAD Gaussian**	**Exigency Value**	**MAD Binomial**	**MAD Centered Binomial**	**MAD Gaussian**
0.1	$5{,}04\text{x}10^{-5}$	$9{,}07\text{x}10^{-5}$	0,01343	0.1	$1{,}71\text{x}10^{-6}$	$9{,}21\text{x}10^{-5}$	0,000869
0.2	$4{,}18\text{x}10^{-5}$	$8{,}72\text{x}10^{-5}$	0,019771	0.2	$1{,}77\text{x}10^{-6}$	$9{,}49\text{x}10^{-5}$	0,001392
0.3	$3{,}58\text{x}10^{-5}$	$8{,}32\text{x}10^{-5}$	0,015044	0.3	$1{,}84\text{x}10^{-6}$	$9{,}81\text{x}10^{-5}$	0,001804
0.4	$5{,}50\text{x}10^{-5}$	$7{,}98\text{x}10^{-5}$	0,017512	0.4	$1{,}91\text{x}10^{-6}$	$9{,}99\text{x}10^{-5}$	0,00143
0.5	$2{,}00\text{x}10^{-4}$	$7{,}58\text{x}10^{-5}$	0,016732	0.5	$1{,}96\text{x}10^{-6}$	$1{,}01\text{x}10^{-4}$	0,001675
0.6	0,000171	$7{,}19\text{x}10^{-5}$	0,019684	0.6	$1{,}96\text{x}10^{-6}$	$1{,}01\text{x}10^{-4}$	0,002014
0.7	0,000392	$6{,}79\text{x}10^{-5}$	0,020673	0.7	$1{,}95\text{x}10^{-6}$	$1{,}01\text{x}10^{-4}$	0,002579
0.8	0,000721	$5{,}64\text{x}10^{-5}$	0,021364	0.8	$1{,}95\text{x}10^{-6}$	$1{,}01\text{x}10^{-4}$	0,003426
0.9	0,000735	$6{,}17\text{x}10^{-5}$	0,018234	0.9	$1{,}94\text{x}10^{-6}$	$1{,}01\text{x}10^{-4}$	0,004679
1	0,001593	$6{,}75\text{x}10^{-5}$	0,017864	1	$1{,}94\text{x}10^{-6}$	$1{,}01\text{x}10^{-4}$	0,003781

V_1 = 6.5 V; V_2 = 3–6.5 V; Θ_1 = 0°; Θ_2 = 0°–180°; f_1 = 10 GHz; $\boldsymbol{f_2}$ **= 12.5 GHz.**

Min–Max				Probabilistic			
Exigency Value	**MAD Binomial**	**MAD Centered Binomial**	**MAD Gaussian**	**Exigency Value**	**MAD Binomial**	**MAD Centered Binomial**	**MAD Gaussian**
0.1	$7{,}13\text{x}10^{-5}$	$1{,}17\text{x}10^{-4}$	0,00811	0.1	$8{,}73\text{x}10^{-6}$	$1{,}25\text{x}10^{-4}$	0,000468
0.2	$1{,}28\text{x}10^{-5}$	$1{,}11\text{x}10^{-4}$	0,008192	0.2	$9{,}06\text{x}10^{-5}$	$1{,}29\text{x}10^{-4}$	0,000625
0.3	$3{,}82\text{x}10^{-5}$	$1{,}03\text{x}10^{-4}$	0,012629	0.3	$9{,}43\text{x}10^{-5}$	$1{,}33\text{x}10^{-4}$	0,00081
0.4	$5{,}49\text{x}10^{-5}$	$9{,}74\text{x}10^{-5}$	0,010784	0.4	$9{,}81\text{x}10^{-5}$	$1{,}35\text{x}10^{-4}$	0,001168
0.5	$1{,}02\text{x}10^{-4}$	$9{,}15\text{x}10^{-5}$	0,011797	0.5	$1{,}00\text{x}10^{-5}$	$1{,}35\text{x}10^{-4}$	0,001628
0.6	0,000182	$8{,}52\text{x}10^{-5}$	0,012547	0.6	$1{,}01\text{x}10^{-5}$	$1{,}35\text{x}10^{-4}$	0,002358
0.7	0,000162	$7{,}89\text{x}10^{-5}$	0,020241	0.7	$1{,}01\text{x}10^{-5}$	$1{,}35\text{x}10^{-4}$	0,002904
0.8	0,000416	$8{,}45\text{x}10^{-5}$	0,016809	0.8	$1{,}01\text{x}10^{-5}$	$1{,}35\text{x}10^{-4}$	0,003168
0.9	0,0006	$6{,}48\text{x}10^{-5}$	0,017491	0.9	$1{,}01\text{x}10^{-5}$	$1{,}35\text{x}10^{-4}$	0,002962
1	0,000787	$4{,}91\text{x}10^{-5}$	0,020638	1	$1{,}02\text{x}10^{-5}$	$1{,}35\text{x}10^{-4}$	0,00199

V_1 = 6.5 V; V_2 = 3–6.5 V; Θ_1 = 0°; Θ_2 = 0°–180°; f_1 = 10 GHz; $\boldsymbol{f_2}$ **= 20 GHz.**

Min–Max				Probabilistic			
Exigency Value	**MAD Binomial**	**MAD Centered Binomial**	**MAD Gaussian**	**Exigency Value**	**MAD Binomial**	**MAD Centered Binomial**	**MAD Gaussian**
0.1	$8{,}12\text{x}10^{-5}$	$1{,}31\text{x}10^{-4}$	0,013571	0.1	$9{,}85\text{x}10^{-6}$	$1{,}34\text{x}10^{-4}$	0,000472
0.2	$9{,}23\text{x}10^{-5}$	$1{,}23\text{x}10^{-4}$	0,016214	0.2	$1{,}02\text{x}10^{-5}$	$1{,}38\text{x}10^{-4}$	0,000627
0.3	$1{,}84\text{x}10^{-5}$	$1{,}12\text{x}10^{-4}$	0,020961	0.3	$1{,}06\text{x}10^{-5}$	$1{,}42\text{x}10^{-4}$	0,001013
0.4	$4{,}74\text{x}10^{-5}$	$1{,}02\text{x}10^{-4}$	0,022476	0.4	$1{,}09\text{x}10^{-5}$	$1{,}44\text{x}10^{-4}$	0,001728
0.5	$7{,}74\text{x}10^{-5}$	$9{,}13\text{x}10^{-5}$	0,019409	0.5	$1{,}11\text{x}10^{-5}$	$1{,}44\text{x}10^{-4}$	0,0027
0.6	$5{,}48\text{x}10^{-5}$	$8{,}13\text{x}10^{-5}$	0,015359	0.6	$1{,}12\text{x}10^{-5}$	$1{,}44\text{x}10^{-4}$	0,003192
0.7	0,000142	$7{,}03\text{x}10^{-5}$	0,016883	0.7	$1{,}12\text{x}10^{-5}$	$1{,}44\text{x}10^{-4}$	0,003559
0.8	0,000392	$6{,}61\text{x}10^{-5}$	0,018525	0.8	$1{,}12\text{x}10^{-5}$	$1{,}44\text{x}10^{-4}$	0,004288
0.9	0,000672	$6{,}73\text{x}10^{-5}$	0,014859	0.9	$1{,}11\text{x}10^{-5}$	$1{,}44\text{x}10^{-4}$	0,00562
1	0,001095	$4{,}70\text{x}10^{-5}$	0,018465	1	$1{,}11\text{x}10^{-5}$	$1{,}44\text{x}10^{-4}$	0,002042

A.6 Validation Indexes Applied to Combs Lines Detection (Section 3.6)

For the case 1:

Min–Max				Probabilistic			
Exigency Value	**MAD Binomial**	**MAD Centered Binomial**	**MAD Gaussian**	**Exigency Value**	**MAD Binomial**	**MAD Centered Binomial**	**MAD Gaussian**
0.1	$5{,}32\text{x}10^{-5}$	0,000117	0,009489	0.1	$1{,}05\text{x}10^{-5}$	$1{,}00\text{x}10^{-4}$	0,002767
0.2	$3{,}98\text{x}10^{-5}$	0,000101	0,011822	0.2	$1{,}08\text{x}10^{-5}$	$1{,}03\text{x}10^{-4}$	0,004713
0.3	$3{,}91\text{x}10^{-5}$	$9{,}85\text{x}10^{-5}$	0,010538	0.3	$1{,}12\text{x}10^{-5}$	$1{,}06\text{x}10^{-4}$	0,005944
0.4	$6{,}35\text{x}10^{-5}$	$8{,}94\text{x}10^{-5}$	0,010684	0.4	$1{,}16\text{x}10^{-5}$	$1{,}08\text{x}10^{-4}$	0,006496
0.5	$6{,}38\text{x}10^{-5}$	$8{,}39\text{x}10^{-5}$	0,015697	0.5	$1{,}19\text{x}10^{-5}$	$1{,}08\text{x}10^{-4}$	0,006608
0.6	$3{,}79\text{x}10^{-5}$	$7{,}88\text{x}10^{-5}$	0,017081	0.6	$1{,}19\text{x}10^{-5}$	$1{,}08\text{x}10^{-4}$	0,006415
0.7	$1{,}07\text{x}10^{-4}$	$2{,}44\text{x}10^{-5}$	0,013703	0.7	$1{,}19\text{x}10^{-5}$	$1{,}08\text{x}10^{-4}$	0,006237
0.8	$1{,}55\text{x}10^{-4}$	$9{,}51\text{x}10^{-5}$	0,014675	0.8	$1{,}19\text{x}10^{-5}$	$1{,}08\text{x}10^{-4}$	0,006583
0.9	$3{,}02\text{x}10^{-4}$	$9{,}39\text{x}10^{-5}$	0,014422	0.9	$1{,}19\text{x}10^{-5}$	$1{,}08\text{x}10^{-4}$	0,007273
1	0,000729	$5{,}03\text{x}10^{-5}$	0,012031	1	$1{,}19\text{x}10^{-5}$	$1{,}08\text{x}10^{-4}$	0,002921

For the case 2:

Min–Max				Probabilistic			
Exigency Value	**MAD Binomial**	**MAD Centered Binomial**	**MAD Gaussian**	**Exigency Value**	**MAD Binomial**	**MAD Centered Binomial**	**MAD Gaussian**
0.1	$6{,}51\text{x}10^{-5}$	0,00011	0,008384	0.1	$1{,}45\text{x}10^{-5}$	$5{,}53\text{x}10^{-5}$	0,005353
0.2	$4{,}73\text{x}10^{-5}$	0,000106	0,010617	0.2	$1{,}51\text{x}10^{-5}$	$5{,}69\text{x}10^{-5}$	0,005221
0.3	$2{,}68\text{x}10^{-5}$	0,000101	0,010324	0.3	$1{,}57\text{x}10^{-5}$	$5{,}88\text{x}10^{-5}$	0,004435
0.4	$7{,}91\text{x}10^{-5}$	0,000134	0,012292	0.4	$1{,}61\text{x}10^{-5}$	$5{,}99\text{x}10^{-5}$	0,002866
0.5	$1{,}10\text{x}10^{-4}$	$8{,}63\text{x}10^{-5}$	0,016575	0.5	$1{,}63\text{x}10^{-5}$	$6{,}09\text{x}10^{-5}$	0,003059
0.6	$5{,}94\text{x}10^{-5}$	$6{,}82\text{x}10^{-5}$	0,013236	0.6	$1{,}63\text{x}10^{-5}$	$6{,}14\text{x}10^{-5}$	0,003208
0.7	$6{,}67\text{x}10^{-5}$	$6{,}37\text{x}10^{-5}$	0,016558	0.7	$1{,}63\text{x}10^{-5}$	$6{,}14\text{x}10^{-5}$	0,003503
0.8	$7{,}34\text{x}10^{-5}$	$6{,}20\text{x}10^{-5}$	0,013719	0.8	$1{,}63\text{x}10^{-5}$	$6{,}15\text{x}10^{-5}$	0,003944
0.9	$8{,}63\text{x}10^{-5}$	$9{,}23\text{x}10^{-5}$	0,008747	0.9	$1{,}63\text{x}10^{-5}$	$6{,}15\text{x}10^{-5}$	0,004171
1	0,000388	$7{,}32\text{x}10^{-5}$	0,017129	1	$1{,}63\text{x}10^{-5}$	$6{,}15\text{x}10^{-5}$	0,0014

For the case 3:

Min–Max				Probabilistic			
Exigency Value	**MAD Binomial**	**MAD Centered Binomial**	**MAD Gaussian**	**Exigency Value**	**MAD Binomial**	**MAD Centered Binomial**	**MAD Gaussian**
0.1	$6{,}44\text{x}10^{-5}$	0,000137	0,017192	0.1	$4{,}56\text{x}10^{-6}$	$1{,}46\text{x}10^{-4}$	0,001738
0.2	$7{,}80\text{x}10^{-5}$	0,000132	0,022418	0.2	$4{,}72\text{x}10^{-6}$	$1{,}50\text{x}10^{-4}$	0,002504
0.3	$6{,}00\text{x}10^{-5}$	$1{,}68\text{x}10^{-4}$	0,016274	0.3	$4{,}88\text{x}10^{-6}$	$1{,}52\text{x}10^{-4}$	0,003185
0.4	$7{,}42\text{x}10^{-5}$	$9{,}78\text{x}10^{-5}$	0,021039	0.4	$5{,}00\text{x}10^{-6}$	$1{,}53\text{x}10^{-4}$	0,004178
0.5	$1{,}19\text{x}10^{-4}$	$9{,}54\text{x}10^{-5}$	0,024507	0.5	$5{,}03\text{x}10^{-6}$	$1{,}53\text{x}10^{-4}$	0,005627
0.6	$1{,}54\text{x}10^{-4}$	$9{,}38\text{x}10^{-5}$	0,03009	0.6	$5{,}04\text{x}10^{-6}$	$1{,}53\text{x}10^{-4}$	0,007513
0.7	$3{,}09\text{x}10^{-4}$	$8{,}69\text{x}10^{-5}$	0,030986	0.7	$5{,}05\text{x}10^{-6}$	$1{,}53\text{x}10^{-4}$	0,00978
0.8	$2{,}43\text{x}10^{-4}$	$1{,}74\text{x}10^{-5}$	0,020277	0.8	$5{,}06\text{x}10^{-6}$	$1{,}53\text{x}10^{-4}$	0,012366
0.9	$5{,}40\text{x}10^{-4}$	$8{,}38\text{x}10^{-5}$	0,034786	0.9	$5{,}07\text{x}10^{-6}$	$1{,}53\text{x}10^{-4}$	0,014248
1	0,001334	$6{,}95\text{x}10^{-5}$	0,031344	1	$5{,}07\text{x}10^{-6}$	$1{,}53\text{x}10^{-4}$	0,011949

A.7 Validation Index Applied to Second–Order PMD Detection (Section 3.7)

Min–Max				Probabilistic			
Exigency Value	**MAD Binomial**	**MAD Centered Binomial**	**MAD Gaussian**	**Exigency Value**	**MAD Binomial**	**MAD Centered Binomial**	**MAD Gaussian**
0.1	$3{,}90\text{x}10^{-5}$	0,000145	0,001007	0.1	$8{,}98\text{x}10^{-6}$	0,000127	0,000284
0.2	$3{,}80\text{x}10^{-5}$	0,000138	0,002113	0.2	$9{,}31\text{x}10^{-6}$	0,000131	0,000424
0.3	$1{,}89\text{x}10^{-5}$	0,000154	0,001606	0.3	$9{,}67\text{x}10^{-6}$	0,000135	0,000319
0.4	$3{,}54\text{x}10^{-5}$	0,000137	0,002612	0.4	$1{,}00\text{x}10^{-5}$	0,00014	0,000243
0.5	$2{,}48\text{x}10^{-5}$	0,000153	0,004022	0.5	$1{,}03\text{x}10^{-5}$	0,000145	0,000217
0.6	$2{,}70\text{x}10^{-5}$	0,00014	0,001409	0.6	$1{,}03\text{x}10^{-5}$	0,000146	0,000248
0.7	$2{,}41\text{x}10^{-5}$	0,000134	0,003298	0.7	$1{,}03\text{x}10^{-5}$	0,000146	0,000315
0.8	$4{,}34\text{x}10^{-5}$	0,000136	0,006328	0.8	$1{,}03\text{x}10^{-5}$	0,000147	0,000407
0.9	$6{,}61\text{x}10^{-5}$	0,00013	0,005331	0.9	$1{,}03\text{x}10^{-5}$	0,000147	0,000476
1	0,00014	0,000123	0,004426	1	$1{,}03\text{x}10^{-5}$	0,000147	0,000491

A.8 Calculation of Validation Indices for the Microresonator Ring Data (Section 5.5)

- *Optical combs lines spectra*:

Min–Max				Probabilistic			
Exigency Value	**MAD Binomial**	**MAD Centered Binomial**	**MAD Gaussian**	**Exigency Value**	**MAD Binomial**	**MAD Centered Binomial**	**MAD Gaussian**
0.1	$3.2259x10^{-5}$	$3.2112x10^{-5}$	0.0013	0.1	$6.6725x10^{-6}$	$1.3841x10^{-5}$	$2.1824x10^{-4}$
0.2	$3.3211x10^{-5}$	$5.2165x10^{-5}$	0.0053	0.2	$6.8382x10^{-6}$	$1.4126x10^{-5}$	$3.4140x10^{-4}$
0.3	$1.7933x10^{-5}$	$5.6882x10^{-5}$	—	0.3	$6.1540x10^{-6}$	$1.4441x10^{-5}$	$4.5973x10^{-4}$
0.4	$2.0094x10^{-5}$	$6.4142x10^{-5}$	—	0.4	$5.8535x10^{-6}$	$1.2985x10^{-5}$	$6.1673x10^{-4}$
0.5	$4.3435x10^{-4}$	$1.0493x10^{-4}$	—	0.5	$5.9545x10^{-6}$	$1.3273x10^{-5}$	$7.9136x10^{-4}$
0.6	$7.1506x10^{-4}$	$9.9709x10^{-5}$	—	0.6	$6.0545x10^{-6}$	$1.1451x10^{-5}$	$9.0445x10^{-4}$
0.7	$9.7167x10^{-4}$	$2.2514x10^{-4}$	—	0.7	$6.1465x10^{-6}$	$1.1608x10^{-5}$	0.0012
0.8	0.0011	0.0032	—	0.8	$6.2030x10^{-6}$	$1.1784x10^{-5}$	0.0015
0.9	—	0.0020	—	0.9	$6.2143x10^{-6}$	$1.1984x10^{-5}$	0.0016
1	—	—	—	1	$6.2186x10^{-6}$	$1.2215x10^{-5}$	$1.9114x10^{-4}$
Min–Max				**Probabilistic**			
Exigency Value	**MAD Binomial**	**MAD Centered Binomial**	**MAD Gaussian**	**Exigency Value**	**MAD Binomial**	**MAD Centered Binomial**	**MAD Gaussian**
0.1	2	2	237	0.1	24	11	121
0.2	2	3	806	0.2	24	11	116
0.3	4	3	—	0.3	22	11	117
0.4	4	4	—	0.4	21	10	123
0.5	91	6	—	0.5	21	10	127
0.6	140	10	—	0.6	21	9	129
0.7	306	78	—	0.7	21	9	136
0.8	918	585	—	0.8	21	9	146
0.9	—	818	—	0.9	21	9	161
1	—	—	—	1	21	9	181

Using the ultrametric distance proposed by [ISA07], the reduction of number of classes is carried out to the best validation indexes for MAD. The results are shown below:

Min–Max, Lamda–1, Exigency value: 0.8, Classes (New): 26, ICC (New): $9.365x10^{-4}$

Min–Max, Lamda–3, Exigency value: 0.8, Classes: 58, ICC: $2.2514x10^{-4}$.

Min–Max, Gauss, Exigency value: 0.2, **Classes (New): 22, ICC (New): $2.2426x10^{-4}$.**

Probabilistic, Gauss, Exigency value: 0.9, **Classes (New): 37, ICC (New): $5.8793x10^{-4}$**

- *Intensity noise*:

Min–Max				Probabilistic			
Exigency Value	**MAD Binomial**	**MAD Centered Binomial**	**MAD Gaussian**	**Exigency Value**	**MAD Binomial**	**MAD Centered Binomial**	**MAD Gaussian**
0.1	0.0022	—	0.0027	0.1	0.0020	0.0011	0.0029
0.2	0.0022	0.0016	0.0026	0.2	0.0020	0.0011	0.0027
0.3	0.0022	0.0015	0.0025	0.3	0.0020	0.0011	0.0025
0.4	0.0021	0.0013	0.0024	0.4	0.0020	0.0012	0.0025
0.5	0.0021	0.0012	0.0023	0.5	0.0020	0.0012	0.0024
0.6	0.0021	0.0018	0.0034	0.6	0.0020	0.0012	0.0023
0.7	0.0021	0.0014	0.0034	0.7	0.0020	0.0012	0.0022
0.8	0.0020	0.0015	0.0026	0.8	0.0020	0.0012	0.0019
0.9	8.6446×10^{-4}	0.0012	0.0036	0.9	0.0020	0.0012	0.0015
1	9.3029×10^{-4}	0.0016	0.0035	1	0.0020	0.0012	3.8641×10^{-4}

Min–Max				Probabilistic			
Exigency Value	**MAD Binomial**	**MAD Centered Binomial**	**MAD Gaussian**	**Exigency Value**	**MAD Binomial**	**MAD Centered Binomial**	**MAD Gaussian**
0.1	2	—	3	0.1	2	2	3
0.2	2	2	3	0.2	2	2	3
0.3	2	2	3	0.3	2	2	3
0.4	2	2	3	0.4	2	2	3
0.5	2	2	3	0.5	2	2	3
0.6	2	2	4	0.6	2	2	3
0.7	2	2	4	0.7	2	2	3
0.8	2	2	5	0.8	2	2	3
0.9	3	2	6	0.9	2	2	3
1	3	2	6	1	2	2	3

A.9 Calculation of HVS and HIFEAN for the Microresonator Ring Data (Section 5.5)

HVS CALCULATION – Optical Combs Lines Spectra						
Classes	**γ = 0.1**	**γ = 0.2**	**γ = 0.3**	**γ = 0.4**	**γ = 0.5**	**Average**
1	0,830243	0,879606	0,839601	0,777342	0,72635	0,80572475
2	0,838462	0,897773	0,861334	0,794757	0,737127	0,8258906
3	0,831993	0,902927	0,882161	0,822999	0,763517	0,8407194
4	0,847487	0,898634	0,854414	0,784894	0,726348	0,8223554
5	0,852207	0,934485	0,920075	0,853271	0,778671	0,8677418
6	0,841056	0,913447	0,891953	0,828864	0,764188	0,8479016
7	0,855238	0,900981	0,851943	0,780007	0,719652	0,8215642
8	0,848388	0,92783	0,91263	0,848272	0,776795	0,862783
9	0,834115	0,893313	0,859951	0,797286	0,741686	0,8252702
10	0,839126	0,898008	0,861296	0,794784	0,737114	0,8260656
11	0,861862	0,936491	0,90955	0,834797	0,759111	0,8603622
12	0,841003	0,905968	0,876091	0,811109	0,750024	0,836839
13	0,844525	0,901285	0,861319	0,792282	0,73299	0,8264802
14	0,868633	0,910764	0,854211	0,775042	0,709833	0,8236966
15	0,875598	0,955214	0,928746	0,847256	0,762661	0,873895
16	0,852367	0,894169	0,841757	0,769871	0,712284	0,8140896
17	0,84724	0,894617	0,847862	0,778574	0,72145	0,8179486
18	0,864414	0,940302	0,91301	0,83644	0,759146	0,8626624
19	0,87404	0,936676	0,895822	0,814073	0,737313	0,8515848
20	0,849642	0,893727	0,844315	0,774274	0,717155	0,8158226
21	0,849633	0,895736	0,84727	0,776769	0,718995	0,8176806
22	0,869679	0,938338	0,903756	0,824469	0,747462	0,8567408
23	0,853416	0,896058	0,844325	0,772335	0,713987	0,8160242
24	0,850003	0,893787	0,844245	0,774211	0,717019	0,815853
25	0,854168	0,896115	0,843316	0,770638	0,712195	0,8152864
26	0,645253	0,793506	0,925433	0,990579	0,984517	0,8678576
HIFEAN CALCULATION – Optical Combs Lines Spectra						
Classes	**γ = 0.1**	**γ = 0.2**	**γ = 0.3**	**γ = 0.4**	**γ = 0.5**	**Average**
1	**0,251613**	0,434568	0,683504	0,93451	0,890849	0,6390088
2	**0,242349**	0,423978	0,677256	0,939596	0,87201	0,6310378
3	**0,219631**	0,3943	0,643972	0,912831	0,880494	0,6102456
4	**0,26243**	0,453598	0,714449	0,897221	0,827944	0,6311284
5	**0,204925**	0,380939	0,641574	0,926191	0,829824	0,5966906
6	**0,225856**	0,404895	0,661285	0,930525	0,845915	0,6136952
7	**0,279219**	0,47797	0,745076	0,860208	0,789498	0,6303942
8	**0,210775**	0,387918	0,647409	0,925967	0,831811	0,600776
9	**0,245637**	0,428129	0,680793	0,936501	0,865676	0,6313472
10	**0,245054**	0,427939	0,682258	0,934102	0,86461	0,6307926
11	**0,228425**	0,412841	0,68044	0,890285	0,800469	0,602492
12	**0,233996**	0,414963	0,670348	0,933084	0,855905	0,6216592
13	**0,250332**	0,436398	0,694176	0,918025	0,848057	0,6293976
14	**0,28923**	0,494196	0,768916	0,827754	0,756723	0,6273638
15	**0,238055**	0,42822	0,705794	0,846256	0,750377	0,5937404
16	**0,282058**	0,480692	0,745766	0,868787	0,802837	0,636028
17	**0,271732**	0,465777	0,727515	0,886994	0,819339	0,6342714
18	**0,241206**	0,429436	0,700855	0,867084	0,777242	0,6031646
19	**0,260713**	0,457685	0,734644	0,836864	0,752373	0,6084558
20	**0,27882**	0,475867	0,739559	0,874453	0,807177	0,6351752
21	**0,274247**	0,469694	0,732836	0,880539	0,813031	0,6340694

22	**0,255209**	0,449086	0,724062	0,845802	0,758915	0,6066148
23	**0,285109**	0,484877	0,751198	0,860311	0,792899	0,6348788
24	**0,283136**	0,481498	0,746052	0,867072	0,799393	0,6354302
25	**0,283303**	0,482758	0,748997	0,863349	0,796726	0,6350266
26	**0,02718**	**0,023311**	**0,128088**	**0,297973**	0,505832	**0,1964768**

HVS CALCULATION – Intensity noise data						
Classes	**γ = 0.1**	**γ = 0.2**	**γ = 0.3**	**γ = 0.4**	**γ = 0.5**	**Average**
1	0,96914	0,79940	0,61006	0,48417	0,41251	0,655056
2	0,82300	0,77213	0,68880	0,62421	0,58348	0,698324
3	0,78970	0,61388	0,50436	0,44189	0,40579	0,551124
4	0,72830	0,49214	0,36178	0,29613	0,26515	0,4287
5	0,62167	0,43385	0,33732	0,28731	0,26351	0,388732
6	0,48651	0,43606	0,41668	0,43047	0,46280	0,446504
HIFEAN CALCULATION – Intensity noise data						
Classes	**γ = 0.1**	**γ = 0.2**	**γ = 0.3**	**γ = 0.4**	**γ = 0.5**	**Average**
1	0,68962	0,48206	0,32248	0,28206	0,25927	0,407098
2	0,62047	0,80605	0,64767	0,58388	0,53890	0,639394
3	0,73632	0,49136	0,40340	0,37445	0,34687	0,47048
4	0,54425	0,26789	0,20254	0,19732	0,18989	0,280378
5	0,50060	0,30224	0,24146	0,22848	0,21642	0,29784
6	0,76199	0,86037	0,79751	0,76927	0,72779	0,783386

A.10 Recent Advances in OFC generation (Brief Overview)

Recently, OFCs have had an extraordinary evolution to create a large number of comb lines in wide optical width, optimal stability, and low flatness variation. In [PFE14], a coherent communications network with a data stream of 392 Gbit/s is developed through microresonator Kerr frequency combs (MKFCs) in order to reduce the phase noise by using quadrature phase–shift keying (QPSK) and 16–state quadrature amplitude modulation (QAM). The same microresonator is used for a feedback stabilization of comb in transmission of a 1.44 Tbit/s data stream over up to 300 km. In [CHI14], an optical generation scheme of high–order modulation formats (16–QAM at 100.4 Gbit/s and 64–QAM at 120 Gbit/s) is developed by using a mode–locked laser that generates comb spacing at 10 GHz. The above shows an optimal transmission of 80 Gbit/s 16–QAM through 80 km SMF after to be compensated with 20 km dispersion compensating fiber (DCF). In [ERI14], a superconducting resonator is proposed to generate frequency combs spanning 0.5 to 20 GHz through thin films of niobium–titanium nitride that guarantee low loss, high nonlinearity, low frequency dispersion, and optimal operation temperature. In [JOH14], an original architecture based on fiber–microresonator dual–cavity is built–up at 880 nm of comb bandwidth without the use of CW pump laser. The above proposal allows simplifying the use of a single frequency laser by carrying out an intrinsic feedback mechanism based on bandpass filter, an Erbium Doped Fiber Amplifier (EDFA), and a fiber–compensating polarization (FCP). In [Li14], a novel frequency combs generation (to obtain until 11 flat comb lines) using a single polarization modulator (PolM) and a Brillouin–assisted power equalizer (BAPE) is proposed. The goal of BAPE is to optimize the flatness of combs spectrum to flatten the uneven OFC lines by attenuating the optical lines creating power beyond a threshold of the stimulated Brillouin scattering (SBS) and increasing the ones having power below the SBS threshold with an EDFA inside the BAPE. In [SCH14], a stabilized Yb–fiber frequency comb operating at 1030 nm and pulse repetition frequency of 375 MHz is built. The comb offset is controlled by a super–continuum with a coherent component at 780.2 nm and Rb–stabilized external cavity diode laser in order to get a radio–frequency (RF) beat used to stimulate in the carrier envelope offset frequency of the Yb–fiber laser. In [KUN14], a novel technique with an Origami–10 mode–locked femtosecond laser from Onefive for generating a 100 MHz pulse train at 1047 nm of central wavelength is created. The experiment allows reducing the relative fluctuations of the optical carrier frequency 1.1×10^{-18} at 1 s and averaging down to the 10^{-22} level at 10000 s. This offset frequency stabilization holds the record low laser relative intensity noise to date. In [BRA14], a soliton induced Cherenkov radiation (also known as dispersive wave emission and explain in [AKH95]) is generated by an optical Kerr microresonator frequency combs that could make useful in frequency metrology and effectiveness of planar microresonator technology. According to the results, the technique is useful in chip frequency combs because expands the frequency comb bandwidth towards normal group–velocity dispersion (GVD) which can extend the frequency comb bandwidth to the visible wavelength range (a regime where most materials have normal GVD). In addition, the technique is able to realize quantitative predictions of the generated coherent spectra possible.

The mentioned recent advances on OFC have carried towards the generation of stable comb lines spectrum, optimal flatness, and a large spectral width with many lines. The most of novel proposals are betting the use of Kerr microresonator frequency combs at different applications but mode–locked lasers have also made interesting progresses for reducing the intensity noise and

guaranteeing stability. In the optical modulator case, the seeking of ultra–flat comb lines with MZMs has been the main topic in the last year for getting an optimal spectrum whose main advances are: ultra–flat comb lines spectrum with dual–parallel MZM (DP–MZM) [WAN14], OFCs with MZM and recirculating frequency shifter loop based on IQ modulator (In–phase and Quadrature) driven by RF clock signals [WU14], and OFC with a flat, rectangular frequency combs with tunable frequency spacing and bandwidth at 260 GHz that guarantees a low flatness variation within 0.6 dB [PRE14].

Inside of the evolution of OFC, several analysis and techniques for anticipating the behavior and performance of an OFC spectrum have been worked from point of view mathematical and simulation. In ultrafast mode–locking process, a mathematical model was proposed to predict the phase noise power spectral density in order to verify the relation between the mode–locking mechanism and quantum noise in the OFC spectrum [MART08]. In other technique, the dynamics of the comb were calculated through a numerical model for predicting the generation of Kerr combs in monolithic whispering–gallery–mode (WGM) resonators [CHEM10]. The dynamic of OFCs was also analyzed to predict the dissipative temporal soliton formation and the minimal soliton width in a microresonator by numerical simulations [HER14]. Other kinds of prediction in OFC were the developing of an analytical model of the cavity–comb to predict an intrinsic spectral filtering action in an OFC spectrum [AVI13], changing the comb bandwidth in several cases [COE13], the stability properties of Kerr frequency combs generated in microresonators [ERK14], and theoretical predictions of tunable comb generator (TCG) [CHEN14]. The most recent advance in prediction of OFC behavior in microresonators is based on mathematical models such as nonlinear oscillations and bifurcations, whose results were corroborated by experimental observations [ABR14].

A.11 Global Average of Computational Cost

From Tables 5.6, 5.7, and 5.8, the averages for each rule are considered to calculate a global average of computational cost. In the following table, the averages for each rule are organized according to the kind of experiment. It is important to clarify the computational cost was calculated with the "clock" function defined by Matlab, where the calculation was carried out in the following steps of algorithm:

- *Acquisition time from OSA to computer*: It is the time to store the data matrix (Power (dBm) vs Wavelength (nm)) from OSA to computer, using an acquisition card from *National Instruments*. This time is measured using the "clock" function.
- *Algorithmic time of method:* It is the used time to start the LAMDA method, the validation index of class, the IFCA−MV, the HIFEAN, and the desfuzzification. This time can increase whether the number of descriptors (number of OFC spectra) and the number of samples (associated with wavelength) are large. To calculate this time, the "clock" function from Matlab is applied in the algorithm.
- *Acquisition time from computer to pulse shaper*: It is the acquisition time to send the vectors of attenuation and phase towards pulse shaper (USB connection). Such vectors are generated as the final response of method after comparing the original spectrum respect to the predicted spectrum by the proposed method (obtained by the desfuzzification step). This time was calculated with the "clock" function from Matlab.
- *Response time inside pulse shaper*: It is the time to store the vectors of attenuation and phase from computer and to configure the voltage magnitudes in the SLM. This time is given by provider and the scale is in miliseconds.

In the following Table, the global computational cost is calculated through the computational costs in each experiment.

RULE	Picosecond pulsed laser (s)	Femtosecond pulsed laser (s)	IMS – MZM (s)	Microresonator ring (Spectra) (s)	Microresonator ring (noise intensity) (s)	AVERAGE (s)
27	91,3274	156,2193	88,2609	264,5759	10,6775	122,2122
29	90,4899	168,4427	88,28044	265,5107	10,5971	124,6642
46	90,1128	175,4453	179,8804	253,5791	11,1341	142,0303
58	89,3282	177,7616	151,5612	260,3564	10,1863	137,8387
78	89,9829	164,2725	152,83	273,8856	10,2971	138,2536
90	90,6183	163,889	154,8798	336,3171	10,1361	151,1681
110	90,4137	163,205	153,9527	371,9643	10,5536	158,0179
172	89,5178	150,1994	88,6654	439,3538	10,186	155,5845
184	89,2808	148,83	90,6212	442,6186	9,6488	156,1999
GLOBAL AVERAGE						**142,88**